APPLIED COMPUTATIONAL ELECTROMAGNETICS SOCIETY JOURNAL

August 2015
Vol. 30 No. 8
ISSN 1054-4887

The ACES Journal is abstracted in INSPEC, in Engineering Index, DTIC, Science Citation Index Expanded, the Research Alert, and to Current Contents/Engineering, Computing & Technology.

The illustrations on the front cover have been obtained from the research groups at the Department of Electrical Engineering, The University of Mississippi.

EMERITUS EDITORIAL ASSISTANTS

AUGUST 2015 REVIEWERS

THE APPLIED COMPUTATIONAL ELECTROMAGNETICS SOCIETY

JOURNAL

Vol. 30 No. 8 August 2015

TABLE OF CONTENTS

Application of Ant Colony Optimization Algorithm to Pattern Synthesis of Uniform Circular Antenna Array

Amir Saman Zare [1] and Saba Baghaiee [2]

[1] Darmstadt University of Technology, Darmstadt, Germany
amirsaman1989@gmail.com

[2] Information Technology Engineering Department
Ershade Alborz University of Tehran, Tehran, Iran
Saba.baghai@gmail.com

Abstract ─ The radiation pattern of the antenna arrays is most important problem in communications technology. In this paper, the optimization of uniform circular antenna array is efficiently solved by ant colony optimization (ACO) Method. The proposed method of optimization is used to determine the suitable cost function which leads to achieve the maximum reduction in side lobe level and provide the maximum directivity towards the direction. To optimize the desired antenna array pattern also one parameter is considered to be optimized which is the angular position of each element.

Index Terms ─ Ant colony optimization, array factor, directivity, side lobe level, uniform circular antenna array.

I. INTRODUCTION

Circular antenna array has been widely used in communications technology in radar, sonar and as it is useful in high power transmission, reduced power consumption and enhanced spectral efficiency [1], [22].The design of this structure is a growing avenue of research in electromagnetics [7], [10], [11], [12] and is very useful in different applications like radio direction finding, space navigation and third generation wireless communication systems [7]-[9].The techniques of the arrays pattern optimization has received considerable attention in the past and is still of great interest [2] and are very important in communications systems. The technique of pattern optimization including the control of the complex weights (the amplitude and phase), the excitation amplitude only and phase-only, and the element position only have been extensively considered in the literature [1], [2], [7]-[30]. The position-only is of particular interest in pattern optimization [22]. In some of the articles [7], [19], [22] the author presents a method of control by phase and angular position for forming signals in prescribed directions with low SLL high directivity and also high signal to interference ratio (SIR) [22]. The technique proposed in this paper is based on ant colony optimization [23], [32]-[34] and ACO will be applied to find the angular positions of the antenna array elements that are optimum to provide the radiation pattern of uniform circular array (UCA). Hence, in this paper the synthesis problem is finding the angular positions of each element by ACO to provide the radiation pattern with maximum reduction in the side lobe level and high directivity at a fixed main beam width. In the final section the performance of ACO is compared GA (genetic algorithm) and IWO (invasive weeds optimization). The parameters used in GA and IWO are selected to be the same as those used in ACO, which ensure a fair comparison in computation efficiency and solution quality.

II. CIRCULAR ANTENNA ARRAY FUNCTION

Consider a circular antenna array of N antenna elements non-uniformly spaced on a circle of radius a in the x-y plane, Fig. 1 .The elements in the circular antenna array are taken to be isotropic sources, so the radiation pattern of this array can be described by its array factor. In the x-y plane, the array factor for the circular array shown in Fig. 1 is given by [4]:

$$AF(\phi,\theta)=\sum_{n=1}^{N} I_n\, e^{j[\beta a \sin\theta \cos(\varphi-\varphi_n)+\alpha_n]}, \tag{1}$$

$$\varphi_n = \frac{2\pi(n)}{N}. \tag{2}$$

In the above equations, I is the excitation amplitude value and is the same for each antenna components. α_n represents the excitation phase of the n-th element and φ_n is the angular position of the n-th element in x-y plane. To direct the peak of the main beam in the φ_0 direction,

Submitted On: December 24, 2013
Accepted On: May 25, 2015

the excitation phase of the *n*-th element is chosen to be:

$$\alpha_n = -\beta a \sin\theta_0 \cos(\varphi_0 - \varphi_n). \quad (3)$$

The array factor can be obtained by considering the elements to be point sources which is given by:

$$AF(\varphi,\theta) = \sum_{n=1}^{N} e^{j\beta a\left[\sin\theta\cos(\varphi-\varphi_n)-\sin\theta_0\cos(\varphi_0-\varphi_n)\right]} = \sum_{n=1}^{N} e^{j\beta a(\cos\psi-\cos\psi_0)}. \quad (4)$$

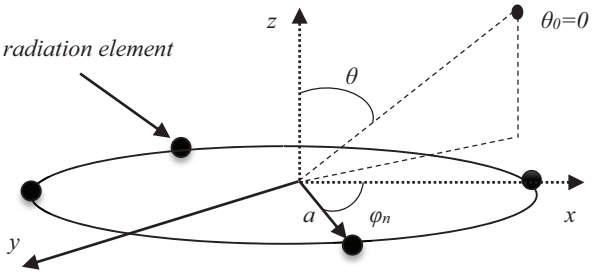

Fig. 1. Geometry of circular antenna array

A general function of optimization that we study consists of the number of objectives. This function value is important to optimize the side lobes level and directivity and also will be obtained by ACO. In this cause the performance of a uniform circular array will be improved substantially, with respect to the circular array with the conventional progressive angular positions of the elements (in terms of the side lobe level and directivity). We should present the basis function to improve the array factor amount which leads to SLL reduction and high directivity [6]. Mathematical problem can be written as follows:

$$\begin{gathered} \textit{Minimize} \quad f(\varphi) \Rightarrow \textit{Objective function} \\ \textit{Subject to } \varphi \in \chi, \\ \chi \textit{ is known as the feasible set, it leads to } (\chi_{Optimum}): \\ f(\varphi_{Optimum}) \le f(\varphi) \\ \min SLL \\ s.t. \quad f(\varphi_{optimum}), \\ 0 \le \varphi_n \le 2\pi \quad n = 1,2,\ldots N \end{gathered} \quad (5)$$

where:

$$f_\theta(\varphi) = 2\sum_{n=1}^{N} \cos\left(\beta a(\cos\psi - \cos\psi_0)\right).$$

The final equation of the notation (5) is the basis function for optimization problem which will be discussed in this paper. In our design, to demonstrate the advantages of the proposed design, the results obtained using angular positions excitations will be displayed in different states of φ_0, therefore in desired design problem we choose φ_0 to be $90°$ and $0°$ for receiving better experimental results. The peak of the main beam is in the *x* direction [4], [5].

III. ANT COLONY OPTIMIZATION

In this part, it will be presented how the ACO can be used for solving the problems. ACO has a very strong ability to solve any hard combinatorial optimization problems and can be a powerful method for the synthesis of antenna array radiation pattern in adaptive beamforming [32]. Desired method inspired by the ant's foraging behavior proposed by Dorigo in his Ph.D. thesis in 1992 and it has been used to solve a different type of problems by employing different realizations of the algorithm [34]. ACO means algorithms based on the ant behavior in searching for food and posterior transportation to the colony have to be stored. These insects have the ability to find the "shortest path" in this task using pheromone. Some ant species use pheromone for making paths on the ground, in their way from the food to the nest. This helps other ants, by sensing pheromone, to follow the path towards food discovered by other ant. Because ants deposit pheromone while walking, a larger number of ants on a path results in a larger amount of pheromone, this larger amount of pheromone stimulates more ants to choose that path and so on until finally, the ants converge to one single (short) path. Also, these pheromone evaporate with time to "delete" the path to an exhausted food source [34].

A. Implementation of the algorithm

The idea behind ACO is to mimic this behavior by using artificial ants. The outline of a basic ACO algorithm is shown in Fig. 2. The ACO version implemented is capable to deal with both continuous and discrete variables. The question that arises is how ACO (first used to solve combinatorial problems) can deal with continuous variables. A possible answer to this question would be the conversion of the continuous optimization problem into a discrete one as proposed in the past in some of the papers. Instead, the present continuous version extends ACO in order to work directly with continuous variables. In this way, the first point that has to be taken into account is how the colony is represented. Following the idea of directly using continuous variables, a colony of *m* ants can be expressed as a $m \times n$ matrix $C = [ant_1, ant_2, \ldots, ant_m]^T$, where $ant = [x_1, x_2, \ldots, x_n]^T$ is a vector of design variables that corresponds to a single ant [33]-[34].

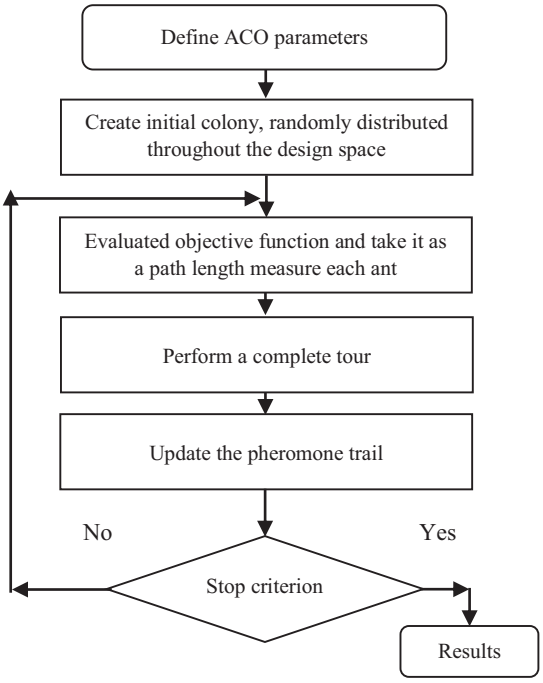

Fig. 2. Basic scheme for ACO.

The second point is how to model the pheromone communication scheme. The continuous version of ACO models the pheromone trail as an amount of pheromone laid on the path. As suggested by Pourtakdoust and Nobahari and Socha, for the continuous model implementation this can be achieved by using a normal probability distribution function (PDF). In this formulation, for the dimension *i* of the design space, the pheromone trail, τ_i, can be described as follows:

$$\tau_i\left(x_i\right) = e^{-\frac{\left(x_i - x_i^*\right)^2}{2\sigma_i^2}}, \tag{6}$$

where x_i^* is the *i*-th coordinate of the best point found by the optimization task within the design space until the current iteration and σ_i is an index related to the ants aggregation around the current minimum for the *i*-th coordinate of the design space. To close the definition of pheromone, τ, the aggregation index, σ, must be defined. Thus, by taking y as the *i*-th column of the colony matrix C, the aggregation index for the *i*-th dimension, σ_i, is given by:

$$\sigma_i = \sqrt{\frac{1}{m-1}\sum_{j=1}^{m}\left(y_i - \overline{y}\right)}, \tag{7}$$

where $\overline{y}$ is the mean value of the vector y. It is worth making some remarks about the updating process of the values of each design variable for all ants of the colony. This is the process in which, for a given iteration, each ant sets the values for the trial solution based on the probability distribution given by Eq. 6. Computationally, this can be achieved through a random number generator based on a normal PDF that plays the role of a variable transition (update) rule to choose the next design variable value associated with each ant. From Eq. 6, it can also be noticed that each variable uses a different random number generator together with its respective PDF. About the pheromone scheme, it is possible to see that the concentration of pheromone increases in the area of the candidate to the optimum. This approach (also called as positive update) reinforces the probability of the choices that lead to good solutions [23], [33], [34]. The number generating and updating processes will be done continuously until the solution meets the error criteria. In other words if best solution does not change after some iteration, the process will be terminated and the best solution is the best value which optimizes the defined cost function. Fast convergence to the best global solution is the most important and desirable feature of the ant colony optimization method. The number of ants and/or iterations in the algorithm can be selected based on the computational capacity. Actually, in the following examples we have used a relatively low number of ants but a number of iterations large enough to guarantee the convergence of the algorithm to the desired solution. The food is defined as the desired condition, i.e., the angular position of the array elements. Finally, the adopted stopping criterion is to complete the selected number of iterations [33].

IV. NUMERICAL RESULTS

In this section, some computer simulations are conducted to verify the validation of the proposed method. We consider circular antenna array with *10* and *12*-element arrays with element spacing $d = \lambda/2$, where λ denotes the wavelength corresponding to the operating frequency of the narrow band sources [3]. As mentioned to illustrate the performance of the ant colony optimization method, some examples were simulated; Figs. 3 and 4 show the normalized unmodified patterns of the uniform circular antenna array with high level of side lobes comparing to main beam. We can point to the some places like: (θ=22.2° and θ=46.3° at φ_0=90° *N=10*), (θ=90° at φ_0=0° *N=10*), (θ=23° and θ=45° at φ_0=90° and φ_0=0° *N=12*). Table 1 consists of the desired unmodified states numerical results.

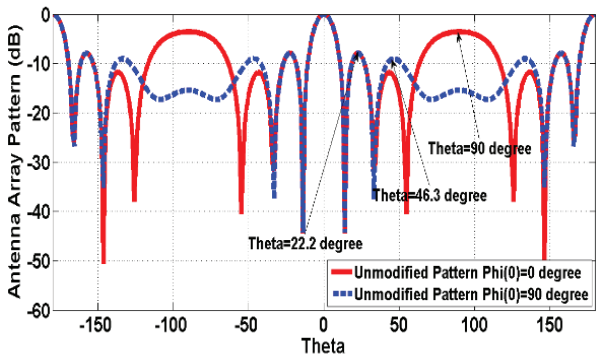

Fig. 3. Unmodified patterns at $\varphi_0 = 90°$ and $\varphi_0 = 0°$ $N=10$.

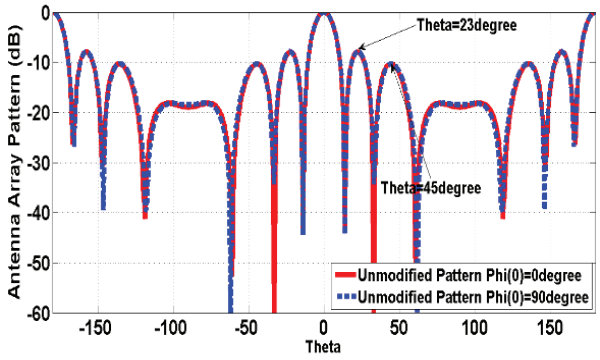

Fig. 4. Unmodified patterns at $\varphi_0 = 90°$ and $\varphi_0 = 0°$ $N=12$.

Table 1: Unmodified patterns information

SLL	Directivity	FNBW	AF	φ0	SIR	N
-7.9 dB	8.2 dB	28°	84.4	90°	7.3 dB	10
-3.6 dB	3.4 dB	28°	112	0°	5.3 dB	10
-7.9 dB	8.53 dB	28°	72.2	90°	7.5 dB	12
-8 dB	8.93 dB	28°	72.8	0°	7.9 dB	12

We assigned the especial way using MATLAB for synthesis the antenna array pattern with the desired values of the proposed antenna parameters and reducing array factor value by optimizing angular positions of the antenna elements after some iterations to optimize the unmodified signals, the number of iterations needed to reach an acceptable solution is *1000-3000*, these values will be investigated and the results will be presented in two different modes, for *10* and *12*-element circular arrays at $\varphi_0=90$ and $\varphi_0=0°$. The cost function will be constructed for maximizing the SLL reduction with high directivity as well as minimizing the array factor value. Finally, the optimized parameters which lead to SLL reduction and high directivity for each directional beam steering will be illustrated all. The excitation positions for each antenna element are constrained to lie between *0* and 2π. The excitation angular positions of the antenna elements are now obtained by ACO to improve the desired parameters values. These obtained results will be computed as given in Tables 2-5.

Table 2: The ACO optimized values (φ_n) at $\varphi_0 = 90°$ for Fig. 5

Iter. 3000	Iter. 2760	Iter. 2340	Iter. 1800	Iter. 870	
79°	90°	90°	90°	90°	φ 1
9°	10°	10°	10°	10°	φ 2
36°	36°	30°	36°	36°	φ 3
12°	9°	7°	12°	7°	φ 4
30°	30°	36°	30°	30°	φ 5
259°	270°	270°	270°	270°	φ 6
189°	190°	190°	190°	190°	φ 7
216°	216°	210°	216°	216°	φ 8
192°	189°	187°	192°	187°	φ 9
210°	210°	216°	210°	210°	φ 10

Table 3: The ACO optimized values (φ_n) at $\varphi_0 = 0°$ for Fig. 6

Iter. 3000	Iter. 2678	Iter. 2115	Iter. 1653	Iter. 675	
78.3°	78.3°	78.3°	78.3°	78.3°	φ 1
2.25°	18°	15°	12°	9°	φ 2
60°	60°	60°	60°	60°	φ 3
98°	98°	99°	99°	99°	φ 4
50°	50°	50°	45°	36°	φ 5
258.3°	258.3°	258.3°	258.3°	258.3°	φ 6
182.25°	198°	195°	192°	189°	φ 7
240°	240°	240°	240°	240°	φ 8
278°	278°	279°	279°	279°	φ 9
230°	230°	230°	225°	216°	φ 10

Table 4: The ACO optimized values (φ_n) at $\varphi_0 = 90°$ for Fig. 7

Iter. 3000	Iter. 2835	Iter. 2215	Iter. 1945	Iter. 908	
49°	48°	51°	56°	60°	φ 1
9°	9°	9°	9°	9°	φ 2
26°	23°	22°	30°	21°	φ 3
6°	6°	7°	6°	6°	φ 4
30°	30°	30°	30°	30°	φ 5
90°	90°	90°	90°	90°	φ 6
229°	228°	231°	236°	240°	φ 7
189°	189°	189°	189°	189°	φ 8
206°	203°	202°	210°	201°	φ 9
186°	186°	187°	186°	186°	φ 10
210°	210°	210°	210°	210°	φ 11
270°	270°	270°	270°	270°	φ 12

Table 5: The ACO optimized values (φ_n) at $\varphi_0 = 0°$ for Fig. 8

Iter. 3000	Iter. 2942	Iter. 2321	Iter. 1825	Iter. 893	
78°	78°	78°	78°	78°	φ 1
40°	45°	36°	30°	30°	φ 2
64°	64°	64°	60°	64°	φ 3
90°	90°	90°	90°	90°	φ 4
60°	58°	50°	50°	50°	φ 5
3.6°	12°	12°	10°	10°	φ 6
258°	258°	258°	258°	258°	φ 7
220°	225°	216°	210°	210°	φ 8
244°	244°	244°	240°	244°	φ 9
270°	270°	270°	270°	270°	φ 10
240°	238°	230°	230°	230°	φ 11
183.6°	192°	192°	190°	190°	φ 12

There are twenty states of array antenna patterns at $\varphi_0=90°$ and $\varphi_0=0°$ in Section 4 that can provide the best conditions for uniform circular array pattern. The Figs. 5-8 present the results obtained with *10* and *12* ants, after *3000* iterations for uniform circular antenna array with *10* and *12* elements (foods were defined as antenna elements angular positions). The figures which we want to present, show the ability of ACO algorithm to improve the circular antenna array pattern in both angles ($\varphi_0=90$ and $\varphi_0=0°$) with good radiation parameters values such as the side lobe level, directivity, SIR, and main pattern beam width, but some of them are right to introduce as optimized signals. We have presented Tables 6-9 to choose the best states.

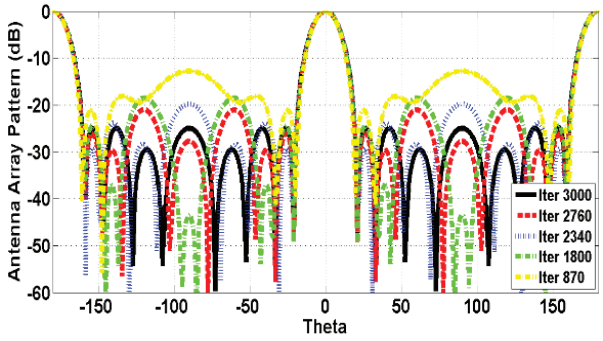

Fig. 5. 10-element array pattern synthesis by ACO $\varphi_0=90°$.

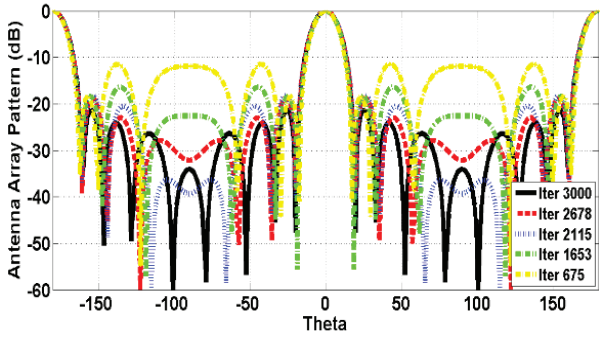

Fig. 6. 10-element array pattern synthesis by ACO $\varphi_0=0°$.

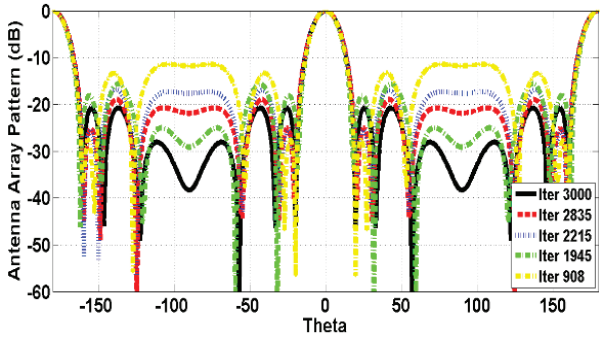

Fig. 7. 12-element array pattern synthesis by ACO $\varphi_0=90°$.

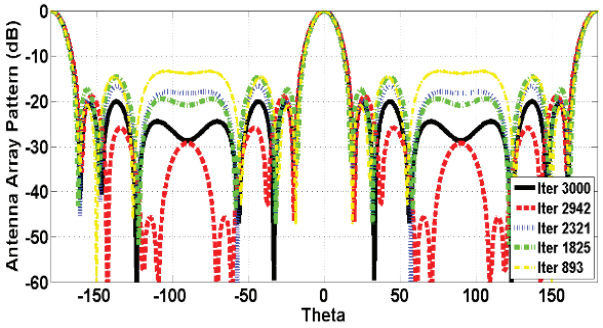

Fig. 8. 12-element array pattern synthesis by ACO $\varphi_0=0°$.

Table 6: Computed parameters for best results at $\varphi_0=90°$ *N=10*

SLL (dB)	-12.8	-18.5	-19.8	-21	-24.9
Directivity	8.9 dB	9.5 dB	9.8 dB	10.3 dB	11 dB
FNBW	45°	44°	42°	42°	41°
AF	60	49	47	46	44
Figure	5	5	5	5	5
Iteration	870	1800	2340	2760	3000
Time (sec)	1234	1700	2361	2678	2856
SIR	25.37 dB	31.2 dB	37.16 dB	37.18 dB	38 dB

Table 7: Computed parameters for best results at $\varphi_0=0°$ *N=10*

SLL (dB)	-11.5	-17.9	-18.21	-18.6	-21.4
Directivity	8.43 dB	9.33 dB	9.58 dB	9.7 dB	10.75 dB
FNBW	35.2°	37.4°	39.8°	39.6°	39.6°
AF	73.3	54.1	48.7	48.3	45.1
Figure	6	6	6	6	6
Iteration	675	1653	2115	2678	3000
Time (sec)	1165	1543	2034	2539	2771
SIR	22.21 dB	25.4 dB	25.6 dB	26.81 dB	34 dB

Table 8: Computed parameters for best results at $\varphi_0=90°$ *N=12*

SLL (dB)	-11.3	-15.5	-16.8	-19	-21.1
Directivity	8.22 dB	8.94 dB	9.18 dB	10.02 dB	10.32 dB
FNBW	40°	39°	40°	42°	40°
AF	74	52.3	59	53.5	47
Figure	7	7	7	7	7
Iteration	908	1945	2215	2835	3000
Time (sec)	1334	1854	2204	2712	2954
SIR	21.7 dB	24.3 dB	30.06 dB	33.7 dB	34.3 dB

Table 9: Computed parameters for best results at $\varphi_0=0°$ *N=12*

SLL (dB)	-13.4	-14.6	-16.6	-18.9	-20.1
Directivity	8.68 dB	8.72 dB	9.11 dB	9.97 dB	10.08 dB
FNBW	39°	39°	39°	40°	40°
AF	67	58.2	58	46	45.7
Figure	8	8	8	8	8
Iteration	893	1825	2321	2942	3000
Time (sec)	1271	1735	2192	2856	2977
SIR	23.1 dB	25.16 dB	26.7 dB	29.7 dB	34.8 dB

Best values include last modified iterations and lesser amounts have been shown in the first modes in Tables 6-9. The information which will be discussed, are presented in Tables 6-9. In these tables the values of directivity and the SLL using ACO are illustrated for array patterns at $\varphi_0=90°$ and $\varphi_0=0°$, which are shown in Figs. 5-8. In Fig. 5 at $\varphi_0=90°$, the best value of directivity for an 10-element array is *11* dB and the best SLL using ACO is *-24.9* dB (3000th iteration). In another mode, Fig. 6 shows 10-element uniform circular array optimized patterns with suitable values of radiation parameters at $\varphi_0=0°$. The best values of directivity and SLL, respectively, for Fig. 6 at $\varphi_0=0°$ (3000th iteration) are *10.75* dB and *-21.4* dB. The best values for 12-element array in Fig. 7 are as follows: directivity is *10.32* dB and SLL is equal to *-21.1* dB at $\varphi_0=90°$ (3000th iteration), the results which are shown in Table 8 are computed for 12-element uniform circular array. In the final state, Fig. 8 shows the 12-element uniform circular array optimized patterns with the suitable measure of desired parameters at $\varphi_0=0°$. The best values of directivity and SLL in this case in order are *10.08* dB and *-20.1* dB (3000th iteration). We analyzed the numerical results from the simulated structures of the antenna patterns and finally we found that the final states (3000th iterations) present better computed results with maximum reduction in SLL and the suitable measures of directivity, so we can introduce them as the states optimized propagations in Figs. 9-12.

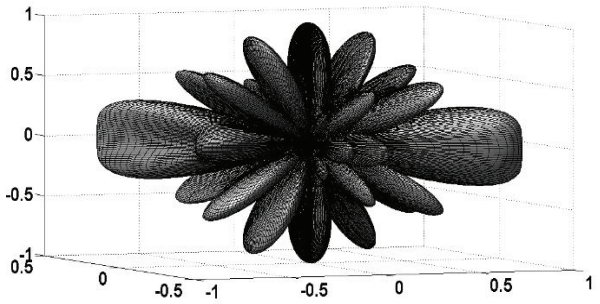

Fig. 9. Optimized state by ACO iteration *3000* at $\varphi_0=90°$ *N=10.*

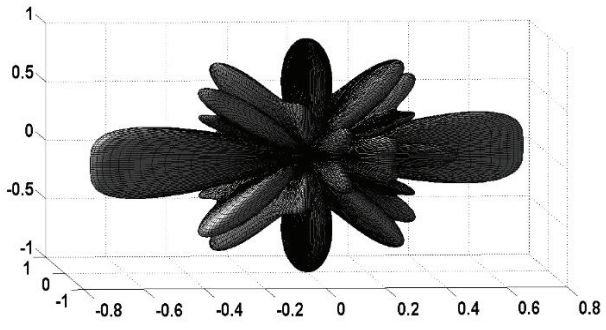

Fig. 10. Optimized state by ACO iteration *3000* at $\varphi_0=0°$ *N=10.*

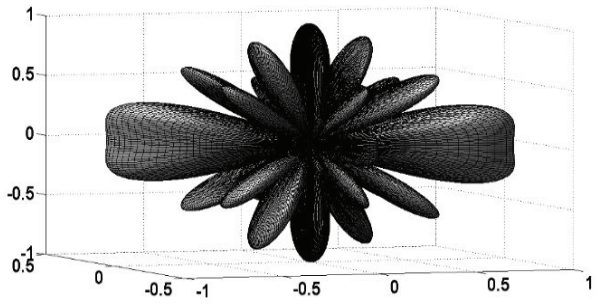

Fig. 11. Optimized state by ACO iteration *3000* at $\varphi_0=90°$ *N=12.*

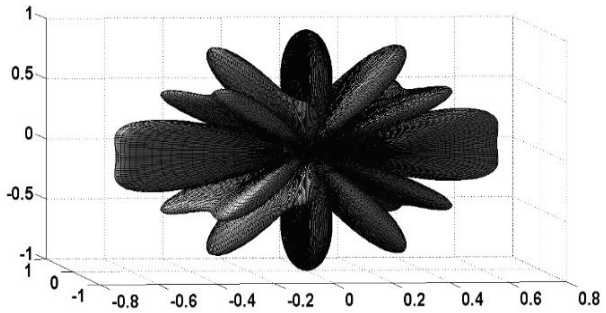

Fig. 12. Optimized state by ACO iteration *3000* at $\varphi_0=0°$ *N=12.*

The methods of ACO, GA and IWO were compared to study the behavior of the desired method to optimize the array pattern [7], [8], [16], [31]. The number of antenna elements was set as *N= 10* at the first case and *N=12* at the second mode in both angles ($\varphi_0=90$ and $\varphi_0=0°$). We also give all algorithms the same computation time with equal computational resources. The stopping criterion is, in both algorithms GA and IWO, the number of *3000* iterations like ACO. The obtained results of excitation angular positions of array elements by GA and IWO have been presented in Tables 10 and 11.

Table 10: The IWO and GA optimized values (φ_n)

GA	IWO	GA	IWO	
78°	40°	90°	40°	φ_1
15°	108°	10°	77°	φ_2
60°	7°	30°	5°	φ_3
99°	90°	8°	14°	φ_4
47°	120°	36°	205°	φ_5
258°	220°	270°	220°	φ_6
195°	288°	190°	257°	φ_7
240°	187°	210°	185°	φ_8
279°	270°	188°	194°	φ_9
227°	300°	216°	25°	φ_{10}
0°	0°	90°	90°	φ_0
3000	3000	3000	3000	Iteration
10	10	10	10	N

Table 11: The IWO and GA optimized values (φ_n)

GA	IWO	GA	IWO	
78	40	90	40	φ_1
15	77	10	77	φ_2
60	7	35	5.5	φ_3
99	90	7.2	14	φ_4
52	120	60	206	φ_5
3.6	58	30	60	φ_6
258	220	270	220	φ_7
195	257	190	257	φ_8
240	187	215	185.5	φ_9
279	270	187.2	194	φ_{10}
232	300	240	26	φ_{11}
183.6	238	210	240	φ_{12}
0°	0°	90°	90°	φ_0
3000	3000	3000	3000	Iteration
12	12	12	12	N

The best results for each run are considered and Tables 12 and 13 show the comparison results; we can say that Figs. 13-16 illustrate the best array factor obtained for all of the algorithms. The numerical values of the side lobe level, directivity and other parameters results shown in Figs. 13-16 are presented in the Tables 12 and 13.

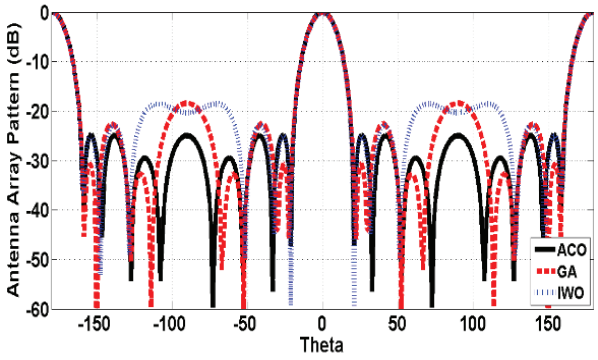

Fig. 13. Compared algorithms results, $\varphi_0 = 90°$ $N=10$.

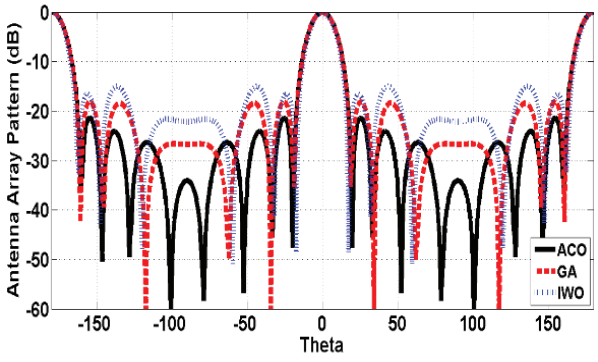

Fig. 14. Compared algorithms results, $\varphi_0 = 0°$ $N=10$.

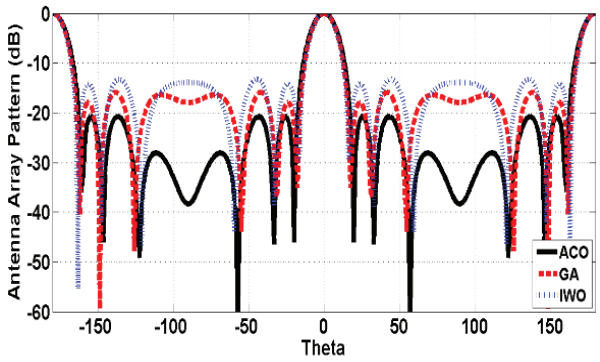

Fig. 15. Compared algorithms results, $\varphi_0 = 90°$ $N=12$.

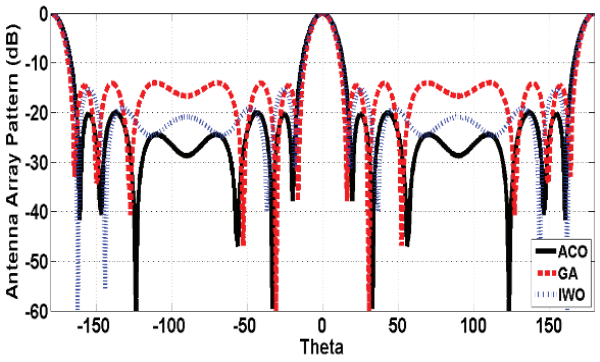

Fig. 16. Compared algorithms results, $\varphi_0 = 0°$ $N=12$.

Table 12: Computed radiation parameters for comparing $N=10$

Method	φ0	SLL (dB)	Directivity	FNBW	SIR	AF
ACO	90°	-24.9	11 dB	41°	38 dB	44
IWO	90°	-18.6	9.16 dB	42°	35.6 dB	55
GA	90°	-18.9	10.13 dB	45°	36.2 dB	49
ACO	0°	-21.4	10.75 dB	39.6°	34 dB	45.1
IWO	0°	-16	8.87 dB	35°	22 dB	56.2
GA	0°	-18	9.5 dB	37°	24.4 dB	51

Table 13: Computed radiation parameters for comparing $N=12$

Method	φ0	SLL (dB)	Directivity	FNBW	SIR	AF
ACO	90°	-21.1	10.32 dB	40°	34.3 dB	47
IWO	90°	-13	8.46 dB	36°	20.5 dB	58.5
GA	90°	-16	8.81 dB	35°	22.8 dB	60
ACO	0°	-20.1	10.08 dB	40°	34.8 dB	45.7
IWO	0°	-15.3	8.53 dB	38°	22.6 dB	56
GA	0°	-14.1	8.71 dB	33°	19.5 dB	66

The method of ACO presents a better performance in terms of the side lobe level with respect to GA and IWO, maintaining very similar values for the directivity in the performance of these three optimization methods. The results of the side lobe level and the directivity for the optimized design are really surprising. In the case of

the optimized designs for uniform circular array with 10 elements at $\varphi_0=90°$, it is obtained a SLL = *-24.9* dB and DIR = *11* dB for ACO, a SLL = *-18.9* dB and DIR = *10.13* dB for GA, and a value of SLL = *-18.6* dB and DIR = *9.16* dB for IWO. The obtained results in this case at $\varphi_0=0°$ are a SLL = *-21.4* dB and DIR = *10.75* dB for ACO, a SLL = *-18* dB and DIR = *9.5* dB for GA, and a value of SLL = *-16* dB and DIR = *8.87* dB for IWO. In another mode of optimization, the values for 12-element uniform circular array are as follows: directivity is *10.32* dB and SLL is equal to *-21.1* dB for ACO, a SLL = *-16* dB and DIR = *8.81* dB for GA and a value of SLL = *-13* dB and DIR = *8.46* dB for IWO at $\varphi_0=90°$. The computed results at $\varphi_0=0°$ in order are a SLL = *-20.1* dB and DIR = *10.08* dB for ACO, a SLL = *-14.1* dB and DIR = *8.71* dB for GA, and a value of SLL = *-15.3* dB and DIR = *8.53* dB for IWO. These values mean a substantial improvement in the performance of the array for the design optimized by the method of ACO, with respect to the conventional case of progressive angular positions excitation, a substantial improvements were obtained in the sense of the side lobe level and the directivity. It can be seen that using the ACO method gives radiation patterns which are generally better than that obtained from the GA and IWO results. Specifically, in range of the SLL and directivity [22], [7].

V. CONCLUSION

In this paper, ant colony optimization (ACO) is used to obtain maximum reduction in side lobe level relative to the main beam and improve the directivity. The ACO method was used to adjust elements angular position in the circular antenna array to optimize the array pattern. This method is very effective and can be used in practice to synthesize other structures. The results of the comparison express that antenna array patterns obtained from ACO are generally have better SLL and directivity than uniform circular array applying the desired algorithm in [22], [7]. All these factors together have been considered for optimal results in our design problem and these accounts for the understatement of this work.

ACKNOWLEDGMENT

We wish to thank everyone who helped us to complete this research. Without their continued efforts and support, we would have not been able to bring our investigations to a successful completion. Prof. Josef. Giglmayr: for guidance. Dr. Ali. Hashemi Talkhunche: for his participation in our study.

REFERENCES

[1] A. A. Lotfi Neyestanak, M. Ghiamy, M. Naser-Moghadasi, and R. A. Sadeghzade, "Investigation of hybrid elliptical antenna arrays," *IET. Microwave Antenna Propagat*., pp. 28-34, 2008.

[2] M. Mouhamadou, P. Vaudon, and M. Rammal, "Smart antenna array patterns synthesis: null steering and multi-user beam forming by phase control," *Progress in Electromagnetics Research, Pier* 60, pp. 95-106, 2006.

[3] D. K. Cheng, *Field and Wave Electromagnetics*, Adison Wesley, 1983.

[4] W. L. Stutzman and G. A. Thiele, *Antenna Theory and Design*, John Wiley and Sons, 1996.

[5] C. A. Balanis, *Antenna Theory*, John Wiley and sons, 2012.

[6] P. J. Bevelacqua, *Antenna Arrays-Performance Limits and Geometry*, Doctoral thesis, Virginia Tech. University, Antenna Engineering Team, 2007.

[7] G. Ghosh Roy, S. Das, and P. N. Suganthan, "Design of none-uniform circular antenna arrays using a modified invasive weed optimization algorithm," *IEEE Trans. Antennas Propagat.*, vol. 59, no. 1, 2011.

[8] Z. D. Zaharis, C. Skeberis, and T. D. Xenos, "Improved antenna array adaptive beamforming with low side lobe level using a novel adaptive invasive weed optimization method," *Progress In Electromagnetics Research*, vol. 124, pp. 137-150, 2012.

[9] F. Gozasht, R. Dadashzadeh, and S. Nikmehr, "A comprehensive performance study of circular and hexagonal array geometries in the LMS algorithm for smart antenna applications," *Progress In Electromagnetics Research, Pier* 68, pp. 281-296, 2007.

[10] M. Shihab, Y. Najjar, N. Dib, and M. Khodier, "Design of none-uniform circular antenna arrays using particle swarm optimization," *Journal of Electrical Engineering*, vol. 59, no. 4, pp. 216-220, 2008.

[11] K. R. Mahmoud, M. El-Adawy, and S. M. M. Ibrahem, "A comparison between circular and hexagonal array geometries for smart antenna systems using particle swarm optimization algorithm," *Progress in Electromagnetics Research, Pier* 72, pp. 75-90, 2007.

[12] Q. Shen, E. K. Mao, and S. Liang Wu, "The performance analysis of circular array antennas in VHF/UHF band," *IEEE AP-S*, 2006.

[13] A. Saman Zare, *Elliptical Antenna Array Pattern Synthesis*, B.S.C. thesis, Islamic Azad University Majlesi Branch, Telecommunications Engineering Department, 2012.

[14] W. B. Wang, Q. Y. Feng, and D. Liu, "Application of chaotic particle swarm optimization algorithm to pattern synthesis of antenna arrays," *Progress in Electromagnetics Research*, vol. 115, pp. 173-189,

2011.

[15] D. Liu, Q. Y. Feng, W. B. Wang, and X. Yu, "Synthesis of unequally spaced antenna arrays by using inheritance learning particle swarm optimization," *Progress in Electromagnetics Research*, vol. 118, pp. 205-221, 2011.

[16] G. K. Mahanti, N. Pathak, and P. Mahanti, "Synthesis of thinned linear antenna arrays with fixed side lobe level using real-coded genetic algorithm," *Progress in Electromagnetics Research, Pier* 75, pp. 319-328, 2007.

[17] F. Ares, G. Franceschetti, and J. A. Rodriguez, "A simple alternative for beam reconfiguration of array antennas," *Progress in Electromagnetics Research, Pier* 88, pp. 227-240, 2008.

[18] M. Dessouky, H. Sharshar, and Y. Albagory, "Efficient side lobe reduction technique for small-sized concentric circular arrays," *Progress in Electromagnetics Research, Pier* 65, pp. 187-200, 2006.

[19] M. Mouhamadou, P. Vaudon, and M. Rammal, "Smart antenna pattern synthesis: null steering and multi-user beam forming by phase control," *Progress in Electromagnetics Research, Pier* 60, pp. 95-106, 2006.

[20] K. Guney and M. Onay, "Amplitude-only pattern nulling of linear antenna arrays with the use of bees algorithm," *Progress in Electromagnetics Research, Pier* 70, pp. 21-36, 2007.

[21] G. K. Mahanti, A. Chakrabarty, and S. Das, "Phase-only and amplitude-phase synthesis of dual–pattern linear antenna arrays using floating-point genetic algorithms," *Progress in Electromagnetics Research, Pier* 68, pp. 247-259, 2007.

[22] A. Saman Zare, "Elliptical antenna array pattern synthesis with fixed side lobe level and suitable main beam width by genetic algorithm," *Progress in American Journal of Electromagnetics and Applications*, vol. 1, no. 1, pp. 8-15, 2013.

[23] D. M. V. Maniezzo and A. Colorni, "The ant system: optimization by a colony of cooperating agents," *IEEE Trans. Systems, Man, and Cybernetics-Part B*, vol. 26, pp. 29-4, 1996.

[24] S. Costanzo, I. Venneri, G. Di Massa, and G. Amendola, "Hybrid array antenna for broadband millimeter-wave applications," *Progress in Electromagnetics Research, Pier* 83, pp. 173-183, 2008.

[25] A. Saman Zare, "Elliptical antenna array pattern synthesis with fixed side lobe level and suitable main beam width by genetic algorithm," *Progress in Majlesi Journal of Telecommunications Devices*, vol. 1, no. 4, pp. 113-120, 2012.

[26] J. Liang and D. Liu, "Two L-shaped array-based 2-D Doas estimation in the presence of mutual coupling," *Progress in Electromagnetics Research*, vol. 112, pp. 273-298, 2011.

[27] M. R. Kamarudin, P. S. Hall, F. Colombel, and M. Himdi, "Electronically switched beam disk-loaded monopole array antenna," *Progress in Electromagnetics Research, Pier* 101, pp. 339-347, 2010.

[28] T. Yuan, N. Yuan, L.-W. Li, and M.-S. Leong, "Design and analysis of phased antenna array with low side lobe by fast algorithm," *Progress in Electromagnetics Research, Pier* 87, pp. 131-147, 2008.

[29] Q. Wang and Q. Q. He, "An arbitrary conformal array pattern synthesis method that includes mutual coupling and platform effects," *Progress in Electromagnetics Research*, vol. 110, pp. 297-311, 2010.

[30] Y. Liu, Z. Nie, and Q. H. Liu, "A new method for the synthesis of non-uniform linear arrays with shaped power patterns," *Progress in Electromagnetics Research*, vol. 107, pp. 349-363, 2010.

[31] L. Gurel and O. Ergul, "Design and simulation of circular arrays of trapezoidal-tooth log-periodic antennas via genetic optimization," *Progress in Electromagnetics Research, Pier* 85, pp. 243-260, 2008.

[32] O. Quevedo-Teruel and E. Rajo-Iglesias, "Application of ant colony optimization based algorithm to solve different electromagnetic problems," *Proc. EuCAP*, Nice, France, Nov. 6-10, 2006 (ESA SP-626, Oct. 2006).

[33] C. A. M. Dorigo and V. Maniezzo, "Distributed optimization by ant colonies," *Proceedings of the First European Conference on Artificial Life*, Paris, France, F. Varela and P. Bourgine (Eds.), Elsevier Publishing, pp. 134-142.

[34] M. Dorigo, *Ottimizzazione apprendimento automatic de algoritmi basati su metafora naturale (Optimization, Learning and Natural Algorithms*, Ph.D. thesis, Politecnico di Milano, Italy, in Italian, 1992.

Space-Frequency Domain Iterative Method for Modes Analysis of Planar Waveguides

Li Bingxin [1,2] and Zhang Baorong [1,2]

[1] School of Information Science and Engineering
University of Yanshan, Qinhuangdao, 066004, China
lbx1999@126.com

[2] The Key Laboratory for Special Optical Fiber and Optical Fiber Sensor of Hebei Province
Qinhuangdao, 066004, China

Abstract ─ We describe a space-frequency domain iterative algorithm to analyze the modes of planar optical waveguides. The one dimensional Maxwell equation was transformed into space-frequency domain by Fourier transform, and became an integral equation which could be solved by an iterative method. For any refractive index profiles, the effective index and mode field distribution are given simultaneously. The numerical result shows that this method is accurate and flexible for planar optical waveguides with any structure.

Index Terms ─ Fourier transform, iterative method, planar waveguide, space-frequency.

I. INTRODUCTION

Planar optical waveguides are the fundamental components in integrated optical circuits and used for optical amplifiers, lasers sensors and other optical devices [1-6]. All the characteristics of planar optical waveguides are based on the analysis of propagating modes which include the propagation constants and field distributions. The modes propagation constants and fields can be obtained by solving Maxwell's equations subject to the appropriate boundary conditions. However, the refractive index profile of planar waveguides is not only step but graded usually, exact solutions are given for only a few class of index profile [7]. For the most planar waveguides, approximate or numerical methods are used to analyze the modes fields. In general, the approximate methods [8,9] such as the method of perturbation and WKB method, have a clear physical insight but are not very accurate; numerical methods [10-16] can give solutions to the desired accuracy but require complex calculation. ATMM [17] is an effective and accurate tool for planar optical waveguides with arbitrary index profile. Unfortunately, ATMM is difficult to expand for two dimensional optical waveguides.

In this paper, a novel iterative algorithm in the space-frequency domain has been introduced to the analysis of planar optical waveguides. The one dimensional wave equation was transformed into space-frequency domain by Fourier transform, and became an integral equation which could be solved by an iterative method. The only complex calculation in the iterative operation is the convolution integral which could be completed by fast Fourier transform (FFT). For any refractive index profiles, the effective index and mode field distribution are given simultaneously. As the test calculation demonstrates that the dispersion curves given by our method agree extremely well with the exact solution.

II. WAVE EQUATIONS IN THE SPACE-FREQUENCY DOMAIN

Considering the TE mode of a planar waveguide, the scalar-wave equation is:

$$\frac{d^2E_y}{dx^2}+\left(k_0^2n^2(x)-\beta^2\right)E_y=0, \tag{1}$$

where k_0 is the free-space wave number, $n(x)$ is the x-dependent refractive index, and β is the propagation constant. It is noticeable that $n(x)$ is given in the form of generalized function which include the boundary conditions expressly. Especially, when $n(x)$ is not a continuous function of x. Given a Fourier transform, the scalar-wave equation (1) in the space-frequency domain is written as:

$$-k^2E_y(k)+k_0^2N(k)*E_y(k)-\beta^2E_y(k)=0, \tag{2}$$

where k is the space frequency, $E_y(k)$ and $N(k)$ are the Fourier transform of $E_y(x)$ and $n^2(x)$ respectively, $*$ represents convolution integral. For a sample transpose, equation (2) changes into:

Submitted On: June 14, 2013
Accepted On: June 13, 2015

$$\frac{N(k)*E_y(k)}{k^2+\beta^2}=\frac{E_y(k)}{k_0^2}. \tag{3}$$

We define an operator $\hat{A}$:

$$\hat{A}f(k)=\frac{N(k)*f(k)}{k^2+\beta^2},$$

where $f(k)$ is an arbitrary function of k. Thus, equation (3) becomes a normal eigenvalue equation, i.e.:

$$\hat{A}E_y=\lambda E_y, \tag{4}$$

where $\lambda=1/k_0^2$.

For TM modes, the scalar-wave equation is:

$$\frac{d^2H_y}{dx^2}-\frac{d\left(\ln n^2(x)\right)}{dx}\frac{dH_y}{dx}+(k_0^2n^2(x)-\beta^2)H_y=0, \tag{5}$$

where $n(x)$ is the x-dependent refractive index for the whole region including the core and cladding.

As doing for equation (1), in space-frequency domain, equation (5) could be written as a general eigenvalue equation:

$$\hat{A}H_y=\lambda\hat{B}H_y, \tag{6}$$

where $\hat{B}$ is an operator:

$$\hat{B}f(k)=f(k)-\frac{\left(k\boldsymbol{F}\left(\ln n^2(x)\right)\right)*\left(kf(k)\right)}{k^2+\beta^2},$$

$\boldsymbol{F}\left(\ln n^2(x)\right)$ is the Fourier transform of $\ln n^2(x)$.

III. ITERATIVE FORMULA FOR THE SOLUTION

Eigenvalue equations (4) and (6) are the integral equations which can be solved by an iterative method. For the purpose of simplicity, let ψ represent E_y or H_y. We are on the assumption that the eigenvalues:

$$\lambda_1>\lambda_2>\lambda_3>\cdots>\lambda_n,$$

correspond to these eigenvalues, the eigenfunctions are:

$$\psi_1,\psi_2,\psi_3\cdots\psi_n.$$

Choose an initial solver function x_0 which can be represented a:

$$x_0=a_1\psi_1+a_2\psi_2+\cdots+a_n\psi_n+\cdots.$$

For equation (4), we give the iterative formula:

$$x_{m+1}=\alpha_m\hat{A}x_m \qquad m=0,1,2\cdots. \tag{7}$$

Thus,

$$x_1=\alpha_0(a_1\lambda_1\psi_1+a_2\lambda_2\psi_2+\cdots+a_n\lambda_n\psi_n),$$

$$x_2=\alpha_1\alpha_0\hat{A}(a_1\lambda_1^2\psi_1+a_2\lambda_2^2\psi_2+\cdots+a_n\lambda_n^2\psi_n),$$

$$x_{m+1}=$$

$$\alpha_0\alpha_1\cdots\alpha_m a_1\lambda_1^m\left(\psi_1+\frac{a_2}{a_1}\left(\frac{\lambda_2}{\lambda_1}\right)^m\psi_2+\cdots+\left(\frac{\lambda_n}{\lambda_1}\right)^m\psi_n\right). \tag{8}$$

Fortunately, as m is increased, except the first one, the other terms in formula (8) converge to zero. This means that when m is large enough, $x_m\to\alpha\psi_1$ is the eigenfunction corresponding to the eigenvalue λ_1 which is the maximum of all the eigenvalues. When you get the maximum of eigenvalues λ_1 and its eigenfunction ψ_1, let $x_i=x_i-\left(x_i^*\cdot\psi_1\right)/\left(\psi_1^*\cdot\psi_1\right)\psi_1$, use the same iterative formula, the second maximum eigenvalues λ_2 will be given.

For equation (6), define another operator $\hat{C}$:

$$\hat{C}f(k)=\frac{\left(k\boldsymbol{F}\left(\ln n^2(x)\right)\right)*\left(kf(k)\right)}{k^2+\beta^2},$$

so the general eigenvalue equation (6) can be written as:

$$\left(\hat{A}+\lambda\hat{C}\right)H_y=\lambda H_y.$$

Like formula (7), the iterative formula is given as:

$$x_{m+1}=\alpha_m(\hat{A}x_m+a\hat{C}x_m) \qquad m=0,1,2\cdots. \tag{9}$$

Searching a when the convergent $\alpha_m a=1$, so the $x_m\to\alpha\psi_1$ is the eigenfunctions corresponding to the eigenvalue $\lambda_1\approx1/\alpha_m$ which is the maximum of all the eigenvalues.

IV. NUMERICAL CALCULATION EXAMPLES

Two numerical calculation examples are given for comparison with theoretical solutions. The first one is step index three layers waveguide, which structure parameters are following: core thickness is $2.0\mu m$, index $n_1=1.50$, cladding index $n_2=1.40$. The dispersion curve of TE_0 mode is given in Fig. 1, and Fig. 2 shows the errors compared with analytical solution. The numerical results conform to the analytical solution very well. Except for very small value of β, the errors are all under 10^{-7}.

At Table 1, the effective index for modes TE_0, TE_1, TM_0 and TM_1 are shown. Contrasted with analytical calculation results, the relative errors are about 10^{-7} for TE modes and 10^{-6} for TM modes.

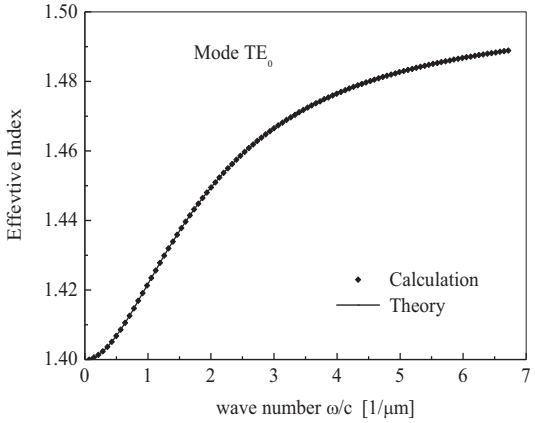

Fig. 1. Dispersion curve of mode TE_0.

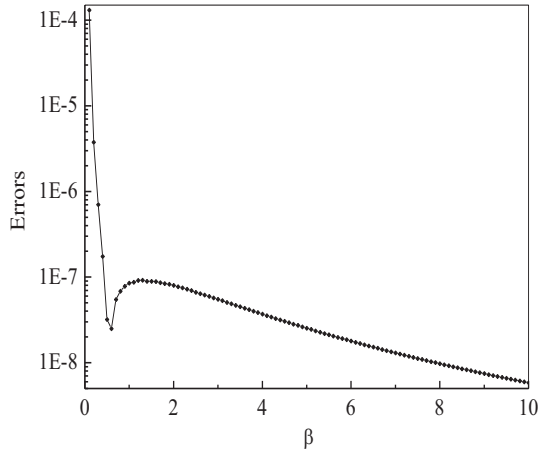

Fig. 2. The errors of dispersion curve for mode TE_0.

Table 1: Effective index of mode TE and TM

	This Work	Analytical	Relative Error
TE_0	1.47429328	1.47429290	2.581×10^{-7}
TE_1	1.41395949	1.41395911	2.735×10^{-7}
TM_0	1.47239343	1.47239162	1.230×10^{-6}
TM_1	1.41221956	1.41221736	1.563×10^{-6}

Figure 3 and Fig. 4 show the field intensity distribution of TE mode and TM mode. It is difficult to distinguish the curve from the theoretical solutions.

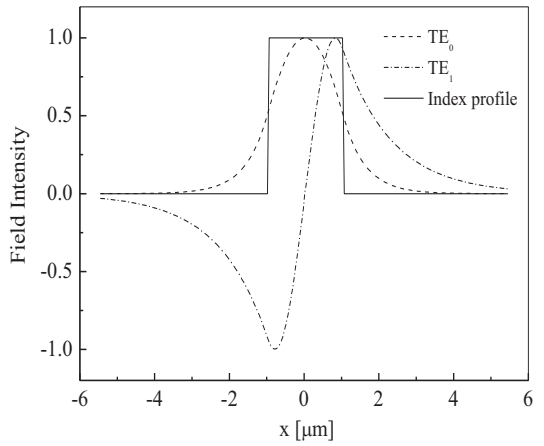

Fig. 3. Field intensity for TE_0 and TE_1 mode in a three layer step index planar waveguide.

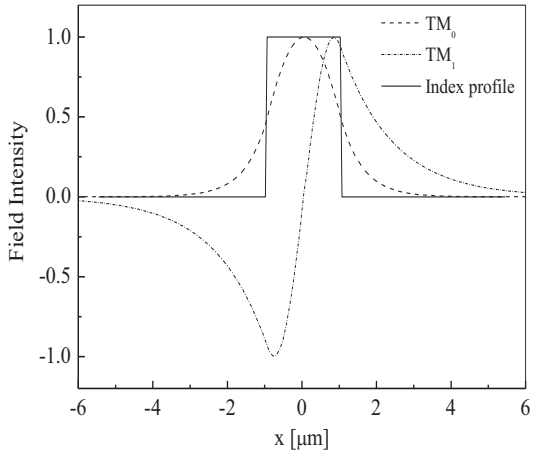

Fig. 4. Field intensity for TM_0 and TM_1 mode in a three layer step index planar waveguide.

Another example is a waveguide with a graded index profile:

$$n^2(x) = n_2^2 + (n_1^2 - n_2^2) / Cosh^2(x/a). \quad (10)$$

For our calculation, the parameters are taken $n_1 = 1.50$, $n_2 = 1.40$ and $a = 2.0\mu m$. For TE modes, the dispersion relation is [7]:

$$\beta^2 = k_0^2 n_2^2 + \left(\sqrt{k_0^2 (n_1^2 - n_2^2) + \frac{1}{4a^2}} - \frac{1}{a}\left(m + \frac{1}{2} \right) \right)^2 \quad (11)$$

$m = 0,1,2,\ldots,$

but there is no analytical solution for TM modes. In Table 2, we can find the difference of effective index between our calculation and analytical solver is tiny. Figure 5 shows the dispersion curve of mode TE_0 and Fig. 6 is the errors of this curve compared with theory. For almost all propagation constants β, the errors are less than 10^{-9}. Field intensity distributions of TE and TM modes are given in Fig. 7 and Fig. 8.

Table 2: Effective index for mode TE and TM

	This Work	Analytical	Relative Error
TE_0	1.462148481	1.462148481	-3.60×10^{-11}
TE_1	1.410160571	1.410160572	-2.23×10^{-10}
TM_0	1.460876908	—	—
TM_1	1.410515558	—	—

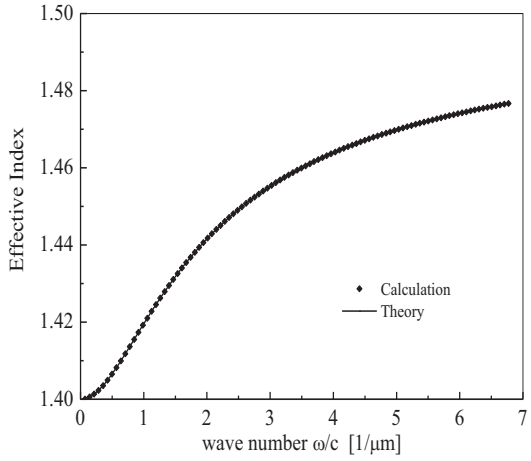

Fig. 5. Dispersion curve of mode TE_0.

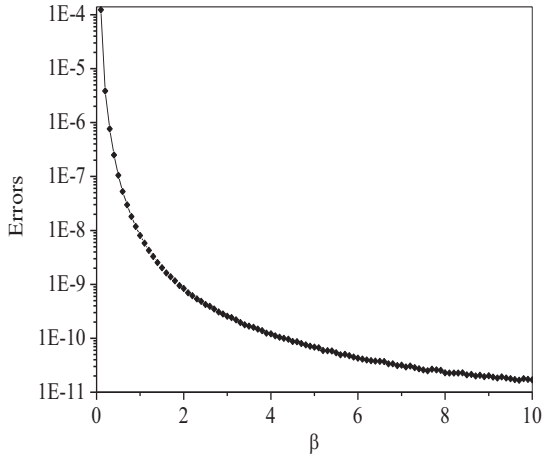

Fig. 6. The errors of dispersion curve for mode TE_0.

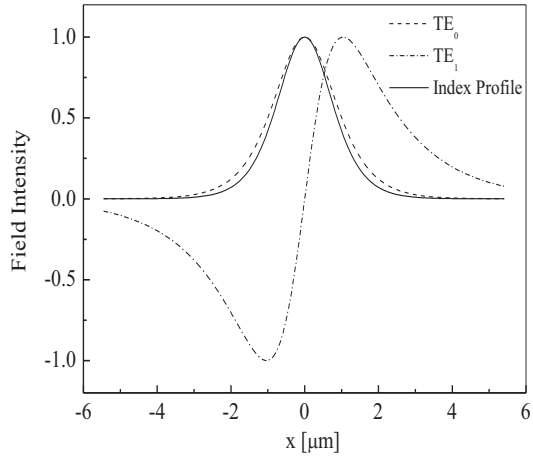

Fig. 7. Field intensity for TE_0 and TE_1 mode in a graded index waveguide.

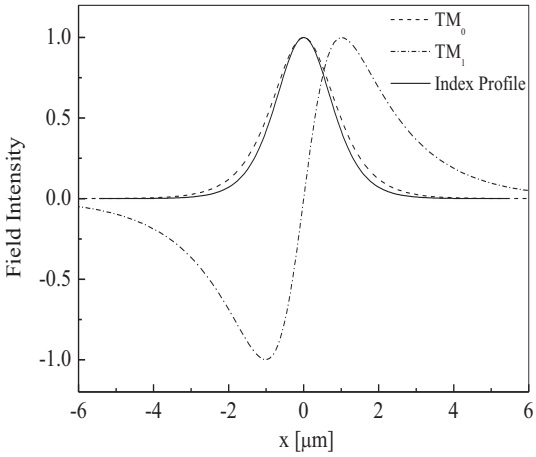

Fig. 8. Field intensity for TM_0 and TM_1 mode in a graded index waveguide.

V. CONCLUSION

In this paper, we find that in space frequency domain the Maxwell's equations for planar optical waveguides become an integral equation. This integral equation is the standard form of eigenvalue problem which can be solved by iterative algorithm. Two numerical calculation examples show that this method has a high accuracy for determining the effective index and mode field distribution simultaneously. Especially, this method is not only used for analysis of arbitrary structure planar optical waveguides, but also can be extended to 2D for optical fibers mode solution.

ACKNOWLEDGMENT

Partial financial support of this work under Grant No. 12963350D from The Key Basic Research Program of Applied Basic Research Project in Hebei Province of China is gratefully acknowledged.

REFERENCES

[1] J-E. Broquin, "Glass integrated optics: state of the art and position toward other technologies," *SPIE*, vol. 6475, pp. 647507, 2007.

[2] L. Ke and E. Y. B. Pun, "Modeling and experiments of packaged Er^{3+}–Yb^{3+} co-doped glass waveguide amplifiers," *Opt. Comm.*, vol. 273, no. 2, pp. 413-420, 2007.

[3] S. Yuyama, T. Nakajima, K. Yamashita, and K. Oe, "Solid state organic laser emission at 970 nm from dye-doped fluorinated-polyimide planar waveguides," *Appl. Phys. Lett.*, vol. 93, pp. 023306, 2008.

[4] H. Mukundan, J. Z. Kubicek, A. Holt, J. E. Shively, J. S. Martinez, K. Grace, W. K. Grace, and B. I. Swanson, "Planar optical waveguide-based

biosensor for the quantitative detection of tumor markers," *Sensor. Actuat. B-Chem*., vol. 138, no. 2, pp. 453-460, 2009.

[5] J. Hu, V. Tarasov, A. Agarwal, L. Kimerling, N. Carlie, L. Petit, and K. Richardson, "Fabrication and testing of planar chalcogenide waveguide integrated microfluidic sensor," *Opt. Express*, vol. 15, no. 5, pp. 2307-2314, 2007.

[6] B. Agnarsson, S. Ingthorsson, T. Gudjonsson, and K. Leosson, "Evanescent wave fluorescence microscopy using symmetric planar waveguides," *Opt. Express*, vol. 17, no. 7, pp. 5075-5082, 2009.

[7] M. Chunsheng and L. Shiyong, *Mode Theory of Optical Waveguides* (in Chinese), Jilin University Press, Changchun, pp. 130-132, 2007.

[8] S. Shouxian, W. Jingyi, and L. Qiao, "Metal-clad graded-index planar optical waveguides: accurate perturbation analysis," *Opt. Comm*., vol. 90, no. 4-6, pp. 238-240, 1992.

[9] L. Qiao and W. Jingyi, "A refined WKB method for planar waveguides with asymmetric graded index profile," *Opt. Comm.*, vol. 83, no. 1-2, pp. 144-153, 1991.

[10] Z. Anping and S. R. Cvetkovic, "Finite- element analysis of hybrid modes in uniaxial planar waveguides by a simple iterative method," *Opt. Lett.*, vol. 20, no. 2, pp. 139-141, 1995.

[11] E. Anemogiannis, E. N. Glytsis, and T. K. Gaylord, "Determination of guided and leaky modes in lossless and lossy planar multilayer optical waveguides: reflection pole method and wavevector density method," *J. Lightwave Technol.*, vol. 17, no. 5, pp. 929-941, 1999.

[12] R. E. Smith, S. N. Houde-Walter, and G. W. Forbes, "Numerical determination of planar waveguide modes using the analyticity of the dispersion relation," *Opt. Lett*., vol. 16, no. 17, pp. 1316-1318, 1991.

[13] P. R. Chaudhuri and S. Roy, "Analysis of arbitrary index profile planar optical wave-guides and multilayer nonlinear structures: a simple finite difference algorithm," *Opt. Quant. Electron.*, vol. 39, pp. 221-237, 2007.

[14] A. A. Stratonnikov, A. P. Bogatov, A. E. Drakin, and F. F. Kamenets, "A semianalytical method of mode determination for a multilayer planar optical waveguide," *J. Opt. A: Pure Appl. Opt.*, vol. 4, pp. 535-539, 2002.

[15] K. Tsakmakidis, D. Aryal, and O. Hess, "Accurate modal analysis of 3D dielectric waveguides using the nonstandard FDTD method," *24th Annual Review of Progress in ACES*, pp. 956-961, Niagara Falls, Canada, 2008.

[16] T. A. Tamadan, "A search-and-track algorithm for controlling the number of guided modes of planar optical waveguides with arbitrary refractive index profiles," *ACES Journal*, vol. 26, no. 1, pp. 45-55, 2011.

[17] C. Zhuangqi, J. Yi, S. Qishun, D. Xiaoming, and C. Yingli, "Exact analytical method for planar optical waveguides with arbitrary index profile," *J. Opt. Soc. Am. A*, vol. 16, no. 9, pp. 2209-2212, 1999.

Zhang Baorong was born in Qiqihar, China in 1967. She received a B.S. degree in Chemistry from Heilongjiang University in 1990, the M.S. degree in Electronics in 2005, and Ph.D. degree in Precision Instrument and Machinery from Yanshan University, in 2010. She is currently an Associate Professor at Yanshan University. Her research interests include fiber and integrated optics, optical amplifiers.

Detect and Pointing Algorithm's Performance for a Planar Smart Antenna Array: A Review

Tiago Varum [1,2], João N. Matos [1,2], and Pedro Pinho [2,3]

[1] Departamento de Engenharia Eletrónica, Telecomunicações e Informática
Universidade de Aveiro, Aveiro, Portugal

[2] Instituto de Telecomunicações
Campus Universitário de Santiago, Aveiro, Portugal

[3] Instituto Superior de Engenharia de Lisboa, Lisboa, Portugal
tiago.varum@ua.pt, matos@ua.pt, ppinho@deetc.isel.pt

Abstract ─ An adaptive antenna array combines the signal of each element, using some constraints to produce the radiation pattern of the antenna, while maximizing the performance of the system. Direction of arrival (DOA) algorithms are applied to determine the directions of impinging signals, whereas beamforming techniques are employed to determine the appropriate weights for the array elements, to create the desired pattern. In this paper, a detailed analysis of both categories of algorithms is made, when a planar antenna array is used. Several simulation results show that it is possible to point an antenna array in a desired direction based on the DOA estimation and on the beamforming algorithms. A comparison of the performance in terms of runtime and accuracy of the used algorithms is made. These characteristics are dependent on the SNR of the incoming signal.

Index Terms ─ Adaptive antenna array, beamforming, direction of arrival, planar array.

I. INTRODUCTION

The adaptive or smart antennas due its benefits have a great potential over all the future wireless communications. These antennas consist of arrays with several elements, which combines the received data from each element of array in such a way that improves the communication, suppressing interfering signals.

The increase of the coverage, the enhancement of the system capacity and the ability to reduce/mitigate some communication impairments such as interferences and multipath fading are relevant features about the impact of this technology in the performance of the wireless communications. The smart antennas has the spatial diversity capabilities, which relies in the possibility to transmit simultaneously several data streams, exploiting the spatial multiplexing gain of MIMO systems, increasing the spectral efficiency and the data rates.

Firstly developed for military applications, in the last century, took part the evolution of wireless communications and, nowadays, the smart antennas are attractive for several areas that range from the military applications, satellites, and mobile communications, especially in base stations, 4G MIMO and the emerging 5G MIMO.

The adaptive antennas can detect the direction of signals that impinge at the antenna using the direction of arrival estimation algorithms, and then weighting each array element can change the radiation pattern of the antenna, not only to point to a preferred zone, but also to place nulls in the others, to mitigate possible interfering signals.

These weights (amplitude and phase) are estimated using the beamforming algorithms. The block diagram of a smart antenna procedure is presented in the Fig. 1. In reception mode, a sample of received signal at each element of the array is used through DOA algorithms to estimate the directions of the arriving signals. Once determined, the directions of interest and of the interfering signals are selected, by some auxiliary intelligence. Then, using the angular locations, the beamforming algorithms are used to compute the needed weight to apply to each element of the array, to point the antenna pattern as is intended.

This paper is organized into six sections. It starts with an introduction, inserting the work in the smart antenna domain. The second section describes the direction of arrival estimation algorithms, with a focus in the two dimensional antenna arrays. The following section, the third, is related to beamforming, exposing the main algorithms applied into planar smart antennas. In the fourth section is made the system integration, combining the DOA and beamforming algorithms to

Submitted On: July 31, 2014
Accepted On: December 11, 2014

create an example of application, detecting signals and pointing the radiation pattern of a planar array antenna for them. Then, there is a section of results with a detailed examination of the performance of the algorithms. Finally, the paper is concluded in the section six, grouping the main results taken from this analysis and some future prospects.

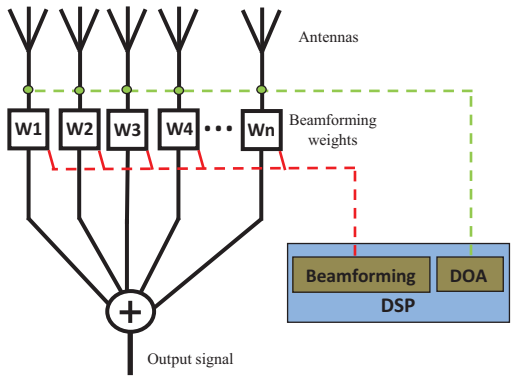

Fig. 1. Adaptive antenna array system.

II. DIRECTION OF ARRIVAL

The algorithms to determine the directions of arrival of the signals are a vital part of the adaptive antenna system, due to its ability to filter out the surrounding noise.

Processing the electromagnetic waves that reach to the antenna array is possible to extract some info about the signal, such the direction whence is arriving to the antenna. Estimating the DOA's, then is possible to distinguish the directions of interest to point the antenna and directions of intrusive signals, to reduce its effects in the communication.

There are three classes of methods to do this, the classical, the maximum likelihood and the subspace methods, which differ mainly in the performance and computational requirements [1], [2]. The classics are based in the beamforming, in which the central idea is to scan the antenna beam over the space and the locals in which more power is received are the DOAs. These methods are theoretically simple but involve a high computational effort and offer a low performance. A different class is based on the maximum likelihood techniques, which present a high performance but with high computational requirements, due to the necessity to solve nonlinear multidimensional optimization problems. Finally, the subspace methods make use of the received signal and noise subspace to achieve a tradeoff between the performance and the computational efficiency. The performance of the subspace-based methods is limited essentially by the accuracy of distinguishing the signal and the noise subspaces in the presence of noise. For the planar uniform array the most applied algorithms are MUSIC and the 2D ESPRIT, that are subspace based [1].

A. Multiple signal classification - MUSIC algorithm

This DOA algorithm is perhaps the most popular method and uses the fact that the steering vectors of the incoming signals lie in signal subspace and are orthogonal to the noise subspace. The MUSIC [2]-[5] search in the all possible steering vectors, those that are orthogonal to the noise subspace of the covariance matrix of the received data.

Using the received information from each array element, the MUSIC through eigenvalue decomposition or singular value decomposition of the correlation matrix of this data, estimates the noise subspace, as exemplified in the diagram of Fig. 2. After the noise subspace be known, U_N, the DOAs are the resulting peaks of the MUSIC spectrum, that is given by equation (1), that is function of θ and φ through the steering vector $s(\theta,\varphi)$:

$$P_{MUSIC}(\theta,\varphi)=\frac{1}{s^H(\theta,\varphi)U_N U_N^H s(\theta,\varphi)}, \quad (1)$$

where M^H represents the conjugate transpose matrix of M (Heremitian). When a steering vector is referring to one arriving signal, the product $s^H(\theta,\varphi)U_N$ is equal to zero, ideally, and the function assumes a high value (peak).

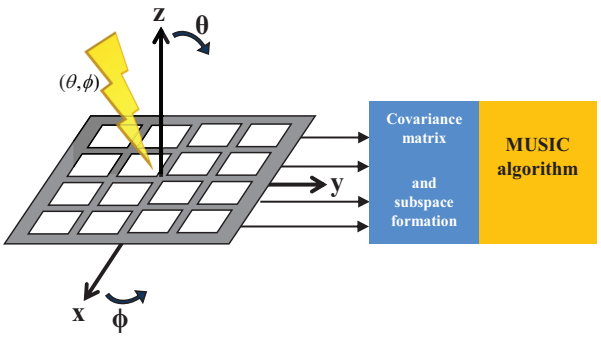

Fig. 2. 2D MUSIC.

The MUSIC algorithm is easily understood and can be implemented in all antenna array geometries, however, computationally requires a lot of resources, since it should calculate the MUSIC spectrum, equation (1), for all possible steering vectors to estimate the desired peaks. The estimation error of MUSIC algorithm is substantially influenced by the angle grid interval in which the equation (1) is evaluated.

In the presence of coherent signals, as in multipath environments, spatial smoothing schemes [6], [7] must be applied to suppress the correlations between the incoming signals.

B. Estimation of signal parameters via rotational invariance techniques - 2D ESPRIT algorithm

An additional known subspace based DOA algorithm is the ESPRIT [8]-[12]. This scheme solves

the issues of the high computational requirements of the MUSIC, and the resulting effects of array calibration errors. The ESPRIT algorithm employs the property of shift invariance of the antenna array, and due to this property is not fundamental to have a high level of calibration in the array.

The computational complexity of the ESPRIT is reduced once this algorithm imposes some constraints on array structure. The ESPRIT assumes that the separation between equivalent elements in each sub-array is fixed, Fig. 3, and therefore the array presents a translational invariance. This translational invariance leads to a rotational invariance of the signal subspace that will allow estimating the DOAs.

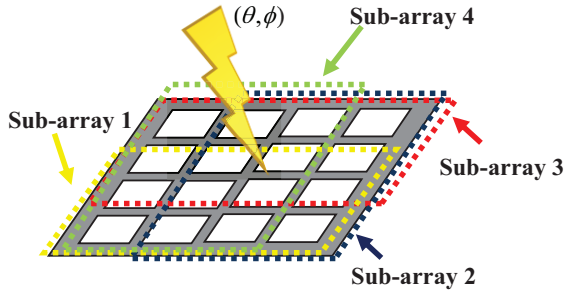

Fig. 3. Sub-array division (3x4) with maximum overlap.

The algorithm follows three steps, the signal subspace estimation, the solution of the invariance equation and the DOA estimation.

1) Signal subspace estimation:

$$\text{Computation of the } U_S. \tag{2}$$

2) Solve the invariance equation:

$$\begin{aligned} K_{u1}U_s Y_u &= K_{u2}U_s, \\ K_{v1}U_s Y_v &= K_{v2}U_s, \end{aligned} \tag{3}$$

where K_{u1}, K_{u2}, K_{v1} and K_{v2} represent the two pairs of transformed selection matrices, while Y_u and Y_v are the real-valued matrices [10].

3) DOA estimation:

$$\begin{aligned} &\lambda_i \quad i = 1 \ldots d \rightarrow \text{eigenvalues of } Y_u + jY_v, \\ &u_i = 2\tan^{-1}(\text{Re}\{\lambda_i\}), \\ &v_i = 2\tan^{-1}(\text{Im}\{\lambda_i\}), \\ &\varphi_i = \arg(u_i - jv_i) \quad \theta_i = \sin^{-1}(\|u_i - jv_i\|), \end{aligned} \tag{4}$$

where θ_i and φ_i are the DOA angular information.

III. BEAMFORMING

In fact, despite the interest and intrusive signals occupying the same frequency range, they are created from different spatial positions. Once identified the directions of arrival of its signals, is necessary the use of spatial filtering techniques, also known as beamforming techniques, due to deal with in the beam pattern of an antenna array. Based on these directions, the beamforming processing to control the antenna pattern is made, improving the performance of the communication.

The control of the radiation pattern of the antenna array is achieved, as is illustrated in the Fig. 4, varying the relative amplitude and phase of each element of the array and is based on this rule that the beamforming techniques operate. There are several algorithms already developed to calculate the complex weights (amplitude and phase) to apply to the antenna array.

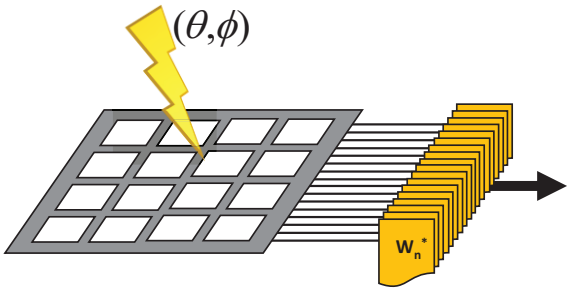

Fig. 4. Beamformer system.

These beamforming techniques can be classified according to the way on how the weights apply to the array are estimated, as data independent or statistically optimum [13], [14]. In the data independent, the weights are chosen to provide a desired response independently of the received data by the antenna, while in the statistically optimum the weights are estimated according to the statistics of the received signal in order to optimize its response, reducing or ideally suppressing the intrusive signals.

Often, statistical information of the collected data from the array are not available or varies in time, therefore adaptive algorithms are typically useful to estimate the weights and are designed in order to their response tend to a solution statistically optimum.

A. Statistically optimum beamformer

These beamformers are applied to diminish the influence of the interfering signals in the communication while pointing the antenna pattern in the direction of interest signal. Some examples of statistically optimum algorithms present in the literature [13] are:

- Multiple sidelobe canceller (MSC),
- Use of reference signal,
- Maximum SNR,
- Linearly constrained minimum variance (LCMV).

The MSC beamformer is composed by a main channel and others auxiliary channels, and the idea is to choose the appropriate weights to apply to the auxiliary channels to cancel the interference signals from the main channel. This procedure presents some limitations, once MSC doesn't point the main beam to a desired signal,

and the weights must be estimated with the absence of the desired signal. Based on this, MSC is only effective when desired signals are weak relative to interferences. The use of a reference signal requires some knowledge about the desired signal, to generate a reference signal in order to minimize the mean square error between the output and the reference signal. Using the maximum SNR solution requires the knowledge of the covariance matrix of the desired signal and of the noise.

Finally, one of the most important statistically optimum algorithms with higher applicability is the LCMV, which is described below followed by a different approach of its formulation known as generalized side lobe canceller (GSC).

1) Linearly Constrained Minimum Variance

Most of the times the desired reference signal is unknown or we don't have enough information about it, being necessary to impose some linear constraints in the weight vector to minimize the variance of beamformer output. This is obtained using the LCMV beamformer [15]. The constraints impose that the desired signals from a known direction are preserved and the interfering signals influence is minimized.

The LCMV formulation problem is to select the complex weights that are suitable to the multiple linearly independent constraints:

$$\min_{w} w^H R_x w \quad subject\ to \quad C^H w = f, \tag{5}$$

where w is the vector of weights, R_x the covariance matrix, C is the constraint matrix and f is the response vector.

The solution of the constrained minimization of LCMV problem can be achieved applying the method of Lagrange multipliers and results in [13]:

$$W_{opt} = R_x^{-1} C(C^H R_x C)^{-1} f. \tag{6}$$

It is important to note the dependence of the optimal weight vector (6) with the data correlation matrix, and therefore with the statistics of the input signal.

a) Generalized Sidelobe Canceller - GSC

The generalized sidelobe canceller is a different approach to solve the LCMV problem, providing a simple implementation of the beamformer and change the constrained minimization problem to an unconstrained scheme [16], [17].

The GSC separates the LCMV problem into two components, one data independent and other data dependent, as is illustrated in Fig. 5. In GSC structure, the optimum weight vector is decomposed in two orthogonal components that are in the range and null space of C, in the manner that $w = w_o - Bw_M$. The array output is $y = w_o^H x - w_M^H B^H x$, as is shown in the Fig. 5.

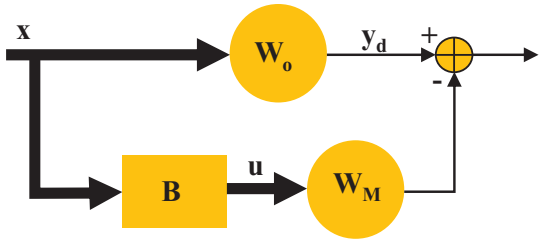

Fig. 5. Generalized sidelobe canceller.

The w_o vector is the quiescent part of w, and is used to constrain the weight subspace, and must satisfy the linear constraints [16]:

$$C^H w_o = f \quad \Rightarrow \quad w_o = C(C^H C)^{-1} f. \tag{7}$$

The w_o is designed respecting the imposed restrictions, is independent of the data and represents the non-adaptive component of the LCMV solution. In inferior branch, the blocking matrix B and w_M will block the interfering signals influence, while minimizing the variance of the output signal y. This is the data dependent component. The blocking matrix B must be orthogonal to the constraint matrix C, so $C^H B = 0$.

The GSC unconstrained problem is:

$$\min_{w_M} (w_o - Bw_M)^H R_x (w_o - Bw_M), \quad subject\ to \quad C^H w = f, \tag{8}$$

and the optimal solution is:

$$w_M = (B^H R_x B)^{-1} B^H R_x w_o. \tag{9}$$

This implementation of beamformer has significant benefits, such the w_o is a data independent beamformer and w_M is an unconstrained beamformer.

B. Adaptive algorithms

The statistically optimum beamformers uses the received data statistics, which often may change over the time or may not be available. Adaptive algorithms solve this issue [13].

The adaptation error corresponding to a weight vector is calculated and then is processed a new weight vector with a reduced error. Examples of adaptive algorithms are the well-known least mean square (LMS), the recursive least squares (RLS) or the Frost's algorithm.

1) Frost's Algorithm for LCMV Beamforming

The Frost's algorithm [14] belongs to the group of LCMV beamformers. The LCMV estimated weights are based on the received data information statistics (R_x), but in many situations the second order statistics are not available or are continuously changing, being necessary the use of adaptive algorithms. Frost's algorithm solution minimizes the mean square error while

maintains the specified response to the desired signal. The weight vector starts with an initial value:

$$w = C(C^H C)^{-1} f, \tag{10}$$

and in each iteration the vector will be updated on negative gradient direction by a factor defined by μ :

$$\begin{aligned} w(n+1) &= C(C^H C)^{-1} f + P(w(n) - \mu e^*(n)x(n)), \\ P &= I - C(C^H C)^{-1} C^H. \end{aligned} \tag{11}$$

2) Least Mean Square

Least mean square algorithm [13], [14], [18], [19] estimates the gradient vector and adjusts the weight vector in the negative gradient direction at each iteration:

$$\begin{aligned} w_M(n) &= w_M(n-1) + \mu u(n-1) y^*(n-1), \\ y(n) &= y_d(n) - w_M{}^H(n) u(n), \\ 0 &< \mu < \frac{1}{\lambda_{\max}}, \end{aligned} \tag{12}$$

where λ_{max} is the largest eigenvalue of the correlation matrix.

The gain μ [13] ($0<\mu<1$) is the parameter that controls the convergence rate. Smaller values result in slow convergence and good approximation, while higher values lead to faster convergence and the stability around the minimum value is not guaranteed. This is a simple algorithm and with a correct choice value of μ, the weight vector tends to an optimum solution.

3) Recursive Least Squares

The recursive least squares [13], [14] has a high convergence rate, faster than the LMS; however, the computational complexity is higher.

The RLS problem is:

$$\min_{w_M(k)} \sum_{n=0}^{N} \lambda^{N-n} \left| y_d(n) - w_M^H(n) u(n) \right|^2, \tag{13}$$

with $0<\lambda<1$ a constant called forgetting factor.

The algorithm can be described as [13]:

$$\begin{aligned} P(0) &= \delta^{-1} I, \\ v(n) &= P(n-1) u(n), \\ k(n) &= \frac{\lambda^{-1} v(n)}{1 + \lambda^{-1} u^H(n) v(n)}, \\ \alpha(n) &= y_d(n) - w_M^H(n-1) u(n), \\ w_M(n) &= w_M(n-1) + k(n) \alpha^*(n), \\ P(n) &= \lambda^{-1} P(n-1) - \lambda^{-1} k(n) v^H(n), \end{aligned} \tag{14}$$

where I is the identity matrix and δ a small value.

IV. SYSTEM INTEGRATION

The simulated system consists of a planar antenna array that receives an input signal x(t), that is a sum of various signals impinging in the antenna and noise, as is shown in the Fig. 6. The received data is after processed to estimate the angles of arrival of each signal. Then, using the beamforming algorithms, the system processes the group of weights to apply to each antenna array element to point the radiation pattern to the desired direction while minimizing the impact of the others signals considered as interferences.

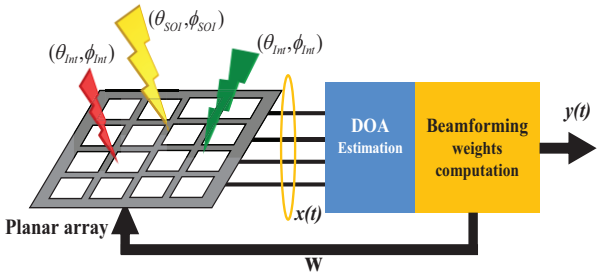

Fig. 6. Implemented system.

Consider a $M \times N$ uniform planar array as presented in the Fig. 7, with spacing between elements of d_1 on rows and d_2 on columns. There are J signals $s(t)$ that collide onto the antenna array with an elevation angle θ and with an azimuth angle φ. The input signal at each array element (m, n) is the sum of the contributions of the J signals and noise n(t):

$$\begin{aligned} x_{mn}(t) &= \sum_{i=1}^{J} s_i(t) e^{j\frac{2\pi}{\lambda}[u_i d_1 (m-1) + v_i d_2 (n-1)]} + n_{nm}(t) \\ u_i &= \sin\theta_i \quad v_i = \cos\theta_i \sin\varphi_i \\ m &= 1,\ldots,M \quad n = 1,\ldots,N \quad i = 1,\ldots,J, \end{aligned} \tag{15}$$

where λ is the wavelength.

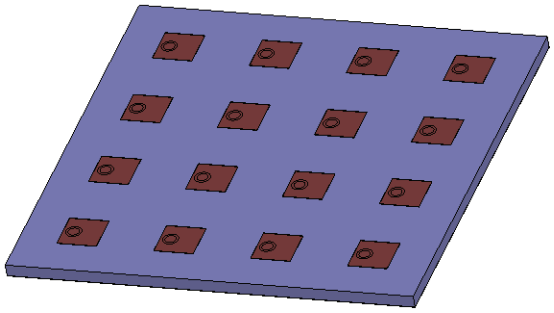

Fig. 7. Planar array.

It is possible to represent the received data in vector structure X(t) and noise vector N(t) as:

$$X(t) = [x_{11}(t)\ x_{21}(t) \cdots x_{N1}(t)\ x_{12}(t) \cdots x_{MN}(t)\ ]^T, \tag{16}$$

$$N(t) = [n_{11}(t)\ n_{21}(t) \cdots n_{N1}(t)\ n_{12}(t) \cdots n_{MN}(t)\ ]^T. \tag{17}$$

The steering vector of the each signal that arrives to the planar array contains the set of phase delays that a wave will take relating to each element of the array, and for a planar array can be represented as [20], [21]:

$$C_u = \left[1 \quad e^{j\frac{2\pi d_1}{\lambda}(2-1)u_i} \quad \cdots \quad e^{j\frac{2\pi d_1}{\lambda}(M-1)u_i}\right]^T, \tag{18}$$

$$C_v = \left[1 \quad e^{j\frac{2\pi d_2}{\lambda}(2-1)v_i} \quad \cdots \quad e^{j\frac{2\pi d_2}{\lambda}(N-1)v_i}\right]^T, \tag{19}$$

$$A = C_u \otimes C_v, \tag{20}$$

where the $\otimes$ is the Kronecker product, C_u and C_v are the steering vectors in x and y direction and A the steering matrix of the planar antenna array.

So, the total input signal X(t) can be expressed in the following formula:

$$X(t) = \sum_{i=1}^{J} s_i(t) A_i + N(t). \tag{21}$$

The output signal of the planar array, with beamforming weights W applied to each array element will be:

$$y(t) = W^H X(t), \tag{22}$$

$$W = [w_{11}\ w_{21} \cdots w_{N1}\ w_{12} \cdots w_{MN}]. \tag{23}$$

In this work, the signal X(t) that collides to the planar array antenna is generated previously. This data is the sum of diverse signals with different directions (θ, φ), the signal of interest, interferences and noise. The set of signal samples that reaches each element of the array is processed by a DOA algorithm to determine the angles of arrival and the number of signals.

With some knowledge to distinguish the interest signal and interferences, one of beamforming algorithms is applied to achieve the correct weights to point the antenna array to the desired location.

The antenna array for test presented in the Fig. 7, was simulated in the electromagnetic simulator HFSS (High Frequency Structure Simulator) [22] and consists of a planar microstrip array of 16 elements with a 4x4 shape, designed for 12 GHz.

Using as a uniform planar antenna array, that uses all elements feed with the same amplitude and phase (unitary weights), the radiation pattern of the antenna is perpendicular to the antenna plane, and points to the origin $(\theta, \varphi) = (0^o, 0^o)$.

In the electromagnetic simulator is possible to modify the relative amplitude and phase of each element of the array, based on this, the calculated weights with beamforming algorithms were tested in the simulated planar antenna array.

V. RESULTS

Using the MATLAB [23], the DOA and beamforming algorithms were implemented and its performance was analyzed when applied to a planar antenna array. The system (DOA and beamforming) simulation was tested using several group of angles of arrival of signals with excellent results. As an example of test, two signals with directions $(\theta, \varphi) = (45^o, 45^o)$ and $(\theta, \varphi) = (70^o, 0^o)$ was employed using a 4x4 planar antenna array with 0.5λ element spacing, as presented in Fig. 7.

A. Direction of arrival

With the received signal (16) from each element of the antenna array (that is a composite of various components of interest signals, interference signals and noise), the direction of arrival algorithms estimates the locals that electromagnetic signals are arriving to the antenna. The MUSIC and ESPRIT algorithms were tested.

a) MUSIC

The 2D MUSIC algorithm creates a two-dimensional grid, in the range which the angles vary $\theta \in [0, 90]$ $\varphi \in [0, 360]$, and then, evaluates the function P_{MUSIC} (1) for each point of the grid. The Fig. 8 illustrates the result of the MUSIC algorithm, a spatial graph that present peaks in the position of incident signals.

According to the Fig. 8, the function contains two peaks, which are evidenced. Note that there is another peak but is assumed to be repeated, once 0º and 360º is the same spatial location. To be easier to define the peaks of the graph, one function to detect correctly the N maxima values was implemented. This function only gives the points of zero gradient.

The result of this function is shown in the Fig. 9, with the two well defined peaks. The output of the MUSIC algorithm is that the incident signals that arrive to antenna are coming from (45.3º, 44.82º) and (70.07º, 0º), which are very close to the initially proposed angles.

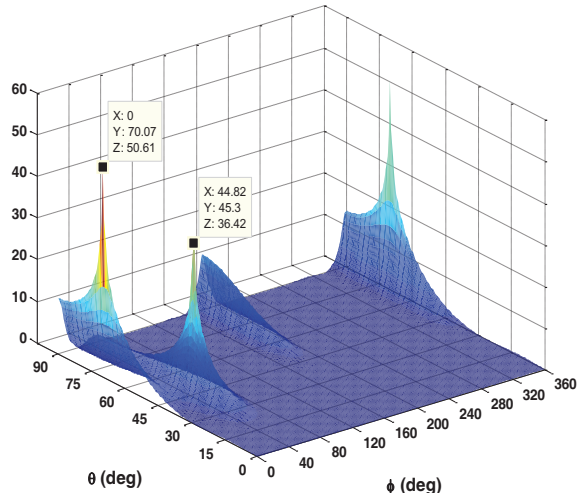

Fig. 8. 2D MUSIC spectrum.

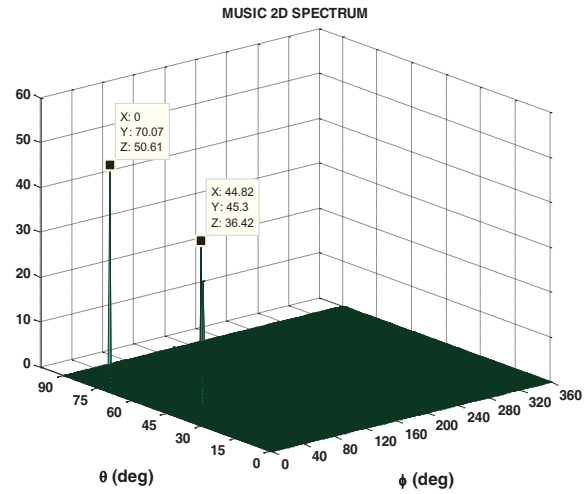

Fig.9. MUSIC 2D spectrum peaks.

b) ESPRIT

Using the equal received signal X(t) by each element of the antenna was processed the other DOA estimator, the ESPRIT algorithm. This algorithm doesn't use a grid to evaluate a function, but the output is just the pair of angles (θ,φ) estimated.

The output of the ESPRIT algorithm estimates that the signals are arriving from $(\theta,\varphi)=(45.02^{o},45.11^{o})$ and $(\theta,\varphi)=(69.82^{o},0.03^{o})$.

The DOA algorithms implemented exhibit estimated results very approximate to the original values. These algorithms only receive the signal X(t), and provides the spatial position of each incoming source which compose it.

Once known the DOA's of the signals, is necessary to apply some knowledge and choose the local to point the antenna and interfering directions. Assuming that the first pair of values (θ,φ) is the direction of interest, and the following the interfering signals, the system then employs the beamforming algorithms to determine the appropriate weights to apply to each element of the antenna array.

B. Beamforming

The beamforming weights are a set of amplitude and phase delays that are applied to an antenna array, to combine the signals in such way that produces constructive interference in some locals and destructive in others. These weights can be displayed in an exponential form $w = A\,e^{j\Phi}$.

The four beamforming algorithms presented before were tested and the resulting weights were inserted in the simulated antenna of the Fig. 7 and evaluated the obtained radiation pattern. The locals (θ,φ) of the considered signals are: signal of interest: (45º, 45º), and interference: (70º, 0º).

a) LCMV

The optimum solution for the LVCM problem were implemented, with input of the angles estimated by DOA algorithm, and using a response vector $f=[1\,0]^{H}$ to consider the first pair of angles the interest direction and the second the local of interference.

The result of the algorithm is presented in the Table 1, this output is composed by the complex weights already decomposed in terms of amplitude and phase, to apply directly to the corresponding element of the 4x4 array.

Table 1: Weights resulting from LCMV beamforming algorithm

Optimum LCMV				
Amplitude ∠ phase				
	1	2	3	4
1	1.0 ∠ 0º	1.0 ∠ -90º	1.0 ∠ -180º	1.0 ∠ 90º
2	1.0 ∠ -90º	1.0 ∠ 180º	1.0 ∠ 90º	1.0 ∠ 0º
3	1.0 ∠ 180º	1.0 ∠ 89º	1.0 ∠ 0º	1.0 ∠ -90º
4	1.0 ∠ 90º	1.0 ∠ 0º	1.0 ∠ -91º	1.0 ∠ 180º

The resultant radiation pattern of the planar antenna with these weights applied is shown in the Fig. 10. It's possible to observe the maximum of the radiation pattern pointed to the local (45º, 45º) of the signal of interest, with green dashed arrow, while in the direction (70º, 0º), with a red filled arrow, exists a low power value to diminish significantly the influence of the interference signal in the received from this direction.

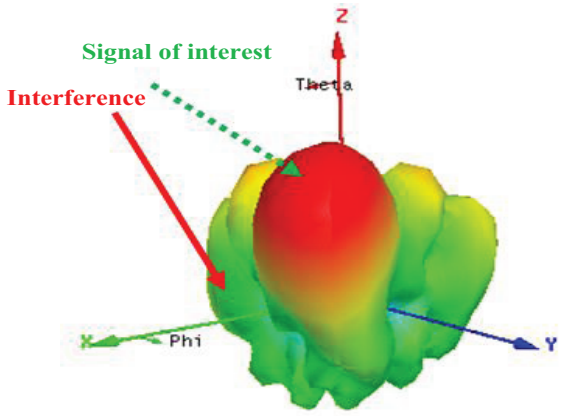

Fig. 10. The radiation pattern of the planar array with optimum LCMV weights applied.

b) Adaptive Frost's Algorithm for LCMV Beamforming

Another solution to solve the problem is using

adaptive algorithms that are a more realistic approach, due to the environment changes.

With the considered pair of angles for the signal of interest and interference directions, was tested the adaptive Frost's algorithm for LCMV beamforming. This algorithm was processed with a 100 samples of the input signal, iteratively, and the output resulting weights is presented in the Table 2.

Table 2: Weights resulting of adaptive Frost's algorithm for LCMV beamforming

Adaptive Frost's LCMV				
Amplitude ∠ phase				
	1	2	3	4
1	1.0 ∠ 0º	1.0 ∠ -90º	1.0 ∠ -180º	1.0 ∠ 90º
2	1.0 ∠ -90º	1.0 ∠ -180º	1.0 ∠ 90º	1.0 ∠ 0º
3	1.0 ∠ 180º	1.0 ∠ 90º	1.0 ∠ 0º	1.0 ∠ -90º
4	1.0 ∠ 90º	1.0 ∠ 0º	1.0 ∠ -90º	1.0 ∠ -180º

With these weights applied in the planar antenna, the new radiation pattern created is presented in the Fig. 11. It's observed that the antenna points to the direction of interest (green dashed arrow) placing a null in the interference zone (red filled arrow), as is pretended.

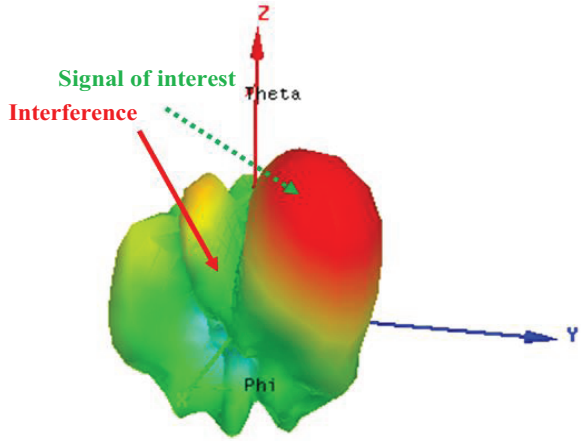

Fig. 11. The radiation pattern of the planar array with Frost's algorithm beamforming weights applied.

c) LMS

The known algorithm of least mean square was also performed in MATLAB, for a planar antenna array and to point to the considered directions. The result of this algorithm is available in the following Table 3.

This adaptive algorithm uses as the previous 100 samples of the received signal X(t). The produced radiation pattern when inserted the LMS weights is illustrated in the Fig. 12.

As is visible, the antenna points its maximum (green dashed arrow) in the direction (45º, 45º) and places a null (red filled arrow) in the (70º, 0º) zone.

Table 3: Weights resulting of the adaptive LMS beamforming algorithm

Adaptive LMS				
Amplitude ∠ phase				
	1	2	3	4
1	1.0 ∠ 0º	1.0 ∠ -83º	0.9 ∠ 156º	0.6 ∠ 83º
2	0.7 ∠ -83º	1.0 ∠ 179º	1.0 ∠ 93º	1.2 ∠ 2º
3	0.9 ∠ -178º	0.9 ∠ 61º	0.9 ∠ 23º	0.6 ∠ -78º
4	0.9 ∠ 69º	0.6 ∠ 13º	0.6 ∠ -59º	0.6 ∠ -169º

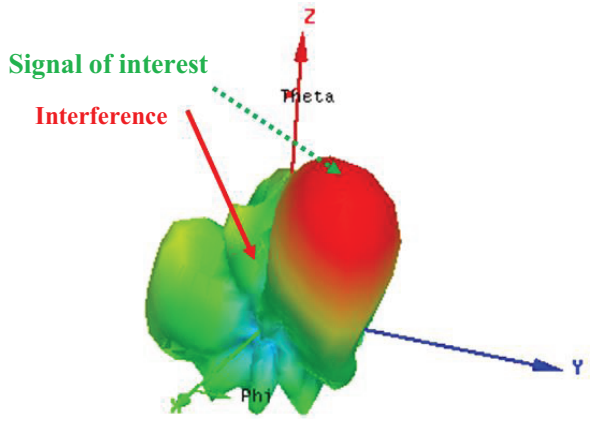

Fig. 12. The radiation pattern of the planar array with LMS algorithm beamforming weights applied.

d) RLS

The recursive least squares algorithm was also implemented to estimate the appropriate weights for this scenario. The output of this algorithm is presented in the Table 4, with the amplitudes and phases calculated to employ in the simulated antenna array.

Table 4: Weights resulting of the adaptive RLS beamforming algorithm

Adaptive RLS				
Amplitude ∠ phase				
	1	2	3	4
1	1.0 ∠ 0º	0.7 ∠ -104º	0.5 ∠ -161º	0.9 ∠ 102º
2	1.2 ∠ -92º	1.2 ∠ 175º	0.8 ∠ 107º	0.9 ∠ -34º
3	0.8 ∠ -163º	0.3 ∠ 127º	0.8 ∠ -100º	0.8 ∠ -73º
4	0.4 ∠ 101º	0.6 ∠ -4º	0.7 ∠ -114º	0.5 ∠ -128º

With this set of weights applied in the array, leads to the resulting radiation pattern that is shown in the Fig. 13.

As expected, the antenna will move its radiation pattern in the direction of interest (45º, 45º) indicated by green dashed arrow, becoming profitable the communication with a signal from this direction.

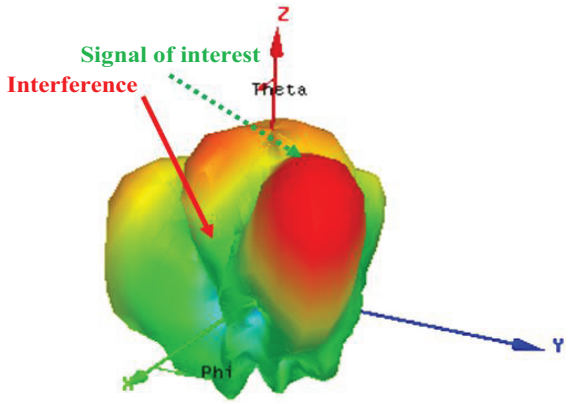

Fig. 13. The radiation pattern of the planar array with RLS algorithm beamforming weights applied.

After the estimation of the arrival directions of the impinging signals to the antenna and the calculation of the weights to steer the radiation pattern, using various algorithms, it is imperative a comparative description about their performance.

C. System performance

The system that consists of DOA estimation and computation of the beamforming weights was evaluated. The performance can be evaluated in terms of running time for all algorithms, the changeability of its results when the noise level alters and in terms of estimation errors.

Varying the signal to noise ratio (SNR), the runtime of the all algorithms was analyzed, applying beamforming and DOA estimation algorithms. The estimation error was also calculated, and the results are presented in Tables 5-8.

In accordance with Table 5, the runtime of LCMV algorithm is less significant than any of the direction of arrival algorithms (MUSIC or ESPRIT), and a variation with SNR is not significantly noted when SNR changes from 10 to 15 dB, although approximately doubles when SNR reduces from 10 to 5 dB. The MUSIC estimation algorithm is temporally extremely heavier than the ESPRIT. Note that the execution times don't have a marked variation with noise, despite the τ_{ESPRIT} tends to diminish when the SNR increase.

In terms of errors in the angle of arrival estimation (θ,φ), this error tends to reduce with increasing of SNR. Using the ESPRIT algorithm is observed the reduction of the errors; however, using the MUSIC algorithm the error is constant. This regular value is a consequence of the choice of the evaluation angle grid of the function P_{MUSIC}, as will see after, whereby must be a compromise between execution time and estimation error.

Table 5: Variation of the runtime and estimation error with SNR using LCMV algorithm

			SNR (dB)		
			5	10	15
LCMV	MUSIC	τ_{MUSIC} (s)	5.92	6.03	5.34
		τ_{LCMV} (s)	0.0199	0.00089	0.00098
		ε_{θ} (degrees)	0.302	0.302	0.302
		ε_{ϕ} (degrees)	0.305	0.305	0.305
	ESPRIT	τ_{ESPRIT} (s)	0.052	0.038	0.013
		τ_{LCMV} (s)	0.0013	0.0011	0.0009
		ε_{θ} (degrees)	0.08	0.04	0.02
		ε_{ϕ} (degrees)	0.167	0.141	0.0275

Using the Frost's algorithm, as it is adaptive, it has a runtime which diminishes with the SNR, Table 6. The DOA algorithm's performance remained with characteristics already described about the execution time. The estimation errors in the case of MUSIC continue mainly affected due to the selection of interval in the grid angle to evaluate the equation (1), while in ESPRIT is visible an error reduction with the increasing of SNR.

Table 6: Variation of the runtime and estimation error with SNR using Frost's algorithm

			SNR (dB)		
			5	10	15
FROST's	MUSIC	τ_{MUSIC} (s)	5.67	5.15	5.53
		$\tau_{Frost's}$ (s)	0.0118	0.0047	0.0007
		ε_{θ} (degrees)	0.302	0.302	0.302
		ε_{ϕ} (degrees)	0.305	0.305	0.305
	ESPRIT	τ_{ESPRIT} (s)	0.015	0.0018	0.0077
		$\tau_{Frost's}$ (s)	0.013	0.001	0.00086
		ε_{θ} (degrees)	0.140	0.042	0.042
		ε_{ϕ} (degrees)	0.0188	0.014	0.010

With the LMS algorithm, according to the Table 7, the execution time reduces while the value of SNR increases, whereas the MUSIC and ESPRIT algorithms keep on with similar characteristics to the preceding cases. The error also shows a reduction with the increase of SNR.

Finally, the Table 8 shows the analysis of the performance using the RLS algorithm. It is possible to see a pronounced reduction of the runtime when SNR changes from 5 dB to 10 dB. The error follows the expected behavior, with a reduction of its value when the DOA ESPRIT algorithm is employed, with the increase

of SNR. When the MUSIC algorithm is used, the error remains constant.

Table 7: Variation of the runtime and estimation error with SNR using LMS algorithm

			SNR		
			5	10	15
LMS	MUSIC	τ_{MUSIC} (s)	5.35	5.37	5.46
		τ_{LMS} (s)	0.020	0.007	0.002
		ε_θ (degrees)	0.302	0.302	0.302
		ε_ϕ (degrees)	0.305	0.305	0.305
	ESPRIT	τ_{ESPRIT} (s)	0.0095	0.0012	0.0011
		τ_{LMS} (s)	0.0054	0.0050	0.0046
		ε_θ (degrees)	0.203	0.042	0.02
		ε_ϕ (degrees)	0.090	0.045	0.024

Table 8: Variation of the runtime and estimation error with SNR using the RLS algorithm

			SNR		
			5	10	15
RLS	MUSIC	τ_{MUSIC} (s)	5.82	5.75	5.71
		τ_{RLS} (s)	0.0163	0.0070	0.0161
		ε_θ (degrees)	0.302	0.302	0.302
		ε_ϕ (degrees)	0.305	0.305	0.305
	ESPRIT	τ_{ESPRIT} (s)	0.00181	0.00180	0.0015
		τ_{RLS} (s)	0.0101	0.01	0.01
		ε_θ (degrees)	0.2294	0.0378	0.0972
		ε_ϕ (degrees)	0.156	0.031	0.01

Globally, is noted that the tendency related to beamforming algorithms is the increase of its execution times from the statistically optimum to each of the adaptive ones. The DOA algorithms present consistent results, with a reduction of estimation error with the increase of SNR, taking into account that with MUSIC algorithm a compromise between error and runtime must be done.

Using a considerable number of experiments, a statistical analysis of this performance of each algorithm can be done. This estimate was based on a sequence of 50 experiments, and the graphical analysis is performed in the next figures.

The Fig. 14 shows the runtime of the LCMV algorithm over the number of the *n* experiments. Despite a couple of experiments presents a more accentuated variation, the mean execution time is about 6.2×10^{-4} seconds (0.62 msec).

The Frost's algorithm execution time is displayed in the Fig. 15. This algorithm presents a mean value of the 5×10^{-4} seconds (0.5 msec), that although is an adaptive algorithm presents a better result than the previous one.

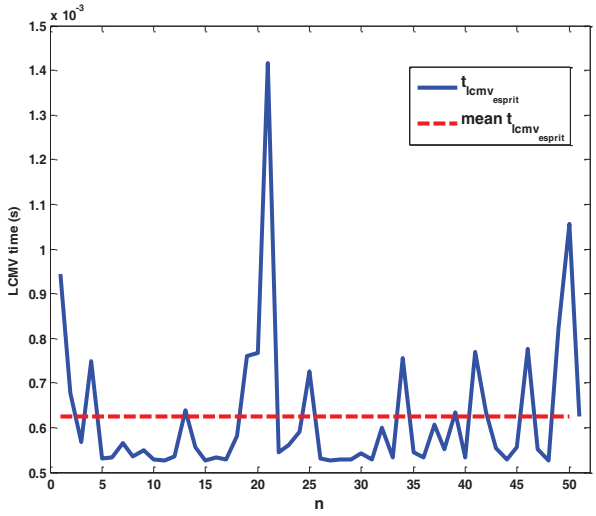

Fig. 14. Execution time of LCMV algorithm.

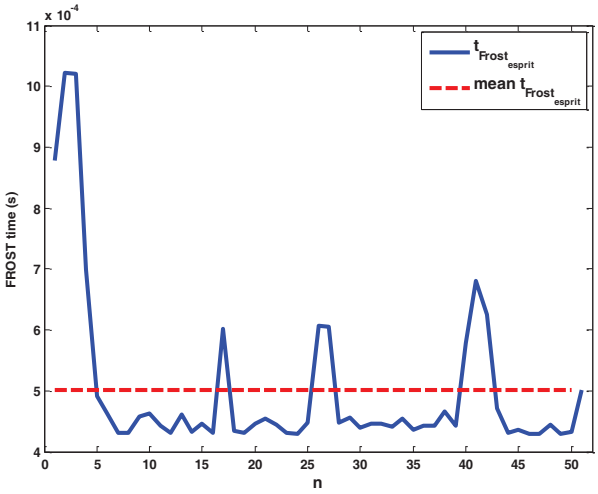

Fig. 15. Execution time of Frost's algorithm.

Using the LMS and RLS algorithms, the used runtime over the experiences are indicated in the Fig. 16 and Fig. 17. The execution times are respectively 2.8×10^{-3} seconds (2.8 msec) and 7.6×10^{-3} seconds (7.6 msec).

Along the *n* experiences, the runtimes of the two DOA estimation algorithms are displayed in graphical form in the Fig. 18. The upper part includes the values relating to the MUSIC algorithm, while the lower part is concerning to the ESPRIT algorithm. In both the graphs are identified the line of the average time of the various

samples.

Immediately, it is possible to note the huge difference in the time it takes to perform the MUSIC algorithm compared with the ESPRIT. The MUSIC algorithm takes *n* samples during 5 to 6 seconds each one, presenting an average execution time of 5.54 seconds as shown in Fig. 18. Much less time requires the ESPRIT algorithm, ranging between 1 and 2 milliseconds as the figure shows, with an only sample with a peak reaching 3.5 msec, and the overall average execution time 1.57 msec.

The last parameter that is possible to examine is the estimation error, between the real coordinates (θ,φ) of the incoming waves, and the estimated position determined by the two dimensional DOA algorithms, MUSIC and ESPRIT.

In the Fig. 19, there are exposed the evolution of the estimating error over the *n* experiences. The superior graph is relating to the coordinate θ, while the bottom is about the φ. In each parts are present the error using the two algorithms of DOA, and further the line of mean of the error. As is possible to see, using the MUSIC algorithm the estimation error have a constant effect, with a mean error of 0.302º in theta and 0.3052º in phi. The ESPRIT algorithm present mean errors much lower, of 0.037º in theta and 0.015º in phi coordinates.

The ESPRIT error is due to the mathematical process and the noise added to the signal. On the other hand, the MUSIC error is strongly due the evaluation interval, as explained in the Fig. 20. The accuracy depends on the number of points on its angle grid, more points lead to longer computations. This is the main issue of MUSIC, and the number of points must be a compromise depending on the required accuracy and computational load.

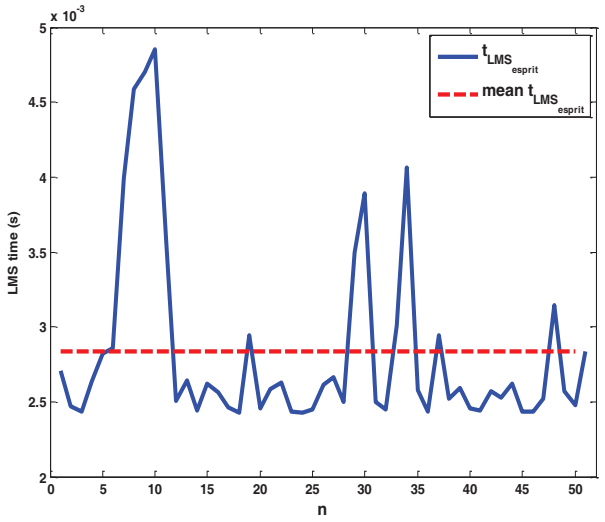

Fig. 16. Execution time of LMS algorithm.

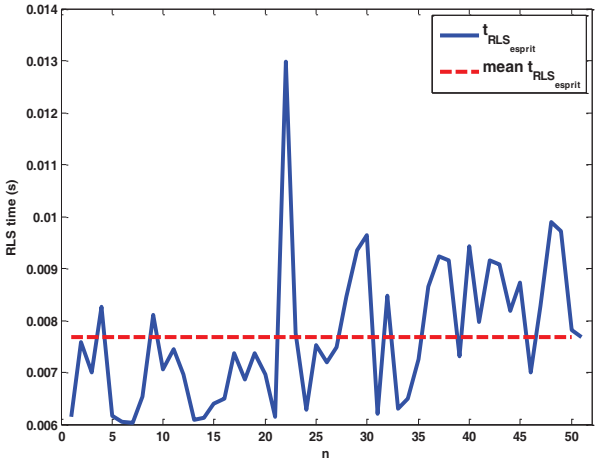

Fig. 17. Execution time of RLS algorithm.

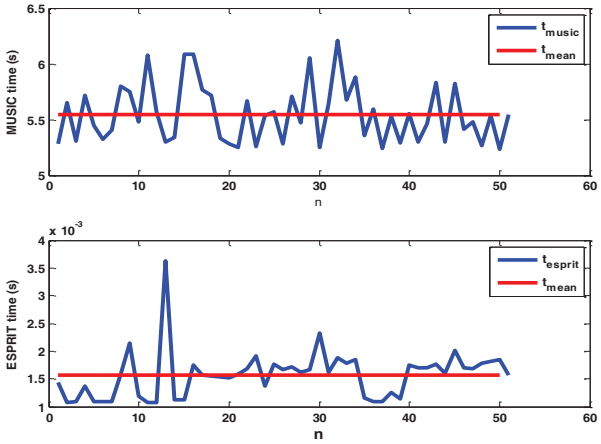

Fig. 18. Execution time evolution of DOA algorithms over *n* samples.

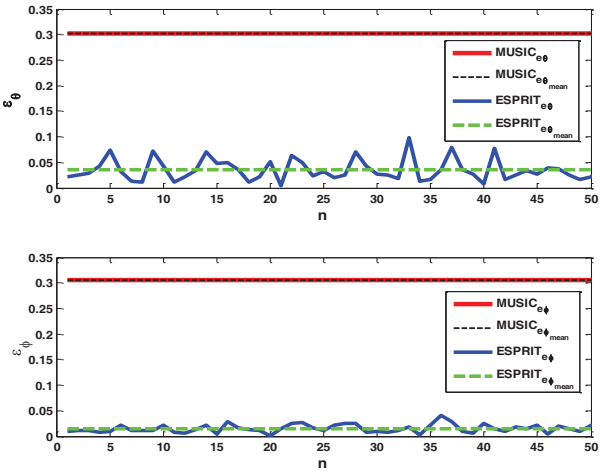

Fig. 19. Estimation error in theta and phi coordinates using each one of DOA algorithms (MUSIC and ESPRIT).

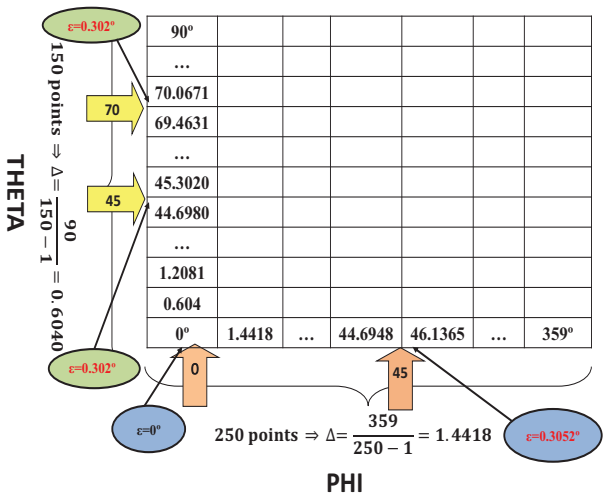

Fig. 20. Evaluation grid of MUSIC algorithm.

VI. DISCUSSION AND FUTURE PROSPECTS

In this paper, the analysis of the main 2D algorithms that are vital in a planar adaptive antenna system, the direction of arrival and the beamforming algorithms, was made.

The developed function to extract the peaks of the MUSIC spectrum is very effective, allowing a correct definition of the maxima values, and the corresponding DOAs. In this work, the weights resulting of the beamforming algorithms, in terms of amplitude and phase, were tested in a simulated array. The intention was to verify that the achieved radiation patterns in electromagnetic simulator present the desired radiation characteristics. About the performance of the algorithms, the runtime of the DOA MUSIC is much higher than ESPRIT, since the MUSIC algorithm must evaluate the MUSIC function to each possible steering vector.

Also about estimating errors, the MUSIC presents some limitations, since the accuracy of the angle results of the interval of evaluating the function. A compromise between the accuracy and the processing time is needed. This fact is something important that is not addressed in [24], so it's a tradeoff to consider. In both DOA algorithms, this error reduces with the increasing of the SNR. The runtime of the beamforming algorithms increases more in the adaptive due to the number of snapshots processed.

The trends involve the use of new, and more complex array topologies, such as three-dimensional arrays, investing in the research of new techniques for determining the DOA's, adapted to them, such as in [25]. Furthermore, advances in beamforming techniques for randomly distributed planar arrays [26], [27] have showed an increased interest, with several applications, either in small satellites or in arrays of sensors, with a non-uniform distribution. Also, is expected the use of smart antennas in the 5th generation of mobile wireless systems (5G) using MIMO, in the millimeter wave frequencies.

ACKNOWLEDGMENT

This work is funded by National Funds through FCT-Fundação para a Ciência e a Tecnologia under the project PEst-OE/EEI/LA0008/2013.

REFERENCES

[1] J. Foutz, et. al., *Narrowband Direction of Arrival Estimation for Antenna Arrays*, Morgan & Claypool Publishers, 2008.

[2] L. C. Godara, "Application of antenna arrays to mobile communications, II. beam-forming and direction-of-arrival considerations," *Proceedings of the IEEE*, vol. 85, no. 8, pp. 1195-1245, Aug. 1997.

[3] R. O. Schmidt, "Multiple emitter location and signal parameter estimation," *IEEE Transactions on Antennas and Propagation*, vol. 34, no. 3, pp. 276-280, Mar. 1986.

[4] S. Sekizawa, "Estimation of arrival directions using MUSIC algorithm with a planar array," *IEEE International Conference on Universal Personal Communications, ICUPC '98*, vol. 1, pp. 555-559, Oct. 1998.

[5] K. V. Rangarao and S. Venkatanarasimhan, "Gold-MUSIC: a variation on MUSIC to accurately determine peaks of the spectrum," *IEEE Transactions on Antennas and Propagation*, vol. 61, no. 4, pp. 2263-2268, Apr. 2013.

[6] C. C. Yeh, J-H. Lee, and Y. Chen, "Estimating two-dimensional angles of arrival in coherent source environment," *IEEE Transactions on Acoustics, Speech and Signal Proc*., vol. 37, no. 1, pp. 153-155, Jan. 1989.

[7] Y. Chen, "On spatial smoothing for two-dimensional direction-of-arrival estimation of coherent signals," *IEEE Transactions on Signal Processing*, vol. 45, no. 7, pp. 1689-1696, Jul. 1997.

[8] Z. Chen, G. Gokeda, and Y. Yu, *Introduction to Direction-of-Arrival Estimation*, Artech House, 2010.

[9] M. Haardt, M. D. Zoltowski, C. P. Mathews, and J. A. Nossek, "2D unitary ESPRIT for efficient 2D parameter estimation," *International Conference on Acoustics, Speech, and Signal Processing, ICASSP-95*, vol. 3, pp. 2096-2099, 1995.

[10] M. D. Zoltowski, M. Haardt, and C. P. Mathews, "Closed-form 2-D angle estimation with rectangular arrays in element space or beamspace via unitary ESPRIT," *IEEE Transactions on Signal Processing*, vol. 44, no. 2, pp. 316-328, Feb. 1996.

[11] Y-Y. Wang and W-W. Chen, "A low complexity 2D-DOA estimation algorithm using signal

decomposition," *High Speed Intelligent Communication Forum*, pp. 1-4, May 10-11, 2012.
[12] J. Hui and Y. Gang, "An improved algorithm of ESPRIT for signal DOA estimation," *International Conference on Industrial Control and Electronics Engineering (ICICEE)*, pp. 317-320, Aug. 23-25, 2012.
[13] B. D. Van Veen and K. M. Buckley, "Beamforming: a versatile approach to spatial filtering," *IEEE ASSP Magazine*, vol. 5, no. 2, pp. 4-24, Apr. 1988.
[14] W. Liu and S. Weiss, *Wideband Beamforming: Concepts and Techniques*, John Wiley & Sons, 2010.
[15] F. Huang, W. Sheng, and X. Ma, "Efficient parallel adaptive beamforming algorithm for planar array system," *International Symposium on Antennas, Propagation and EM Theory*, pp. 282-285, Nov. 2-5, 2008.
[16] J-H. Lee and Y-H. Lee, "Two-dimensional adaptive array beamforming with multiple beam constraints using a generalized sidelobe canceller," *IEEE Transactions on Signal Processing*, vol. 53, no. 9, pp. 3517-3529, Sept. 2005.
[17] A. M. G. Guerreiro, A. D. D. Neto, and F. A. Lisboa, "Beamforming applied to an adaptive planar array," *IEEE Radio and Wireless Conference, RAWCON 98*, pp. 209-212, Aug. 9-12, 1998.
[18] S. Razia, T. Hossain, and M. A. Matin, "Performance analysis of adaptive beamforming algorithm for smart antenna system," *Informatics, Electronics & Vision (ICIEV), 2012 International Conference on*, pp. 946-949, May 18-19, 2012.
[19] S. K. Imtiaj, I. S. Misra, and R. Biswas, "Performance comparison of different adaptive beamforming algorithm in smart antennas," *International Conference on Computers and Devices for Communication (CODEC)*, pp. 1-4, Dec. 17-19, 2012.
[20] S-J. Yu and J-H. Lee, "Design of two-dimensional rectangular array beamformers with partial adaptivity," *IEEE Transactions on Antennas and Propagation*, vol. 45, no. 1, pp. 157-167, Jan. 1997.
[21] R. Li, C. Rao, L. Dai, and S. Zhao, "Adaptive-adaptive beamforming algorithm of planar array based on one-dimensional auxiliary beam," *International Congress on Image and Signal Processing (CISP)*, vol. 7, pp. 3300-3303, Oct. 16-18, 2010.
[22] Ansoft High Frequency Structure Simulator (HFSS), User's Guide, ed.: REV1.0, Software ver.: 10.0, Ansoft Corporation, Jun. 21, 2005.
[23] MATLAB, ver. 7.10.0 (R2010a), The MathWorks Inc., Natick, Massachusetts, 2010.
[24] O. A. Oumar, M. F. Siyau, T. P. Sattar, "Comparison between MUSIC and ESPRIT direction of arrival estimation algorithms for wireless communication systems," *International Conference on Future Generation Communication Technology*, pp. 99-103, Dec. 12-14, 2012.
[25] B. Errasti-Alcala and R. Fernandez-Recio, "Meta-heuristic approach for single-snapshot 2D-DOA and frequency estimation: array topologies and performance analysis," *Antennas and Propagation Magazine, IEEE*, vol. 55, no. 1, pp. 222-238, Feb. 2013.
[26] C. G. Christodoulou, M. Ciaurriz, Y. Tawk, J. Costantine, and S. E. Barbin, "Recent advances in randomly spaced antenna arrays," *European Conference on Antennas and Propagation (EuCAP)*, pp. 732-736, Apr. 6-11, 2014.
[27] M. Ciaurriz, Y. Tawk, C. G. Christodoulou, and J. Costantine, "Adaptive beamforming for random planar arrays," *Antennas and Propagation Society International Symposium (APSURSI), 2014 IEEE*, pp. 1728-1729, Jul. 6-11, 2014.

Tiago Varum got his Master's degree in Electronic and Telecommunications Engineering from Aveiro University in 2010, and started research activities in Telecommunications Institute. His main interest of research is in vehicular communications (DSRC systems), antenna design, non-uniform antenna arrays, beam-forming and smart/adaptive antennas. In 2012, he started his doctoral research (for Ph.D.) in Electrical Engineering, at Aveiro University, in the field of adaptive beamforming antennas. During this time, he participated in some projects and published several papers in this field, some for conference proceedings and one for a journal. He has also supported teaching activities in the Department of Electronics, Telecommunications and Informatics (DETI) of Aveiro University.

João N. Matos received his diploma in Electronics and Telecommunications Engineering, from Aveiro University, Portugal, in 1982, Master's degree in Computer Science, from the University of Coimbra, Portugal, in 1989, and Ph.D. degree in Electrical Engineering in 1995, from Aveiro University, Portugal. From 1982 to 1983 he was with Portugal Telecom Innovation. From 1983 to 1995, he was an Assistant Lecturer at University of Aveiro, and a Professor since

1995. Currently he is an Associate Professor at the same University and a Senior Research Scientist at the Institute of Telecommunications. His main scientific interests are in the development of circuits and systems for wireless power transfer and for ITS (Intelligent Transport Systems). He has authored or co-authored more than 70 papers for international journals and conferences.

Pedro Pinho was born in Vale de Cambra, Portugal in 1974. He received the Licenciado and Master's degrees in Electrical and Telecommunications Engineering, and the Ph.D. degree from the University of Aveiro in 1997, 2000, and 2004 respectively. He is currently a Professor Adjunto at the Department of Electrical Telecommunications and Computers Engineering in Instituto Superior de Engenharia de Lisboa, in Instituto Politécnico de Lisboa, and a Member of the research staff at the Institute for Telecommunications, Aveiro, Portugal from 1997. His current research interest is in antennas for location systems, reconfigurable antennas and antenna design for passive sensors in non-conventional materials. He has authored or co-authored more than 90 papers for conferences and international journals and 4 book chapters.

Integrated Bluetooth and UWB Antenna with Single Band-Notched

Zheng Han [1], Zhenyang Ma [2], and Qiannan Xue [2]

[1] Basic Experimental Center
Civil Aviation University of China, Tianjin, 300300, China
hanzhengcauc@163.com

[2] Tianjin Key Laboratory of Civil Aircraft Airworthiness and Maintenance
Civil Aviation University of China, Tianjin, 300300, China
zyma@mail.xidian.edu.cn, qiannanxue@163.com

Abstract ─ A novel integrated Bluetooth and ultra-wideband (UWB) antenna with single band-notched is proposed in this paper. The operating frequency ranges of the proposed antenna is 2.3 GHz - 2.56 GHz, 2.96 GHz - 5.11 GHz and 5.95 GHz - 11.44 GHz, which covers Bluetooth (2.4 GHz - 2.484 GHz) and UWB (3.1 GHz - 10.6 GHz) band, besides the range of IEEE 802.11a WLAN (5.15 GHz - 5.825 GHz) with VSWR less than 2. Its main part consists of a hexagonal geometry, an L-shaped strip and two mushroom-like electromagnetic band gap (EBG) cells. The performance of the antenna is simulated and optimized by CST Microwave Studio and the simulated results meet the design requirements well.

Index Terms ─ Antenna, band-notched antenna, Bluetooth, electromagnetic band gap (EBG), ultra-wideband (UWB).

I. INTRODUCTION

In recent years, UWB systems have attracted a lot of attentions since the Federal Communications Commission (FCC) released the frequency band from 3.1 GHz to 10.6 GHz for communication applications [1]. Meanwhile, Bluetooth is a short-range wireless technology that has been widely used in wireless portable devices, cell phones, and other mobile devices. Many papers focusing on ultra-wideband and Bluetooth integrated antenna have been reported [2-6]. However, over the frequency range of UWB, there are other narrowband wireless communication systems, such as IEEE 802.11a wireless local area network (WLAN), operating in the range 5.15 GHz - 5.825 GHz. Therefore, in order to avoid mutual interference, a stop band should be designed to reject such used band. To solve the problems, people have made lots of attempts. One method is etching slots in the patch of the antenna or ground [7-12]. The other method is adding parasitic structures in antenna [13-15]. In recent years, the EBG structure is another choice to serve in the band-notched antennas, which has the advantage of compact size and good band-notched property [16-19].

Based on aforesaid studies, a novel integrated Bluetooth and UWB antenna with single band-notched is presented. It can cover the frequency bands of Bluetooth and UWB antenna. In order to avoid interference from IEEE 802.11a WLAN systems, two mushroom-like EBG cells are loaded on both sides of the feeding line to generate notch band. The notch band can be tuned by changing the size of EBG cell. All the simulations are carried out by CST Microwave Studio. The simulation results reveal that the Bluetooth function can be easily realized by adding an additional L-shaped strip and the band-notched function can be realized by adding a pair of EBG cells. At last, voltage standing wave ratio (VSWR), radiation pattern characteristics, gain, efficiency, and group delay of the proposed antenna are presented and discussed.

II. ANTENNA DESIGN

The details of the proposed monopole antenna are illustrated in Fig. 1. A patch is etched on an FR-4 substrate with a relative dielectric constant of $\varepsilon_r = 4.4$. The dimension of the substrate is $36\times42\times1$ mm^3. The antenna constants a hexagonal pattern, an L-shaped strip, two mushroom-like EBG cells, a rectangular ground plane on the back side of the substrate and a 50 Ω microstrip line as feeding structure. The hexagonal structure serves as an UWB antenna. The L-shaped strip serves as Bluetooth antenna, which is integrated with the UWB antenna. The two mushroom-like EBG cells are used to achieve single band-notched characteristic, loaded on the both sides of transmission line. L is the length of EBG cell, and D is the distance from EBG cell to transmission line.

The mushroom-like EBG cell we adopted has the advantages in terms of simple structure and easy to fabricate. In order to study the impact of the EBG cells

Submitted On: September 29, 2014
Accepted On: May 20, 2015

on the UWB element, we analyze the performance of them by tuning the parameters L and D using CST Microwave Studio. Figure 2 shows the simulation results of VSWR with different values of L and D. Figure 2 (a) indicates that center frequency becomes smaller with the increasing of L when the value of D remains (0.3 mm). And Fig. 2 (b) shows that the decreasing of D will lead to wide and sharp band-notch when the value of D remains (6.2 mm). In summary, band-notched characteristic mainly depends on the size of the metal patch and the distance between the metal patch and the microstrip. The frequency center can be adjusted by changing the length of patch, while the bandwidth can be adjusted by changing distance from metal patch to microstrip. Finally, the optimal parameters of L and D are chosen to be 6.2 mm and 0.3 mm, respectively.

The design of the proposed antenna includes three steps. First, a UWB antenna (without added L-shaped and EBG cells) is designed, which operates from 3.3 GHz to 12 GHz (VSWR≤2) in Fig. 3. Second, an L-shaped strip is attached to one side of the UWB antenna which serves as a resonance occurred at 2.4 GHz. At last, the proposed single band-notched integrated antenna (with added L-shaped strip and EBG cells) is achieved by adding two EBG cells. It has a usable Bluetooth passband about 260 MHz (2.3 GHz - 2.56 GHz) and a notch band about 840 MHz (5.11 GHz - 5.95 GHz) with the center frequency of 5.6 GHz. It is clearly observed that the proposed antenna with added L-shaped strip and EBG cells cannot change the property of ultra-wideband, and we can add notch band by this approach easily.

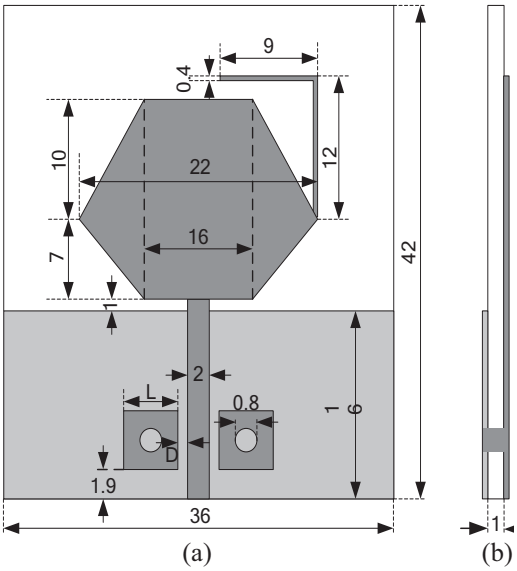

Fig. 1. Structure of the proposed antenna: (a) top view, and (b) side view (Units in mm).

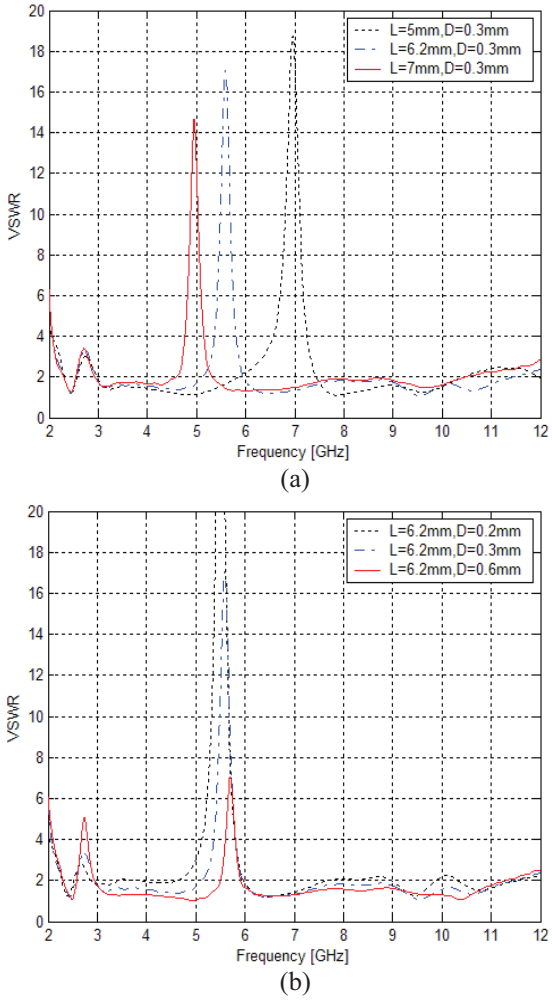

Fig. 2. Simulated VSWR with different: (a) L, and (b) D.

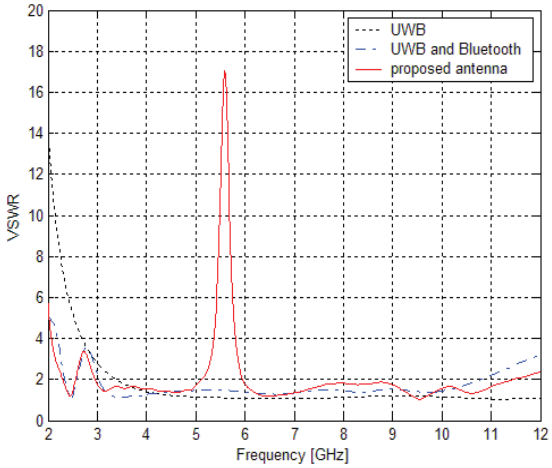

Fig. 3. Simulated VSWR of UWB, UWB and Bluetooth, and proposed single band-notched integrated antenna.

III. RESULTS AND ANALYSIS

For better understanding of the proposed antenna behavior, the current distributions on the integrated antenna at 2.4 GHz, 5.6 GHz, and 8.5 GHz are presented in Fig. 4. The current density is significantly high in L-shaped strip as shown in Fig. 4 (a), which denotes that the L-shaped strip resonates at 2.4 GHz. As shown in Fig. 4 (a) and (c), the current density is very low in EBG cells at 2.4 GHz and 8.5GHz, while relatively high at resonant frequency 5.6 GHz in Fig. 4 (b). At 5.6 GHz, the currents mainly distribute in metal patches and few are coupled to radiation patch. Therefore, the input power will be prevented within the notch band. The current distribution results confirm that the L-shaped and EBG cells are relatively independent, and they have significant effect on Bluetooth and band-notch performance separately.

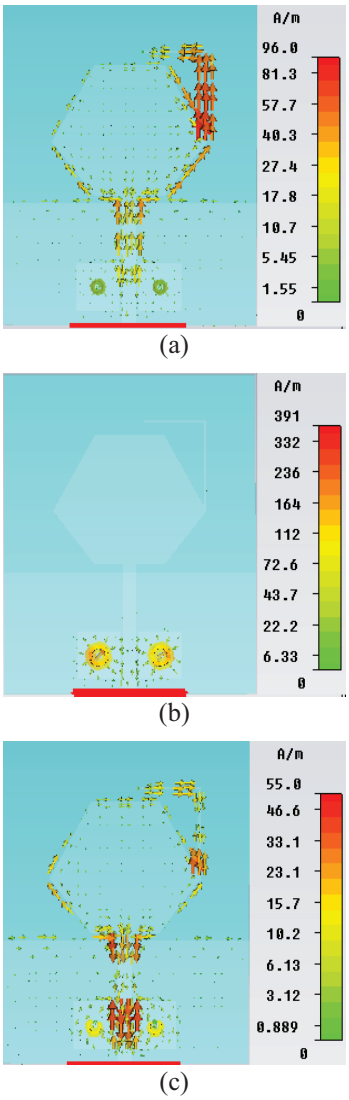

Fig. 4. Simulated current distribution at frequencies of: (a) 2.4 GHz, (b) 5.6 GHz, and (c) 8.5 GHz.

The co-polarization and cross-polarization radiation patterns of the proposed antenna in both E- and H-planes at three frequency points of 2.4 GHz, 6 GHz, and 10 GHz are shown in Fig. 5. The antenna is design in *x*-*y* plane, and the maximum radiation direction is along the *y*-axis. As shown in Fig. 5, the values of co-polarization is bigger than the values of cross-polarization in E-plane, and the values of cross-polarization are all less than -10 dB. In H-plane, the values of co-polarization are also bigger than the values of cross-polarization except the point of 10 GHz. The radiation patterns of E-plane are nearly figure-eight and H-plane are stable omni-directional.

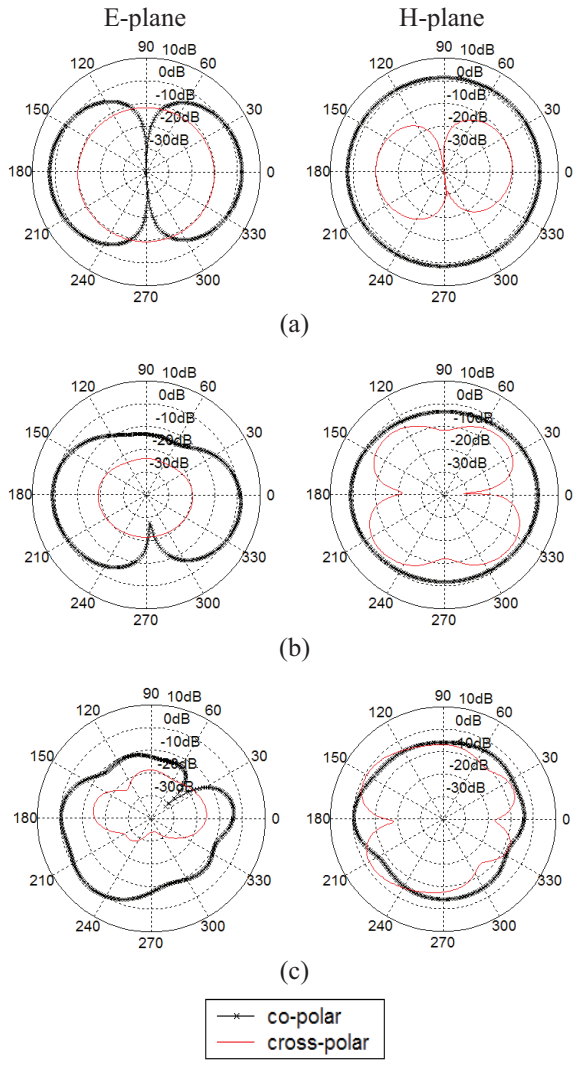

Fig. 5. Simulated radiation patterns of the proposed antenna at: (a) 2.4 GHz, (b) 6 GHz, and (c) 10 GHz.

The simulated antenna gain is shown in Fig. 6. It varies approximately from 2.1 dB to 5.5 dB over the operating frequency range, and decreases to -0.18 dB at

5.6 GHz. It also can be seen from the figure, the gain below 7 GHz is less than the value of above, which is because the wavelength gets longer below 7 GHz. By comparison, the size of the UWB element is small relative to the wavelength. The simulated radiation efficiency varies from 55% to 97% over the operating frequency range of the proposed antenna, and drops to 11% at center frequency of WLAN band, as shown in Fig. 7. The trend is consistent with the gain. The value of the group delay simulated by CST is mainly between 0 ns and 1 ns, which is nearly constant besides 2.4 GHz and 9.5 GHz in Fig. 8.

At last, the proposed antenna and the other antennas cited in this paper are compared in Table 1. From the table, the antenna proposed in this paper not only can work in the UWB and Bluetooth bands, but also has the advantages of good WLAN band ranges and gain.

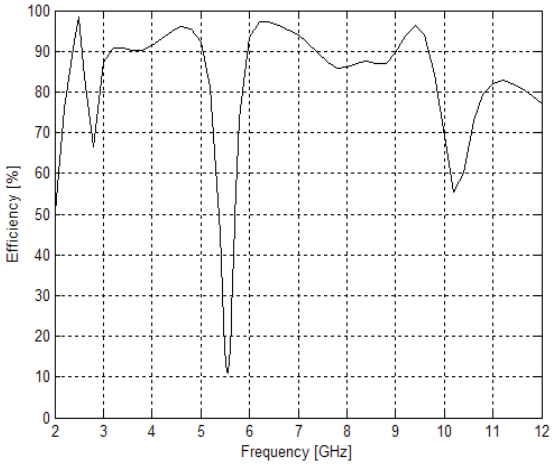

Fig. 7. Simulated efficiency of the proposed antenna.

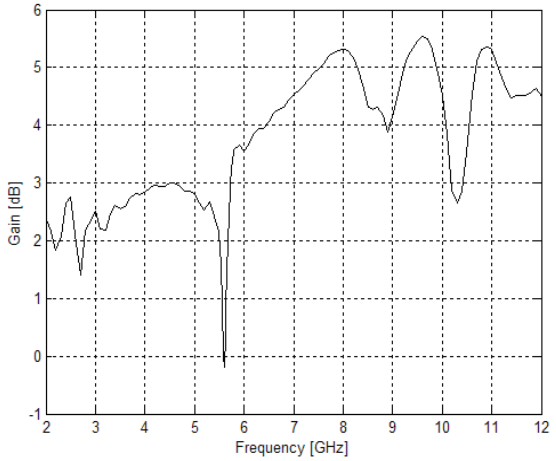

Fig. 6. Simulated gain of the proposed antenna.

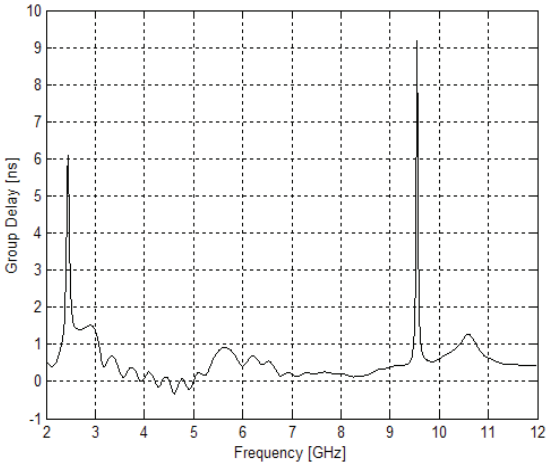

Fig. 8. Simulated group delay of the proposed antenna.

Table 1: Performance comparison

Antennas	Dimensions (mm^3)	ε_r of Substrate	Operating Bands	WLAN Band Ranges (GHz)	Gain Except WLAN Band (dB)
This paper	36×42×1	4.4	Bluetooth and UWB	5.11-5.95	2.1-5.5
A in Ref. [6]	42×46×1	4.4	Bluetooth and UWB	5.2-5.8	2.8-7.2
B in Ref. [6]	42×46×1	4.4	Bluetooth and UWB	5.2-5.8	2.8-6.6
Ref. [10]	24×28×1	2.65	UWB	4.65-6.4	3-6
Ref. [11]	25×30×0.8	4.4	UWB	5.17-6.14	2.7-6
Ref. [16]	38×40×1	4.4	UWB	5.2-5.9	1.5-4.5
Ref. [17]	30×32×1.6	4.4	UWB	5-5.9	2-6.9

IV. CONCLUSION

A compact and planar Bluetooth and UWB antenna with single band-notched is presented. On the basis of ultra-wideband, we add Bluetooth function by embedding an L-shaped parasitic strip. Hence, the antenna can operate on both Bluetooth and UWB frequency range for VSWR≤2. Through adding two simple mushroom-like EBG cells on both sides of the microstrip line, a notch band from 5.11 GHz to 5.95 GHz is generated to suppress the interference of IEEE 802.11a WLAN. The simulation results show that the proposed antenna with a compact size, simple structure, good WLAN band-notched characteristics, and wide bandwidth can be a good candidate for UWB application. Therefore, the results of the work are useful for short-range wireless communication systems.

ACKNOWLEDGMENT

This research was supported by the Fundamental Research Funds for the Central Universities (3122014C024) and the Fundamental Research Funds for the Central Universities (3122014C025).

REFERENCES

[1] *Federal Communications Commission*, "First report and order, revision of part 15 of commission's rule regarding UWB transmission system," FCC 02-48, Washington, DC, Apr. 22, 2002.

[2] Y. F. Weng, S. W. Cheung, and T. I. Yuk, "An antenna for UWB and Bluetooth standards with band-notched characteristic," *IEEE International Conference on Ultra-Wideband*, pp. 170-174, Sep. 2009.

[3] M. M. S. Taheri, H. R. Hassani, and S. M. A. Nezhad, "UWB printed slot antenna with Bluetooth and dual notch bands," *IEEE Antennas Wireless Propag. Lett*., vol. 10, pp. 255-258, Feb. 2011.

[4] B. S. Yildirim, B. A. Cetiner, G. Roqueta, and L. Jofre, "Integrated Bluetooth and UWB antenna," *IEEE Antennas and Wireless Propagation Letters*, vol. 8, pp. 149-152, Apr. 2009.

[5] Y. F. Liu, P. Wang, and H. Qin, "Compact ACS-fed UWB monopole antenna with extra Bluetooth band," *Electronics Letters*, vol. 50, no. 18, pp. 1263-1264, Aug. 2014.

[6] A. Shaker, S. H. Zainud-Deen, K. R. Mahmoud, and S. M. Ibrahem, "Compact Bluetooth/UWB antenna with multi-band notched characteristics," *Journal of Electromagnetic Analysis and Applications*, pp. 512-518, Mar. 2011.

[7] D. H. Bi and Z. Y. Yu, "A CPW-fed diamond monopole antenna with dual stopband characteristic for UWB communications," *Journal of Electromagnetic Waves and Applications*, vol. 22, no. 13, pp. 140-143, Nov. 2008.

[8] J. Y. Deng, Y. Z. Yin, S. G. Zhou, and Q. Z. Liu, "Compact ultra-wideband antenna with tri-band notched characteristic," *Electron. Lett*., vol. 44, no. 21, pp. 1231-1233, Oct. 2008.

[9] Y. L. Zhao, Y. C. Jiao, G. Zhao, L. Zhang, Y. Song, and Z. B. Wong, "Compact planar monopole UWB antenna with band-notched characteristic," *Microw. Opt. Technol. Lett*., vol. 50, no. 10, pp. 2656-2658, Oct. 2008.

[10] W. J. Lui, C. H. Cheng, and H. B. Zhu, "Compact frequency notched ultra-wideband fractal printed slot antenna," *IEEE Microw. Wireless Compon. Lett*., vol. 16, no. 4, pp. 224-226, Apr. 2006.

[11] P. Wang, "Compact dual band-reject monopole antenna for UWB applications," *Appl. Comp. Electro. Society (ACES) Journal*, vol. 28, no. 8, pp. 725-730, Aug. 2013.

[12] N. Ojaroudi, M. Ojaroudi, and N. Ghadimi, "Disc-shaped monopole antenna with dual band-notched function for UWB applications," *Appl. Comp. Electro. Society (ACES) Journal*, vol. 28, no. 6, pp. 528-534, Jun. 2013.

[13] K. H. Kim, Y. J. Cho, S. H. Hwang, and S. O. Park, "Band-notched UWB planar monopole antenna with two parasitic patches," *Electronics Letters*, vol. 41, no. 14, pp. 783-785, Jul. 2005.

[14] N. Ojaroudi, M. Ojaroudi, and N. Ghadimi, "UWB slot antenna with band-stop operation by using H-shaped parasitic structures for UWB applications," *Appl. Comp. Electro. Society (ACES) Journal*, vol. 28, no. 12, pp. 1259-1264, Dec. 2013.

[15] M. Ojaroudi, N. Ojaroudi, and N. Ghadimi, "A novel design of dual band-notched slot antenna using a pair of ɾ-shaped protruded strips for UWB Applications," *Appl. Comp. Electro. Society (ACES) Journal*, vol. 28, no. 4, pp. 327-332, Apr. 2013.

[16] H. Liu and Z. Q. Xu. "Design of UWB monopole antenna with dual notched bands using one modified electromagnetic-bandgap structure," *Scientific World Journal*, vol. 2013, pp. 96-105, Sep. 2013.

[17] P. Kumar and Z. C. Alex, "Realization of band-notch UWB nonopole antenna using AMC structure," *International Journal of Engineering & Technology*, vol. 5, no. 3, pp. 3020-3028, Jun. 2013.

[18] A. Pirhadi, H. Bahrami, and A. Mallahzadeh, "Electromagnetic band gap (EBG) superstrate resonator antenna design for monopulse radiation pattern," *Appl. Comp. Electro. Society (ACES) Journal*, vol. 27, no. 11, pp. 908-917, Nov. 2012.

[19] L. Peng, C. L. Ruan, and J. Xiong, "Compact EBG for multi-band applications," *IEEE Trans. Antennas Propag*., vol. 60, no. 9, pp. 4440-4444, Sep. 2012.

Zheng Han received the B.S. degree in Communication Engineering from Tianjin University of Technology in 2006, and the M.S. degree in Signal and Information Processing from Civil Aviation University of China in 2009. Her research interests include analysis and design of microstrip antenna, ultra-wideband antenna, and electromagnetic compatibility of airborne equipment.

Zhenyang Ma received the B.S. degree in Applied Physics from Shandong Normal University, Jinan, China, in 2008, and the Ph.D. degree in Microelectronics and Solid State Electronics from XiDian University, Xi'an, China, in 2013. His research interests include VLSI technology and reliability, the damage effect and mechanism of micro-devices and circuits induced by high-power microwaves and lightning/HIRF protection technology.

Qiannan Xue received the B.S. degree in Physical Electronics from Institute of Electronics, Chinese Academy of Sciences, China, in 2012. Her research interests include micro sensor and system, microwave sensor, system on a chip, and wireless sensor network.

Modification of Vivaldi Antenna for 2-18 GHz UWB Application with Substrate Integration Waveguide Structure and Comb Slots

Ferdows B. Zarrabi [1], Navid P. Gandji [2], Rahele Ahmadian [3], Hamed Kuhestani [3], and Zahra Mansouri [3]

[1] School of Electrical and Computer Engineering
Tarbiat Modares University, Tehran, Iran
ferdows.zarrabi@modares.ac.ir

[2] Electrical and Computer Engineering Department
Michigan Technological University, MI, USA
npourram@mtu.edu

[3] Faculty of Eng., Science and Research Branch
Islamic Azad University, Tehran-Iran
zm.mansouri@gmail.com, h.kuhestani@srbiau.ac.ir, raheleahmadian@gmail.com

Abstract ─ In this paper have been developed two new Vivaldi antenna for UWB application at 2-18 GHz with SIW structure for linear phase center labeled as antenna I and antenna II. The proposed antennas have high gain and directional patterns with symmetric radiation pattern in phi=0 and phi=90 planes. The SIW structure is combined with Vivaldi antenna in order to improve the gain, pattern and phase center linearity. Similarly, for gain improvement at lower frequencies for SIW antenna and with less divergence in the gain, slots with comb models are proposed. The prototype antenna is printed and fabricated on Roger 4003 with εr = 3.45 and thickness of 1.5 mm. The antenna's total dimension is 120 mm × 160 mm. The simulation and experimental VSWR and the gain of antenna I and II is less than 2.5 and 6 dBi - 15 dBi, and 2.4 for 2.17-18 GHz and 8.2 dBi - 15.5 dBi in the entire frequency range of 2-18 GHz respectively. Likewise, the Vivaldi antenna phase center is investigated and finally the linear characteristic of the antenna phase center is presented with linear variation.

Index Terms ─ Substrate integration waveguide, UWB, Vivaldi antenna.

I. INTRODUCTION

Nowadays, broadband systems are designed for faster communication and more data transfer, so it is required to design ultra-wideband (UWB) and multiband antennas in order to support all protocols of wireless applications [1-2]. UWB radio is a transmission technology that is based on short pulses, and this technology usually covered more than several GHz. UWB systems because of their wide bandwidth and economics advantages have been used in communication systems, radio communication, and medical imaging such as breast cancer radar [3-4]. All the above-mentioned applications require small sized, easily feed and low cost antennas. Microstrip compact antennas can be used in mobile communication, WLAN, radar and microwave imaging systems [5-6]. Microstrip circular, elliptical, and spiral models of patch antenna are being used for designing UWB structures for omni directional applications. CPW circular patches and small ground are two methods, which are used for increasing the antenna impedance bandwidth [7-8]. However, the circular and elliptical CPW (coplanar waveguide) patch has a semi omni-directional pattern and cavity back spiral antenna have limited gain. Therefore, it is proposed to design new UWB antenna with high gain and directive pattern. For this reason, some types of quasi Yagi and Log periodic antennas with high gain and directivity have been introduced up to now. On the other hand, Vivaldi antennas are much more noticed than other types of directional antennas because of its advantages such as improved inner band characteristic, large bandwidth, good directional radiation pattern in the entire frequency band, favorable symmetrical end-fire radiation characteristic and high gain in the central frequency band [9-11]. Too many models of Vivaldi antennas are being considered in many researches and they divided this antenna into different groups such as antipodal and tapered slot Vivaldi. All types of Vivaldi

Submitted On: July 30, 2014
Accepted On: May 26, 2015

antenna have sufficient gain and bandwidth for radar application and they also use for breast cancer thermotherapy and microwave imaging [12-18]. Phase center is the point which the electromagnetic radiation spreads spherically outward, which the phase of the signal being equal at any point on the sphere. In the proposed antenna, the phase center Vivaldi antenna is investigated and linear characteristic of the antenna phase center is presented. The phase center location of antennas is important for pulse transmission/reception, as the movement of the phase center will distort the signal. The most conventional method for finding phase center is measuring the phase pattern of the antenna under test (AUT) [16]. The position of the antenna phase centre is not necessarily the geometric centre of the antenna. The phase centre is defined as the apparent source of radiation. If the source is ideal it would have a spherical equiphase contour, but the real case is slightly different, because the equiphase contour is irregular and each segment has its own apparent radiation origin. Phase center distance from antenna shows the radius of curvature in the equal-phased polar plot and it uses to calculate the phase center [17].

In this paper, a combination of Vivaldi antenna with SIW structure is presented. The Vivaldi antenna is known as antenna with UWB characteristic and directional pattern. In this article by using SIW structure we are able to control the field distribution on the surface of the antenna in order to achieve higher gain with symmetric radiation pattern. Antenna I has high gain and directional pattern with symmetric radiation pattern in phi=0 and phi=90 planes.

II. ANTENNA DESIGN

Figure 1 shows the two prototypes, Vivaldi antenna and fabricated antenna. It was designed and fabricated on Roger 4003 with relative permittivity of 3.45 and loss tangent of 0.0027. Thickness of the substrate is 1.5 mm. The antenna is connected to 50 Ω tapered feed line. L and W are the antenna dimensions and they are 160 mm and 120 mm respectively. The antenna contains two slant rows of via with diameter of 0.6 mm. These vias have connected both sides of antenna together. Table 1 shows the antenna dimensions for both antennas.

Usually a Vivaldi antenna was introduced by exponential equations and exponentially tapered slot antenna was called Vivaldi antenna [18]. Therefore, it can be defined by equation (1). The maximum and minimum opening widths are calculated based on equations (3) and (4) respectively [19]:

$$y = c_1 e^{Rz} + c_2, \tag{1}$$

$$\lambda_g = \frac{c}{f_{\min}\sqrt{\varepsilon_r}}, \tag{2}$$

$$H_{\max} = \frac{\lambda_g}{2}, \tag{3}$$

$$H_{\min} = \frac{C}{f\sqrt{\varepsilon_r}}. \tag{4}$$

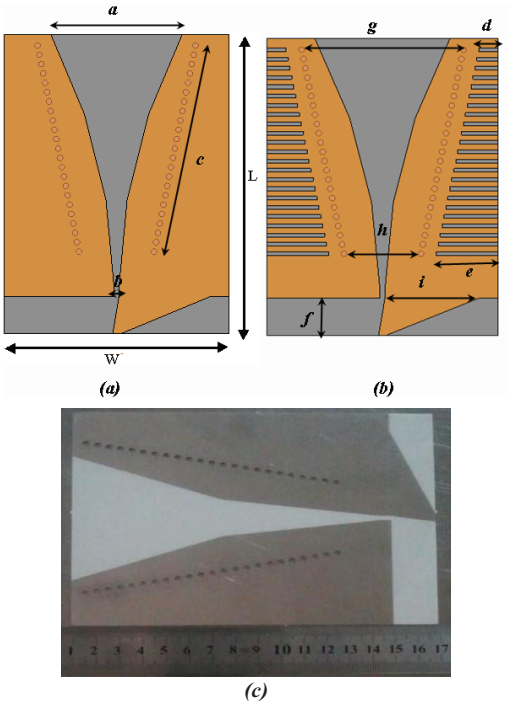

Fig. 1. The prototype Vivaldi antenna: (a) simple model of Vivaldi antenna with SIW, (b) Vivaldi antenna with comb slots, and (c) fabricate antenna.

Table 1: Geometrical parameters of proposed antenna

Parameter	mm
a	70
b	2.6
c	110
d	10
e	32
f	20
g	84
h	40
i	48.7
L	160
W	120

III. SIMULATION RESULT

As previously mentioned, two different full wave methods, FEM and TDM are employed for simulation of the prototype antenna. VSWR comparison between HFSS and CST with experimental results of antenna I and II is presented in Fig. 2 (a). As it can be seen in Fig. 2 (b), the VSWR is less than 2.4 but it is mostly less

than 2 for the entire frequency range of 2-18 GHz. Figure 2(a) shows the VSWR of the Vivaldi antenna with comb slots. The VSWR of antenna II is typically under 2.5 for the entire frequency of 2-18 GHz. Figure 2 (c) shows the antenna VSWR simulation for 2-50 GHz, and in Table 2 highlights that in [22] with lower profile frequency range of 6-50 is approachable, so here with size incensement lower is frequency available for prototype antenna without any resistive element. In addition, the feed line effect on the bandwidth of the antenna is studied. As shows in Fig. 2 (d), the feed width in junction to Vivaldi (i) is an effective factor in antenna bandwidth. For difference value of (i), we have compared the antenna VSWR at range of 2-18. For this aim i=40, 50, 60 mm is checked and best result is obtained for 50 mm.

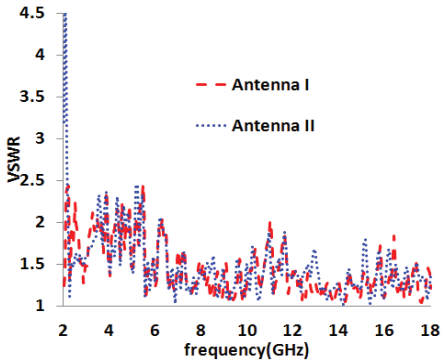

(a)

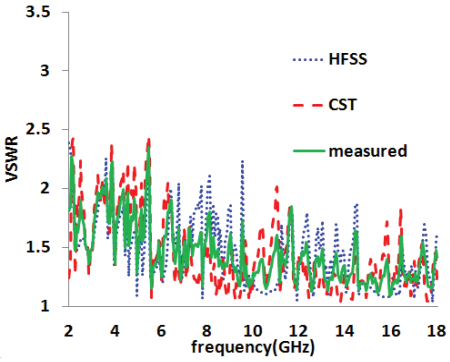

(b)

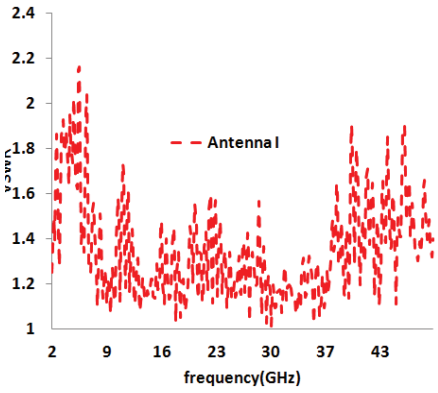

(c)

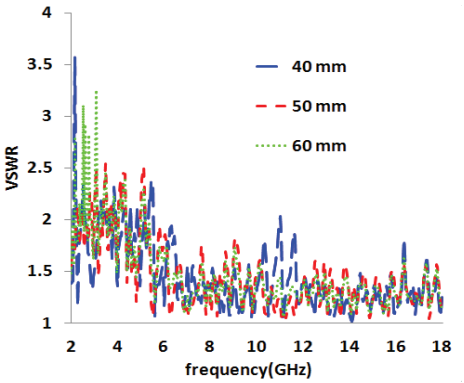

(d)

Fig. 2. The simulated and measured VSWR: (a) simulated VSWR by CST for comb slot Vivaldi antenna, (b) simulated and experimental VSWR for first antenna, (c) antenna VSWR simulation 2-50 GHz, and (d) feed line effect on antenna VSWR.

Table 2: Comparisons between current models with previous research

Parameter	Prototype Model	Ref. (20)	Ref. (21)	Ref. (22)
Bandwidth	2-18 GHz	1-15 GHz	6-18 GHz	6-50 GHz
Gain (dBi)	8-14.9	8-13	6.8-11.6	6.5-16
Efficiency	73-95.6%	---------	93-96%	94-98%
HPBW	40° to 70°	24° to 49°	20° to 80°	24° to 71°
Size (mm)	120×160×1.6	80×140×0.5	50×101×1.5	64×48×0.78

Figure 3 shows the radiation pattern of the prototype of antenna I for four samples in different frequencies at phi=0 and phi=90 for cross- and co-polarization at 2 GHz, 6 GHz, 10 GHz, 14 GHz. As shown in Fig. 3, the antenna patterns for all frequencies are relatively symmetrical. A symmetrical pattern is needed for decreasing the antenna detecting error. Indeed, this symmetrical pattern is very important in identification systems, such as passive radar and microwave imaging for breast cancer detection. In addition, the antenna gain is between 6 dBi and 14.8 dBi and in comparison to other types of the Vivaldi antenna; the prototype antenna has higher gain. As shown in Fig. 3, the half power beam width for 2 GHz occurs around 70° and it reduces to 40° as the frequency increases to 18 GHz.

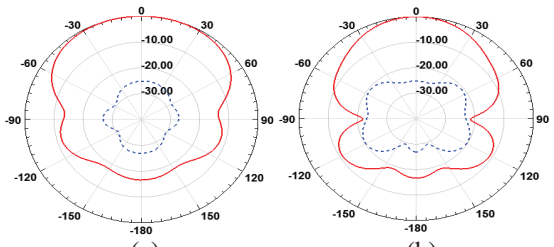
(a) (b)

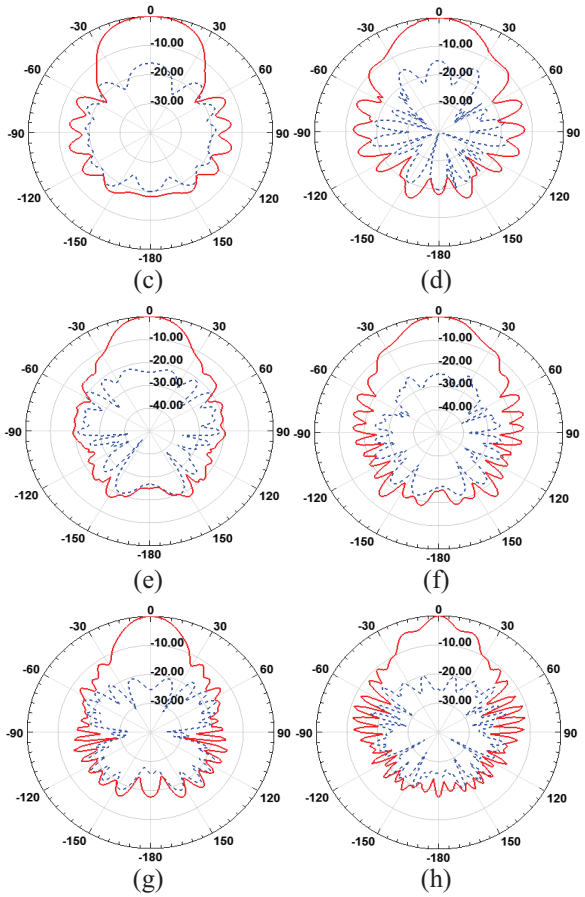

Fig. 3. The prototype antenna pattern for phi=0 and 90: (a) 2 GHz at phi=0, (b) 2 GHz at phi=90, (c) 6 GHz at phi=0, (d) 6 GHz at phi=90, (e) 10 GHz at phi=0, (f) 10 GHz at phi=90, (g) 14 GHz at phi=0, and (h) 14 GHz at phi=90.

Figure 4 shows the gain and the efficiency for both antennas I and II in the entire frequency range of 2-18 GHz. The simulated realized gain of antenna I is 6.06 dBi to 14.9 dBi and it is compared with the experimental result in which a good agreement is achieved. Similarly, the simulated realized gain of antenna II is 7.98 dBi - 14.9 dBi. It can be seen that the comb slot has enhanced the gain of the antenna since antenna II has demonstrated higher gain than antenna I in the lower frequency of the antennas.

Actually, the Vivaldi antenna in combination with SIW technology helps to increase the gain and efficiency of the antenna at 2 GHz but at higher frequency, some reduction of the gain and efficiency can be observed. The antenna's efficiency simulated with CST has been presented in Fig. 4 for both antennas. As shown in Fig. 4, the efficiency is between 80% to 91% at 2 GHz - 18 GHz for antenna I, while antenna II the efficiency is between 73% to 95.6%. The efficiency is reduced suddenly at 5 GHz to 80% and 73% for antenna I and II respectively, due to mismatching as shown in the respective VSWR results for both antennas.

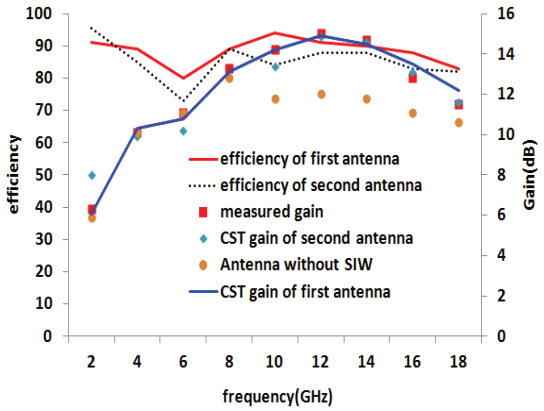

Fig. 4. The prototype antenna gain simulation and experimental for 2-18 GHz and antenna efficiency simulated with CST.

Phase center of antenna has important performance in the time domain. The width of transmitted impulse is about several hundreds of nanoseconds, therefore small change in phase center influences the far field wave dispersion [16]. The phase center for H-plane is calculated in phi-plane. Figure 5 shows the prototype Vivaldi antenna phase center for H-plane. It can be seen that as the frequency increases, the phase center will increase from 9 mm to 109 mm in a linear manner. By comparison of both antennas, it shows the comb slot despite of its effect on gain and efficiency has less effect on antenna phase center.

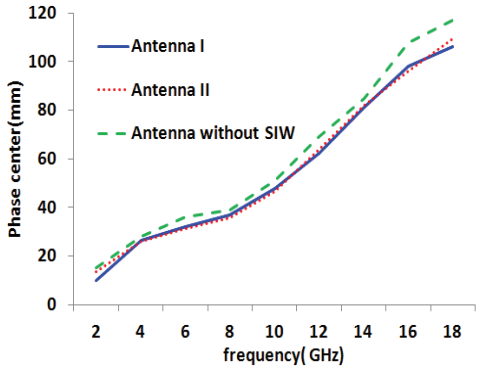

Fig. 5. The prototype Vivaldi antenna phase center for H-plane.

In order to achieve symmetric patterns, it is required to significantly reduce the H-plane beam width, and in here, SIW structure is used for modification of the beam width. Additionally, Vivaldi antennas have an unacceptable phase center variation in the H-plane [16], which may not have significant

effects in pulse transmission, but do cause a noticeable error in the high precision localization applications (as indicated in [16]). However, by implementation of linear phase center, the prediction of localization became possible when localization in directional finding application is based on phase calculation.

IV. CONCLUSION

The VSWR of the antenna is less than 2.3 for 2-18 (up to 50) GHz frequency range, and in this range, the antenna gain is 6 to 15 dBi. The Vivaldi antenna phase center is investigated and the phase center in the prototype bandwidth for H-plane is checked. Finally, the linear characteristic of the antenna phase center is presented. By increase of the frequency, the phase center will increase linearly from 9 mm to 109 mm. Half power beam width for 2 GHz occurs around 70° and will reduce to 40° at 18 GHz. In continue, comb slot is used for gain enhancement. The gain of antenna II is 8.2-15.5 dBi. Antenna I has high gain directional pattern with symmetric radiation pattern in phi=0 and phi=90 planes. The simulation and experimental results are emphasized that the SIW structure combination improved antenna gain and linearity characteristic of phase center.

REFERENCES

[1] F. B. Zarrabi, A. M. Shire, M. Rahimi, and N. P. Gandji, "Ultra-wideband tapered patch antenna with fractal slots for dual notch application," *Microwave Opt. Technol. Letts.*, vol. 56, pp. 1344-1348, 2014.

[2] M. H. B. Ucar and Y. E. Erdemli, "Triple-band microstripline-fed printed wide-slot antenna for WiMAX/WLAN operations," *Applied Computational Electromagnetic Society (ACES) Journal*, vol. 29, no. 10, pp. 793-800, 2014.

[3] M. H. B. Ucar, A. Sondas, and Y. E. Erdemli, "Dual-band loop-loaded printed dipole antenna with a wideband microstrip balun structure," *Applied Computational Electromagnetic Society (ACES) Journal*, vol. 27, no. 6, pp. 458-465, Jun. 2012.

[4] C. Van Niekerk, E. Zastrow, S. C. Hagness, and J. T. Bernhard, "UWB radar target sensing and imaging for granular materials research applications," *IEEE Int. Symp. Antennas Propagat. (APSURSI), 2010 IEEE*, pp. 1-4, 2010.

[5] A. M. Abbosh, "Strain imaging of breast using ultra-wideband pulse," In *Microwave Conference Proceedings (APMC), Asia-Pacific*, pp. 1376-1379, 2010.

[6] X. Liu, X. Xiao, Z. Fan, and J. Yu, " Study on the imaging resolution of ultra-wideband microwave imaging for breast cancer detection," *3rd International Conference on Bioinformatics and Biomedical Engineering,* IEEE, pp. 1-4, 2009.

[7] M. Rahimi, R. A. Sadeghzadeh, F. B. Zarrabi, and Z. Mansouri, "Band-notched UWB monopole antenna design with novel feed for taper rectangular radiating patch," *Prog. Electromagn. Res. C*, vol. 47, pp. 147-155, 2014.

[8] A. M. Abbosh and M. E. Bialkowski, "Design of ultrawideband planar monopole antennas of circular and elliptical shape," *IEEE Trans. Antennas Propag.*, vol. 56, no. 1, pp. 17-23, 2008.

[9] D. S. Woo, Y. G. Kim, K. W. Kim, and Y. K. Cho, "Design of quasi-Yagi antennas using an ultra-wideband balun," *Microwave Opt. Technol. Letts*., vol. 50, no. 8, pp. 2068-2071, 2008.

[10] A. A. Eldek, A. Z. Elsherbeni, and C. E. Smith, "Wideband microstrip-fed printed bow-tie antenna for phased-array systems," *Microwave Opt. Technol. Letts*., vol. 43, no. 2, pp. 123-126, 2004.

[11] J. Ou Yang, S. Bo, J. Zhang, and F. Yang, "A low-profile unidirectional cavity-backed log-periodic slot antenna," *Prog. Electromagn. Res.*, vol. 119, pp. 423-433, 2011.

[12] A. Abu Bakar, D. Ireland, A. M. Abbosh, and Y. Wang, "Experimental assessment of microwave diagnostic tool for ultra-wideband breast cancer detection," *Prog. Electromagn. Res. M*, vol. 23, pp. 109-121, 2012.

[13] B. J. Mohammed, A. M. Abbosh, D. Ireland, and M. E. Bialkowski, "Compact wideband antenna for microwave imaging of brain," *Prog. Electromagn. Res. C*, vol. 27, pp. 27-39, 2012.

[14] S. Nikolaou, G. E. Ponchak, J. Papapolymerou, and M. M. Tentzeris, "Conformal double exponentially tapered slot antenna (DETSA) on LCP for UWB applications," *IEEE Trans. Antennas Propag.*, vol. 54, no. 6, pp. 1663-1669, 2006.

[15] K. Kota and L. Shafai, "Gain and radiation pattern enhancement of balanced antipodal Vivaldi antenna," *Electron. Lett.*, vol. 47, no. 5, pp. 303-304, 2011.

[16] Q. Wu, B.-S. Jin, L. Bian, Y.-M. Wu, and L.-W. Li, "An approach to the determination of the phase center of Vivaldi-based UWB antenna," *IEEE Int. Symp. Antennas Propagat.*, pp. 563-566, 2006.

[17] A. Elsherbini, C. Zhang, S. Lin, M. Kuhn, A. Kamel, A. E. Fathy, and H. Elhennawy, "UWB antipodal vivaldi antennas with protruded dielectric rods for higher gain, symmetric patterns, and minimal phase center variations," *IEEE Int. Symp. Antennas Propagat.*, pp. 1973-1976, 2007.

[18] S. Chamaani, S. Mirtaheri, and M. S.

Abrishamian, "Improvement of time and frequency domain performance of antipodal vivaldi antenna using multi-objective particle swarm optimization," *IEEE Trans. Antennas Propag.*, vol. 59, no. 5, pp. 1738-1742, 2011.

[19] N. Hamzah and K. A. Othman, "Designing Vivaldi antenna with various sizes using CST software," In *Proceedings of the World Congress on Engineering*, vol. 2, pp. 6-8, 2011.

[20] B. Zhou, H. Li, X. Zou, and T.-J. Cui, "Broadband and high-gain planar Vivaldi antennas based on inhomogeneous anisotropic zero-index metamaterials," *Prog. Electromagn. Res.*, vol. 120, pp. 235-247, 2011.

[21] P. Wang, H. Zhang, G. Wen, and Y. Sun, "Design of modified 6-18 GHz balanced antipodal Vivaldi antenna," *Prog. Electromagn. Res. C*, vol. 25, pp. 271-285, 2012.

[22] A. R. H. Alhawari, A. Ismail, M. A. Mahdi, and R. S. A. Raja Abdullah, "Antipodal Vivaldi antenna performance booster exploiting snug-in negative index metamaterial," *Prog. Electromagn. Res. C*, vol. 27, pp. 265-279, 2012.

B. Zarrabi was born in Iran, Babol in 1983. He studied Electrical Engineering at the University of Tabriz in the major of Communication Engineering in 2008 and he is perusing his M.S. at Tarbiat Modares University. His major research interest is designing of antenna for wireless and UWB application for breast cancer detection radar, microwave devices, absorber, metamaterial, plasmonic, nano antenna, cloak, photocell development and THz antenna. He's authored and co-authored more than 33 papers and he published more than 18 ISI and Scopus indexed papers. He is currently work focused on fluid plasmonic and nano chain with statistics optic for bio sensing, based on nano-antenna. He is also invited Reviewer of the Journal of ACES, PIER, Wireless Personal Communication and a few other journals.

Navid P. Gandji was born in 1983 in Iran. He received his M.Sc. Engineering from Iran University of Science and Technology (IUST), Tehran, Iran in 2009. He is currently a Research Assistance in Michigan Technological University, Michigan, USA. His area of research includes cancer detection antennas, MRI related patch antennas, conventional microstrip narrow and UWB antennas, microstrip filters, meta-material structures and antenna external wave effect on transmission lines and electromagnetic compatibility (EMC).

Rahele Ahmadian was born in Tehran, Iran, in 1984. She received the B.Sc. degree in Electrical Engineering from Semnan University, Semnan, Iran, in 2006 and the M.Sc. degree in Electrical Engineering from Imam Khomeini International University, Qazvin, Iran in 2013. Her major interest is designing of metamaterial shield and absorbers.

Hamed Kuhestani was born in Iran, in April 1987. He received the B.S. degree from Islamic Azad University of Mashhad in 2011 and the M.S. degree from Islamic Azad University, Sciences & Research Branch, Tehran, Iran. His current research interests include microwave and millimeter-wave passive circuits, numerical technique in electromagnetic and nano antenna.

Zahra Mansouri was born in Zanjan, Iran in 1987. She received her B.Sc. degree in Electrical Engineering (Telecommunication) from Zanjan University, Zanjan, Iran, in 2008 and M.Sc. degree in Electrical Engineering (Tele-communication) from Islamic Azad University, Science and Research Branch, Tehran, Iran, in 2012 where she is currently working on her Ph.D. Her primary research interests are in microwave components such as couplers and power dividers and metamaterials and UWB antenna.

Low-Profile Asymmetrical-CSRR-Loaded Stacked Microstrip Patch Antenna

Ming-Chun Tang[1], Ting Shi[1], Han Xiong[1], and Shaowei Qing[2]

[1]College of Communication Engineering, Chongqing University, Chongqing 400044, China
tangmingchunuestc@126.com, shiting100220@gmail.com, xiong1226han@126.com

[2]Power Engineering Institute, Chongqing University, Chongqing 400044, China
qshaowei@gmail.com

Abstract **–** By introducing an asymmetrical-CSRR-loaded parasitic patch beneath the radiating patch of a traditional low-profile microstrip antenna, a novel stacked antenna with both 22.46% fractional bandwidth, and stable and uniform radiation patterns in the entire operating frequency range is achieved, even the total height is only approximate $0.04\lambda_L$ (where λ_L indicates the free-space wavelength corresponding to the lower bound of the operating frequency band). The antenna is designed, fabricated and tested. The experimental results agree with the simulations.

Index Terms **–** Low-profile antenna, microstrip patch antenna, wideband.

I. INTRODUCTION

Low-profile microstrip patch antenna is one of the most commonly used antenna types, due to its excellent performance characteristics, including robust design, low cost, easy integration with other microwave devices, and so on. However, one typical low-profile microstrip patch antenna in the basic form of a rectangle- or circular-shaped conducting radiating patch in a grounded substrate is inherently narrowband and is thus not able to meet the requirements of most wireless communication systems nowadays [1-3]. In order to increase the operational bandwidth, a lot of effective approaches arise to the date [4]. As one of the popular technologies, parasitic patches were applied to place on the second layer of patch antennas to design new stacked antennas. This resort could create another resonance in conjunction with the main resonance, which exploring wide overall operational bandwidth. On one hand, by employing a parasitic patch on the second layer with identical configuration and with the electrical size close to the main radiating patch, a wider operational frequency range, which is contributed by two adjacent resonances, i.e., radiating patch resonance and parasitic patch inherent resonance, was accomplished [5]. On the other hand, with the usage of a slotted parasitic patch on the second layer, the distributed LC circuit originating from the slot introduces a second resonance, which could combine the main patch resonance to widen the impedance bandwidth [6]. While effective, these approaches witness a drawback that the addition of one layer could produce only one resonance to do good to bandwidth increase. Logically, one can anticipate that, while maintaining the antenna's low profile, more resonances or wider bandwidth could be explored by only applying more layers based on above stacked antenna design technologies, which would significantly increase the complexity in design and fabrication process. In this letter, by introducing only one asymmetrical-CSRR-slotted parasitic patch on the second layer in a typical low-profile microstrip antenna design, two other adjacent resonances are obtained simultaneously to gain much wider operating frequency range.

II. ANTENNA DESIGN AND CONFIGURATION

The antenna configurations are presented in Fig. 1. The antenna is constructed by two pieces of 0.018-mm-thick copper, 1.6 mm FR4 substrate (ε_r=4.4, μ_r=1.0, loss tangent = 0.02) in sandwich stacking arrangement. And two sheets are connected with two pairs of long hexagonal plastic nuts and screws. In simulation, they are modeled as vias/posts that pass slightly through the substrates of both sheets, which are depicted in Fig. 1 (a). As shown in Figs. 1 (b) and (c), a radiating patch with modified configuration is designed on layer 1, which has one rectangle slot ($L_4\times W_5$) and one rectangle strip ($L_3\times W_3$). The rectangle slot is designed to make more EM energy leaking from the complementary split ring resonator (CSRR) slot resonance, in order to make high overall efficiency from the slot resonance. The rectangle strip on the other side of radiating patch is to provide more tuning freedoms to accommodate the degradation of impedance match characteristics due to the presence of the slotted parasitic patch, instead of only tuning the

Submitted On: December 4, 2014
Accepted On: June 11, 2015

position of feed probe along the *x*-axis. In Fig. 1 (d), a slotted parasitic patch is designed with the length L_7 on layer 2, which is determined a little lower than the radiating patch (L_2+L_3). It could provide a little higher and overlapping resonance frequency band to aid the impedance bandwidth improvement. In order to avoid shorting with the feeding probe (with the radius R_4), a larger hole (with the radius R_3) on the parasitic patch is constructed. Note that, the hole is a little offset from the centre of parasitic patch. The offset could tune the parasitic patch operating in good impedance match performances. Moreover, a CSRR structure with asymmetrical configuration, serving as an additional near-field-resonant-parasitic (NFRP) element [7,8], is placed offset from the centre of parasitic element (L_{10}-L_9).

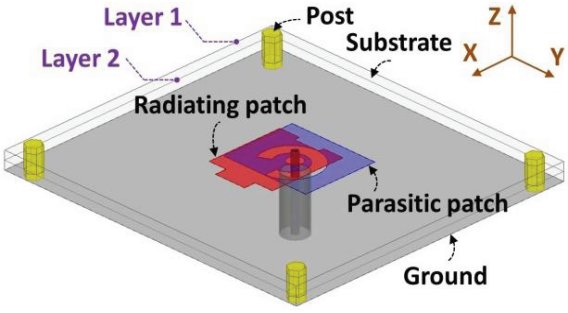

(a)

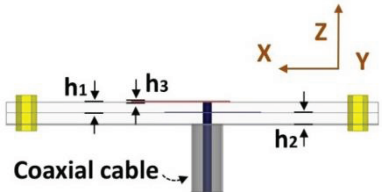

(b)

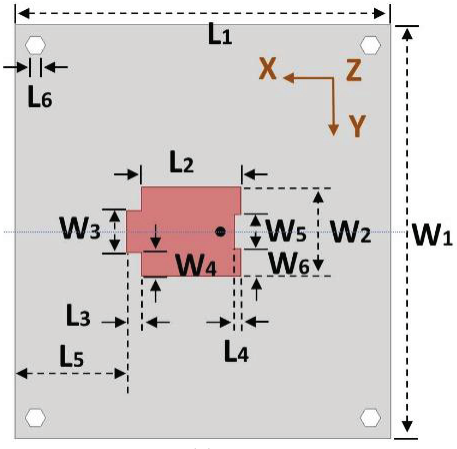

(c)

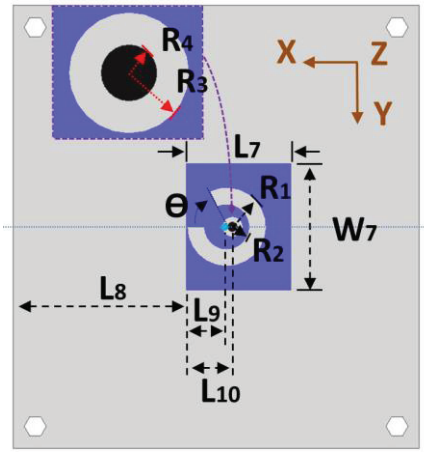

(d)

Fig. 1. Patch antenna: (a) 3D isometric view, (b) side view, (c) top view of layer 1, and (d) top view of layer 2.

It is worth pointing out that, the reason for designing the CSRR with such asymmetrical configuration is that, while maintaining the fundamental resonance frequency (which is corresponding to the total electrical length) of CSRR structure close enough to the two resonances from the patches, the surface current around the slot structure could be well induced to create a considerably wide operating band to be overlapping with the other two operating bands, thus widen the entire operating frequency range. The determined geometry parameters are as follows (in millimeters): h_1=1.6, h_2=1.6, h_3=0.018, L_1=55, L_2=14.55, L_3=2.2, L_4=1, L_5=16.35, L_6=1.5, L_7=14.2, L_8=23.45, L_9=5.475, L_{10}=6.275, W_1=60, W_2=13, W_3=6, W_4=3.5, W_5=5, W_6=4, W_7=17, R_1=5.35, R_2=3, R_3=1.4, and R_4=0.65. And the arc-shaped gap radian of the CSRR is $\theta = 0.36\pi$. We note that, according to our simulation investigation, tuning θ could not only change the resonance frequency centre of CSRR, but also shift the impedance characteristics in the entire operating band.

III. EXPERIMENTAL RESULTS AND DISCUSSION

The NFRP-based patch antenna shown in Fig. 1 was fabricated and its performance characteristics were obtained experimentally. The reflection coefficient of the antenna was measured using an Agilent E8361A PNA Vector Network Analyzer (VNA). The simulated and measured $|S_{11}|$ values together with the fabricated prototype are depicted in Fig. 2. As anticipated from the frequency domain ANSYS/ANSOFT High Frequency

Structure Simulator (HFSS) simulations, the antenna operates from 4.115 GHz to 5.045 GHz (20.31% fractional bandwidth), with three resonance dips located at 4.230 GHz, 4.555 GHz and 4.955 GHz, respectively. The measured results show that, it operates from 4.15 GHz to 5.20 GHz (22.46% fractional bandwidth), with three resonance dips located at 4.25 GHz, 4.655 GHz, and 5.12 GHz, respectively. Accordingly, the antenna total height ($h_1+h_2+2\times h_3$), evaluated at the lower frequency bound f_L=4.15GHz, is $0.044\lambda_L$, where λ_L is the free-space wavelength corresponding to the lower frequency bound ($\lambda_L=c/f_L$). Obviously, the measured results, together with the full-wave simulations, show expected wide impedance bandwidth with three resonance modes, which are mainly from the radiating and parasitic patches' inherent resonances and the sub-wavelength resonance from CSRR slot, respectively. A little lack of agreement between the operating bandwidths of the simulated and measured designs may be due to an air gap between the two substrate layers which is absent in simulations, and some other minor errors in the fabrication, installation, and experimental process [9]. Moreover, acting as the reference antenna, one antenna without parasitic patch is designed and its impedance match is shifted to optimum (by only moving the radiating patch position (L_5) from 15.35 mm to 18.35 mm along *x*-axis). The refection coefficient is also presented in Fig. 2 for comparison. Clearly, it could operate in the centre of 4.14 GHz with $|S_{11}|_{min}$ < -20 dB and bandwidth from 4.05 GHz to 4.24 GHz (only 4.58% fractional bandwidth), as was expected [4]. Therefore, it could be readily concluded from the comparison that, the addition of the parasitic patch provides a little higher (only 2.5% blue shift of the lower frequency bound) but much wider impedance bandwidth (approximately 5 times fractional bandwidth achievement).

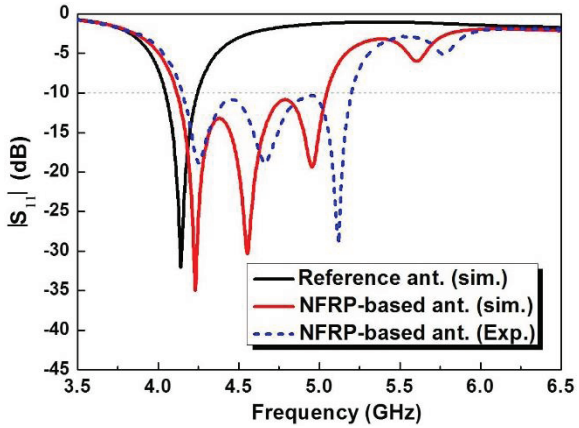

(a)

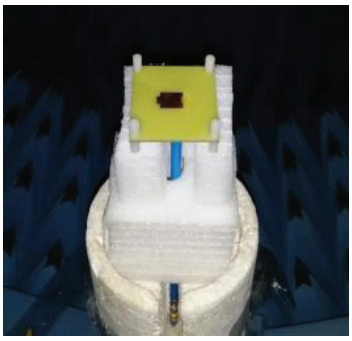

(b)

Fig. 2. Simulated and measured input impedance characteristics of two low-profile patch antennas: (a) reflection coefficients ($|S_{11}|$ values in dB), and (b) the fabricated phototype in the chamber.

The far-field realized gain patterns were measured in an anechoic chamber. The chamber is based mainly on the Agilent EB362C PNA VNA and the SATIMO passive measurement system. The corresponding simulated and measured *E*- and *H*-plane total realized gain patterns at three selected frequency points within the operational bandwidth are shown in Fig. 3. In details, the measured (simulated) peak realized gains are 4.96 dB (5.0045 dB), 5.55 dB (4.9520 dB), and 2.61 dB (3.0523 dB) at 4.25 GHz (4.23 GHz), 4.66 GHz (4.555 GHz), and 5.12 GHz (4.955 GHz), respectively. It is clear in Fig. 3 that, almost uniform radiation patterns and around 3 dB peak realized total gain variations in both the simulation and experimental results indicate its relatively stable radiation performance characteristics. In addition, as is observed in Fig. 3 (c), only a little asymmetry of main radiation beam appears in the higher frequency range. This phenomenon is ascribed to the asymmetrical CSRR structure.

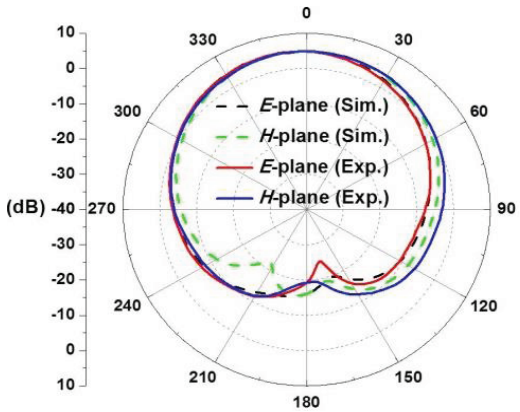

(a)

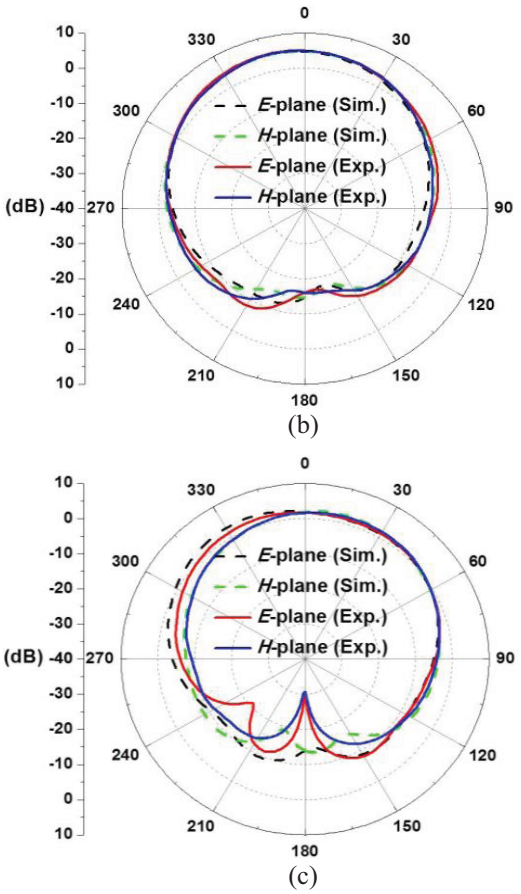

Fig. 3. Simulated and measured total realized gain patterns in the *E*- and *H*-planes at three frequency points: (a) 4.230 GHz in simulation and 4.25 GHz in measurement, (b) 4.555 GHz in simulation and 4.66 GHz in measurement, and (c) 4.955 GHz in simulation and 5.12 GHz in measurement.

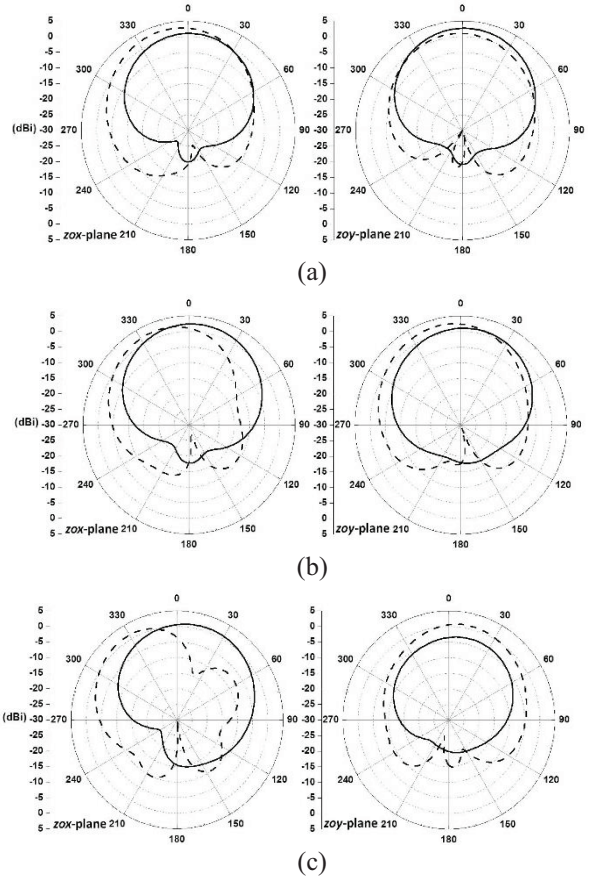

Fig. 4. Simulated realized gain patterns in the *E*- and *H*-planes at three frequency points: (a) at 4.230 GHz, (b) at 4.555 GHz, and (c) at 4.955 GHz. Here, *E*-phi and *E*-theta are indicated in solid and dashed lines, respectively.

To further study its radiation characteristics in the entire frequency band, more simulated results are presented in Figs. 4-5. Figure 4 gives its corresponding realized gain patterns in *zox* (*E*)-plane and *zoy* (*H*)-plane at the three resonance frequency centers. According to the radiation patterns, it is obvious that the cross-polarization is significantly higher than the traditional patch antenna. This characteristic could make the proposed antenna be advantageous for some special applications, such as the indoor wireless communication since it would lead to better transmission capability in rich multipath environment [10-11]. On the other hand, as is shown in Fig. 5, in such a wide operational frequency range, the peak realized gain value fluctuates in the range from 2.56 dBi to 5.25 dBi (2.69 dB variation), and the radiation efficiency is varied from 45.1% to 67.9% (22.8% fluctuation).

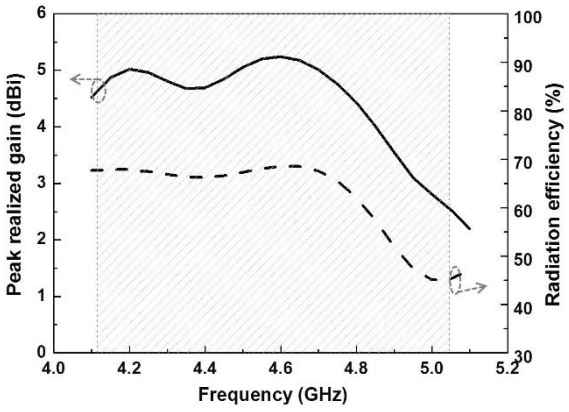

Fig. 5. Simulated peak realized gain and radiation efficiency values as a function of frequency.

IV. CONCLUSION

A NFRP-based, low-profile, wideband stacked

microstrip patch antenna is introduced in this letter. By introducing an asymmetrical-CSRR-loaded parasitic patch on the second layer beneath the radiating patch of a traditional microstrip antenna, a much wider bandwidth (approximate 5 time achievement), and relatively stable and uniform radiation patterns in the entire operating frequency range, are both obtained. Measured performance agrees well with simulation. The performance is very advantageous for wideband and low-cost stacked microstrip patch antenna designs on future mobile terminals.

ACKNOWLEDGMENT

This work was supported in part by the National Natural Science Foundation of China contract number 61471072, and in part by the Fundamental Research Funds for the Central Universities contract numbers 106112015CDJZR165510 and 106112015CDJXY160007.

REFERENCES

[1] M.-C. Tang, S. Xiao, D. Wang, C. Wei, and B. Wang, "A compact planar negative permittivity ZOR antenna," *J. of Electromagn. Waves and Appl.*, vol. 25, pp. 1122-1130, 2011.

[2] J. Xiong, X. Lin, Y. Yu, M.-C. Tang, S. Xiao, and B. Wang, "Novel flexible dual-frequency broadside radiating rectangular patch antennas based on complementary planar ENZ or MNZ metamaterials," *IEEE Trans. Antennas Propag.*, vol. 60, no. 8, pp. 3958-3961, Aug. 2012.

[3] M.-C. Tang, S. Xiao, T. Deng, H. Zhu, and B.-Z. Wang, "Design of compact, low-profile, wideband, dual-frequency patch antennas based on complementary co-directional SRRs," *IEEE Antennas Propag. Mag.*, vol. 56, no. 6, pp. 72-89, Dec. 2014.

[4] K.-F. Lee and K.-F. Tong, "Microstrip patch antennas - basic characteristics and some recent advances," *Proc. IEEE*, vol. 100, pp. 2169-2180, 2012.

[5] L. Barlatey, J. R. Mosig, and T. Sphieopoulos, "Analysis of stacked microstrip patches with a mixed potential integral equation," *IEEE Trans. Antennas Propag.*, vol. 38, pp. 608-615, 1990.

[6] Y. Chen, S. Yang, and Z. Nie, "Bandwidth enhancement method for low profile E-shaped microstrip patch antennas," *IEEE Trans. Antennas Propag.*, vol. 58, pp. 2442-2447, 2010.

[7] M.-C. Tang and R. W. Ziolkowski, "Efficient, high directivity, large front-to-back-ratio, electrically small, near-field-resonant-parasitic antenna," *IEEE Access*, vol. 1, pp. 16-28, 2013.

[8] M.-C. Tang, R. W. Ziolkowski, S. Xiao, and M. Li, "A high-directivity, wideband, efficient, electrically small antenna system," *IEEE Trans. Antennas Propag.*, vol. 62, pp. 6541-6547, 2014.

[9] A. Buerkle, K. Sarabandi, and H. Mosallaei, "Compact slot and dielectric resonator antenna with dual-resonance, broadband characteristics," *IEEE Trans. Antennas Propag.*, vol. 53, pp. 1020-1027, 2005.

[10] K.-L Wong, *Compact and Broadband Microstrip Antennas*, New York: Wiley, ch. 3, 2002.

[11] J.-Y. Pang, S.-Q. Xiao, S.-T. Chen, and B.-Z. Wang, "Compact and wideband PIFA for DCS/PCS/UMTS/WLAN communication system," *Microw. Opt. Technol. Lett.*, vol. 52, pp. 1097-1100, May 2010.

Band-Notched Compact Rectangular Ring Antenna Using Triple Ω-Shaped Structures for UWB Systems

M. Akbari [1], S. Zarbakhsh [1], N. Rojhani [2], K. Zendeh bi zadeh [3], and R. Ghazian [3]

[1] Young Researchers and Elite Club
Central Tehran Branch, Islamic Azad University, Tehran, Iran
akbari.telecom@gmail.com

[2] Young Researchers and Elite Club
South Tehran Branch, Islamic Azad University, Tehran, Iran

[3] Young Researchers and Elite Club
Share Rey Branch, Islamic Azad University, Tehran, Iran

Abstract ─ In this letter, a new ultra wideband monopole antenna with frequency band-stop function is designed and manufactured. The antenna contains a rectangular ring radiating patch and a partial ground. In the structure, by etching a Ω-shaped slot on the ground plane, extra resonance is excited and therefore more extended impedance bandwidth can be achieved. In order to create band-rejected function, a Ω-shaped sleeve into the rectangular ring patch and an inverted Ω-shaped slot on it and feed-line are used. The measured results depict that the antenna is able to cover the bandwidth from 2.6 to 10.4 GHz for VSWR ≤ 2 excluding the rejected bands from 3.1 to 3.8 GHz and from 5.0 to 6.0 GHz. Acceptable VSWR and radiation pattern characteristics are earned on the frequency band of interest.

Index Terms ─ Notch band, stop band, UWB antenna.

I. INTRODUCTION

Ultra-wideband (UWB) technologies have attracted noticeable attention since the FCC allocated the frequency band of 3.1 GHz to 10.6 GHz for commercial use in 2002. Different sorts of antennas have been investigated for UWB systems, and among which printed monopole antennas have been widely regarded as an excellent candidate, since they are very compact in size and can be easily integrated with RF circuits and devices [1-2]. However, over the released UWB operation bandwidth, there are some narrow bands occupied by the existing wireless systems. Most notable among them are the Wireless Local Area Network (WLAN) and Worldwide Interoperability for Microwave Access (WiMAX), which operate with the center frequencies of 5.2 GHz (5150-5350 MHz), 5.8 GHz (5725-5825 MHz) for WLAN and 3.5 GHz (3400-3690 MHz), 5.5 GHz (5250-5850 MHz) bands for WiMAX. Therefore, the potential electromagnetic interference (EMI) problems should be paid much attention. Recently, numerous band-notched UWB antennas have been investigated and reported, which can reject the certain band within the ultra-wide passband without mounting additional bandstop filters [3-9]. Although, the set of these antennas are designed to generate only one notched frequency band so that just one narrow band of disturbance can be eliminated. Consequently, these antennas are still open to other potential disturbance from neighboring RF systems. In this paper, a monopole antenna with band-notched characteristics for UWB applications is proposed. By utilizing a series of new techniques on radiating patch and ground plane, wide band and band-notched UWB characteristics can be resulted. The practical prototype was implemented and tested, and the measured results show a suitable agreement with the simulated ones. Details of the antenna design and parameter study are presented and discussed as follows.

II. ANTENNA DESIGN

The geometry of the antenna is shown in Fig. 1. The antenna is fabricated on a 22×15 mm^2 FR4 substrate with thickness of 1 mm and relative permittivity εr = 4.4. The antenna contains a rectangular ring radiating patch and a partial ground. As shown in Fig. 1, to obtain desirable impedance bandwidth, a Ω-shaped slot is etched from partial ground plane symmetrically and in order to achieve the lower notched band at centre frequency of 3.5 GHz, a Ω-shaped sleeve is placed into rectangular ring radiating patch. On the other hand, to earn the upper stop band at center frequency of 5.5 GHz, an inverted Ω-shaped slot is etched on both patch and feed-line. The radiating patch is connected to a 50-ohm microstrip line with width and length 1.9 mm and 7.5 mm, respectively.

Submitted On: October 31, 2013
Accepted On: June 24, 2015

The whole antenna is optimized by the electromagnetic simulation software of Ansoft High Frequency Simulation Structure (HFSS) based on the finite element method (FEM) [10], and values of some optimized parameters are shown in Fig. 1. The next section is related to the antenna design process and the effect of various parameters on VSWR.

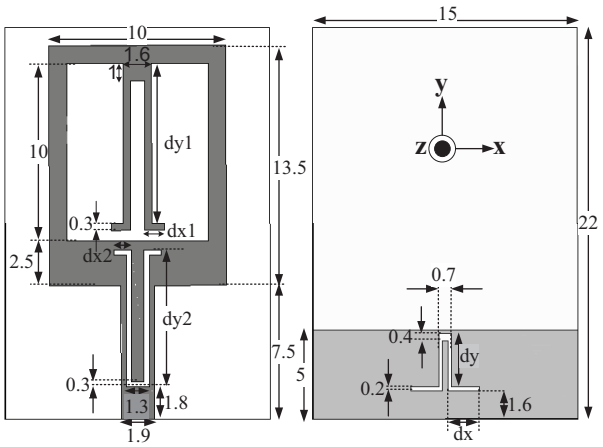

Fig. 1. Geometry of the proposed antenna (dx=1.8 mm, dy=3 mm, dx1=1.1 mm, dy1=9 mm, dx2=1 mm, and dy2=7.7 mm).

III. ANTENNA PERFORMANCE AND DISCUSSION

In this section, the rectangular monopole antenna with various design parameters were constructed, and the numerical and experimental results of the input impedance and radiation characteristics are presented and discussed. The parameters of this proposed antenna are studied by varying one parameter at a time and fixing the others. As shown in Fig. 2, the simulated reflection coefficient loss characteristics for three antennas with different ground structures are presented. Regarding to it, Ant. 1 (primary monopole square antenna) has an impedance bandwidth from 3.2 to 9.15 GHz, while Ant. 2 with an inverted T-shaped slot on the ground plane increases the bandwidth from 3.15 to 9.6.

By replacing the Ω-shaped slot instead of the inverted T-shaped slot on the ground plane in Ant. 3, a considerable resonance is created at 10.4 GHz which improves impedance bandwidth from 3.15 to 10.7 GHz. As far as Fig. 3 is concerned, simulated reflection coefficient characteristics of the antenna are depicted for different values dx where dy is constant (dy=3 mm). On the other hand, the effect of varying parameter dy on reflection coefficient characteristics where dx is constant (dx=1.8 mm) has been studied in Fig. 4.

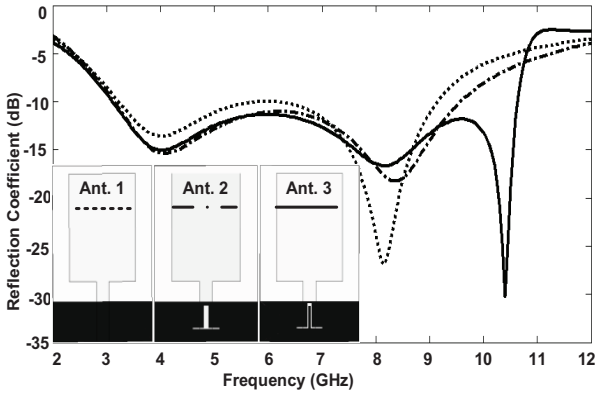

Fig. 2. The comparison of simulated reflection coefficient characteristics of the various antenna structures.

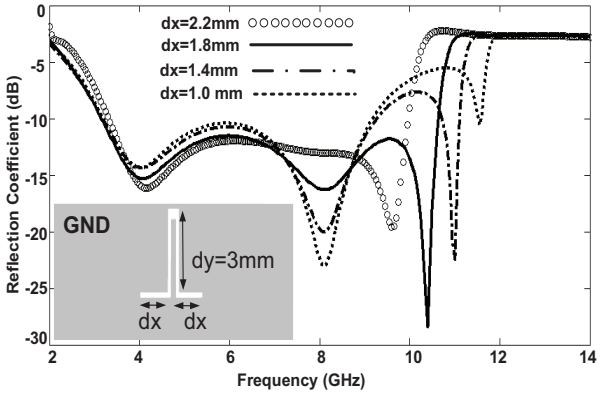

Fig. 3. Simulated reflection coefficient characteristics of the antenna with a Ω-shaped slot on the ground for different values of dx where dy is constant (dy=3 mm).

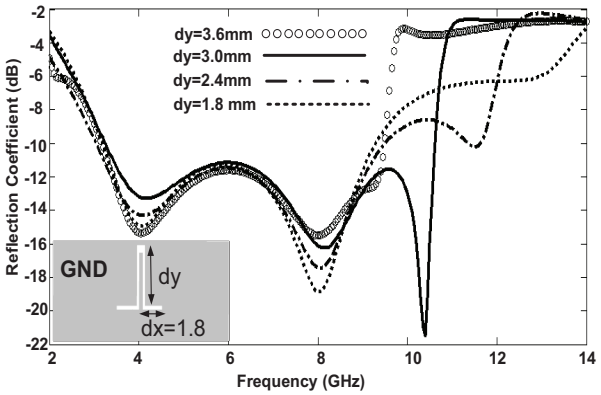

Fig. 4. Simulated reflection coefficient characteristics of the antenna with a Ω-shaped slot on the ground for different values dy where dx is constant (dx=1.8 mm).

From Fig. 3 can be concluded that the upper frequency of the impedance bandwidth is affected by using the Ω-shaped slot on the ground plane, and also by optimizing it, additional third resonant frequency is more excited. Meanwhile, the upper-edge frequency of the impedance bandwidth is decreased from 11.8 to 9.8 GHz with increasing value dx from 1.0 to 2.2 mm. Therefore, the optimized dx is 1.8 mm.

It can be found out that the effect of dy at the upper-edge frequency of the impedance bandwidth is more than dx. With regard to Fig. 4, the best value for dy is 3 mm. As mentioned before, to obtain an UWB antenna with notched band function, two new techniques are employed including the Ω-shaped sleeve into rectangular ring radiating patch and the inverted Ω-shaped slot on both patch and feed-line. The former for the lower notched band at center frequency 3.5 GHz, the latter for the upper notched band at center frequency 5.5 GHz. As illustrated in Fig. 5, the VSWR characteristics for four different antenna structures indicating design procedure are compared to each other. As it is apparent in Fig. 5, Ant. I was optimized and it led to a desirable impedance bandwidth. With comparison Ant. II and III, by adding the Ω-shaped sleeve into rectangular ring radiating patch, firstly the bandwidth is improved and secondly the desirable lower notched band at center frequency of 3.5 GHz is produced. Furthermore, with etching an inverted Ω-shaped slot on both of the patch and feed-line in Ant. IV as compared to Ant. III, another notched band on the upper band at center frequency 5.5 GHz is appeared. There is an interesting point to note that, two notched bands are exactly independent from each other which means that by emerging the second notched band, the first one has not been shifted.

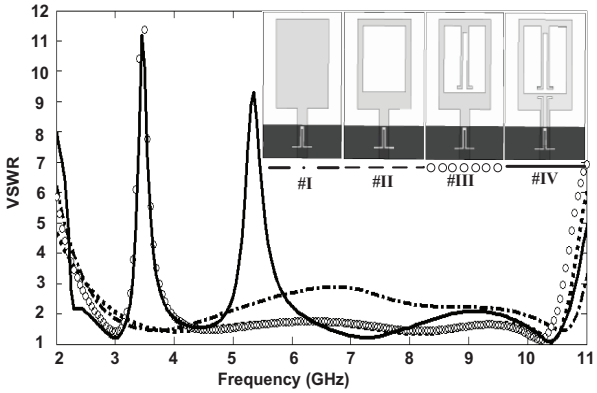

Fig. 5. The comparison of simulated VSWR characteristics of the various antenna structures.

Figure 6 exhibits that simulated VSWR characteristics of the antenna for different values of dx1 has a direct effect on the control of central frequency of the lower notched band. In other words, the center frequency is decreased from 3.8 GHz to 2.8 GHz with increasing dx1 from 0.5 mm to 2.9 mm. Since by shifting the lower notched band, the upper notched band is nearly station, therefore two notched bands are controllable and independent. Regarding to desirable notched band (3.3-3.69), the best value of dx1 is 1.1 mm.

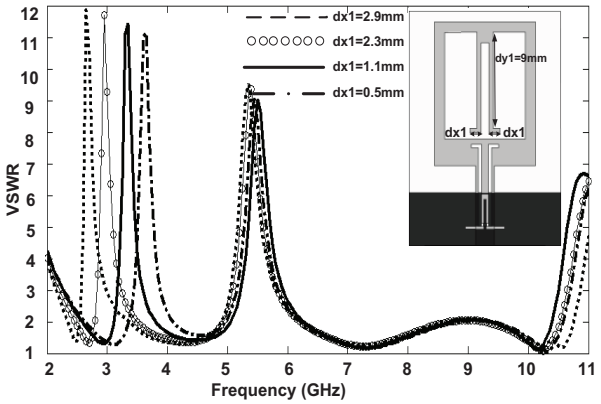

Fig. 6. Simulated VSWR characteristics of the antenna for different values of dx1 where value of dy1 is constant (dy1=9 mm).

As mentioned before, to achieve notched band at center frequency 5.5 GHz, an inverted Ω-shaped slot has been etched on both of the patch and feed-line. Figure 7 depicts the simulated band-rejected feature with varying dy2 where dx2 is constant (dx2=1 mm). As shown in Fig. 7, tuning the length of the slots can achieve a controllable center-rejected frequency range from 5 to 6 GHz for the second notched band. Figure 7 also demonstrates that dy2 is a key factor to control the rejected VSWR value. As length of dy2 of the slots increase from 5.7 to 8.7 mm, the central frequency of the notched band is varied from 7.2 to 4.8 GHz. The acceptable value of dy2 is 7.7 mm.

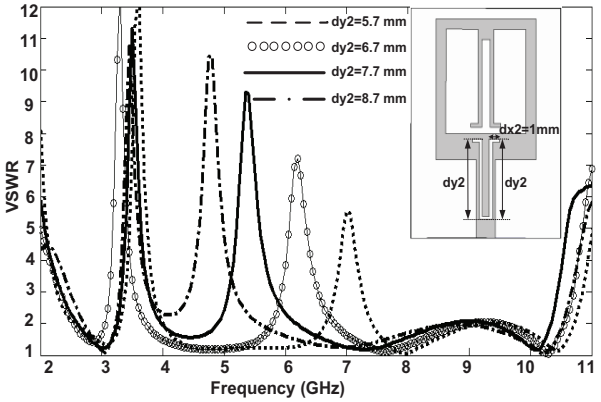

Fig. 7. Simulated VSWR characteristics of the antenna for different values of dy2 where value of dx2 is constant (dx2=1 mm).

To understand the phenomenon behind this dual stop-band function, the simulated current distributions on the radiating patch at both 3.5 GHz and 5.5 GHz are depicted in Fig. 8. It can be found out from Fig. 8 that, at frequency 3.5 GHz the greatest current is concentrated at around of the Ω-shaped sleeve into rectangular ring radiating patch, while at 5.5 GHz it is focused at around the inverted Ω-shaped slot. All of them consequently end up the acceptable VSWR within both notched bands. This is apparent from Fig. 8 that the Ω-shaped sleeve and the inverted Ω-shaped slot are responsible for the first and second notch band, respectively. The proposed antenna has been implemented based on the dimensions presented in Fig. 1. It also was tested in the Antenna Measurement Laboratory at Iran Telecommunication Research Center. The VSWR of the proposed antenna has been measured using an Agilent E8362B network analyzer in its full operational span (10 MHz - 20 GHz). The simulated and measured VSWR of the fabricated antenna are also depicted in Fig. 8. The fabricated antenna are able to cover impedance bandwidth from 2.6 to 10.4 GHz for VSWR ≤ 2 with two notch bands around 3.1 to 3.8 GHz and from 5.0 to 6.0 GHz. As exhibited in Fig. 8, there exists a discrepancy between measured data and the simulated results, and this could be due to the effect of the SMA port. The photo of fabricated antenna is apparent in Fig. 9. To confirm the accurate reflection coefficient characteristics for the designed antenna, it is recommended that the manufacturing and measurement process need to be performed carefully.

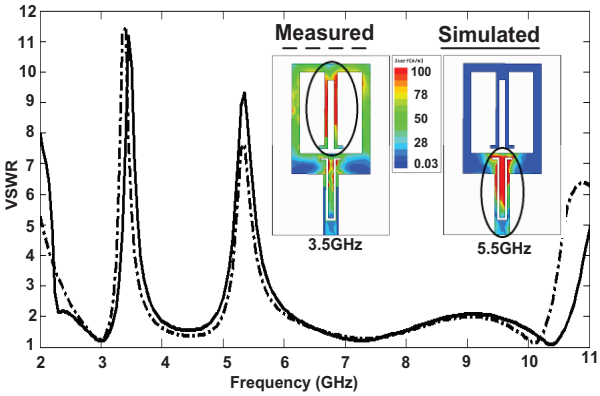

Fig. 8. Measured and simulated VSWR for the antenna and current distribution at both central frequencies of notched bands 3.5 and 5.5 GHz.

Fig. 9. Photograph of the fabricated antenna.

Figure 10 illustrates the measured radiation patterns of the proposed antenna with notched bands at frequencies of 4.5 and 7 GHz in E-plane (yz-plane) and H-plane (xz-plane). It is distinctly revealed from the figure that H-plane patterns are purely omni directional at all frequencies, while the E-plane patterns similarly exhibit the expected monopole-like behaviors. Figure 11 shows the measured maximum gain of the proposed antenna with and without notched band. A sharp decrease of maximum gain in the notched bands at both 3.5 GHz and 5.5 GHz are shown. For other frequencies outside the notched frequency band, the antenna gain with the slot is similar to those without it.

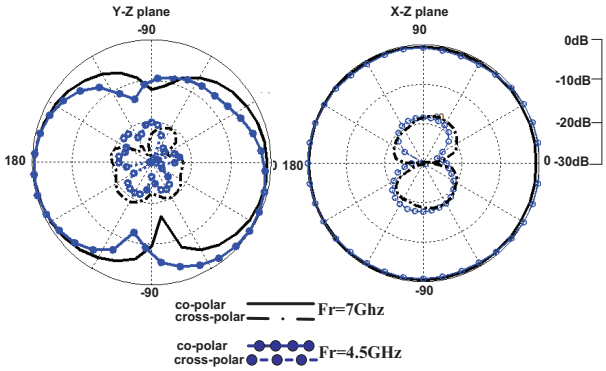

Fig. 10. Measured radiation patterns of the proposed antenna at 4.5 and 7 GHz.

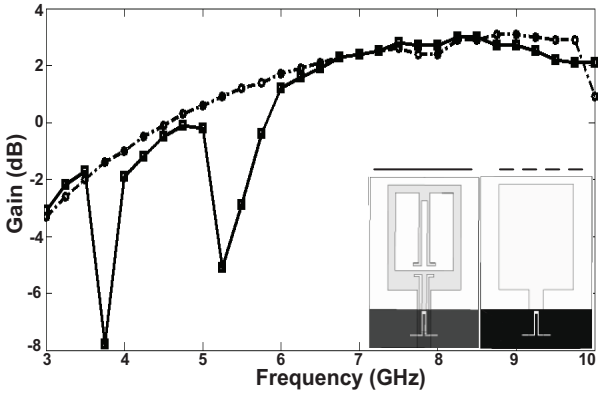

Fig. 11. Maximum gain comparisons for the ordinary square antenna (without notched band), and the proposed antenna (with notched band).

IV. CONCLUSION

A new ultra wideband monopole antenna with frequency band-stop function has been presented. The desired band-rejected property is achieved by embedding a Ω-shaped sleeve into a rectangular ring radiating patch and etching an inverted Ω-shaped slot on it. Experimental and measured results reveal the dual notched bands can be tuned flexibly and independently. The measured results depicted that the antenna is able to cover the bandwidth from 2.6 to 10.4 GHz for VSWR ≤ 2 excluding the rejected bands from 3.1 to 3.8 GHz and 5.0 to 6.0 GHz. Acceptable VSWR and radiation pattern characteristics are earned on the frequency band of interest.

REFERENCES

[1] J. X. Liang, C. C. Chiau, X. D. Chen, and C. G. Parini, "Study of a printed circular disc monopole antenna for UWB systems," *IEEE Trans. on Antennas and Propag*., vol. 53, pp. 3500-3504, 2005.

[2] Z. N. Chen, T. S. P. See, and X. M. Qing, "Small printed ultrawideband antenna with reduced ground plane effect," *IEEE Trans. on Antennas and Propag*., vol. 55, pp. 383-388, 2007.

[3] M. Mighani, M. Akbari, and N. Felegari, "A CPW dual band notched UWB antenna," *Applied Computational Electromagnetics Society (ACES) Journal*, vol. 27, no. 4, pp. 352-359, Apr. 2012.

[4] C. C. Lin, P. Jin, and W. Ziolkowski, "Single, dual and tri-band-notched ultrawideband (UWB) antennas using capacitively loaded loop (CLL) resonators," *IEEE Trans. on Antennas and Propag*., vol. 60, pp. 102-109, 2012.

[5] L. Peng and C. L. Ruan, "UWB band-notched monopole antenna design using electromagnetic-bandgap structures," *IEEE Trans. on Microwave Theory and Tech*., vol. 59, pp. 1074-1081, 2011.

[6] J. R. Kelly, P. S. Hall, and P. Gardner, "Band-notched UWB antenna incorporating a microstrip open-loop resonator," *IEEE Trans. on Antennas and Propag*., vol. 59, pp. 3045-3048, 2011.

[7] K. G. Thomas and M. Sreenivasan, "A simple ultrawideband planar rectangular printed antenna with band dispensation," *IEEE Trans. on Antennas and Propag*., vol. 58, pp. 27-34, 2010.

[8] A. M. Abbosh and M. E. Bialkowski, "Design of UWB planar band-notched antennas using parasitic elements," *IEEE Trans. on Antennas and Propag*., vol. 57, pp. 796-799, 2009.

[9] C. R. Medeiros, J. R. Costa, and C. A. Fernandes, "Compact tapered slot UWB antenna with WLAN band rejection," *IEEE Antennas and Wireless Propagation Letters*, vol. 8, pp. 661-664, 2009.

[10] Ansoft High Frequency Structure Simulation (HFSSTM), ver. 13, Ansoft Corporation, 2010.

Compact Quasi-Yagi Antenna for Handheld UHF RFID Reader

Zhibo Du [1], Zhen Wu [1], Min Wang [1], Jintao Rao [1], and Peng Luo [2]

[1] Department of Network Engineering
Chengdu University of Information Technology, Chengdu, 610225, China
du139123456789@163.com, wzhen@cuit.edu.cn, wmcuit@cuit.edu.cn

[2] State Commercial Cryptography Testing Center
Beijing 100161, P. R. China

Abstract ─ This paper describes a compact printed Quasi-Yagi antenna for ultra high frequency (UHF) radio frequency identification (RFID) reader that can be used in both Europe and US regions. The proposed antenna is a Yagi type structure with a microstrip-to-coplanar stripline transition, a meander dipole, a folded finite-size ground plane and a rectangle ground plane. The proposed antenna has compact size (0.18λ×0.24λ). The proposed antenna has an endfire radiation pattern within operation bandwidth, with peak gain values of more than 3 dBi and return loss is less than -10 dB in approximately 100 MHz band that can cover European and US RFID bands (860 MHz - 960 MHz). We described the antenna structure and presented the comparison of simulation results with experimental data. Good return loss and radiation pattern characteristic are obtained, measured results are presented to validate the usefulness of the proposed antenna structure for RFID reader.

Index Terms ─ Endfire radiation pattern, gain, Quasi-Yagi antenna, RFID reader.

I. INTRODUCTION

In recent years, radio frequency identification (RFID) in the UHF band (860-960 MHz) has become popular in many applications. These applications include supply chain management, automatic retail item management, warehouse management, access control system, electronic toll collection and etc. [1]. Many typical RFID tags have been studied [2-4]. For applications, the RFID handheld reader plays an important role owing to its advantages of compactness, flexibility and maneuverability. The antenna design in a RFID handheld reader should fulfil several unique requirements [5]. One of the important considerations is the size, weight and shape. The broadband antenna designs to cover total frequency span of the UHF band for RFID applications. Several RFID antennas have been reported [6,7]. The size of the broadband antennas are bulky and not suitable for handheld or portable reader applications. Antenna development for RFID applications has focused on the size reduction and wideband performance to cover multiple service at the same time [8]. Also, wideband antennas for RFID system has been reported [9,10]. But these antennas are too large and not suitable for the RFID handheld antenna. The majority of devices have become small and compact. Therefore, the compact antenna is more important and practical. The antenna [11] has endfire pattern and compact dimension for RFID handheld reader, but the antenna can only cover narrow bandwidth.

In this paper, the proposed antenna is compact and still efficient to provide desired performance. The antenna consists of a meander dipole, a microstrip-to-coplanar stripline transition and a folded finite-size ground plane which is optimized for the operation of 860 MHz - 960 MHz. The proposed antenna is compact and can be easily fabricated. The performance of the designed antenna is simulated using the simulation tool HFSS v13. According to the measured results of the proposed antenna, the antenna has well-defined endfire radiation patterns and the gain of the presented antenna is more than 3 dBi around Europe and US RFID bands (860 MHz - 960 MHz).

II. ANTENNA CONFIGURATION AND DESIGN

The configuration of the proposed Quasi-Yagi antenna is shown in Fig. 1. The final antenna parameters are optimized using the commercial electromagnetic (EM) solver HFSS 13.0, and are given in the Table 1. The proposed antenna is designed for UHF RFID applications in North America and Europe. Simple microstrip patch antenna is considered in proposed design due to their numerous advantages such as low profile, low cost easy to manufacture and easy to integrate with other electronics. The length of the driven dipole and reflector elements are optimized for

Submitted On: July 18, 2013
Accepted On: September 6, 2014

simultaneously achieving excellent input impedance matching, and dipole arms are meandered to reduce the occupied dimension. Unlike conventional Quasi-Yagi antennas, here a reflector element is in close proximity to the driven element, and is also meandered in accordance with the outline of the dipole element. Accordingly, in addition to the surface wave excited in the substrate, in the proposed design the strong near-field coupling between the driven dipole and the reflector elements also helps improve the antenna impedance matching over a wide frequency range. Meander elements affect the resonant frequency of the antenna. The antenna elements are bent into meander shape, suitable for the handheld RFID reader. The antenna has a high directional gain which results in the operating range around the RFID bands (860 MHz - 960 MHz). Both top and bottom ground planes, which serve as reflectors in the design, keep the surface wave from propagating towards the backward direction. With such an arrangement, the backward-propagated surface wave can be substantially bounced back and further facilitates the endfire radiation.

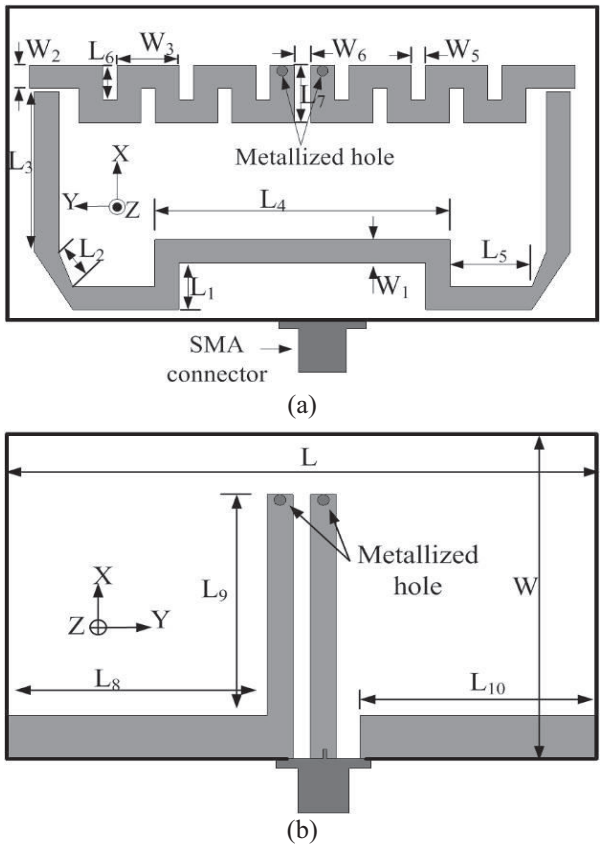

Fig. 1. The construction of the proposed antenna: (a) the top layer, and (b) the bottom layer.

Table 1: The dimensions of the antenna (in mm)

L	L_1	L_2	L_3	L_4
100	9	7.09	30.8	54
L_5	L_6	L_7	L_8	L_9
7	6.6	11	44.1	40.7
L_{10}	W	W_1	W_2	W_3
40	50	4.4	4.4	10.4
W_4	W_5	W_6	W_7	W_8
10.4	1.6	3	8	4.4
W_9	W_{10}	W_{11}	-	-
3	8	4.4	-	-

All these elements are shaped to fit into the available footprint while maintaining their resonant frequencies in the desired band. The lengths and shapes of antenna elements and their mutual spacing are key parameters in the design. The length of every meander part of antenna is less than the wavelength of the central frequency. So the transmission module of antenna is equal to the dipole antenna with inductance. The meander part of the proposed antenna balance the negative imaginary part of the dipole antenna, and the current distribution changed.

According to the transmission theory [14], the input resistance of every meander part is:

$$Z_{in} = jZ_0 \tan\left(KL_m\right), \tag{1}$$

$K = K_O\sqrt{\varepsilon_{re}}$, K_O is the wave numbers in free space. ε_{re} is effective dielectric constant. L_m is the length of the meander part.

The characteristic impedance of the meander part is:

$$Z_O = \frac{\eta}{\pi} cosh^{-1}\left(\frac{\alpha}{\beta}\right), \tag{2}$$

α is the distance among the every meander part. β is the width of the meander part. $\eta = \sqrt{\mu\varepsilon}$ is the characteristic impedance. According to above equations, the distance among meander lines, width of lines, length of the meander lines can change the impedance of antenna. So we can change these parameters to design the proposed antenna. Antenna design is tuned to achieve 50 ohm (RFID reader) impedance without using any external matching circuit that will occupy additional footprint.

For demonstration purpose in the laboratory, the proposed antenna is designed on a 1.6 mm FR4 substrate with a dielectric constant ε=4.4 and loss tangent tanδ=0.02. The overall dimension of the antenna is 50 mm × 100 mm, or equivalently roughly 0.18λ×0.24λ. The finally chosen dimensions of the proposed antenna are in Table 1.

III. SIMULATION AND MEASUREMENT

For ease of practical applications, important parameters of the proposed antenna are studied.

One parameter is changed, while the other parameters are kept as in Table 1. Figure 2 (a) shows that the center frequency is decreasing while the length of the meander dipoles, W_3, varies in a range when it is changed from 9 mm to11 mm. Figure 2 (b) shows that the center frequency is increasing while the width of the meander dipoles, L_6, varies in a range when it is changed from 6 mm to 8 mm.

A prototype is fabricated to verify the proposed antenna design as shown in Fig. 3. All the measured results are carried out in anechoic chamber using the NSI300V-30X30 far-field measurement system and Agilent N5230A series vector network analyzer. All simulated results are obtained using HFSS (High Frequency Structure Simulator) based on the finite-element method (FEM) [12,13]. The antenna simulated and measured S11 are shown in Fig. 4. The measurement is taken by an Agilent network analyzer. As shown in Fig. 4, the agreement between the results is fairly good over the frequency band from 860 MHz to 960 MHz.

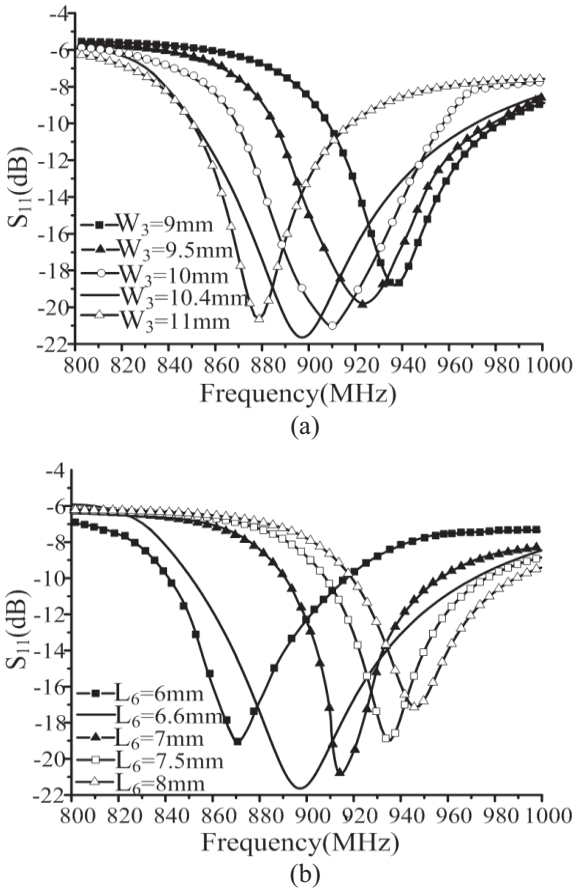

Fig. 2. Effects of varying driver mender dipoles, W_3, L_6.

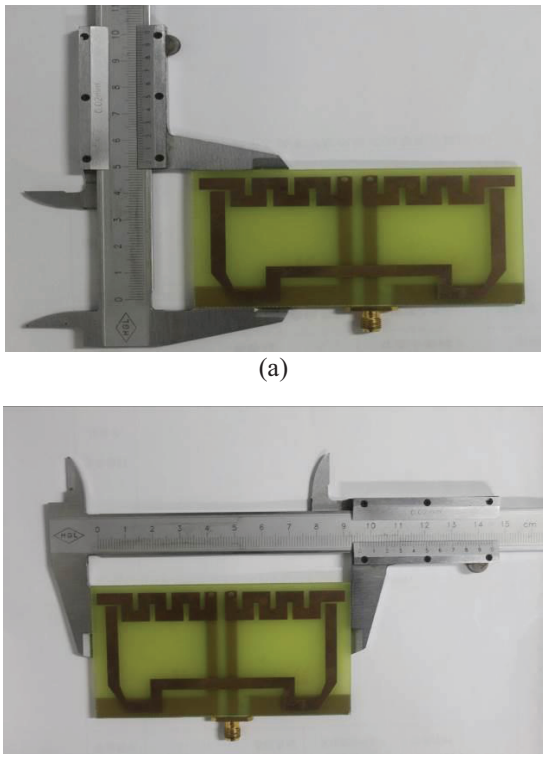

Fig. 3. Fabricated prototype of the proposed antenna: (a) top layer, and (b) bottom layer.

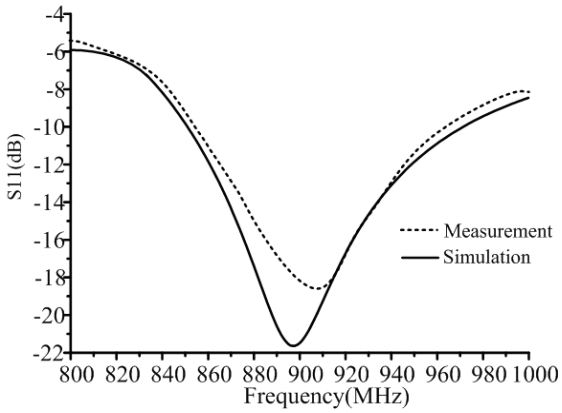

Fig. 4. Simulation and measurement S_{11}.

The simulated and measured center frequencies are given by 896 and 909 MHz, respectively. The slight frequency shift between the results can be mostly attributed to the fabrication tolerance. The measured XY-plane and XZ-plane radiation pattern at 860, 915 MHz are illustrated in Fig. 5, respectively. The radiation patterns are measured in a 7×3×3 m^3 anechoic chamber and the measurement is performed by an Agilent network analyzer along with far-field measurement software.

In the measurement, the connecting cables along the Bakelite support ware carefully shielded by absorbers to reduce the multi-reflection interference. Meanwhile, the simulated -10 dB reflection coefficient bandwidths are from 850 MHz to 970 MHz and the corresponding measurement data are given by 855 MHz - 963 MHz. The experimental results demonstrate that the proposed design completely complies with the stringent requirement of impedance matching imposed on a handheld reader antenna, and the operating bandwidth with reflection coefficient better than -10 dB covers the whole allocated spectrum for UHF RFID applications in North America and Europe.

Figure 5 shows the comparison between the simulated and measured radiation pattern at 860 MHz and 915 MHz in the XY-plane and XZ-plane, respectively, which shows good agreement. It is seen that the proposed antenna has endfire radiation pattern and a symmetrical radiation pattern across the operating bandwidth and its maximum beam is always directed to the +X-axial direction, which have great advantages in practical applications. Radiation pattern can be controlled by placement of radiation elements (director and reflectors).

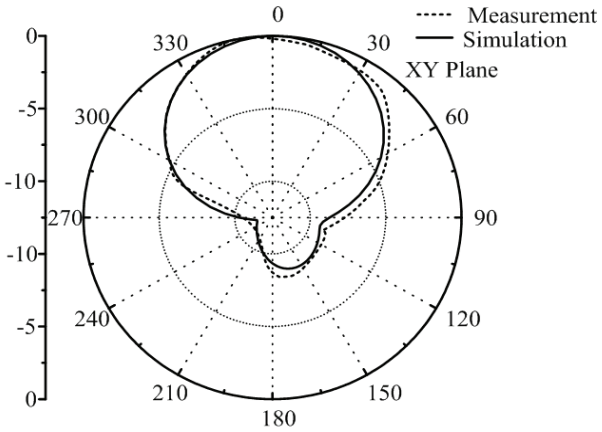

(a)

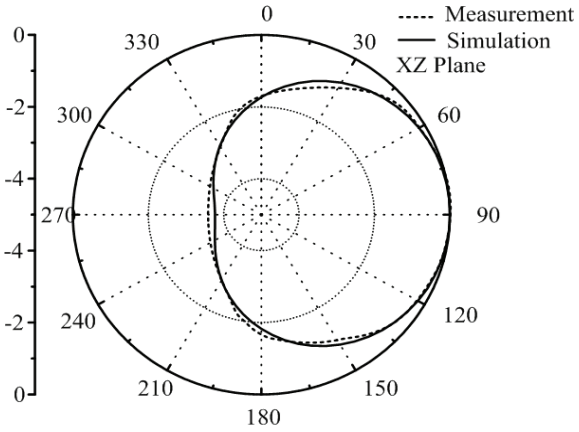

(b)

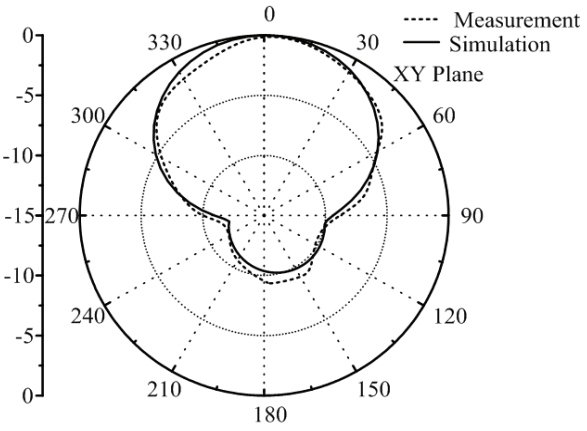

(c)

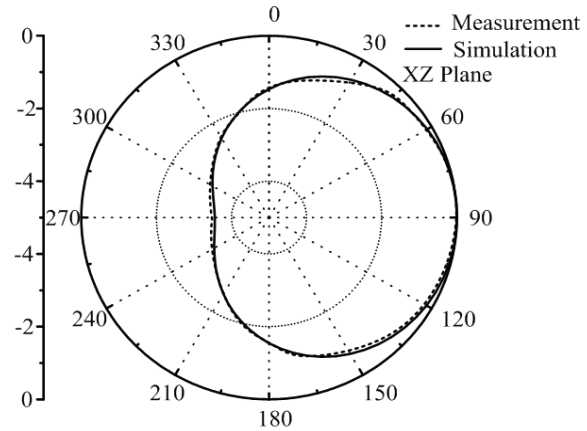

(d)

Fig. 5. Simulated and measured radiation patters of the proposed antenna: (a) XY-plane (860 MHz), (b) XZ-plane (860 MHz), (c) XY-plane (915 MHz), and (d) XZ-plane (915 MHz).

Referring to the Fig. 4, measured result can cover the required frequency band. Figure 5 shows the radiation patterns similar to conventional Yagi radiation characteristics. The gain of proposed endfire antenna reaches 3.6 dBi at 915 MHz and remains better than 3 dBi over the whole UHF RFID band from 860 to 960 MHz. By adding director elements can increase the front-to-back ratio, but these will increase the dimension of the antenna. The gain of the antenna was measured using the gain comparison method [14], where the received power of the antenna under test is compared with known gain of a standard horn antenna. The simulated and measured gain and efficiency are shown in Fig. 6, variation between the simulated and measured gain is within 0.2 dBi, and this may be due to higher dielectric losses of the substrate, additional loss in the surface roughness of the microstrip patch.

The measured bore sight gain is illustrated in Fig. 6. Referring to Fig. 6, the antenna gain rises steadily from

3 dB at 860 MHz to 3.45 dBi at 960 MHz. The efficiency of the proposed antenna rises steadily from 92% to 94%.

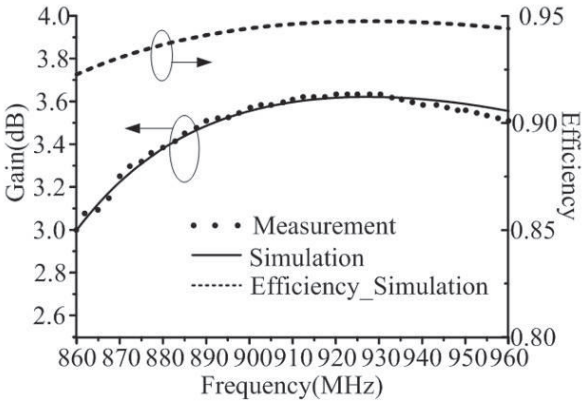

Fig. 6. Simulated and measured gain in the +X direction and efficiency.

IV. CONCLUSION

The compact printed Quasi-Yagi antenna for UHF RFID reader has been presented, constructed and tested. The proposed antenna is based on the conventional printed Quasi-Yagi antenna, where half-wavelength dipole driver element is replaced with two meander dipoles. The input impendence of the folded dipole Quasi-Yagi antenna and its resonance frequency can be tuned by properly adjusting the parameters of the mender dipoles giving freedom for optimization. The proposed antenna is suitable for fabrication on low-cost, low dielectric constant materials such as FR4. The size of the antenna is 0.18λ×0.24λ and suitable for UHF RFID handheld reader. The measured results meet the frequency bandwidth and gain requirements for RFID reader applications. The proposed antenna is easy to fabricate and suitable to be an attractive solution for handheld reader in various production, asset management, supply chain including item-level applications.

ACKNOWLEDGMENT

This work is supported by The 12th Five-Years National Cryptogram Development Fund (No. MMJJ201101022), Sichuan Science and Technology Support Programme (No. 2011GZ0170), Sichuan Provincial Education Department Key Scientific Research Projects (No. 13ZA0091), Project Supported by the Scientific Research Foundation of CUIT (No. CRF201301), and National Science and Technology Major Project (No. 2014ZX01032401).

REFERENCES

[1] K. Finkenzeller, *RFID Handbook*, 2nd ed., New York: Wiley, 2003.

[2] D. D. Arumugam, D. W. Engels, and M. H. Mickle, "The effect of curvature on the performance and readability of passive UHF RFID tags," *Applied Computational Electromagnetics Society (ACES) Journal*, vol. 25, no. 3, pp. 206-217, Mar. 2010.

[3] H. Rajagopalan and Y. Rahmat-Samii, "Platform tolerant and conformal RFID tag antenna: design, construction and measurements," *Applied Computational Electromagnetics Society (ACES) Journal*, vol. 25, no. 6, pp. 406-497, Jun. 2010.

[4] B. D. Braaten, R. P. Scheeler, M. Reich, R. M. Nelson, C. Bauer-Reich, J. Glower, and G. J. Owen, "Compact metamaterial-based UHF RFID antennas: deformed omega and split-ring resonator structures," *Applied Computational Electromagnetics Society (ACES) Journal*, vol. 25, no. 6, pp. 530-542, Jun. 2010.

[5] L. Ukkonen, L. Sydanheimo, and M. Kivikoski, "Read range performance comparison of compact reader antennas for a handheld UHF RFID reader," *IEEE International Conference on RFID*, pp. 63-70, 2007.

[6] Z. N. Chen, X. Qing, and H. L. Chung, "A universal UHF RFID reader antenna," *IEEE Transactions on Microwave Theory and Techniques*, vol. 57, pp. 1275-1282, 2009.

[7] H. L. Chung, X. Qing, and Z. N. Chen, "Broadband circularly polarized stacked probe-fed patch antenna for UHF RFID applications," *Int. J. Antennas Propag*., pp. 1-9, 2007.

[8] J. Kim, C. Yang, T. Yun, and C. Jung, "Multimode multiband (VHF/UHF/L/802.11a/b) antennas for broadcasting and telecommunication services," *IEEE Antennas and Wireless Propagation Letters*, vol. 10, pp. 41-44, 2011.

[9] J. Choi, U. Kim, and T. Kim, "Design of RFID reader antennas for UHF RFID handheld systems," *2011 International Workshop on Antenna Technology (iWAT)*, pp. 33-36, 2011.

[10] Z. N. C. Nasimuddin and X. Qing, "Asymmetric-circular shaped slotted microstrip antennas for circular polarization and RFID applications," *IEEE Trans. Antennas and Propagation*, vol. 28, pp. 3821-3828, 2010.

[11] Y. Sun, G. Wen, P. Wang, Y. Huang, and Z. Du, "A compact printed end-fire antenna for radio frequency identification (RFID) handheld reader," *Applied Computational Electromagnetics Society (ACES) Journal*, vol. 28, no. 1, pp. 72-76, Jan. 2010.

[12] K. ElMahgoub, T. Elsherbeni, F. Yang, A. Z. Elsherbeni, L. Sydänheimo, and L. Ukkonen, "Logo-antenna based RFID tags for advertising application," *Applied Computational Electromagnetics Society (ACES) Journal*, vol. 25, no. 3, pp. 174-181, Mar. 2010.

[13] Ansoft High Frequency Structure Simulator (HFSS) Based on the Finite Element Method, Ansoft.
[14] C. A. Balanis, *Antenna Theory: Analysis and Design*, 2nd ed., John Wiley & Sons, Inc., New York, 1997.

Zhibo Du received the B.E. degree in Computer Science and Technology from the Hebei University of Science and Technology in 2007, and M.E. degree in Computer Application from Chengdu University of Information Technology in 2010. He is working as Lecturer in Chengdu University of Information Technology. His research interests include application of antenna, the internet security of things and side channel attack on the security chip, for example electromagnetic attack, power attack and so on.

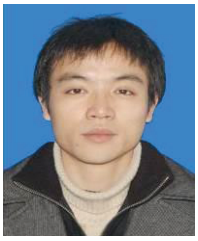

Zhen Wu received the B.E. degree in Computer Communication from the Sichuan University in 2001, and M.E. degree in Software Engineering from the University of Electronic Science and Technology of China in 2006. He is working as Associate Professor in Chengdu University of Information Technology. His research interests include application of antenna, signal processing, the information security and side channel attack on the security equipment.

Min Wang received the M.E. degree in Communication and Information System from the Sichuan University in 2005. She is working as Lecturer in Chengdu University of Information Technology. Her research interests include application of antenna, the attack and defense of network and side channel attack on the security chip.

Jintao Rao received the B.E. degree in Computer Science and Technology from the Huanggang University of Electronic and Information in 2009, and M.E. degree in Computer Application from Chengdu University of Information Technology in 2012. He is working as Assistant in Chengdu University of Information Technology. His specific research interests include cryptography, cryptographic implementations, and physical attacks (side channel and fault analysis).

Peng Luo received the Ph.D. degree in Information Security from the Chinese Academy of Sciences in 2013. He is working as Senior Engineer in State Commercial Cryptography Testing Center. His research interests include network security and IC security.

CPW-Fed Slot Antenna for Major Wireless Communication Systems

Nahid Adlband [1] and Yasser Ojaroudi [2]

[1] Department of Electrical Engineering
Kazerun Branch, Islamic Azad University, Kazerun, Iran

[2] Young Researchers and Elite Club
Germi Branch, Islamic Azad University, Germi, Iran

Abstract ─ In this paper, we present a new co-planar waveguide (CPW)-fed slot antenna for wireless communication systems. The proposed antenna is fabricated on an *FR4* substrate with dielectric constant of 4.4. Configuration of the antenna structure is based on S-shaped structures in both of the radiating stub and ground plane where it operates over a very wide bandwidth and improves the impedance matching. By converting the S-shaped structure at the antenna radiating stub, a new resonance at the lower frequencies is generated, and also by converting the ground plane to the modified S-shaped structure, a good multi-band operation and bandwidth enhancement can be achieved. The measured impedance bandwidth of the proposed antenna for 10 dB return loss is from 1.04 GHz to 1.42 GHz and 1.88 GHz to 2.51 GHz, covering the major wireless communication bands like GPS, MDS/WCS, PCS, WiBro, Bluetooth, HiperLAN, and etc. Simulated and experimental results obtained for this antenna show that the proposed slot antenna has a good isolation and radiation behavior.

Index Terms ─ CPW-fed antenna, wireless communication systems.

I. INTRODUCTION

Recently, microstrip slot antennas have been largely used in a lot of useful applications, because of their inherent characteristics of low cost, low profile, ease of fabrication, light, weight, conformability and integration with RF devices [1-2]. Operation in two or more discrete bands with an arbitrary separation of bands is desired in many applications, such as global positioning system (GPS), wireless communication service (WCS), high performance local area network (HiperLAN), and so on [3-5].

Dual band or multi frequency operations are a main requirement of this type communication. A single antenna is highly desirable if it can operate at these bands. The antenna should be in the planar form, lightweight and compact, so that it can easily be embedded in the cover of communication devices. To reduce the transmission line length and the radiation losses, a simplified feeding circuit is also an important component [6-7].

In this paper, a novel design of a CPW-fed slot antenna for major wireless communication bands is proposed, which have many advantages such as simple structure of a wide bandwidth and easy integration with active devices. The proposed antenna covers frequency bands of 1.04-1.42 GHz and 1.88-2.51 GHz. The resonant frequency of the antenna can be adjusted by changing the sizes of S-shaped structures. Good return loss and radiation pattern characteristics are obtained in the frequency band of interest.

II. MICROSTRIP ANTENNA DESIGN

The antenna is fabricated on an FR4 epoxy substrate with dielectric constant $\varepsilon r=4.4$ and loss tangent $\tan \delta=0.02$ and thickness h=1.6 mm.

As shown in the Fig. 1, an S-shaped radiator is fed by a 50 CPW transmission line which is terminated with a sub miniature A (SMA) connector for measurement purpose. Since both the antenna and the feeding are implemented on the same plane, only one layer of substrate with single-sided metallization is used, and the manufacturing of the antenna is very easy and extremely low cost. Both the radiating patch and the ground plane are beveled, which results in a smooth transition from one resonant mode to another and ensures good impedance match over a broad frequency range.

The presented slot antenna is fed by a CPW. A CPW is a one type of strip transmission line defined as a planar transmission structure for transmitting microwave signals. It comprises of at least one flat conductive strip of small thickness and conductive ground plates.

A CPW structure consists of a median metallic strip of deposited on the surface of a dielectric substrate slab with two narrow slits ground electrodes running adjacent and parallel to the strip on the same surface.

Submitted On: April 25, 2014
Accepted On: December 11, 2014

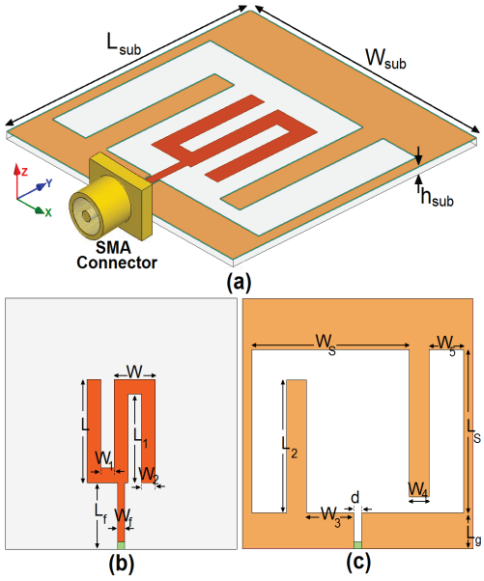

Fig. 1. Geometry of the proposed CPW-fed slot antenna: (a) side view, (b) radiating stub, and (c) ground plane.

As shown in Fig. 1, besides the microstrip line, the CPW is the most frequent use as planar transmission line in RF/microwave integrated circuits. It can be regarded as two coupled slot lines. Therefore, similar properties of a slot line may be expected. The CPW consists of three conductors with the exterior ones used as ground plates. These need not necessarily have same potential. The width of the CPW-feed line is:

$$W_f \le \frac{120h\pi}{z_0\sqrt{\varepsilon_r}}. \quad (1)$$

For good accuracy of CPW:

$$\frac{d}{h} \le 0.5mm. \quad (2)$$

As illustrated in Fig. 1, the conductors placed together with distance of d=0.135 mm.

The proposed antenna configuration is shown in Fig. 2. Final values of the antenna design parameters are specified in Table 1.

In this study, to achieve the wideband operation, the radiating stub is converted to S-shaped structure as shown in the figure. By using this structure, a new resonator at 1.25 GHz will be excited whose resonant frequency is higher than the basic structure resonant frequency. Also, in order to achieve another resonance at 2.5 GHz, we used an S-shaped slotted ground plane. Regarding to have S-shaped structures in both of the radiating stub and ground plane, two resonators will be excited, when combined gives a wideband response;

$$W_{sub} = L_{sub} = \frac{c}{2f_L\sqrt{\varepsilon_{eff}}}, \quad (3)$$

$$\varepsilon_{eff} = (\varepsilon_r + 1)/2. \quad (4)$$

In this design, the final length $L_{resonance}$ is set to resonate at $0.25\lambda_{resonance}$:

$$f_{resonance} = \frac{c}{4L\sqrt{(\varepsilon_r + 1)/2}}, \quad (5)$$

where $L_{resonance1}=W_1+0.5L_1$ and $L_{resonance2}=0.25L_2+0.5W_4$ correspond to new resonance frequencies at 1.25 and 2.5 GHz. To investigate the performance of the proposed antenna configuration in terms of achieving wideband operation, a commercially available Ansoft HFSS was used for the required analysis and to obtain the proper geometrical parameters. The simulation processes flow chart is given below in Fig. 3.

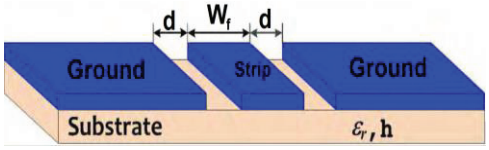

Fig. 2. Coplanar waveguide structure (CPW).

Table 1: Final dimensions of the antenna

Parameter	W_{sub}	L_{sub}	h_{sub}
Value (mm)	34	34	0.8
Parameter	L_f	W	L
Value (mm)	8	7.5	15
Parameter	L_2	W_3	L_g
Value (mm)	20	8.365	5
Parameter	W_S	L_S	W_f
Value (mm)	23	22	1
Parameter	W_1	L_1	W_2
Value (mm)	2	12.25	2.5
Parameter	W_4	d	W_5
Value (mm)	2	1.27	3

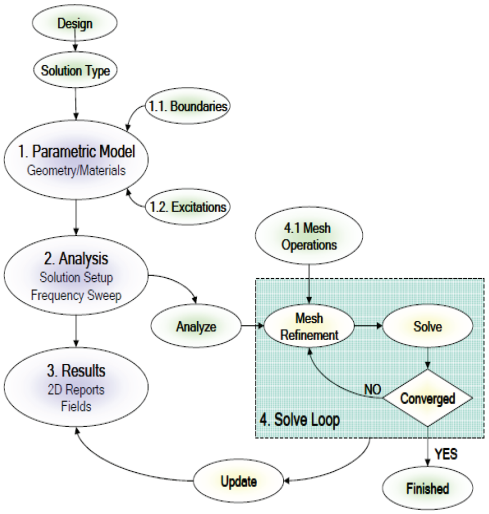

Fig. 3. Flow chart of simulation processes.

III. RESULTS AND DISCUSSIONS

The proposed CPW-fed slot antenna with various design parameters was constructed, and the numerical and experimental results of the input impedance and radiation characteristics are presented and discussed. Ansoft HFSS simulations are used to optimize the design and agreement between the simulation and measurement results is obtained [9].

The configuration of the various antennas used for simulation studies are shown in Fig. 4. Return loss characteristics for the ordinary CPW-fed slot antenna [Fig. 4 (a)], the antenna with an S-shaped radiating stub [Fig. 4 (b)], the antenna with S-shaped radiating stub and modified ground plane [Fig. 4 (c)], and the proposed slot antenna [Fig. 4 (b)] structures are compared in Fig. 5.

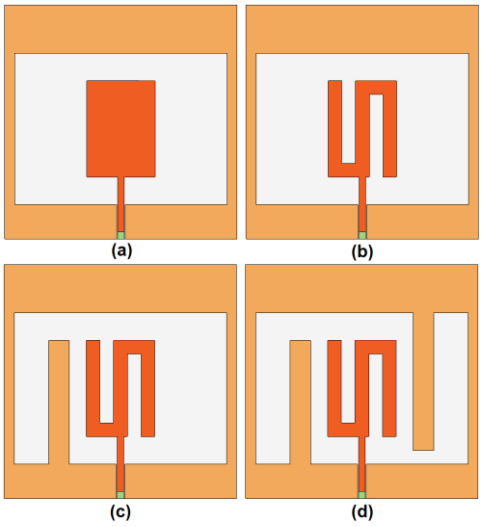

Fig. 4. (a) Ordinary CPW-fed slot antenna, (b) the antenna with an S-shaped radiating stub, (c) the antenna with S-shaped radiating stub and modified ground plane, and (d) the proposed antenna structure.

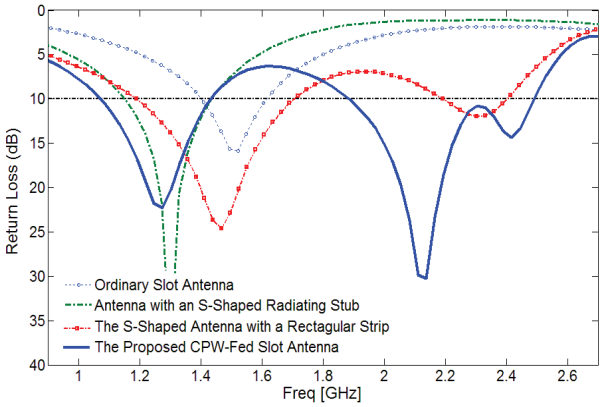

Fig. 5. Simulated return loss characteristics for the various structures shown in Fig. 4.

As shown in Fig. 5, it is observed that the lower frequency bandwidth is affected by using an S-shaped radiating stub and generation of multi-band performance is sensitive to the modified S-shaped ground plane. Also, the input impedance of the proposed antenna on a Smith Chart is shown in Fig. 6.

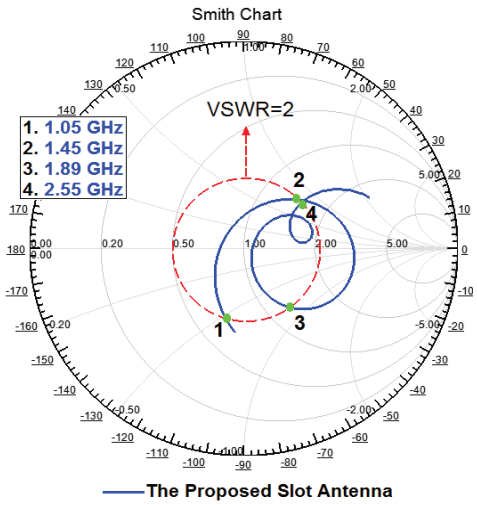

Fig. 6. Simulated input impedance of the proposed antenna on a Smith Chart.

In order to know the phenomenon behind this multi-band performance, the simulated current distributions for the presented antenna at 1.25, 2.15 and 2.4 GHz are presented in Fig. 7. It can be observed in Fig. 7 (a), at the lower frequency (2.1 GHz) the current concentrated on the edges of the interior and exterior of the S-shaped radiating stub. Therefore, the antenna impedance changes at this frequency due to the resonant properties of the S-shaped structure [6].

Another important design parameter of this structure is the modified ground plane structure. Figures 7 (b) and (c) present the simulated current distributions in the ground plane of the proposed antenna at 2.15 and 2.4 GHz (upper frequencies), respectively. As seen, at the upper resonance frequencies, the current flows are more dominant around of the modified S-shaped ground plane.

The proposed antenna with final design was built and tested. The below Fig. 8 shows the antenna fabrication setup.

The VSWR characteristic of the antenna was measured using the HP 8720ES network analyzer in an anechoic chamber. The radiation patterns have been measured inside an anechoic chamber using a double-ridged horn antenna as a reference antenna placed at a distance of 2 m. Also, two-antenna technique using an Agilent E4440A spectrum analyzer and a double-ridged horn antenna as a reference antenna placed at a distance of 2 m is used to measure the radiation gain in the z

axis direction (x-z plane). Measurement set-up of the proposed antenna for the VSWR, antenna gain and radiation pattern characteristics are shown in Fig. 9.

The measured and simulated return loss characteristics for the proposed antenna were shown in Fig. 10. The fabricated antenna has a frequency band from 1.04 GHz to 1.42 GHz and 1.88 GHz to 2.51 GHz.

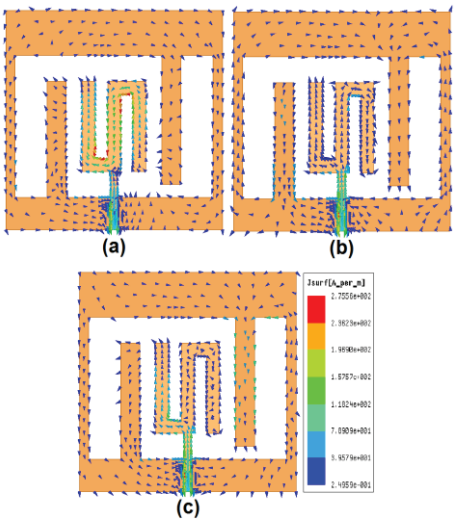

Fig. 7. Simulated surface current distributions for the proposed antenna at: (a) 1.25 GHz, (b) 2.15 GHz, and (c) 2.4 GHz.

Fig. 8. Fabrication setup.

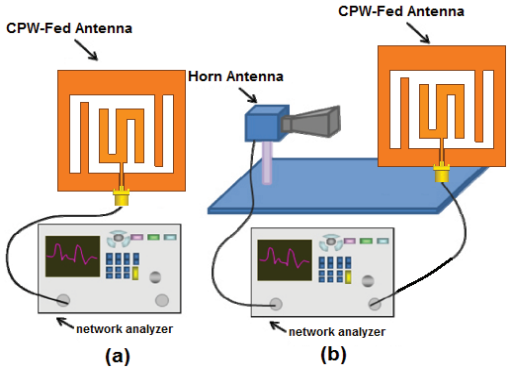

Fig. 9. Measurement set-up of the proposed antenna: (a) return loss, and (b) antenna gain and radiation patterns.

Figure 11 shows the measured radiation patterns including the co-polarization and cross-polarization in the *H*-plane (*x-z* plane) and *E*-plane (*y-z* plane). The main purpose of the radiation patterns is to demonstrate that the antenna actually radiates over a wide frequency band. It can be seen that the radiation patterns in *x-z* plane are nearly omnidirectional for the three frequencies. With the increase of frequency, the radiation patterns become worse because of the increasing effects of the cross-polarization [10-13]. Figure 12 shows the measured maximum gain of the proposed antenna for operation frequency bands.

The radiation intensity corresponding to the isotropic ally radiated power is equal to the power accepted by the antenna divided by 4π. This can be expressed as:

$$G = \frac{4\pi U(\varphi,\theta)}{P_{in}}. \tag{6}$$

It is assumed that the antenna is receiving a signal in the direction of maximum gain. It is also common for the gain to be expressed in decibels and referenced to an isotropic source (G=1), as shown:

$$G(dBi) = 10\,Log\,(G/1). \tag{7}$$

As illustrated the antenna has sufficient and acceptable gain level in these bands [14-15].

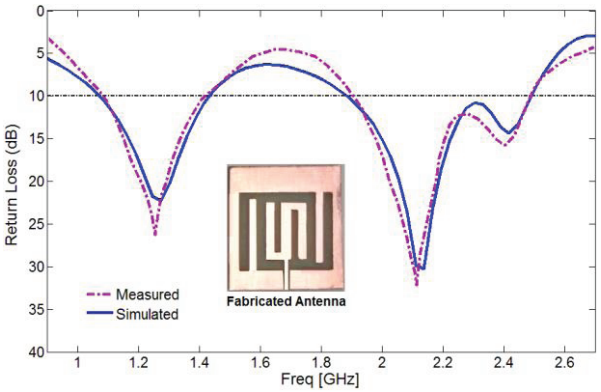

Fig. 10. Measured and simulated return loss characteristics for the proposed antenna.

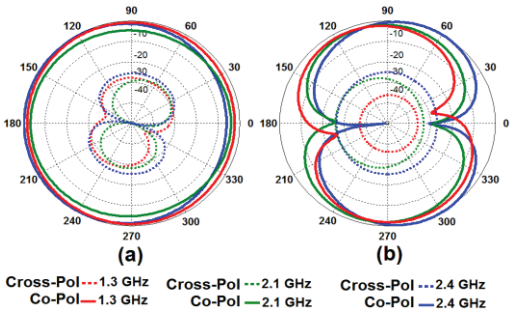

Fig. 11. Measured radiation patterns of the proposed antenna: (a) H-plane, and (b) E-plane.

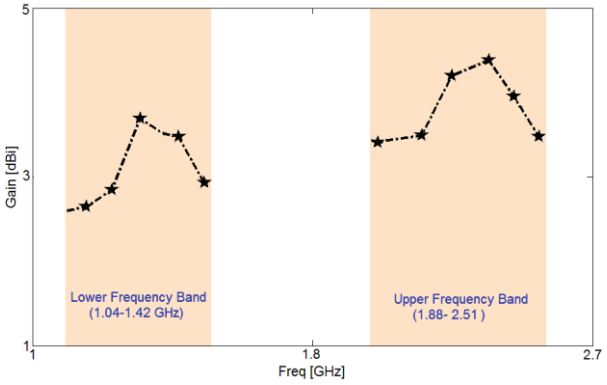

Fig. 12. Measured maximum gain for the proposed slot antenna.

IV. CONCLUSION

A novel dual-band CPW-fed slot antenna for major wireless communication bands is presented in this paper. The antenna configuration consist of modified S-shaped radiating patch and ground plane. The proposed antenna can operate from 1.04 GHz to 1.42 GHz and 1.88 GHz to 2.51 GHz. The designed antenna has a small size of 34×34 mm^2. The proposed antenna configuration is simple and easy to fabricate.

ACKNOWLEDGMENT

The authors are thankful to MWT Company staff for their help (www.microwave-technology.com).

REFERENCES

[1] C. A. Balanis, *Antenna Theory: Analysis and Design*, 3/e, Hoboken, New Jersey: John-Wiley and Sons, 2015.

[2] B. F. Wang and Y. T. Lo, "Microstrip antenna for dual-frequency operation," *IEEE Trans. Antennas Propag*., vol. AP-32, no. 9, pp. 938-943, 1994.

[3] N. Ojaroudi, "Frequency reconfigurable microstrip antenna integrated with PIN diodes for cognitive radio," *22nd Telecommunications Forum, TELFOR 2014*, Belgrade, Serbia, Nov. 25-27, 2014.

[4] H. Nakano and K. Vichien, "Dual-frequency square patch antenna with rectangular notch," *Electron. Lett*., vol. 25, pp. 1067-1068, 1998.

[5] S. Maci, G. Biffi Gentili, and G. Avitabile, "Single-layer dual- frequency patch antenna," *Electron. Lett*., vol. 29, pp. 1441-1443, 1993.

[6] N. Ojaroudi, "New design of multi-band PIFA for wireless communication systems," *19th International Symposium on Antenna and Propagation, ISAP2014*, Kaohsiung, Taiwan, Dec. 2-5, 2014.

[7] M. Hirvonen, P. Pursula, K. Jaakkola, et al., "Planar inverted-F antenna for radio frequency identification," *Electron. Lett*., vol. 40, pp. 848-850, 2004.

[8] M. Tzortzakakis and R. J. Langley, "Quad-band internal mobile phone antenna," *IEEE Trans. Antennas Propag*., vol. 55, no. 7, pp. 2097-2103, 2007.

[9] Ansoft High Frequency Structure Simulator (HFSS), ver. 13, Ansoft Corporation, 2010.

[10] N. Ojaroudi, "Novel design of low-profile microstrip band-stop filter (BSF) with koch fractal RSLRs," *22nd Telecommunications Forum, TELFOR 2014*, Belgrade, Serbia, Nov. 25-27, 2014.

[11] N. Ojaroudi, "Microstrip-fed antenna design for use in circular cylindrical microwave imaging applications," *22nd Telecommunications Forum*," *TELFOR 2014*, Belgrade, Serbia, Nov. 25-27, 2014.

[12] N. Ojaroudi, "Design of small reconfigurable microstrip antenna for UWB-CR applications," *19th International Symposium on Antenna and Propagation, ISAP2014*, Kaohsiung, Taiwan, Dec. 2-5, 2014.

[13] N. Ojaroudi, "Application of protruded Γ-shaped strips at the feed-line of UWB microstrip antenna to create dual notched bands," *International Journal of Wireless Communications, Networking and Mobile Computing*, vol. 1, no. 1, pp. 8-13, 2014.

[14] N. Ojaroudi, "Bandwidth improvement of monopole antenna using π-shaped slot and conductor-backed plane," *International Journal of Wireless Communications, Networking and Mobile Computing*, vol. 1, no. 2, pp. 14-19, 2014.

[15] N. Ojaroudi, "A modified compact microstrip-fed slot antenna with desired WLAN band-notched characteristic," *American Journal of Computation, Communication and Control*, vol. 1, no. 3, pp. 56-60, 2014.

Frequency Selection for Accurate Radar System of 2D Airplane in Turbulence Using Beam Wave Incidence

Hosam El-Ocla

Department of Computer Science
Lakehead University, 955 Oliver Road, Thunder Bay, Ontario, Canada P7B 5E1
hosam.elocla@lakeheadu.ca

Abstract **–** Selection of the proper frequencies that are able to detect civil and military aircrafts is a challenging issue in radar engineering. Proposed algorithm measures the effect of the linear polarization including H-wave polarization on the radar detection behavior in random medium, and hence, compares it with the E-wave polarization case. Effects of random medium properties on the scattered waves are analyzed. In doing this, laser radar cross section (LRCS) of targets is calculated using a boundary value method with a beam wave incidence. As a result, performance of the backscattering enhancement is studied with the object configuration considering the creeping waves that have an obvious impact, particularly in the resonance region.

Index Terms **–** Airplane, beam, conducting, frequency, object, polarization, scattering, radar, turbulence.

I. INTODUCTION

Recently, plenty of researchers presented useful quantitative studies for a range of frequencies able to detect a variety of conducting objects such as aircrafts and ships [1-3]. The case where targets are embedded in random media produces a backscattering enhancement in electromagnetic waves [4-6] compared to the free space case. Accordingly, the double passage effect [4] is applied on waves backscattering from point targets where RCS is enhanced by a factor ranging from one to two (Rayleigh) to three, because of the correlation between the forward and backward fields in turbulence [6].

In [7], it was handled the problem of backscattering enhancement where authors discussed the importance of using a boundary value problem method to calculate the generated surface current, essentially the effect of the shadow region when the object dimensions are larger than the wavelength λ. Over the past years, a current generator method (CGM) has been presented to solve the scattering problem as a boundary value problem [8,9]. This method computes reflected waves from the whole surface of arbitrary shape objects with reasonable processing time. Actually, our results are in excellent agreement with those assuming a cylinder with circular cross section in free space in [10]. Recently, CGM was verified using FDFD method and proved a fair agreement with an accuracy below 5% error rate for objects in random media and even less error in the free space [11]. In [12], it was concluded that RCS and accordingly the backscattering enhancement for a plane wave incidence depends greatly on the incident angle and the configuration of the target regardless of the incident wave polarization. However, this is not the case with E-beam wave incidence, particularly in the range of $a \geq \lambda$ [13].

In this paper, we extend our work to investigate the effect of beam wave incidence assuming H-polarization on objects having different configurations. With H-polarization, creeping waves [14] are generated and their effect maximizes in the resonance region where the target size is close to λ [15]. To improve radar imaging in the sense of having an accurate RCS calculation of objects such as aircrafts in turbulence, resonance effect [16] should be avoided or at least minimized to its minimal by controlling the incident aspects as it is investigated here. This is to obtain a radar system almost independent of the incident angle and complexity of aircrafts shapes. Therefore, the range of frequencies to detect accurately civil and military airplanes is selected despite of the coherence function of the surrounding medium, the incident wave polarization, and the illumination region complexity for some canonical examples. The time factor exp(−iwt) is assumed and suppressed in the following section.

II. SCATTERING PROBLEM

Geometry of the problem is shown in Fig. 1. A random medium is assumed as a sphere of radius L around a target of the mean size $a \ll L$, and also to be described by the dielectric constant ε(r), the magnetic permeability μ, and the electric conductivity σ. For simplicity ε(r) is expressed as:

$$\varepsilon(\mathbf{r}) = \varepsilon_0[1+\Delta\varepsilon(\mathbf{r})], \quad (1)$$

Submitted On: December 14, 2014
Accepted On: June 6, 2015

where ε_0 is assumed to be constant and equal to the permittivity of free space and $\Delta\varepsilon(\mathbf{r})$ is a random function with:

$$\langle\Delta\varepsilon(\mathbf{r})\rangle = 0, \qquad \langle\Delta\varepsilon(\mathbf{r})\,\Delta\varepsilon(\mathbf{r}')\rangle = B(\mathbf{r},\mathbf{r}'), \tag{2}$$

and

$$B(\mathbf{r},\mathbf{r}'),\ll 1, \qquad kl(\mathbf{r}) \gg 1. \tag{3}$$

Here, the angular brackets denote the ensemble average and $B(\mathbf{r},\mathbf{r}')$, $l(\mathbf{r})$ are the local intensity and local scale-size of the random medium fluctuation, respectively, and $k = \omega\sqrt{\varepsilon_0\mu_0}$ is the wavenumber in free space. Also μ and σ are assumed to be constants; $\mu = \mu_0$, $\sigma = 0$. For practical turbulent media the condition (3) may be satisfied. Therefore, we can assume the forward scattering approximation and the scalar approximation [15].

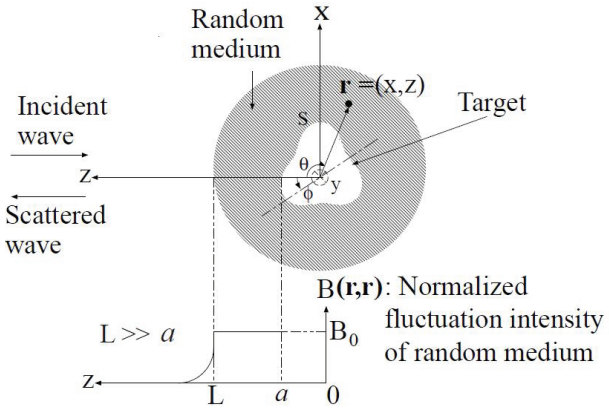

Fig. 1. Problem description of wave scattering from a conducting cylinder in random medium.

Consider the case where a directly incident wave is produced by a line source $f(\mathbf{r}')$ distributed uniformly along the y-axis. The line source is located at r_t beyond the random medium and it is quite far from the target. An electromagnetic wave radiated from the source propagates in the random medium illuminating the target and induces a current on its surface. A scattered wave from the target is produced by the surface current and propagates back to the observation point that coincides with the source point. The target is assumed to be a conducting cylinder of which cross-section is expressed by:

$$r = a\left[1-\delta\cos 3\left(\theta-\phi\right)\right], \tag{4}$$

where ϕ is the rotation index, δ is the concavity index. We can deal with this scattering problem two dimensionally under the condition (3); therefore, we represent $\mathbf{r}$ as $\mathbf{r} = (x, z)$. Assuming an H-polarization of incident waves (H-wave incidence), we can impose the Neumann boundary condition for wave field $u(\mathbf{r})$ on the cylinder surface S. That is,

$$\frac{\partial}{\partial n}u(\boldsymbol{r}) = 0, \tag{5}$$

where $u(\mathbf{r})$ represents E_x. Here, let us designate the incident wave by $u_{in}(\mathbf{r})$, the scattered wave by $u_s(\mathbf{r})$, and the total wave by $u(\mathbf{r}) = u_{in}(\mathbf{r}) + u_s(\mathbf{r})$. According to the current generator method [9] that uses the current generator Y_H and the Green's function in random medium $G(\mathbf{r}|\mathbf{r}')$ and as in [12], we can express the surface current wave as:

$$u(\boldsymbol{r_2}) = J_H(\boldsymbol{r_2}) = -\int_S Y_H(\boldsymbol{r_2}|\boldsymbol{r_1})\,u_{in}(\boldsymbol{r_1}|\boldsymbol{r_t})\,d\boldsymbol{r_1}, \tag{6}$$

where $\mathbf{r}_t$ represents the source point location and it is assumed that $\mathbf{r}_t = (0, z)$ in Section 3. Accordingly, the scattered wave is given as:

$$u_s(\boldsymbol{r}) = \int_S J_H(\boldsymbol{r_2})\frac{\partial G(\boldsymbol{r}|\boldsymbol{r_2})}{\partial n_2}\,d\boldsymbol{r_2}. \tag{7}$$

This can be represented as:

$$u_s(\boldsymbol{r}) = -\int_S d\boldsymbol{r_1}\int_S d\boldsymbol{r_2}\left[\left(\frac{\partial}{\partial n_2}G(\boldsymbol{r}|\boldsymbol{r_2})\right)\times Y_H(\boldsymbol{r_2}|\boldsymbol{r_1})u_{in}(\boldsymbol{r_1}|\boldsymbol{r_t})\right]. \tag{8}$$

Here, Y_H is the operator that transforms incident waves into surface currents on S and depends only on the scattering body. The current generator can be expressed in terms of wave functions that satisfy the Helmholtz equation and the radiation condition. Y_H is well formulated in [12] for H-polarization.

The incident wave is cylindrical and becomes plane approximately around the target because the line source is very far from the target. As a result, we consider $u_{in}(\mathbf{r}_1|\mathbf{r}_t)$ to be represented as:

$$u_{in}(\boldsymbol{r_1}|\boldsymbol{r_t}) = \int_{V_T} G(\boldsymbol{r_1}|\boldsymbol{r}')\times\exp\left[-\left(\frac{kx_1}{kW}\right)^2\right]f(\boldsymbol{r}')d\boldsymbol{r}' = G(\boldsymbol{r_1}|\boldsymbol{r_t})\exp\left[-\left(\frac{kx_1}{kW}\right)^2\right], \tag{9}$$

where W is the beam width. The beam expression is approximately useful only around the cylinder. The average intensity of the backscattering wave for H-wave incidence in turbulence is given by:

$$\langle|u_{sb}(\boldsymbol{r})|^2\rangle = \int_S d\boldsymbol{r}_{01}\int_S d\boldsymbol{r}_{02}\int_S d\boldsymbol{r}'_1\int_S d\boldsymbol{r}'_2 Y_H(\boldsymbol{r}_{01}|\boldsymbol{r}'_1)\,Y_H^*(\boldsymbol{r}_{02}|\boldsymbol{r}'_2)\exp\left[-\left(\frac{kx'_1}{kW}\right)^2\right]\times\exp\left[-\left(\frac{kx'_2}{kW}\right)^2\right]\frac{\partial}{\partial n_{01}}\frac{\partial}{\partial n_{02}}\langle G(\boldsymbol{r}|\boldsymbol{r}_{01})G(\boldsymbol{r}|\boldsymbol{r}_{02})G^*(\boldsymbol{r}|\boldsymbol{r}'_1)G^*(\boldsymbol{r}|\boldsymbol{r}'_2)\rangle. \tag{10}$$

We can obtain the LRCS σ_b using (10):

$$\sigma_b = \langle|u_{sb}(\boldsymbol{r})|^2\rangle\,.\,k(4\pi z)^2\,. \tag{11}$$

We express $|u_{sb0}(\boldsymbol{r})|^2$ in free space as:

$$|u_{sb0}(\boldsymbol{r})|^2 = \int_S d\boldsymbol{r}_{01}\int_S d\boldsymbol{r}_{02}\int_S d\boldsymbol{r}'_1\int_S d\boldsymbol{r}'_2 Y_H(\boldsymbol{r}_{01}|\boldsymbol{r}'_1)\,Y_H^*(\boldsymbol{r}_{02}|\boldsymbol{r}'_2)\exp\left[-\left(\frac{kx'_1}{kW}\right)^2\right]\times\exp\left[-\left(\frac{kx'_2}{kW}\right)^2\right]\frac{\partial}{\partial n_{01}}\frac{\partial}{\partial n_{02}}G_0(\boldsymbol{r}|\boldsymbol{r}_{01})G_0(\boldsymbol{r}|\boldsymbol{r}_{02})G_0^*(\boldsymbol{r}|\boldsymbol{r}'_1)G_0^*(\boldsymbol{r}|\boldsymbol{r}'_2). \tag{12}$$

We can obtain the LRCS σ_{b0} using (12):

$$\sigma_{b0} = |u_{sb0}(\boldsymbol{r})|^2\,.\,k(4\pi z)^2\,. \tag{13}$$

Final forms for (10) and (12) are derived in [16]. To

formulate the fourth moment of the Green's function in these equations, it is needed to use the structure function of turbulence D, defined in [9], as was explained in [13]. It should be noted that equation (3) puts a condition and assumes that the randomness density B is quite low enough to the extent that the medium has a fairly small number of particles resulting in having large separations ρ among particles. In [17], it was proved that D agrees better with the two-dimensional isotropic relation for larger ρ among particles than for smaller ρ. It was concluded that random medium can be considered as a two-dimensional turbulence in the enstrophy inertial range. This was derived and compared with calculations based on wind data from 5754 airplane flights. As a result, three-dimensional problems can be analyzed two-dimensionally under condition (3) in the absence of vortex stretching the nonlinear inertial force in the direction of y-axis of the cylinder that is aligned with the line source. Solving the problem two-dimensionally would in turn reduce greatly the calculation time of the scattered waves intensity in addition to minimizing the memory resources of the computers needed to process the three-dimensional problem that has been pursued in [11].

Let us assume that the coherence of waves is kept almost complete in propagation of a distance $2a$ equal to the mean diameter of the cylinder. This assumption is acceptable in practical cases under condition (3). On the basis of the assumption, it is important here to point out that we are going to present a quantitative discussion for the numerical results in Section 3.

The calculation of scattering data has been restricted to the interval $0.1 \le ka \le 30$. It is quite difficult to exceed this ka limit since greater ka requires a large M which consequently increases the calculation time dramatically.

III. NUMERICAL RESULTS

Although some of the incident wave rays become sufficiently incoherent in the propagation through random medium particles, we should pay attention to the spatial coherence length (SCL) of incident waves around the target. The degree of spatial coherence is defined as:

$$\Gamma(\rho,z)=\frac{\left\langle G(\mathbf{r}_1\,|\,\mathbf{r}_t)G^*(\mathbf{r}_2\,|\,\mathbf{r}_t)\right\rangle}{\left\langle\left|G(\mathbf{r}_0\,|\,\mathbf{r}_t)\right|^2\right\rangle}, \qquad (14)$$

where $\mathbf{r}_1 = (\rho, 0)$, $\mathbf{r}_2 = (-\rho, 0)$, $\mathbf{r}_0 = (0, 0)$, and $\mathbf{r}_t = (0, z)$. In the following calculations, we assume $B(\mathbf{r}, \mathbf{r}') = B_0$ and $kB_0L = 3\pi$; therefore the coherence attenuation index α defined as $k^2B_0Ll/4$ given in [9] is $15\pi^2$, $44\pi^2$, and $59\pi^2$ for kl = 20π, 58π, and 118π, respectively, which means that the incident wave becomes sufficiently incoherent. The SCL is defined as the $2k\rho$ at which $|\Gamma| = e^{-1} \cong 0.37$. In [13], a simplified form of the Γ function in random medium is formulated. Figure 2 shows a relation between SCL and kl in this case and that the SCL is equal to 3, 5.2, and 7.5. We use the SCL to represent one of the random medium effects on the LRCS.

In the following, we conduct numerical results for normalized LRCS (NLRCS), defined as σ_b expressed in (11) to σ_{b0} expressed in (13).

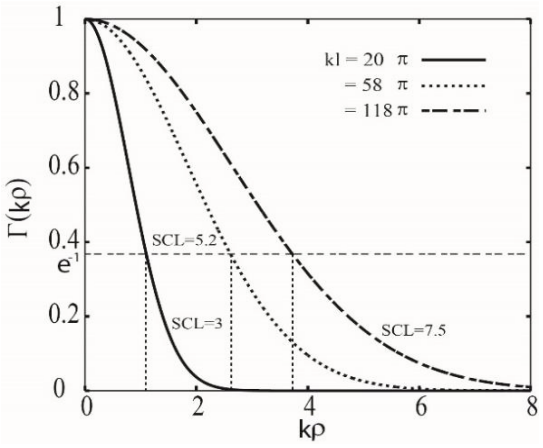

Fig. 2. The degree of spatial coherence of an incident wave about the cylinder.

A. Backscattering enhancement

Airplanes have models where their fuselages have different curvature slopes with the wings. In the numerical results we assume contours of cylinders with different cross section complexities shown in Fig. 3. Intensity of scattered waves varies with the illumination region complexity of such models and the random medium coherence function *SCL*, so we present results in Figs. 4 to 6 showing effects of these cases on the NLRCS. That is, when waves are scattered from fuselage only, we assume that $\delta = 0$ where the cross-section is circular. While waves scattering from other locations in the neighborhood of the fuselage attachment with the wings requires other values for δ such as Q-170 and X-47A airplane ($\delta \cong 0.1$), F16 and F117 airplane ($\delta \cong 0.18$–0.2) [13].

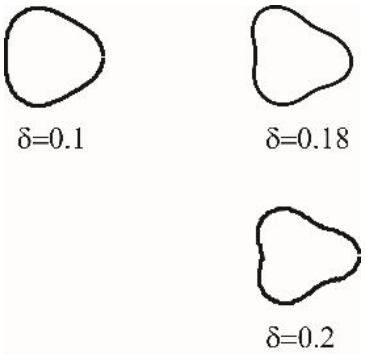

Fig. 3. Contours of cylinders with different cross section complexities.

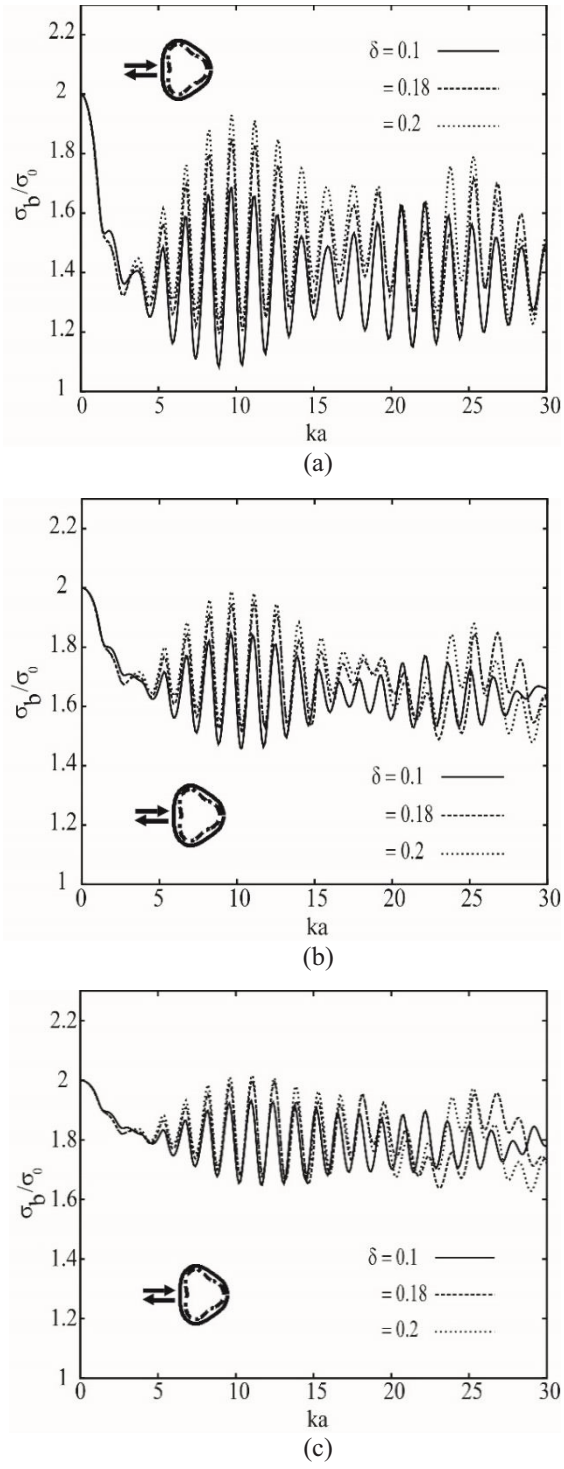

Fig. 4. Normalized LRCS vs. target size at different δ for kW = 2 where: (a) SCL = 3, (b) SCL = 5.2, (c) SCL = 7.5, and σb, σ0 are LRCS in random media and in free space, respectively.

At $ka \cong 0$, NLRCS is two owing to the double passage effect. As *ka* is getting greater, NLRCS undergoes a substantial oscillating behavior due to the random medium fluctuations. NLRCS is closer to two when having a greater *SCL* which represents a less medium randomness around the object. At the low *ka* band, target complexity has a less effect on the scattered waves and, therefore, NLRCS is almost invariant and does not change much with different δ. On the other hand, in the high frequency range where $ka \geq 20$, or alternatively at $a \geq 3\lambda$, NLRCS changes relatively more than with the low *ka* case but yet limitedly with δ. As *ka* enlarges, as the number of inflection points and accordingly their scattering contributions increase which in turn augments NLRCS. This behavior contradicts with the case of E-wave incidence where NLRCS does not differ with δ within the range $a \geq \lambda$ irrespective of the illumination region [13]. Also, we can notice that, the intensity of the NLRCS fluctuations is greater with H-wave incidence than with the E-wave incidence. This is due to the coupling between the direct waves and the creeping waves. NLRCS have anomaly increases in the resonance region [16] where the mean target size *a* is close to λ [15]. In addition NLRCS is closer to two with reducing the intensity of the oscillations when the *SCL* is wide enough around the object.

In Fig. 5, we investigate the effect of the illumination region curvature for both concave and convex portions where the incident angle represented in ϕ of Fig. 1 is 0 and π, respectively. It is important to refer to [16], where the illumination region was focused only on the convex portion ($\phi = \pi$) of concave-to-convex objects. It is apparent that the performance of NLRCS with δ discussed above is opposite to its performance with ϕ in Fig. 5. In other words, NLRCS is obviously different with the illumination region curvature at the low *ka* up to a certain value regardless of the *kW* limit. That is, NLRCS is different with ϕ at about $a \leq 3\lambda$ and vice versa. In Fig. 6, this observation is valid with *SCL* = 30. While this range is nearly indifferent with *kW* with the H-wave incidence, the NLRCS performance is, however, different in the case of E-wave incidence where *kW* would be a factor to determine this certain value of wavelength. This is also attributed to the effect of creeping waves coupling.

From this discussion, we can accept to consider $a \geq 3\lambda$ to be the range where NLRCS would not change obviously with the airplanes dimensions including wingspan and fuselage diameters that can be represented by 2*a* as in Fig. 1. Also within this range, NLRCS can be considered almost invariant with the incident angle, and accordingly with the illumination region complexity, and also with the incident wave polarization. Furthermore, NLRCS avoids having great peaks in the resonance region assuming this range.

As the wingspan is usually greater than the fuselage diameter, then we consider the wingspan to calculate the

proper frequency range for radar system that would reduce and minimizes the error rate of the radar detection system accuracy. Also, it should be noted that the wingspan for civil and military planes are quite different. For example, the wingspan for F16 and X-47A are 10 *m* and 8.465 *m*, respectively, which equals to the diameter 2*a* of the cylinder. As a result, for both models we can accept $\lambda \leq 1.7$ *m* and $\lambda \leq 1.41$ *m* for F16 and X-47A, respectively, and accordingly the frequency can be about 290 MHz or above. For the civil plane, we can consider the Boeing 777 where the wingspan is about 60 *m*. Therefore, $\lambda \leq 10$ *m*, and accordingly the frequency can be about 30 *MHz* or above. Having frequencies above these ranges would reduce the radar error rate and, therefore, maximizes the radar accuracy. As a result, the range of frequencies that can detect the military airplanes can also detect the civil planes, but not necessarily vice versa.

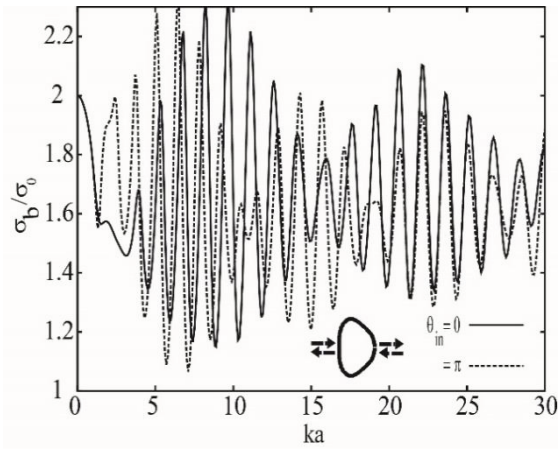

(a)

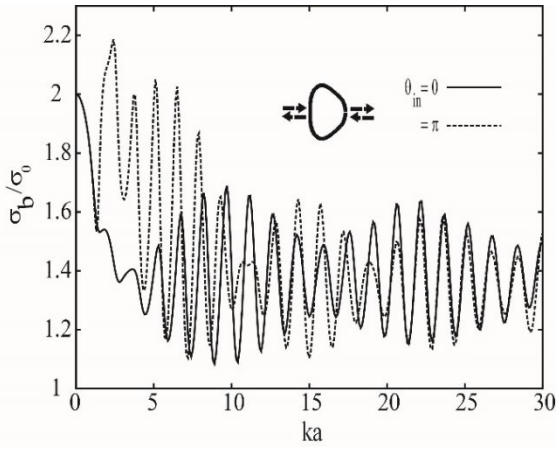

(b)

Fig. 5. Normalized LRCS vs. target size at δ = 0.1 for SCL = 3 where: (a) kW = 1.5, (b) kW = 2, and σb, σ0 are LRCS in random media and in free space, respectively.

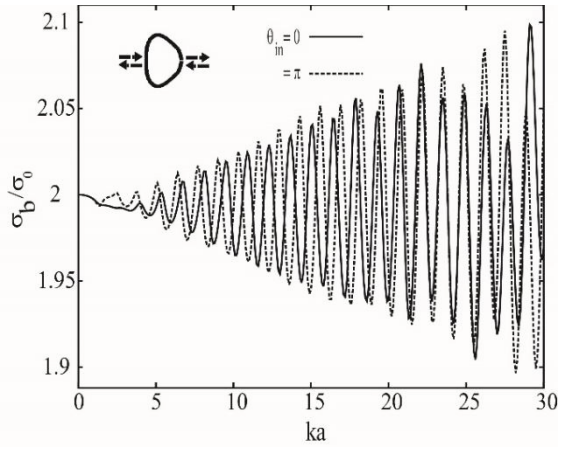

(a)

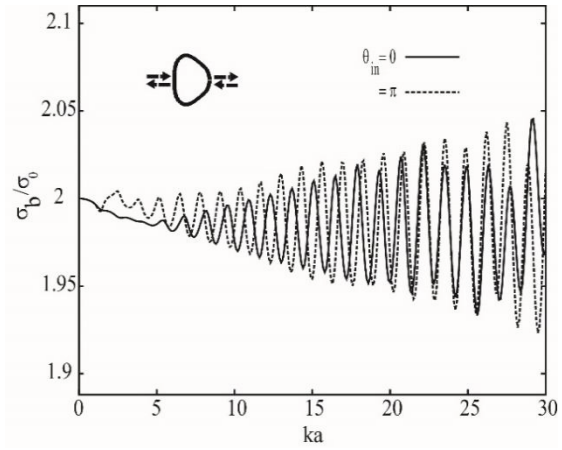

(b)

Fig. 6. As Fig. 5, but for SCL = 30.

IV. CONCLUSION

In this paper, we aim at selecting the range of frequencies that would enhance the capability of radar system to detect airplanes in random medium such as turbulence accurately. In doing this, we investigate the performance of the backscattering enhancement assuming an H-beam wave incidence and compare with the E-beam wave incidence. To maximize the efficiency of a radar system, the normalized laser RCS (NLRCS) should tend to two where the double passage is the only effect for a point target in random medium. This can be achieved with wider SCL and/or wider *kW* and that would also minimize the strength of the peak-to-peak oscillating behavior of NLRCS. On the other hand, NLRCS should be independent of the incident angle and incident wave polarization. Also, the radar frequencies should guarantee that NLRCS avoids having anomaly increases particularly in the resonance region with the convex illumination region.

The range of $a \geq 3\lambda$ can fulfill these requirements,

and hence, the frequencies of 290 *MHz* or above can be used to detect the arbitrary examples of military and civil airplanes assumed in this paper. Higher frequency spectrum minimizes the error rate of the radar system. It should be noted that less frequencies can detect only civil aircrafts but not military ones.

REFERENCES

[1] M. Tropea, F. De Rango, and S. Marano, "Current issues and future trends: DVB-RCS satellite systems," *IEEE A&E Systems Magazine*, pp. 15-22, 2009.

[2] Y. Alvarez, M. Elena De Cos, and F. Las-Heras, "RCS measurement setup for periodic-structure prototype characterization," *IEEE Antennas and Propagation Magazine*, vol. 52, no. 3, pp. 100-106, 2010.

[3] L. Sevgi, Z. Rafiq, and I. Majid, "Radar cross section (RCS) measurements," *IEEE Antennas and Propagation Magazine*, vol. 55, no. 6, pp. 278-291, 2013.

[4] Y. A. Kravtsov and A. I. Saishev, "Effects of double passage of waves in randomly inhomogeneous media," *Sov. Phys. Usp*., vol. 25, pp. 494-508, 1982.

[5] E. Jakeman, "Enhanced backscattering through a deep random phase screen," *J. Opt. Soc. Am*., vol. 5, no. 10, pp. 1638-1648, 1988.

[6] A. Ishimaru, "Backscattering enhancement: from radar cross sections to electron and light localizations to rough surface scattering," *IEEE Antennas and Propagation Magazine*, vol. 33, no. 5, pp. 7-11, 1991.

[7] C. Clemente and J. J. Soraghan, "GNSS-based passive bistatic radar for micro-doppler analysis of helicopter rotor blades," *IEEE Trans. on Aerospace and Electronic Systems*, vol. 50, no. 1, pp. 491-450, 2014.

[8] Z. Q. Meng and M. Tateiba, "Radar cross sections of conducting elliptic cylinders embedded in strong continuous random media," *Waves in Random Media*, vol. 6, pp. 335-345, 1996.

[9] M. Tateiba and Z. Q. Meng, "Wave scattering from conducting bodies in random media−theory and numerical results," *Electromagnetic Scattering by Rough Surfaces and Random Media*, ed. by M. Tateiba and L. Tsang, PIER 14, PMW Pub., Cambridge, MA, USA, pp. 317-361, 1996.

[10] M. Kerker, *The Scattering of Light and Other Electromagnetic Radiation*, Academic Press, New York, 1969.

[11] M. Al Sharkawy and H. El-Ocla, "Electromagnetic scattering from 3D targets in a random medium using finite difference frequency domain," *IEEE Transactions on Antenna and Propagation*, vol. 61, no. 11, pp. 5621-5626, 2013.

[12] H. El-Ocla, "Effect of illumination region of targets on waves scattering in random media with H-polarization," *Waves in Random and Complex Media*, vol. 19, no. 4, pp. 637-653, 2009.

[13] H. El-Ocla and M. Al Sharkawy, "Using CGM and FDFD techniques to investigate the radar detection of 2D airplanes in random media for beam wave incidence," *IEEE Antenna and Propagation Magazine*, vol. 56, no.5, pp. 91-100, 2014.

[14] M. L. Harbold and B. N. Steinberg, "Direct experimental verification of creeping waves," *The Journal of the Acoustical Society of America*, vol. 45, pp. 592-603, 1969.

[15] A. Ishimaru, *Wave Propagation and Scattering in Random Media*, IEEE Press, 1997.

[16] H. El-Ocla, "Influence of incident waves on resonance in backscattering from rargets in random media," *Electromagnetics*, vol. 33, iss. 1, pp. 23-39, 2013.

[17] E. Lindborg, "Can the atmospheric kinetic energy spectrum be explained by two dimensional turbulence?," *Journal of Fluid Mechanics*, vol. 388, pp. 259-288, 1999.

Hosam El-Ocla received the M.Sc. degree in the Electrical Engineering Department of Cairo University in 1996, and the Ph.D. degree from Kyushu University in 2001. He joined the Graduate School of Information Science and Electrical Engineering, Kyushu University, Japan in 1997 as Research Student. He joined Lakehead University in 2001 as an Assistant Professor and has been an Associate Professor since 2007. His current main interests are in wave propagation and scattering in random media.

Vector Parabolic Equation Method for the EM Scattering from PEC Objects in Half-Space

Z. He, T. Su, and R. S. Chen

Department of Communication Engineering
Nanjing University of Science and Technology, Nanjing, 210094, China
eerschen@njust.edu.cn

Abstract ─ The vector parabolic equation method was widely used to analyze the electromagnetic scattering from electrically large PEC objects in free space. In this paper, it is applied for the analysis of the electromagnetic scattering from PEC objects in half-space. By introducing both the incident field and the reflected field to illuminate the objects, the vector parabolic equation method can be used to efficiently calculate the radar cross-section of PEC objects with electrically large size in half-space. The numerical results demonstrate that the proposed method can efficiently give reasonably accurate results.

Index Terms ─ Electromagnetic scattering, half-space, parabolic equation method.

I. INTRODUCTION

The differential methods such as the finite differential method (FD) and the finite element method (FEM) in frequency domain [1-2] were widely used for computing the radar cross-section (RCS) of complex objects in free space. However, a large number of unknowns were needed to analyze three dimensional electromagnetic scattering from electrically large objects for these methods. The parabolic equation (PE) method was an approximation of the wave equation with marching gradually from one plane to another along the paraxial direction [3-5]. By this way, the three-dimensional problem could be converted into a series of two-dimensional problems to be solved by the PE method. Therefore, the electromagnetic scattering from electrically large PEC objects could be analyzed efficiently. However, the PE method could not provide the full bistatic scattering pattern of an object because of intrinsic paraxial limitations [6]. And it has not been reported that the electrically large conductive objects in half-space were calculated by the parabolic equation method so far.

With the development of the electromagnetism, more and more attention was paid to the electromagnetic scattering from electrically large objects above the earth or the sea [7-10]. The electromagnetic scattering from the electrically large objects in half-space could be analyzed by both the FDTD [11] and the FEM [12], but there were difficulties in the procedures of modeling and computing. Moreover, the half-space Green's function was used to be combined with the method of moments (MoM) for the electromagnetic scattering from PEC objects in half-space [13-15]. And the multilevel fast multipole method (MLFMM) was applied to accelerate the calculation [8]. But memory requirements and computation time were still excessive by this method, which led to bad computational efficiency.

In this paper, the vector PE method is used for the analysis of the electromagnetic scattering from PEC objects in half-space. Both the incident field and the reflected field from the ground plane are considered to illuminate the objects through the inhomogeneous boundary conditions. Then the scattered electric fields can be calculated from one plane to another with the parabolic equations. Moreover, the scattered magnetic fields can be gotten from the scattered electric fields through the Maxwell equations with the finite difference scheme. As a result, both the scattered electric current and the scattered magnetic current of the last transverse plane can be computed by them. At last, the RCS can be obtained by the reciprocal theory with the scattered electric current and the scattered magnetic current of the last transverse plane.

The remainder of this paper is organized as follows. In Section 2, the theory and the formulations are given. Two numerical experiments are presented in Section 3 to show the efficiency of the proposed method. Section 4 concludes this paper.

II. THEORY AND FORMULATIONS

A. PE framework for scattering problems

The three-dimensional electromagnetic scattering from PEC objects in free space can be analyzed by the three-dimensional wave equation. The scattered field components $\vec{E}_x^S, \vec{E}_y^S, \vec{E}_z^S$ satisfy scalar wave equation as follows:

Submitted On: December 1, 2014
Accepted On: May 26, 2015

$$\begin{aligned}
&\frac{\partial^2 \vec{E}_x^s}{\partial x^2}+\frac{\partial^2 \vec{E}_x^s}{\partial y^2}+\frac{\partial^2 \vec{E}_x^s}{\partial z^2}+k^2\vec{E}_x^s=0\\
&\frac{\partial^2 \vec{E}_y^s}{\partial x^2}+\frac{\partial^2 \vec{E}_y^s}{\partial y^2}+\frac{\partial^2 \vec{E}_y^s}{\partial z^2}+k^2\vec{E}_y^s=0\\
&\frac{\partial^2 \vec{E}_z^s}{\partial x^2}+\frac{\partial^2 \vec{E}_z^s}{\partial y^2}+\frac{\partial^2 \vec{E}_z^s}{\partial z^2}+k^2\vec{E}_z^s=0,
\end{aligned} \tag{1}$$

where k is the wave number.

The reduced scattered fields u_x^s, u_y^s, u_z^s are introduced with the scattered field components:

$$u_\xi^s(x,y,z)=e^{-jkx}\vec{E}_\xi^s(x,y,z) \qquad \xi=x,y,z. \tag{2}$$

Define the pseudo-differential operator Q as the following format:

$$Q=\frac{1}{k^2}\left(\frac{\partial^2}{\partial y^2}+\frac{\partial^2}{\partial z^2}\right). \tag{3}$$

Substitute equation (1) with the equations (2) and (3), the following equations can be gotten:

$$\left[\frac{\partial}{\partial x}+jk(1-\sqrt{1+Q})\right]\left[\frac{\partial}{\partial x}+jk(1+\sqrt{1+Q})\right]u_\xi^s=0 \qquad \xi=x,y,z. \tag{4}$$

The two parts of the equation (4) correspond to forward and backward propagating waves, respectively. The first order Taylor expansions of the square root and the exponential are used in this paper. This yields the well-known standard vector parabolic equations:

$$\frac{\partial^2 u_\xi^s}{\partial y^2}(x,y,z)+\frac{\partial^2 u_\xi^s}{\partial z^2}(x,y,z)+2jk\frac{\partial u_\xi^s}{\partial x}(x,y,z)=0 \qquad \xi=x,y,z. \tag{5}$$

When the FD scheme of the Crank-Nicolson type is used to the equation (5), the forward vector parabolic wave equations can be written as follows:

$$\begin{aligned}
&\frac{\Delta x}{2jk(\Delta y)^2}u_\xi^s(x+\Delta x,y+\Delta y,z)+\\
&\frac{\Delta x}{2jk(\Delta z)^2}u_\xi^s(x+\Delta x,y,z+\Delta z)+\\
&\left(1-\frac{\Delta x}{jk(\Delta y)^2}-\frac{\Delta x}{jk(\Delta z)^2}\right)u_\xi^s(x+\Delta x,y,z)+\\
&\frac{\Delta x}{2jk(\Delta y)^2}u_\xi^s(x+\Delta x,y-\Delta y,z)+\\
&\frac{\Delta x}{2jk(\Delta z)^2}u_\xi^s(x+\Delta x,y,z-\Delta z)\\
&\qquad =u_\xi^s(x,y,z) \qquad \xi=x,y,z.
\end{aligned} \tag{6}$$

The reduced scattered fields at $(x+\Delta x)$ plane can be calculated from those at x plane by the use of the equation (6). As shown in Fig. 1, the calculation starts in the plane before the scatterer and stops in the plane beyond the scatterer. The initial fields are set to be zero in the first transverse plane. In order to truncate the computational domain, the perfectly matched layer (PML) is selected to truncate each transverse plane [16-17]. The radar cross section (RCS) can be obtained by the reciprocal theory with the scattered electric current and the scattered magnetic current of the last transverse plane.

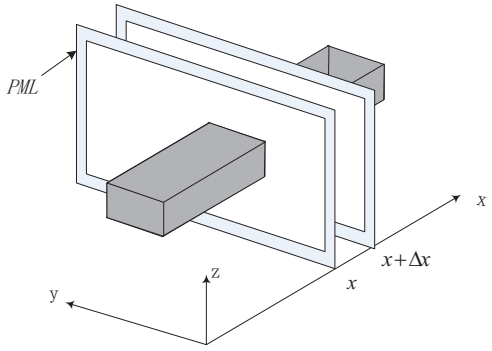

Fig. 1. The marching strategy of the PE method.

B. Boundary conditions for scattering problems in half-space

As shown in Fig. 2, the scattered fields $\vec{E}^s$ of the electrically large conductive objects in half space can be composed of three parts approximately [18-19]. They are the reflected fields of the ground, the reflected fields of the object and the reflected fields of both the ground and the object. And the PEC object in half-space is illuminated by both the incident field $\vec{E}^i$ and the reflected field in the ground plane $\vec{E}^r$. The intersection angle between the incident field and the reflected field is 2α. As shown in Fig. 2, the marching direction of the PE method is given for backward scattering from a PEC object.

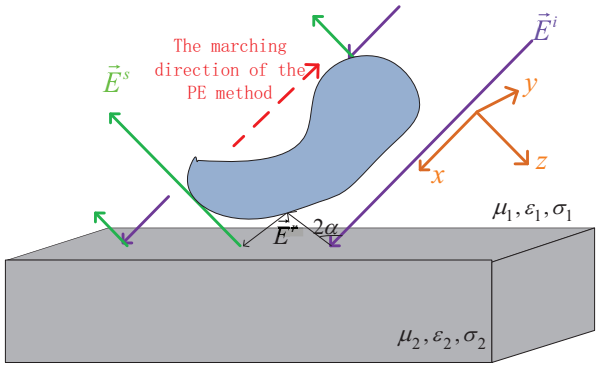

Fig. 2. The object in half-space.

The reduced scattered fields in equation (6) are coupled through boundary conditions on the PEC objects. For a PEC, the tangential electric field must be zero on the surface of the scatterer:

$$\begin{aligned}
&n_x u_y^s-n_y u_x^s=-e^{-jkx}[n_x(E_y^i+E_y^r)-n_y(E_x^i+E_x^r)]\\
&n_x u_z^s-n_z u_x^s=-e^{-jkx}[n_x(E_z^i+E_z^r)-n_z(E_x^i+E_x^r)]\\
&n_y u_z^s-n_z u_y^s=-e^{-jkx}[n_y(E_z^i+E_z^r)-n_z(E_y^i+E_y^r)],
\end{aligned} \tag{7}$$

in which (E_x^i, E_y^i, E_z^i) are the components of the incident field for the directions $\vec{x}, \vec{y}, \vec{z}$, (E_x^r, E_y^r, E_z^r) are the ones of the reflected field, and (n_x, n_y, n_z) denote the surface outward pointing unit normal.

Another equation is needed because the equations in (7) are not independent. As a result, the divergence-free condition is added to the equation for guaranteeing the unicity of the solution [6]:

$$\frac{j}{2k}\left(\frac{\partial^2 u_x^s}{\partial y^2}+\frac{\partial^2 u_x^s}{\partial z^2}\right)+jku_x^s+\frac{\partial u_y^s}{\partial y}+\frac{\partial u_z^s}{\partial z}=0. \tag{8}$$

The incident field and the reflected field can be expressed by the following equations, respectively:

$$\begin{aligned}
&\vec{E}^i=(\hat{\theta}_i\cos\beta+\hat{\varphi}_i\sin\beta)e^{-j\vec{k}^i\cdot\vec{r}}\\
&for\quad \vec{k}^i=-k(\cos\theta^i\hat{x}+\sin\theta^i\cos\varphi^i\hat{y}+\sin\theta^i\sin\varphi^i\hat{z})\\
&\hat{\theta}_i=-\sin\theta^i\hat{x}+\cos\theta^i\cos\varphi^i\hat{y}+\cos\theta^i\sin\varphi^i\hat{z}\\
&\hat{\varphi}_i=-\sin\varphi^i\hat{y}+\cos\varphi^i\hat{z},
\end{aligned} \tag{9}$$

$$\begin{aligned}
&\vec{E}^r=(\hat{\theta}_t R^{TM}\cos\beta+\hat{\varphi}_t R^{TE}\sin\beta)e^{-j\vec{k}^t\cdot\vec{r}}\\
&for\quad \vec{k}^t=-k(\cos\theta^t\hat{x}+\sin\theta^t\cos\varphi^t\hat{y}+\sin\theta^t\sin\varphi^t\hat{z})\\
&\hat{\theta}_t=-\sin\theta^t\hat{x}+\cos\theta^t\cos\varphi^t\hat{y}+\cos\theta^t\sin\varphi^t\hat{z}\\
&\hat{\varphi}_t=-\sin\varphi^t\hat{y}+\cos\varphi^t\hat{z}.
\end{aligned} \tag{10}$$

In equations (9) and (10), $\beta=0$ represents vertical polarization while $\beta=\frac{\pi}{2}$ represents horizontal polarization, (θ^i,φ^i) is the angle of the incident field and (θ^t,φ^t) is the angle of the reflected field. The reflection coefficients R^{TM}, R^{TE} can be expressed as follows, respectively [20]:

$$\begin{aligned}
R^{TM}&=\frac{(\varepsilon_2/\varepsilon_1)\cos\theta^i-\sqrt{\varepsilon_2/\varepsilon_1-\sin^2\theta^i}}{(\varepsilon_2/\varepsilon_1)\cos\theta^i+\sqrt{\varepsilon_2/\varepsilon_1-\sin^2\theta^i}}\\
R^{TE}&=\frac{\cos\theta^i-\sqrt{\varepsilon_2/\varepsilon_1-\sin^2\theta^i}}{\cos\theta^i+\sqrt{\varepsilon_2/\varepsilon_1-\sin^2\theta^i}}.
\end{aligned} \tag{11}$$

C. Far-field calculations

Combining the equations (6), (7) and (8) with the finite difference scheme of the Crank-Nicolson type, the scattered electric fields $\vec{E}^s(x,y,z)$ can be computed. And the scattered magnetic fields $\vec{H}^s(x,y,z)$ of the last transverse (y,z) plane can be gotten by the following equation with the scattered electric fields $\vec{E}^s(x,y,z)$ of the last two transverse (y,z) planes:

$$\begin{aligned}
\vec{H}^s&=\frac{j}{\omega\mu_1}\nabla\times\vec{E}^s\\
&=\frac{j}{\omega\mu_1}[\vec{e}_x(\frac{\partial E_z^s}{\partial y}-\frac{\partial E_y^s}{\partial z})+\\
&\vec{e}_y(\frac{\partial E_x^s}{\partial z}-\frac{\partial E_z^s}{\partial x})+\vec{e}_z(\frac{\partial E_y^s}{\partial x}-\frac{\partial E_x^s}{\partial y})].
\end{aligned} \tag{12}$$

Moreover, the scattered electric current and the scattered magnetic current of the last transverse plane can be computed by the scattered electric fields and the scattered magnetic fields in the last transverse (y,z) planes:

$$\begin{aligned}
\vec{J}^s&=\vec{n}_p\times\vec{H}^s\\
&=\vec{e}_x(n_{y,p}H_z^s-n_{z,p}H_y^s)+\vec{e}_y(n_{z,p}H_x^s-n_{x,p}H_z^s)\\
&\quad+\vec{e}_z(n_{x,p}H_y^s-n_{y,p}H_x^s),
\end{aligned} \tag{13}$$

$$\begin{aligned}
\vec{M}^s&=\vec{E}^s\times\vec{n}_p\\
&=\vec{e}_x(E_y^s n_{z,p}-E_z^s n_{y,p})+\vec{e}_y(E_z^s n_{x,p}-E_x^s n_{z,p})\\
&\quad+\vec{e}_z(E_x^s n_{y,p}-E_y^s n_{x,p}),
\end{aligned} \tag{14}$$

where $\vec{n}_p=(n_{x,p},n_{y,p},n_{z,p})$ denotes the unit normal of the last transverse (y,z) plane. Once both the scattered electric current and the scattered magnetic current are obtained in the last transverse plane, the far field components can be calculated by them with the reciprocal theory. And the RCS in direction (θ,φ) is given by:

$$\sigma(\theta,\varphi)=\lim_{r\to\infty}4\pi r^2\frac{\left|\vec{E}^s(x,y,z)\right|^2}{\left|\vec{E}^i(x,y,z)\right|^2}=$$

$$\frac{k^2\cos^2\theta}{\pi}\left|\int_{-\infty}^{\infty}\int_{-\infty}^{\infty}(\vec{E}^s(x,y,z)\bullet\vec{t})\bullet e^{-jk\sin\theta(y\cos\varphi+z\sin\varphi)}dydz\right|^2, \tag{15}$$

where $\vec{t}$ is the receiver polarization.

III. NUMERICAL RESULTS

In this section, a series of examples are presented to demonstrate the efficiency of the proposed method.

A. The bistatic RCS for a PEC cylinder

Firstly, the electromagnetic scattering from a PEC cylinder is considered at the frequency of 300 MHz with the radius 2 m and the height 1 m. The model of the PEC cylinder is shown in Fig. 3. The incident wave propagates along the x-axis. The PEC cylinder is placed $\lambda/5$ above the half space with $\varepsilon_r=4.0$, $\mu_r=1.0$ and $\sigma=0.01$, where λ represents the wavelength in the vacuum. As shown in Fig. 4, the bistatic RCS curves above the half space are compared between the proposed method and software FEKO. It can be seen that there is a good agreement between them and it should be noted that seven rotating PE runs are used to obtain the full bistatic RCS [6]. Moreover, comparisons of the memory requirement, the matrix size, the matrix-filling time and the CPU time are made between the proposed method and the MLFMM, as shown in Table 1. It can be found that memory requirement and CPU time can be reduced 40.1% and

88.3% for the proposed method, respectively. At last, the bistatic RCS values of different spacing values between the cylinder and the soil are computed in Fig. 5.

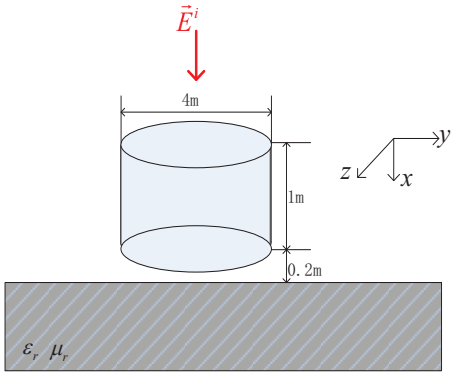

Fig. 3. The cylinder model in half space.

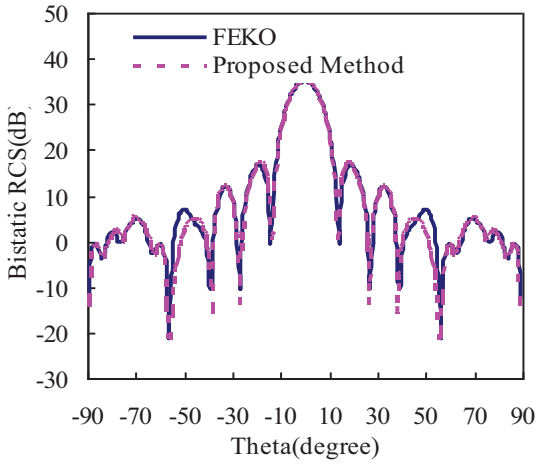

Fig. 4. Bistatic RCS of a PEC cylinder at the frequency of 300 MHz.

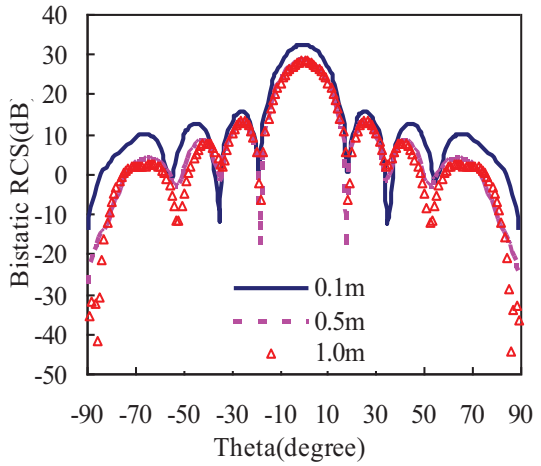

Fig. 5. Bistatic RCS values of different spacing values for the PEC cylinder.

Table 1: Comparisons of the memory requirement, the matrix size, the matrix-filling time and the CPU time for the PEC cylinder

Methods	Matrix Size	Matrix-Filling Time (s)	CPU Time (s)	Memory Requirement (MB)
Proposed Method	10000	23	97	225.3
MLFMM	25506	511	826	376.2

B. The monostatic RCS for a PEC polygon

Secondly, the analysis of monostatic RCS is taken for a PEC polygon at the frequency of 0.3 GHz. The PEC polygon is placed $\lambda/2$ above the soil with $\varepsilon_r = 2.3$, $\mu_r = 1.0$ and $\sigma = 0.01$. The size of the polygon is shown in Fig. 6. It should be noted that there are different numbers of transverse planes to be computed for each observation angle, since the length of the scatterer along the x-axis (the paraxial direction) is changing for different angles of the incident wave. As shown in Fig. 7, the monostatic RCS curves are compared between the proposed method and FEKO. As shown in Table 2, the comparisons of the memory requirement, the matrix size, the matrix-filling time and the CPU time are made between the proposed method and the MLFMM. It can be seen that memory requirement and CPU time can be reduced 65.4% and 34.2% for the proposed method, respectively. Therefore, the vector parabolic equation method can be utilized for the efficient analysis of the electromagnetic scattering from the conductive objects with electrically large size in half-space.

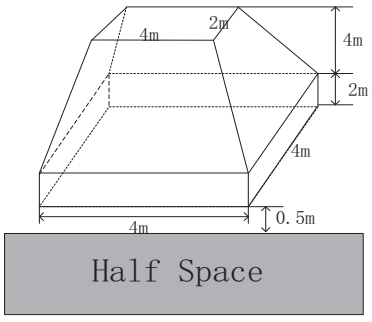

Fig. 6. Model of the PEC polygon in half space.

Table 2: Comparisons of the memory requirement, the matrix size, the matrix-filling time and the CPU time for the PEC polygon

Methods	Matrix Size	Matrix-Filling Time (s)	CPU Time (s)	Memory Requirement (MB)
Proposed Method	10000	4391	10978	339.7
MLFMM	34245	10007	16679	980.4

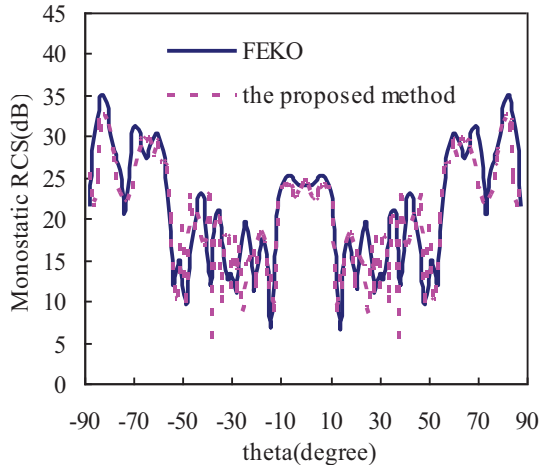

Fig. 7. Monostatic RCS of a PEC polygon at the frequency of 300 MHz in half space.

C. Comparisons of the bistatic RCS curves in free space and in half space for an aircraft

At last, we consider the scattering from an aircraft both in the free space and in the half space at the frequency of 1 GHz. Its maximum sizes in x, y and z directions are 4.8 m, 3.3 m, 1.06 m. The full bistatic RCS curves in free space and in half space are given in Fig. 8 with 7 PE runs. The aircraft is placed 2λ above the half space with $\varepsilon_r = 4.5$, $\mu_r = 1.0$ and $\sigma = 0.01$.

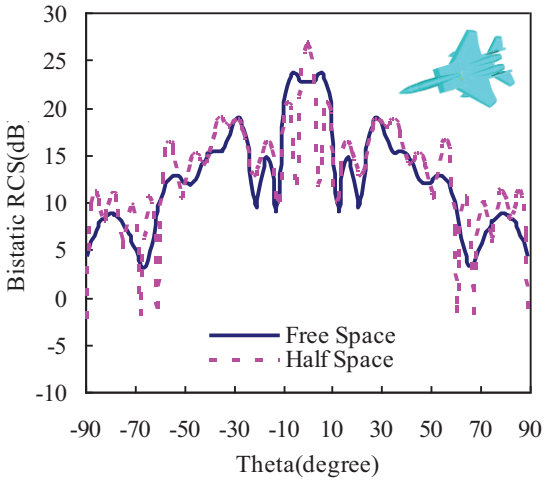

Fig. 8. Bistatic RCS of an aircraft at the frequency of 1 GHz.

IV. CONCLUSION

In this paper, the vector parabolic equation method is used to analyze the electromagnetic scattering from electrically large PEC objects in half-space. Both the incident field and the reflected field from the ground plane illuminate the objects through the inhomogeneous boundary conditions. The numerical results are compared between the proposed method and the MLFMM. It can be found that there is a good agreement between them for the three-dimensional electromagnetic scatterings in half-space. Moreover, the proposed method can give encouraging results with less CPU time and smaller memory requirement than the MLFMM.

ACKNOWLEDGMENT

This work was supported in part by Natural Science Foundation of 61431006, 61271076, 61171041, the Fundamental Research Funds for the central Universities of No. 30920140111003, No. 30920140121004, and in part by Jiangsu Natural Science Foundation of BK2012034.

REFERENCES

[1] M. A. Sharkawy and H. E. Ocla, "Electromagnetic scattering from 3-D targets in a random medium using finite difference frequency domain," *IEEE Trans. Antennas and Propagation*, vol. 61, no. 11, Nov. 2013.

[2] N. Godel, N. Nunn, T. Warburton, and M. Clemens, "Accelerating multi GPU based discontinuous Galerkin FEM computations for electromagnetic radio frequency problems," *Applied Computational Electromagnetics Society (ACES) Journal*, vol. 25, no. 4, pp. 331-338, 2010.

[3] M. F. Levy, *Parabolic Equation Methods for Electromagnetic Wave Propagation*, London: The Institution of Electrical Engineers, 2000.

[4] Z. He and R. S. Chen, "A vector meshless parabolic equation method for three-dimensional electromagnetic scatterings," *IEEE Trans. Antennas and Propagation*, accepted, 2015.

[5] Z. He, Z. H. Fan, D. Z. Ding, and R. S. Chen, "Efficient radar cross-section computation of electrically large targets with ADI-PE method," *Electronics Letters*, vol. 51, no. 4, pp. 360-362, 2015.

[6] A. A. Zaporozhets and M. F. Levy, "Bistatic RCS calculations with the vector parabolic equation method," *IEEE Trans. Antennas and Propagation*, vol. 47, no. 11, Nov. 1999.

[7] J. Zhu, M. M. Li, Z. H. Fan, and R. S. Chen, "Analysis of EM scattering from 3D bi-anisotropic objects above a lossy half space using FE-BI with UV method," *Applied Computational Electromagnetics Society (ACES) Journal*, vol. 28, no. 10, pp. 917-923, 2013.

[8] W. Yang, Z. Zhao, and Z. Nie, "Fast fourier transform multilevel fast multipole algorithm in rough ocean surface scattering," *Electromagnetics*, vol. 29, pp. 541-552, 2009.

[9] M. M. Li, H. Chen, C. Y. Li, R. S. Chen, and C. J.

Ong, "Hybrid UV/MLFMA analysis of scattering by PEC targets above a lossy half-space," *Applied Computational Electromagnetics Society (ACES) Journal*, vol. 26, no. 1, pp. 17-25, 2011.

[10] S. M. Yucedag and A. Kizilay, "Time domain analysis of ultra-wide band signals from buried objects under flat and slightly rough surfaces," *Applied Computational Electromagnetics Society (ACES) Journal*, vol. 28, no. 8, pp. 646-652, 2013.

[11] Q. L. Li, D. B. Ge, Y. Shi, and Y. B. Yan, "An approach for solving ground wave scattering from objects," *J. Microw*., vol. 14, pp. 23-28, 1998.

[12] D. H. Han and A. C. Polycarpou, "Ground effects for VHF/HF antennas on helicopter air frames," *IEEE Trans. Antennas and Propagation*, vol. 49, pp. 402-412, 2001.

[13] T. Su, Z. W. Yang, M. M. Li, and R. S. Chen, "Computation for electromagnetic scattering from electrically large 3-D PEC objects buried in a lossy stratified medium," *In Microwave and Millimeter Wave Technology (ICMMT)*, vol. 1, pp. 1-4, 2012.

[14] N. Geng, A. Sullivan, and L. Carin, "Multilevel fast multipole algorithm for scattering from conducting objects above or embedded in a lossy half space," *IEEE Trans. Antennas and Propagation*, vol. 38, pp. 1567-1579, 2000.

[15] D. Z. Ding, J. M. Ge, and R. S. Chen, "Well-conditioned CFIE for scattering from dielectric coated conducting bodies above a half-space," *Applied Computational Electromagnetics Society (ACES) Journal*, vol. 25, no. 11, pp. 936-946, 2010.

[16] J. P. Berenger, "A perfectly matched layer for the absorption of electromagnetic waves," *J. Comput. Phys*., vol. 114, pp. 185-200, Oct. 1994.

[17] F. Collino, "Perfectly matched absorbing layers for the paraxial equations," *J. Comp. Phys*., 94:1~29, 1991.

[18] X. F. Li, Y. J. Xie, P. Wang, and T. M. Yang, "High-frequency method for scattering from electrically large conductive targets in half-space," *IEEE Antennas and Wireless Propagation Letters*, vol. 6, pp. 259-262, 2007.

[19] L. Cao, B. Wei, and D. B. Ge, "Computation of far radiation field of an arbitrarily oriented dipole above layered anisotropic half space," *Waves Random Complex*, vol. 23, no. 4, pp. 446-460, 2013.

[20] W. C. Chew, *Waves and Fields in Inhomogeneous Media*, New York: IEEE Press, 1995.

Zi He received the B.Sc. degree in Electronic Information Engineering from the School of Electrical Engineering and Optical Technique, Nanjing University of Science and Technology, Nanjing, China, in 2011.

She is currently working towards the Ph.D. degree in Electromagnetic Fields and Microwave Technology at the School of Electrical Engineering and Optical Technique, Nanjing University of Science and Technology. Her research interests include antenna, RF-integrated circuits, and computational electromagnetics.

Ting Su was born in Anhui Province, China, in 1985. She received the B.Sc. degree in Communication Engineering from the School of Electrical Engineering and Optical Technique, Nanjing University of Science and Technology, Nanjing, China, in 2006.

She is currently working towards the Ph.D. degree in Electromagnetic Fields and Microwave Technology at the School of Electrical Engineering and Optical Technique, Nanjing University of Science and Technology. Her research interests include antenna, RF-integrated circuits, and computational electromagnetics.

Rushan Chen (M'01) was born in Jiangsu, China. He received the B.Sc. and M.Sc. degrees from the Department of Radio Engineering, Southeast University, China, in 1987 and 1990, respectively, and the Ph.D. degree from the Department of Electronic Engineering, City University of Hong Kong, in 2001.

He joined the Department of Electrical Engineering, Nanjing University of Science and Technology (NJUST), China, where he became a Teaching Assistant in 1990 and a Lecturer in 1992. Since September 1996, he has been a Visiting Scholar with the Department of Electronic Engineering, City University of Hong Kong, first as Research Associate, then as a Senior Research Associate in July 1997, a Research Fellow in April 1998, and a Senior Research Fellow in 1999. From June to September 1999, he was also a Visiting Scholar at Montreal University, Canada.

In September 1999, he was promoted to Full Professor and Associate Director of the Microwave and Communication Research Center in NJUST, and in 2007, he was appointed as the Head of the Department of Communication Engineering, NJUST. He was appointed as the Dean in the School of Communication and Information Engineering, Nanjing Post and Communications University in 2009. And in 2011, he was appointed as Vice Dean of the School of Electrical Engineering and Optical Technique, NJUST. Currently, he is a Principal Investigator of more than 10 national projects. His research interests mainly include computational electromagnetics, microwave integrated circuit and nonlinear theory, smart antenna in communications and radar engineering, microwave material and measurement, RF-integrated circuits, etc. He has authored or co-authored more than 260 papers, including over 180 papers in international journals.

Chen is an expert enjoying the special government allowance, member of Electronic Science and Technology Group, Fellow of the Chinese Institute of Electronics (CIE), Vice-Presidents of Microwave Society of CIE and IEEE MTT/APS/EMC Nanjing Chapter and an Associate Editor for the International Journal of Electronics. He was also the recipient of the Foundation for China Distinguished Young Investigators presented by the China NSF, a Cheung Kong Scholar of the China Ministry of Education, New Century Billion Talents Award. Besides, he received several Best Paper Awards from the National and International Conferences and Organizations. He serves as the Reviewer for many technical journals, such as the IEEE Transactions on Antennas and Propagation, the IEEE Transactions on Microwave Theory and Techniques, Chinese Physics, etc.

Application of an IE-Based Domain Decomposition Method for Analysis of Planar Microstrip Array Structures: Meshless Approach

B. Honarbakhsh [1] and A. Tavakoli [2,3]

[1] Department of Electrical Engineering
Shahid Beheshti University, Tehran, IRAN
b_honarbakhsh@sbu.ac.ir

[2] Department of Electrical Engineering
[3]Institute of Communications Technology and Applied Electromagnetics
Amirkabir University of Technology (Tehran Polytechnic), Tehran, IRAN
tavakoli@aut.ac.ir

Abstract ─ In this paper, application of an integral equation based domain decomposition method (DDM), developed for numerical solution of one-dimensional Fredholm integral equations of the second kind, is extended to electric field and mixed potential integral equations in two dimensions. Even though the original DDM was developed based on the Nyström method, results of the present work shows that meshfree approach can also be utilized. The extended DDM is employed for efficient meshfree analysis of planar microstrip array structures in the sense of reduced-size shape function and stiffness matrices. Results are validated by method of moments.

Index Terms ─ Array, domain decomposition, EFIE, meshfree, microstrip, MPIE.

I. INTRODUCTION

The purpose of Schwarz, when developed the domain decomposition method (DDM), was solution of boundary value problems over non-canonical domains [1]. Currently, this method follows diverse targets which the most famous of them is parallel processing [2]. In this application, the problem is decomposed to several smaller size problems and each of them is passed to a processor of a parallel processing architecture. DDMs are also a mean for hybridizing different numerical methods, where each domain of the problem is analyzed by its own proper numerical method [3]. The said two applications of DDMs are independent of numerical method(s) used for discretization of the original problem domain. Besides, DDMs are helpful in efficient solution of problems by meshfree methods (MFMs), at least, from two aspects. First, when using radial basis functions in a problem with large number of nodes, application of DDMs leads to several small size shape function matrices with relatively low order of condition numbers, which in turn, increases the efficiency of the interpolation process [4]. Second, noting to intrinsic deficiency of meshfree methods in handling problems with step-wise constitutive parameters, DDMs can be used to decouple different media and thus, significantly improve the efficiency of MFMs in the sense of convergence [5]. Currently, DDMs are mostly developed for solution of partial differential equations, with some few ones for integral equations [6-11]. It is worth mentioning that domain decomposition methods, regardless of their application, can be implemented in serial or parallel, especially, when the purpose of their application is not parallel processing.

In this paper, the DDM proposed in [11] is arranged for efficient meshfree solution of planar microstrip array structures in the sense of reduced-size shape function and stiffness matrices. This DDM is originally developed for numerical solution of one-dimensional Fredholm integral equations of the second kind based on the Nyström method. Results of the present work show that meshfree approach can also be utilized. The main claims of the present work are: first, the said DDM can be generalized to handle electric field integral equation (EFIE) and mixed potential integral equation (MPIE) in two dimensions. Second, it can be applied to the meshless collocation method and thus, its usage is not restricted to the Nyström method. It should be noted that this DDM is non-overlapping; therefore, it is best fitted to handle array structures.The results are validated by method of moments (MoM).

II. OVERVIEW OF THE OIRIGNAL IDEA

In this section, the DDM proposed in [11] is briefly introduced by considering the following IE:

$$\lambda u(x)+\int_{\Omega} u(x')K(x,x')dx' = f(x), \quad x\in\Omega, \qquad (1)$$

where Ω, u, f, K and λ are, respectively, problem domain,

Submitted On: October 15, 2014
Accepted On: June 19, 2015

unknown function, excitation function, equation kernel and a scalar constant. Assume:

$$\begin{cases}\Omega=\Omega_1\bigcup\Omega_2\\ \Omega_1\bigcap\Omega_2=\varnothing\end{cases}. \tag{2}$$

This means that the problem domain is partitioned to two sub-domains. In addition, assume:

$$u(x)=\begin{cases}u_1(x), & x\in\Omega_1\\ u_2(x), & x\in\Omega_2\end{cases}. \tag{3}$$

Thus, (1) can be re-written as:

$$\begin{aligned}\lambda u(x)&+\int_{\Omega_1}u_1(x')K(x,x')dx'\\ &+\int_{\Omega_2}u_2(x')K(x,x')dx'\\ &=f(x),\quad x\in\Omega.\end{aligned} \tag{4}$$

As well, let:

$$f(x)=\begin{cases}f_1(x), & x\in\Omega_1\\ f_2(x), & x\in\Omega_2\end{cases}. \tag{5}$$

Therefore, solution of (1) can be obtained by solution of the following system of IEs [11]:

$$\begin{cases}\lambda u_1(x)+\int_{\Omega_1}u_1(x')K(x,x')dx'=h_1(x), & x\in\Omega_1\\ \lambda u_2(x)+\int_{\Omega_2}u_2(x')K(x,x')dx'=h_2(x), & x\in\Omega_2\end{cases}, \tag{6}$$

where:

$$\begin{cases}h_1(x)=f_1(x)-\int_{\Omega_2}u_2(x')K(x,x')dx', & x\in\Omega_1\\ h_2(x)=f_2(x)-\int_{\Omega_1}u_1(x')K(x,x')dx', & x\in\Omega_2\end{cases}, \tag{7}$$

which states that solution of (1) over Ω can be found by solution of (6) wherein, its first equation is over Ω_1, only, and its second equations is over Ω_2, only. Numerical solution of the (6) can be obtained iteratively by choosing $u_1^{(0)}$ as an initial guess for u_1 and evaluating its value at the kth iteration from:

$$\begin{cases}h_2^{(k-1)}(x)=f_2(x)\\ \quad-\int_{\Omega_1}u_1^{(k-1)}(x')K(x,x')dx', & x\in\Omega_2\\ \lambda u_2^{(k-1/2)}(x)+\int_{\Omega_2}u_2^{(k-1/2)}(x')K(x,x')dx'\\ \quad=h_2^{(k-1)}(x), & x\in\Omega_2\\ h_1^{(k-1/2)}(x)=f_1(x)\\ \quad-\int_{\Omega_2}u_2^{(k-1/2)}(x')K(x,x')dx', & x\in\Omega_1\\ \lambda u_1^{(k)}(x)+\int_{\Omega_1}u_2^{(k)}(x')K(x,x')dx'\\ \quad=h_1^{(k-1/2)}(x), & x\in\Omega_1\end{cases}, \tag{8}$$

for k = 1, 2, …. The solution can also be computed by starting from an initial guess for u_2. Extension of the method to more sub-domains is straightforward.

III. GENERALIZATION OF THE ORIGINAL DDM TO 2D-EFIE AND 2D-MPIE

The formulation reported in this section is restricted to planar microstrip structure. Consider two equi-plane non-overlapping microstrip circuits as depicted in Fig. 1. The global domain and perimeter of the structure are Ω and $\partial\Omega$, respectively (not shown in the figure). Unit normal vectors to Ω and $\partial\Omega$ are **n** (normal to the paper) and **m**, respectively. It is assumed that the structure is perfect electric conductor, placed on the *xy* plane and is excited by the field $\mathbf{E}^{\mathrm{i}}$, which induces the surface current density $\mathbf{J}_{\mathrm{s}}$ on the conductors.

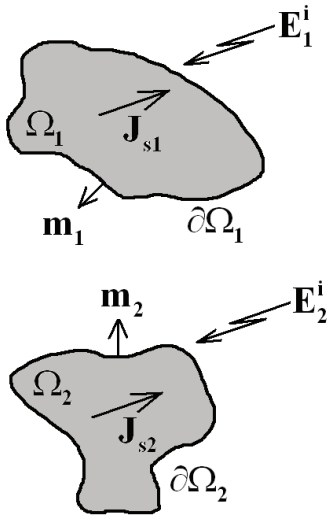

Fig. 1. Two equi-plane non-overlapping microstrip circuits.

Equations governing $\mathbf{J}_{\mathrm{s}}$ in the EFIE and MPIE formulations are:

$$\begin{cases}\mathbf{n}\times O\left[\mathbf{J}_{\mathrm{s}}(\boldsymbol{\rho})\right]=\mathbf{n}\times\mathbf{E}^{\mathrm{i}}(\boldsymbol{\rho}), & \boldsymbol{\rho}\in\Omega\\ \mathbf{m}\cdot\mathbf{J}_{\mathrm{s}}(\boldsymbol{\rho})=0, & \boldsymbol{\rho}\in\partial\Omega\end{cases}, \tag{9}$$

with:

$$O(\cdot)=\begin{cases}j\omega\mu_0\left(1+k_0^{-2}\nabla\nabla\cdot\right)\int_\Omega\overline{\overline{\mathbf{G}}}_A(\boldsymbol{\rho},\boldsymbol{\rho}')\cdot(\cdot)\,\mathrm{d}\Omega, & \text{2D-EFIE}\\ j\omega\mu_0\int_\Omega\overline{\overline{\mathbf{G}}}_A(\boldsymbol{\rho},\boldsymbol{\rho}')\cdot(\cdot)\,\mathrm{d}\Omega\\ \quad-\left(j\omega\varepsilon_0\right)^{-1}\nabla\int_\Omega G_V(\boldsymbol{\rho},\boldsymbol{\rho}')\nabla'\cdot(\cdot)\,\mathrm{d}\Omega, & \text{2D-MPIE}\end{cases}, \tag{10}$$

where $\overline{\overline{\mathbf{G}}}_A$ and G_V are dyadic and scalar Green's function of the microstrip substrate, respectively [12]. Following the previous section, let:

$$\mathbf{J}_{\mathrm{s}}=\begin{cases}\mathbf{J}_{\mathrm{s1}}, & \boldsymbol{\rho}\in\Omega_1\\ \mathbf{J}_{\mathrm{s2}}, & \boldsymbol{\rho}\in\Omega_2\end{cases}, \tag{11}$$

and

$$\mathbf{m}=\begin{cases}\mathbf{m}_1, & \boldsymbol{\rho}\in\partial\Omega_1\\ \mathbf{m}_2, & \boldsymbol{\rho}\in\partial\Omega_2\end{cases}, \tag{12}$$

and

$$\mathbf{E}^{\mathrm{i}}=\begin{cases}\mathbf{E}_1^{\mathrm{i}}, & \boldsymbol{\rho}\in\Omega_1\\ \mathbf{E}_2^{\mathrm{i}}, & \boldsymbol{\rho}\in\Omega_2\end{cases}, \tag{13}$$

and

$$\begin{cases}\mathbf{h}_1(\boldsymbol{\rho})=\mathbf{E}_1^{\mathrm{i}}(\boldsymbol{\rho})-O\left[\mathbf{J}_{\mathbf{s}2}(\boldsymbol{\rho})\right], & \boldsymbol{\rho}\in\Omega_1\\ \mathbf{h}_2(\boldsymbol{\rho})=\mathbf{E}_2^{\mathrm{i}}(\boldsymbol{\rho})-O\left[\mathbf{J}_{\mathbf{s}1}(\boldsymbol{\rho})\right], & \boldsymbol{\rho}\in\Omega_2\end{cases}. \tag{14}$$

Thus, taking initial guess for $\mathbf{J}_{s1}$, unknown current densities $\mathbf{J}_{s1}$ and $\mathbf{J}_{s2}$ can be iteratively found from:

$$\begin{cases}\mathbf{h}_2^{(k-1)}(\boldsymbol{\rho})=\mathbf{E}_2^{\mathrm{i}}(\boldsymbol{\rho})-O\left[\mathbf{J}_{\mathbf{s}1}^{(k-1)}(\boldsymbol{\rho})\right], & \boldsymbol{\rho}\in\Omega_2\\ \begin{cases}\mathbf{n}\times O\left[\mathbf{J}_{\mathbf{s}2}^{(k-1/2)}(\boldsymbol{\rho})\right]=\mathbf{n}\times\mathbf{h}_2^{(k-1)}(\boldsymbol{\rho}), & \boldsymbol{\rho}\in\Omega_2\\ \mathbf{m}_2\cdot\mathbf{J}_{\mathbf{s}2}^{(k-1/2)}(\partial\Omega_2)=0,\end{cases}\\ \mathbf{h}_1^{(k-1/2)}(\boldsymbol{\rho})=\mathbf{E}_1^{\mathrm{i}}(\boldsymbol{\rho})-O\left[\mathbf{J}_{\mathbf{s}2}^{(k-1/2)}(\boldsymbol{\rho})\right], & \boldsymbol{\rho}\in\Omega_1\\ \begin{cases}\mathbf{n}\times O\left[\mathbf{J}_{\mathbf{s}1}^{(k)}(\boldsymbol{\rho})\right]=\mathbf{n}\times\mathbf{h}_1^{(k-1/2)}(\boldsymbol{\rho}), & \boldsymbol{\rho}\in\Omega_1\\ \mathbf{m}_1\cdot\mathbf{J}_{\mathbf{s}1}^{(k-1/2)}(\partial\Omega_1)=0,\end{cases}\end{cases}, \tag{15}$$

for $k = 1, 2, \ldots$.

IV. NUMERICAL RESULTS

In this section, the generalized DDM is applied to three microstrip array structures. The meshfree collocation method proposed in [13] is used for discretization of the problem domains. Results obtained from the first two structures are compared with the Agilent® Momentum® 2009, and result of the last one is validated by FEKO® suite 5.5. Convergence curves corresponding to DDM are generated based on relative error of successive iterations, defined by:

$$r_e^{(k)}=\left\| u^{(k+1)}-u^{(k)}\right\| \Big/ \left\| u^{(k)}\right\|, \tag{16}$$

where $\|u\|=\left(\int_\Omega |u|^2\, d\Omega\right)^{1/2}$.

A. Two-element array

This structure consists of two line-fed patch antennas, placed vertically apart each other at distance d, as depicted in Fig. 2. Each array element is a line-fed patch antenna, similar to one introduced in [13]. The excited element is the element number one. For investigating the effect of different parameters on the convergence trend, the array is analyzed for two different vertical offsets; *i.e.*, d = 20 and 2.5 mm. Simulated S-parameter of the excited element at d = 20 mm is reported in Fig. 3.

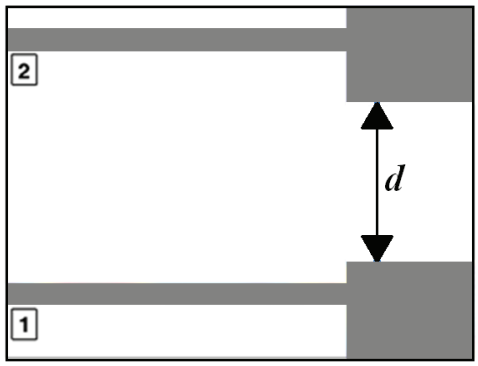

Fig. 2. Arrangement of the two-element array.

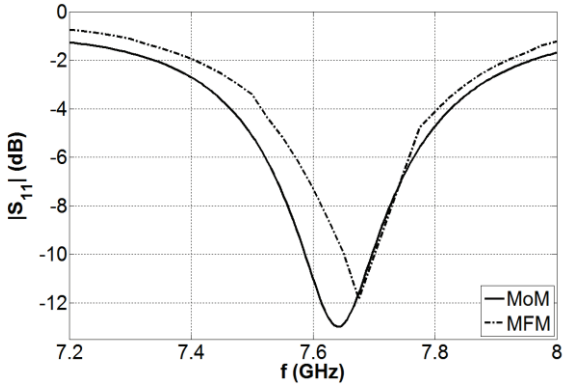

Fig. 3. Two-element array: $|S_{11}|$ at d = 20 mm.

The effect of initial guess on convergence is reported in Fig. 4, where analysis is performed at the antenna resonance frequency; *i.e.*, 7.675 GHz. It can be observed that the convergence is affected by the initial guess. However, the overall convergence of the method seems to be independent of it. The zero-valued initial vector shows faster convergence. Thus, hereafter, all initial guesses will be taken to be zero.

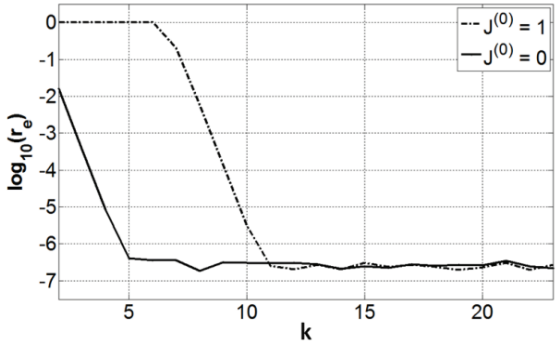

Fig. 4. Two-element array: effect of initial guess on DDM convergence at d = 20 mm.

The current distribution over the elements at $d = 20$ mm are reported in Fig. 5, wherein for better visualization of the coupling effect, it is also depicted in logarithmic scale.

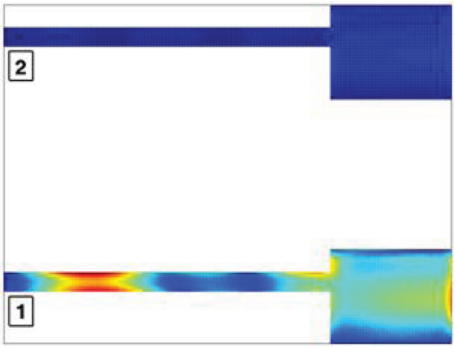

(a)

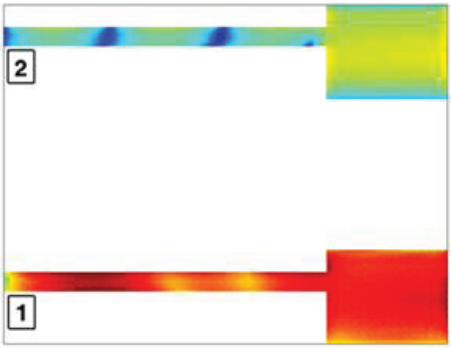

(b)

Fig. 5. Two-element array: current distribution at $d = 20$ mm: (a) linear scale, (b) logarithmic scale.

To study the effect of element coupling on the convergence, the array is analyzed at 2.5 mm distance, which ensures considerable EM interaction. The S-parameter of the exited element and its corresponding convergence curves are reported in Figs. 6 and 7, respectively.

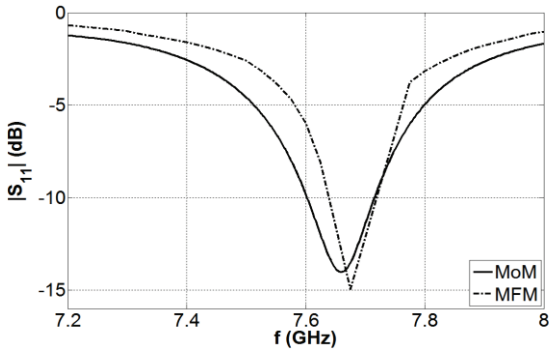

Fig. 6. Two-element array: $|S_{11}|$ at $d = 2.5$ mm.

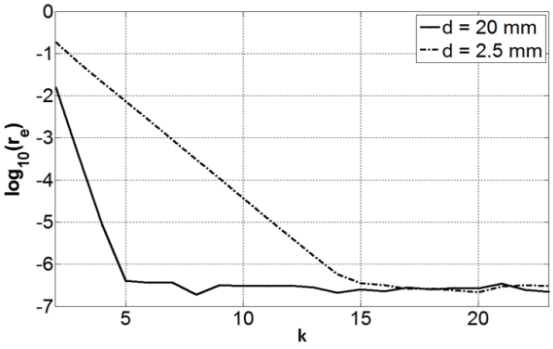

Fig. 7. Two-element array: effect of initial guess on DDM convergence at $d = 2.5$ mm.

As can be predicted, increase in the amount of coupling, defers the convergence of the method. As in the previous case, the current distributions are depicted in Fig. 8.

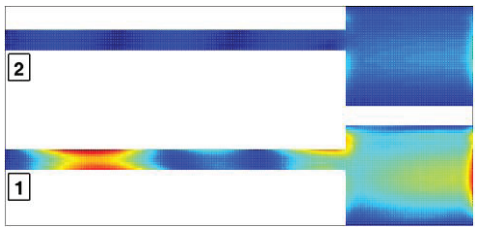

(a)

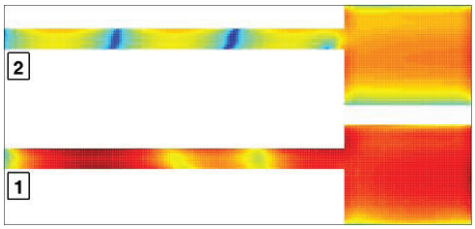

(b)

Fig. 8. Two-element array: current distribution at $d = 2.5$ mm: (a) linear scale, (b) logarithmic scale.

B. Four-element array

This array is composed from four line-fed patch antennas in a cross arrangement with $d = 8$ mm inter-element spacing. Each element of this structure is a square patch antenna with 16 mm side length, fed by a microstrip line of 2.5 mm width. The transmission line is placed 8.5 mm apart from the corner of each patch. Relative electric permittivity and thickness of the microstrip substrate are taken to be 2.2 and 0.794 mm, respectively. The arrangement of the array is depicted in Fig. 9. The excited element is again, the element number one. Such a structure can be used for generation of circular polarized waves [14].

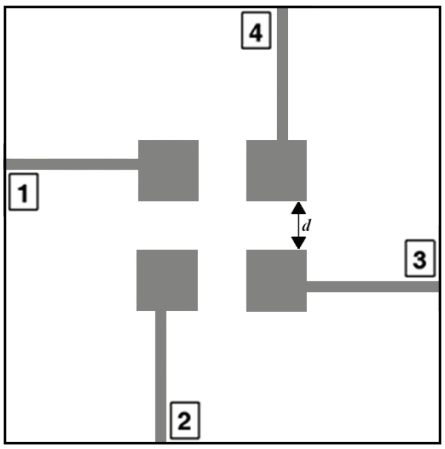

Fig. 9. Arrangement of the four-element array.

Simulated S-parameter of the excited element is reported in Fig. 10. Effect of frequency on convergence is reported in Fig. 11, wherein $f = 8.4$ GHz represents the situation which the delivered EM energy to the patch is negligible and $f = 8.825$ GHz, the antenna resonance frequency, is the frequency that the input EM energy is maximum. As can be seen, convergence of the method is deferred at the resonance frequency. The current distribution at resonance is depicted in Fig. 12.

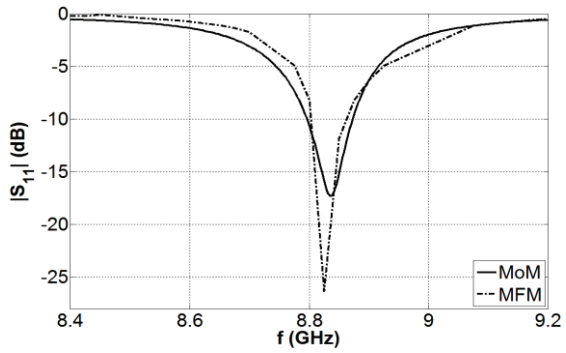

Fig. 10. Four-element array: $|S_{11}|$.

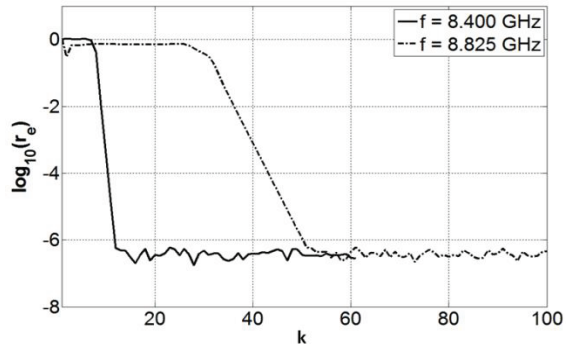

Fig. 11. Four-element array: effect of frequency on DDM convergence.

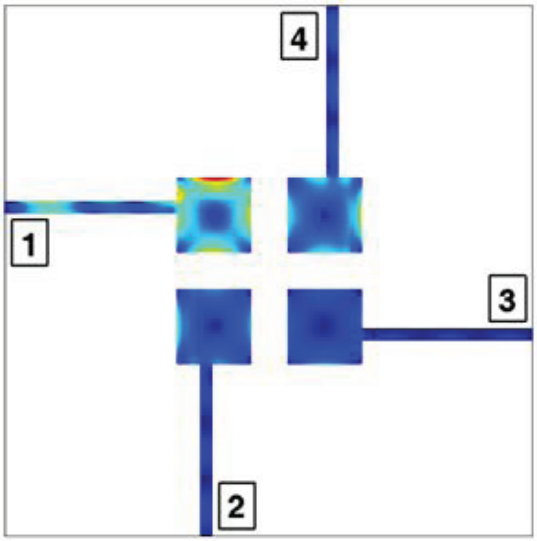

(a)

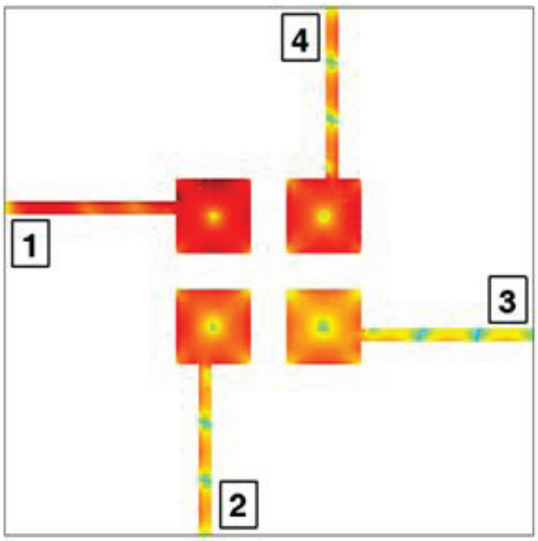

(b)

Fig. 12. Four-element array: current distribution at resonance: (a) linear scale, (b) logarithmic scale.

C. 225 element array

The last analyzed structure is a 225 element array of $\lambda/2$ square patches, suspended $\lambda/10$ above an infinite ground plane, where λ is the working wavelength. The patches are placed in a 15×15 square arrangement with $\lambda/2$ inter-element spacing. An equivalent microstrip substrate for this case has unit electric permittivity and thus, its analysis can be performed based on the EFIE formulation. This array is illuminated by a plane wave at sixty degree angle with respect to the array normal direction. The corresponding normalized scattered field and convergence curve are depicted in Figs. 13 and 14, respectively. The current distributions over the nine central elements are depicted in Fig. 15.

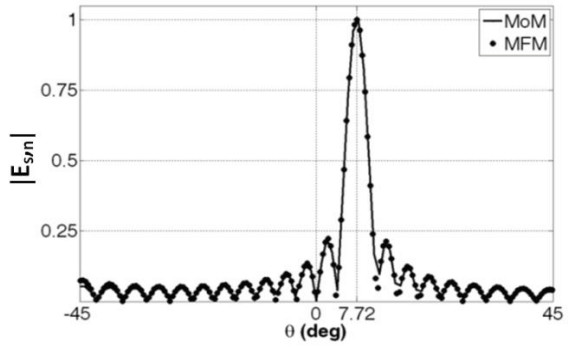

Fig. 13. 225 element array: normalized scattered field.

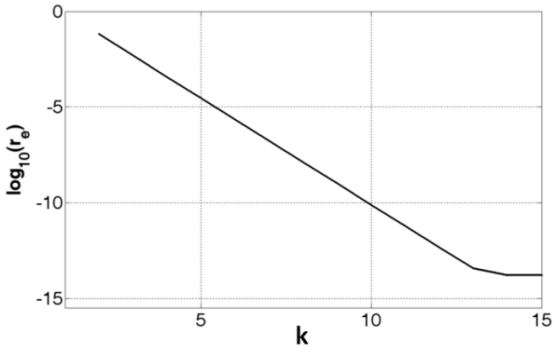

Fig. 14. 225 element array: DDM convergence curve.

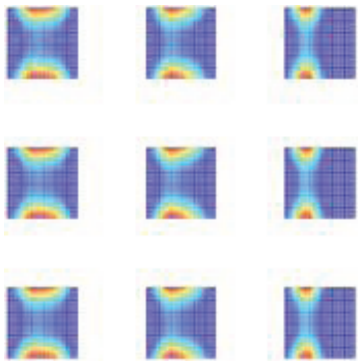

Fig. 15. 225 element array: current distribution over the nine central elements.

V. CONCLUSION

In this work, it is shown that the application of the domain decomposition method, developed for numerical solution of one-dimensional Fredholm integral equations of the second kind with Nyström discretization, can be extended for efficient meshfree analysis of planar microstrip array structures. Both of the EFIE and MPIE formulations are considered. The initial guess can affect the convergence trend, although the overall convergence seems to be independent of it. The increase of EM coupling between the elements defers the convergence of the method. The same behavior is observed when the frequency of the analysis approaches the resonance frequency of the structure. The results are validated by method of moments.

ACKNOWLEDGMENT

The authors appreciate Prof. M. Dehghan for inputs regarding meshfree methods and Dr. R. Mirzavand for inputs regarding domain decomposition methods.

REFERENCES

[1] H. A. Schwarz, "Uber einige abbildungsaufgaben," *Ges. Math. Abh.*, vol. 70, pp. 105-120, 1869.

[2] Domain Decomposition Methods in Science and Engineering, 1-12, *Proc. Int. Conf.*, *SIAM*, *AMS*, John Wiley & Son, DD Press, 1987-1999.

[3] C. Carstensen, M. Kuhn, and U. Langer, "Fast parallel solvers for symmetric boundary element domain decomposition methods," *Numer. Math.*, vol. 79, pp. 321-347, 1998.

[4] R. Schaback, "Error estimates and condition numbers for radial basis function interpolation," *Adv. Comput. Math.*, vol. 3, pp. 251-264, 1995.

[5] T. Kaufmann, "The meshless radial point interpolation method for electromagnetics," *Doctoral and Habilitation Theses*, ETH, 2011.

[6] Z. Peng, X. C. Wang, and J. F. Lee, "Integral equation based domain decomposition method for solving electromagnetic wave scattering from non-penetrable objects," *IEEE Trans. Antennas Propag.*, vol. 59, no. 9, pp. 3328-3338, 2011.

[7] J. Hu, W. Hong, H. X. Zhou, W. D. Li, and Z. Song, "An overlapped domain decomposition method for solving electromagnetic surface integral equations," *IEEE Int. Conf. Comput. Problem-Solving* (*ICCP*), pp. 1-4, 2010.

[8] E. P. Stephan and T. Tran, "Domain decomposition algorithms for indefinite hypersingular integral equations: the *h* and *p* versions," *SIAM J. Sci. Comput.*, vol. 19, no. 4, pp. 1139-1153, 1998.

[9] W. D. Li, W. Hong, and H. X. Zhou, "Integral equation-based overlapped domain decomposition method for the analysis of electromagnetic scattering of 3D conducting objects," *Microwave Opt. Tech. Lett.*, vol. 49, no. 2, pp. 265-274, 2007.

[10] P. Ylä-Oijala, V. Lancellotti, B. P. de Hon, and S. Järvenpää, "Domain decomposition methods combining surface equivalence principle and macro basis functions," *ACES J.*, vol. 25, no. 12, pp. 1017-1025, 2010.

[11] M. Campos and C. E. Perez, "A domain decomposition scheme for Fredholm integral equations using Nyström discretization," *Technical Report 98-21*, Departamento de Ingenieria Matematica, Universidad de Concepcion, 1998.

[12] J. R. Mosig, "Arbitrarily shaped microstrip structures and their analysis with a mixed potential

integral equation," *IEEE Trans. Microwave Theory Tech*., vol. MTT-36, pp. 314-323, 1988.

[13] B. Honarbakhsh and A. Tavakoli, "Analysis of thick microstrip antennas by meshfree collocation method," *ACES J*., vol. 28, no. 2, pp. 99-109, 2013.

[14] P. S. Hall, "Review of techniques for dual and circularly polarized microstrip antennas," in *Microstrip Antennas, the Analysis and Design of Microstrip antennas and Arrays*, D. M. Pozar and D. H. Schaubert, IEEE Press, pp. 107-116, 1995.

B. Honarbakhsh born in Tehran, Iran, in 1981. He received his B.S., M.S. and Ph.D. degrees in Electrical Engineering, all from Amirkabir University of Technology, in 2004, 2007 and 2012. He is currently an Assistant Professor in the Department of Electrical Engineering at Shahid Beheshti University. His research interest is numerical electromagnetics.

Ahad Tavakoli was born in Tehran, Iran, on March 8, 1959. He received his B.S. and M.S. degrees from the University of Kansas, Lawrence, and the Ph.D. degree from the University of Michigan, Ann Arbor, all in Electrical Engineering, in 1982, 1984, and 1991, respectively. He is currently a Professor in the Department of Electrical Engineering at Amirkabir University of Technology. His research interests include EMC, scattering of electromagnetic waves and microstrip antennas.

Study on Crosstalk Between Space Transient Interference Microstrip Lines Using Finite Difference Time Domain Method

Y. X. Sun, Q. Li, W. H. Yu, Q. H. Jiang, and Q. K. Zhuo

College of Information and Communications Engineering
Harbin Engineering University, Harbin 150001, China
sunyaxiu@hrbeu.edu.cn, liqian_dianci@163.com, wenyu@2comu.com, clj1-1@163.com,
zhuoqingkun@hrbeu.eu.cn

Abstract ─ In the paper, a Carson reciprocity theorem-based numerical method is proposed to analyze the crosstalk of space transient interference microstrip lines. Firstly, the proposed method is realized via solving the coupling voltage between the space transient interference and the microstrip lines by the use of Carson reciprocity theorem. Then the crosstalk between the microstrip lines caused by the coupling voltage is studied based on the finite difference time domain (FDTD) method. Lastly, compared with the Baum-Liu-Tesche (BLT) equation method, the proposed method reduces the computational complexity without solving the complex scattering field. In this paper, coupling between a dipole and a microstrip line will be considered and its coupling model will be given. FDTD and the parasitic parameter model between the microstrip lines are used to get the crosstalk. In addition, the crosstalk between the microstrip lines caused by the space transient interference is analyzed in comparison with the impedance match and mismatch of the terminals. The simulated results show that the voltages of the reflection and crosstalk which are on the victim line with mismatched loads are larger than that with matched loads, and the fluctuate time of the signal on the victim line with mismatched loads is over two times than that with matched loads, which help to verify the effectiveness of the proposed method. Moreover, when we analyze the electromagnetic problems on the surface of the arbitrary shaped ideal conductor, the image method is unavailable because the surface of ideal conductor is not infinite, while the analytic method is unavailable either, on account of the boundary of the ideal conductor is irregular. So the conventional approach is difficult to solve the problems, but the proposed method can work well for the problems due to the fact that it has nothing to do with the boundary shape, and it is only connected with the source and its field. Therefore, the proposed method is suitable for a wide range.

Index Terms ─ Carson reciprocity theorem, crosstalk, FDTD, space transient interference.

I. INTRODUCTION

Printed circuit board has been widely applied to various kinds of electronic devices due to its small size and high integration. With the rapid development of integrated circuit technologies, the PCB has been developed to carry out the high density, high speed and multiple stratification, which may cause electromagnetic coupling in high frequency and signal integrity problems such as ringing, overshoot, and crosstalk and so forth, Among these signal integrity problems, crosstalk is one of the most serious issues, which has been widely studied.

Crosstalk has been extensively researched and reported [1-8]. Shahid studied on the model structures inside the coupled microstrip lines and their correlation with crosstalk between the microstrip lines by using FDTD and singular value decomposition methods [4]. Lee and Jung investigated the crosstalk in parallel high speed interfaces [5].

However, the space electromagnetic interference is ignored in these reported results. The coupling between the space electromagnetic interference and transmission lines has been discussed [9-13]. A coupling analysis method is proposed based on the BLT equation to study the coupling terminal response between electromagnetic wave and microstrip line [9]. The time-domain variant of generalized telegrapher equations for transient electromagnetic coupling is proposed to analyze a finite-length wire above a lossy half-space [10]. Transmission line (TL) applied in lightning electromagnetic field coupling has been reported [13]. However, these proposed methods have a high computational complexity. And then the researchers carried on the further research about this problem [14-19]. Pual proposed a SPICE model that is used to predict the voltage and currents of the multiconductor transmission line (MTL) excited by an electromagnetic field [14]. Gad proposed a new algorithm to analyze the electromagnetic (EM) coupling for non-uniform multiconductor

Submitted On: January 5, 2015
Accepted On: June 4, 2015

transmission lines based on Maxwell equations [15]. Canavero gave an efficient iterative solution in the frequency domain for electromagnetic pulse (EMP) coupling to multiconductor transmission line (MTL) based on distributed analytic representation [16]. However, the crosstalk between microstrip lines caused by the coupling voltage has not been discussed in these researches.

For these reasons, a new method is proposed to calculate the crosstalk caused by the coupling voltage between space transient interference and transmission lines on the basis of the Carson reciprocity theorem. The proposed method avoids calculating the complex scattering field, which reduces the computational complexity. Moreover, the proposed method is effective to deal with the complex boundary. We get the crosstalk voltage between the microstrip lines by the use of FDTD and the parasitic parameter mode. In addition, the space transient interference of the microstrip lines is discussed in comparison with the impedance match and mismatch of the terminals. The simulated results show that the voltage of the reflection and crosstalk on the victim line with mismatched loads are larger than that with matched loads, and the fluctuate time of the signal on the victim line with mismatched loads is over two times than it with matched loads, which help to verify the accuracy of the proposed method.

II. SPACE TRANSIENT INTERFERENCE AND MICROSTRIP LINES COUPLING ANALYSIS BASED ON CARSON RECIPROCITY THEOREM

Carson reciprocity theorem has been used to describe the relationship between the two different fields, which are given by two different field sources. A typical example shown in Fig. 1 is considered to discuss the Carson reciprocity theorem. Here, we consider a volume Ω, which is filled with linear dielectric. Additionally, two current source $\vec{J}_a$ and $\vec{J}_b$ are distributed in the sub-volumes Ω_2 and Ω_1. The electric field and magnetic field are $\vec{E}_a$, $\vec{H}_a$ and $\vec{E}_b$, $\vec{H}_b$ respectively.

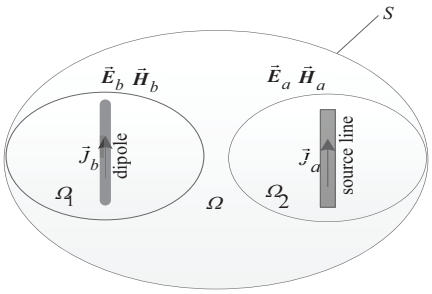

Fig. 1. Description of Carson reciprocity theorem.

According to the vector equation:

$$\nabla\cdot(\vec{A}\times\vec{B})=\vec{B}\cdot(\nabla\times\vec{A})-\vec{A}\cdot(\nabla\times\vec{B}), \tag{1}$$

where $\vec{A}$ and $\vec{B}$ are the arbitrary vectors. Combining Fig. 1 with formula (1), we can get the following equations in Ω:

$$\nabla\cdot(\vec{E}_a\times\vec{H}_b)=\vec{H}_b\cdot(\nabla\times\vec{E}_a)-\vec{E}_a\cdot(\nabla\times\vec{H}_b), \tag{2}$$

$$\nabla\cdot(\vec{E}_b\times\vec{H}_a)=\vec{H}_a\cdot(\nabla\times\vec{E}_b)-\vec{E}_b\cdot(\nabla\times\vec{H}_a). \tag{3}$$

According to the Maxwell equations in frequency domain, we can obtain:

$$\begin{cases}\nabla\times\vec{E}=-\mathrm{j}w\mu\vec{H}\\ \nabla\times\vec{H}=\vec{J}+\mathrm{j}w\varepsilon\vec{E}\end{cases}. \tag{4}$$

On the basis of the Maxwell equation and the formula (2), (3), we get:

$$\nabla\cdot[(\vec{E}_a\times\vec{H}_b)-(\vec{E}_b\times\vec{H}_a)]=\vec{E}_b\cdot\vec{J}_a-\vec{E}_a\cdot\vec{J}_b, \tag{5}$$

where $\vec{J}_a$ is the current source of source line, and $\vec{J}_b$ is the current source of the dipole. Considering formula (5) and Gaussian theorem, we get:

$$\oint_S[(\vec{E}_a\times\vec{H}_b)-(\vec{E}_b\times\vec{H}_a)]\cdot dS=\int_\Omega(\vec{E}_b\cdot\vec{J}_a-\vec{E}_a\cdot\vec{J}_b)\,d\Omega. \tag{6}$$

In formula (6), S is the boundary of Ω. When Ω is an infinite space, S can be regarded as an infinite surface of a sphere. Thus, the electromagnetic wave on S is TEM wave, which satisfies $\vec{E}=Z\vec{H}\times\vec{e}_r$, where Z is wave impedance and $\vec{e}_r$ is unit vector. Then, the integration of left hand of formula (6) is zero. Thus, the right hand of formula (6) can be written as:

$$\int_\Omega\vec{E}_b\cdot\vec{J}_a d\Omega=\int_\Omega\vec{E}_a\cdot\vec{J}_b d\Omega, \tag{7}$$

which is the so called Carson reciprocity theorem equation. In order to better understand the coupling between microstrip lines and space transient interference, a model of microstrip line marked as source line and interference source dipole is built as shown in Fig. 2.

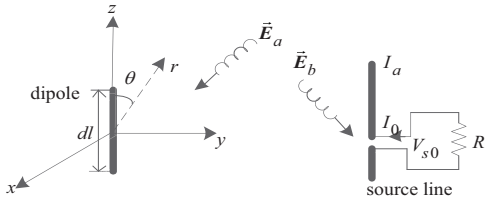

Fig. 2. Coupling model between the dipole and the source line.

The far field of the dipole is expressed as:

$$\vec{E}_b=\frac{j\omega\mu}{4\pi r}(I_b d\vec{l})e^{-jkr}\sin\theta. \tag{8}$$

Then, according to the Fig. 2, the coupling voltage on the source line caused by the dipole is below:

$$V_{s0} = \frac{1}{I_0}\int_l \vec{\boldsymbol{E}}_b \cdot I_a d\vec{l}, \tag{9}$$

where I_0 is the inspiriting current, when the source line acts as the emission antenna, I_a is the current distribution in the emission antenna. After that, we have:

$$V_{s0} = \frac{1}{I_0}\int_\Omega \vec{\boldsymbol{E}}_b \cdot \vec{\boldsymbol{J}}_a d\Omega, \tag{10}$$

where $I_b d\vec{l} = \vec{\boldsymbol{J}}_b d\Omega$ is used in (10). Considering Carson reciprocity theorem, we have:

$$V_{s0} = \frac{1}{I_0}\int_\Omega \vec{\boldsymbol{E}}_a \cdot \vec{\boldsymbol{J}}_b d\Omega, \tag{11}$$

and

$$\vec{\boldsymbol{J}}_b = \vec{\boldsymbol{E}}_b \frac{4\pi r}{j\omega\mu} e^{jkr} \frac{1}{d\Omega} \sin^{-1}\theta. \tag{12}$$

Based on (11) and (12), we have:

$$V_{s0} = \frac{1}{I_0}\vec{\boldsymbol{E}}_a \cdot \vec{\boldsymbol{E}}_b \frac{4\pi r}{j\omega\mu} e^{jkr} \sin^{-1}\theta. \tag{13}$$

By using (13), the coupling voltage V_{s0} between the source line and the dipole can be obtained.

III. CROSSTALK ANALYSIS ON MICROSTRIP LINES USING FDTD

In this section, V_{s0} is added to a homogeneous and loss-less microstrip line, as shown in Fig. 3. Here, the port 1 is excited by V_{s0}, while other ports are terminated with the linear loads. Port2, port3 and port4 are terminated with R_{L0}, R_1 and R_2 respectively. The voltage and current of the homogeneous and loss-less parallel microsrip lines meet the following telegraph equations:

$$\frac{\partial \boldsymbol{V}(z,t)}{\partial z} = -\boldsymbol{L}(z)\frac{\partial \boldsymbol{I}(z,t)}{\partial t}, \tag{14}$$

$$\frac{\partial \boldsymbol{I}(z,t)}{\partial z} = -\boldsymbol{C}(z)\frac{\partial \boldsymbol{V}(z,t)}{\partial t}. \tag{15}$$

Then combine the boundary equations of the parallel microstrip lines with the telegraph equations we can obtain the crosstalk voltage.

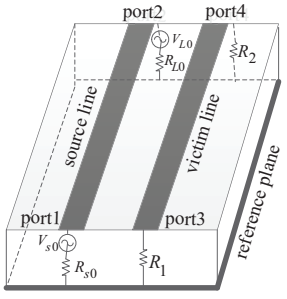

Fig. 3. Model of microstrip lines with coupling voltage V_{s0}.

Taking the FDTD into consideration, the discrete model of the microstrip lines is shown in Fig. 4, where:

$$\boldsymbol{V}_s = \begin{bmatrix} V_{s0} \\ 0 \end{bmatrix}, \quad \boldsymbol{R}_s = \begin{bmatrix} R_{s0} & 0 \\ 0 & R_1 \end{bmatrix},$$

$$\boldsymbol{V}_L = \begin{bmatrix} V_{L0} \\ 0 \end{bmatrix}, \quad \boldsymbol{R}_L = \begin{bmatrix} R_{L0} & 0 \\ 0 & R_2 \end{bmatrix}.$$

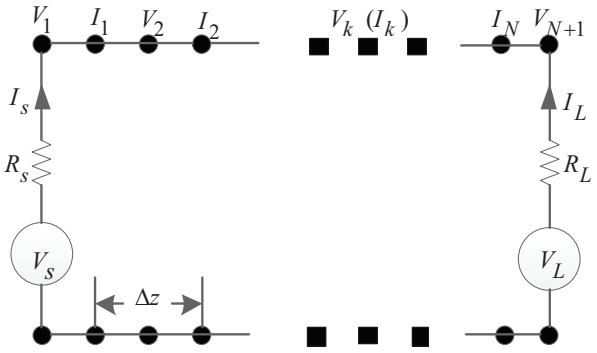

Fig. 4. Discrete model of the microstrip lines based on FDTD method.

Then, combine the Fig. 4 with the formula (15) we get the difference equations at the source end and load end as shown in formula (16), (17) respectively:

$$\frac{1}{\Delta z}(\boldsymbol{I}_1^{n+\frac{1}{2}} - \boldsymbol{I}_0^{n+\frac{1}{2}}) + \frac{1}{\Delta t}\boldsymbol{C}(\boldsymbol{V}_1^{n+1} - \boldsymbol{V}_1^{n}) = 0, \tag{16}$$

$$\frac{1}{\Delta z}(\boldsymbol{I}_{N+1}^{n+\frac{1}{2}} - \boldsymbol{I}_N^{n+\frac{1}{2}}) + \frac{1}{\Delta t}\boldsymbol{C}(\boldsymbol{V}_{N+1}^{n+1} - \boldsymbol{V}_{N+1}^{n+1}) = 0. \tag{17}$$

By considering the average $\boldsymbol{I}_0$ and $\boldsymbol{I}_{N+1}$, we have:

$$\frac{1}{\Delta z}(\boldsymbol{I}_1^{n+\frac{1}{2}} - \frac{\boldsymbol{I}_s^{n+1} + \boldsymbol{I}_s^{n}}{2}) + \frac{1}{\Delta t}\boldsymbol{C}(\boldsymbol{V}_1^{n+1} - \boldsymbol{V}_1^{n}) = 0, \tag{18}$$

$$\frac{1}{\Delta z}(\frac{\boldsymbol{I}_L^{n+1} + \boldsymbol{I}_L^{n}}{2} - \boldsymbol{I}_N^{n+\frac{3}{2}}) + \frac{1}{\Delta t}\boldsymbol{C}(\boldsymbol{V}_{N+1}^{n+1} - \boldsymbol{V}_{N+1}^{n}) = 0. \tag{19}$$

From the discussions above, the boundary equations at source end and load end as shown in formula (20), (21) respectively:

$$\boldsymbol{V}_1^{n+\frac{1}{2}}(t) = \boldsymbol{V}_s^{n+\frac{1}{2}}(t) - \boldsymbol{R}_s\boldsymbol{I}_s^{n+\frac{1}{2}}(t), \tag{20}$$

$$\boldsymbol{V}_{N+1}^{n+\frac{1}{2}}(t) = \boldsymbol{V}_L^{n+\frac{1}{2}}(t) - \boldsymbol{R}_L\boldsymbol{I}_L^{n+\frac{1}{2}}(t). \tag{21}$$

Then we have:

$$\frac{\boldsymbol{V}_1^{n+1} + \boldsymbol{V}_1^{n}}{2} = \frac{\boldsymbol{V}_s^{n+1} + \boldsymbol{V}_s^{n}}{2} - \boldsymbol{R}_s\frac{\boldsymbol{I}_s^{n+1} + \boldsymbol{I}_s^{n}}{2}, \tag{22}$$

$$\frac{\boldsymbol{V}_{N+1}^{n+1} + \boldsymbol{V}_{N+1}^{n}}{2} = \frac{\boldsymbol{V}_L^{n+1} + \boldsymbol{V}_L^{n}}{2} - \boldsymbol{R}_L\frac{\boldsymbol{I}_L^{n+1} + \boldsymbol{I}_L^{n}}{2}. \tag{23}$$

From the equations (18), (22) and (19), (23), we can obtain the following iterative equations of $\boldsymbol{V}_1$ and $\boldsymbol{V}_{N+1}$:

$$\begin{aligned}\boldsymbol{V}_1^{n+1} = {} & (\frac{\Delta z}{\Delta t}\boldsymbol{R}_s\boldsymbol{C} + \boldsymbol{E})^{-1}[(\frac{\Delta z}{\Delta t}\boldsymbol{R}_s\boldsymbol{C} - \boldsymbol{E})\boldsymbol{V}_1^{n} - \\ & 2\boldsymbol{R}_s\boldsymbol{I}_1^{n+\frac{1}{2}} + (\boldsymbol{V}_s^{n+1} + \boldsymbol{V}_s^{n})],\end{aligned} \tag{24}$$

$$\boldsymbol{V}_{N+1}^{\,n+1}=(\frac{\Delta z}{\Delta t}\boldsymbol{R}_L\boldsymbol{C}+\boldsymbol{E})^{-1}[(\frac{\Delta z}{\Delta t}\boldsymbol{R}_L\boldsymbol{C}-\boldsymbol{E})\boldsymbol{V}_{N+1}^{\,n}+ 2\boldsymbol{R}_L\boldsymbol{I}_N^{\,n+\frac{1}{2}}+(\boldsymbol{V}_L^{\,n+1}+\boldsymbol{V}_L^{\,n})], \quad (25)$$

where $\boldsymbol{C}$ and $\boldsymbol{L}$ are the distributed parameter matrices and $\boldsymbol{E}$ is identity matrix. From (14) and (15), the iterative equations of voltage and current at k segment are:

$$\boldsymbol{V}_k^{\,n+1}=\boldsymbol{V}_k^{\,n}-\frac{\Delta t}{\Delta z}\boldsymbol{C}^{-1}(\boldsymbol{I}_k^{\,n+\frac{1}{2}}-\boldsymbol{I}_{k-1}^{\,n+\frac{1}{2}}) \quad k=2,3,.....N, \quad (26)$$

$$\boldsymbol{I}_k^{\,n+\frac{3}{2}}=\boldsymbol{I}_k^{\,n+\frac{1}{2}}-\frac{\Delta t}{\Delta z}\boldsymbol{L}^{-1}(\boldsymbol{V}_{k+1}^{\,n+1}-\boldsymbol{V}_k^{\,n+1}) \quad k=1,....N, \quad (27)$$

where Δt is the temporal offset and Δz is the spatial offset, which should satisfy $\Delta t \le \frac{\Delta z}{c}$ and c is the speed of light.

IV. NUMERICAL RESULTS

In this section, the performance of the proposed method is verified in comparison with Carson reciprocity theorem and BLT. To show the performance of the Carson reciprocity theorem, coupling voltage in the time domain is studied and compared with BLT. We get the BLT equations of the load voltage:

$$\begin{bmatrix}V_{s0}\\V_{L0}\end{bmatrix}=\begin{bmatrix}1+\rho_1 & 0\\0 & 1+\rho_2\end{bmatrix}\begin{bmatrix}-\rho_1 & e^{\gamma l}\\e^{\gamma l} & -\rho_2\end{bmatrix}^{-1}\begin{bmatrix}S_1\\S_2\end{bmatrix}. \quad (28)$$

In the equation, Z_0 is the characteristic impedance and γ is the propagation constant of the microstip line, $\rho_1=\frac{R_{s0}-Z_0}{R_{s0}+Z_0}$, $\rho_2=\frac{R_{L0}-Z_0}{R_{L0}+Z_0}$. In this paper, we consider the ρ_1 and ρ_2 are zero, then we can get the $V_{s0}=\frac{S_2}{e^{\gamma l}}$. While according to the Agrawal model, we can solve:

$$S_2=-\frac{1}{2}\int_0^l e^{\gamma(l-x)}[V_s^{'}(\mathrm{x})-Z_0 I_s^{'}(\mathrm{x})]dx = e^{\gamma l}\frac{[e^{-(\gamma+jk)l}-1](Z_0+\frac{j\omega\mu}{120\pi})\vec{E}_b d}{2(\gamma+jk)}, \quad (29)$$

where

$$V_s^{'}=\vec{E}_x^{inc}(x,d)-\vec{E}_x^{inc}(x,0), \quad (30)$$

and

$$I_s^{'}=-j\omega c\int_0^l \vec{E}_z^{inc}(x,z)dz. \quad (31)$$

Here, $\vec{E}_x^{inc}$ and $\vec{E}_z^{inc}$ are the components of $\vec{E}_b$ in the x direction and z direction. l is the length of the microstrip line, d is the distance from the microstrip line to the reference plane, $k=\omega/\mathrm{c}$. Then,

$$V_{s0}=\frac{[e^{-(\gamma+jk)l}-1](Z_0+\frac{j\omega\mu}{120\pi})\vec{E}_b d}{2(\gamma+jk)}. \quad (32)$$

We make Fourier inversion for equations (13) and (32), and then we can get the waveform figure in time domain as shown in Fig. 5.

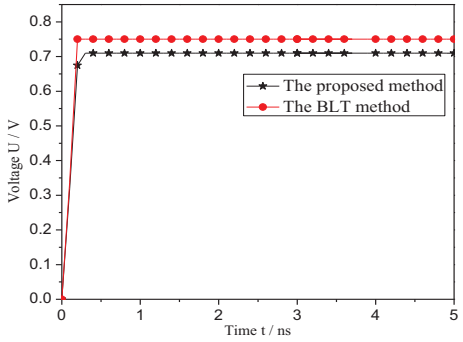

Fig. 5. Coupling voltage characteristics.

It is found from Fig. 5 that, the trend of the voltages between Carson reciprocity theorem and the BLT methods are coincident, but there is a little bit difference in the value of the voltage between the proposed method and the BLT method. As shown in formula (32), when we solve the coupling voltage V_{s0} with the BLT method, it is only considering the coupling from the field $\vec{E}_b$ to the microstrip line without considering the radiation field $\vec{E}_a$ caused by the current on the microstrip line. While the proposed method considered it. So the Carson reciprocity theorem method is more accurate to solve the coupling between space transient interference and microstrip lines. Moreover, we can see the BLT method has a complex calculation from formula (29) and (32). Since the radiation of dipole is spherical wave, the current distribution on the microstrip lines caused by the dipole is shown in Fig. 6. The line on the left side is the source line, and the right one is the victim line. It is observed that the crosstalk exists on the microstrip lines.

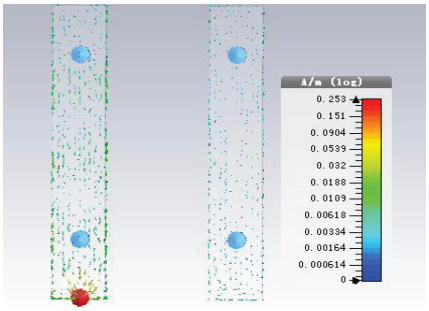

Fig. 6. Surface current distribution on the microstrip lines excited by dipole.

In the simulation, the substrate was FR4 with a relative permittivity of 4.7, loss tangent of 0.002, and substrate thickness of 1.5 mm. We set $\Delta t = 10^{-11}$s and $\Delta z = 3*10^{-3}$ m. The maximum time step was $t_{max} = 500$ in the FDTD simulation. The length of the parallel microstrip lines is set as 6 cm and the width of the microstrip lines is set as 1 mm. The distance between the two microstrip lines is 2 mm and the thickness of the microstrip lines is set as 1.4 mm. The distributed parameter matrices are:

$$\boldsymbol{L} = \begin{bmatrix} 309 & 21.7 \\ 21.7 & 309 \end{bmatrix} nH/m, \tag{33}$$

and

$$\boldsymbol{C} = \begin{bmatrix} 144 & -6.4 \\ -6.4 & 144 \end{bmatrix} pF/m. \tag{34}$$

Example 1: *All the ports with matched loads*

To solve the near-end crosstalk (NEXT) and the far-end crosstalk (FEXT) between the source line and victim lines, all the ports were matched with 50 Ω linear loads in this example. The simulated voltage of the source line was shown in Fig. 7. It can be seen that the signal transmission period on the source line without distortion is $\frac{6\times10^{-2}m}{1.524\times10^{8}m/s} = 3.9\times10^{-10}s = 0.39ns.$

Then according to the voltage of the source line, we get the voltage distribution of the victim line at near-end and far-end with HyperLynx software and Carson reciprocity theorem method as shown in Fig. 8 and Fig. 9, respectively. We can see the trend of the voltages distribution is accordant between the Carson reciprocity theorem and the HyperLynx software. This indicates that the proposed method is effective to analyze the crosstalk between the microstrip lines. But we can see the voltage appearing with fluctuation at the near-end and far-end with the Carson reciprocity theorem method, which is the meshing sparseness when we solve the voltage with the proposed method. It can be improved by increasing the grid. Then we analyzed the crosstalk of all ports with mismatched loads based on the proposed method as shown in Example 2.

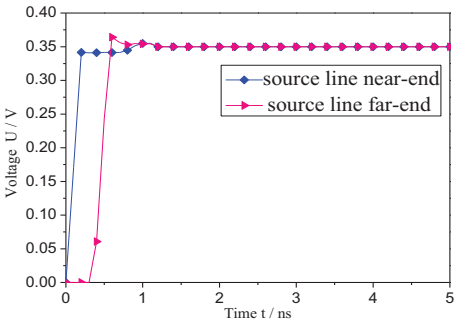

Fig. 7. Voltage distribution of source line.

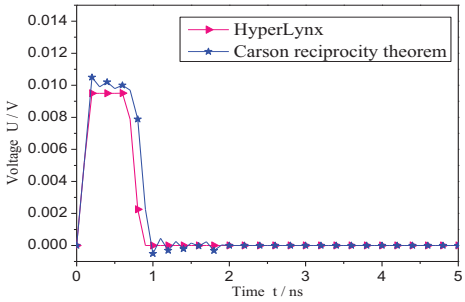

Fig. 8. Voltage distribution of victim line at near-end.

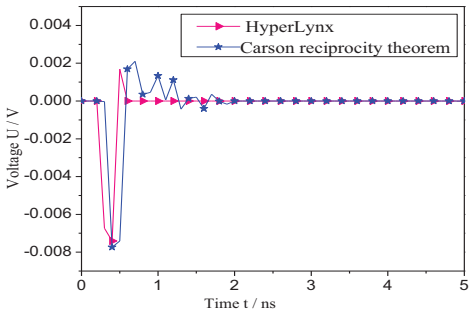

Fig. 9. Voltage distribution of victim line at far-end.

Example 2: *All ports with mismatched loads*

In this experiment, the port1 was 100 Ω, the port2 was 150 Ω, the port3 was 120 Ω and port4 was 300 Ω. The voltage of the source line and victim line were described in Fig. 10 and Fig. 11. We can see that the signal appears with serious reflection on source line in Fig. 10. In Fig. 11, the signal on victim line appeared seriously fluctuate, which is not only caused by the mismatched loads, but also caused by the crosstalk voltage from the source line. The waveform in Fig. 11 is formed by the overlap of the reflection and the crosstalk, which tends to be stable after 4 ns. It is two times longer than that in Fig. 8 and Fig. 9. Thus, we can see that the loads play a great role in the reflection and crosstalk. Additionally, if we cannot make all the ports with matched load, it can effectively reduce the reflection and crosstalk by making the source end with matched load, in the design of system.

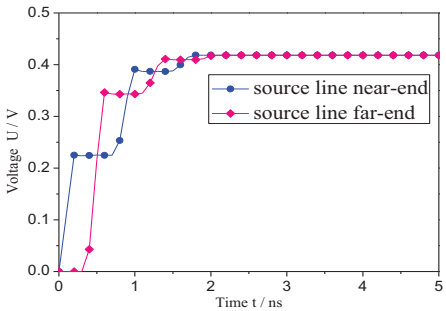

Fig. 10. Voltage distribution of source line.

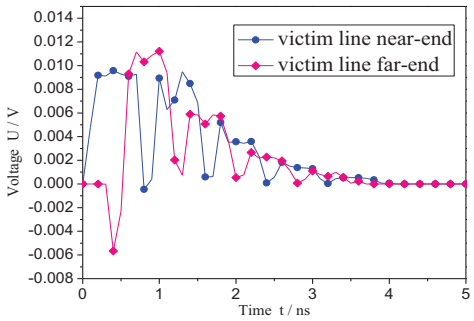

Fig. 11. Voltage distribution of victim line.

V. CONCLUSION

A new method has been proposed and investigated by using the Carson reciprocity theorem to calculate the coupling between the space transient interference and microstrip lines. We get the coincident trend in comparison with the proposed method and BLT. However, the proposed method avoids analyzing the complex scattered field, which reduces the computational complexity. Combining Carson reciprocity theorem and FDTD, we have discussed the crosstalk performance caused by the coupling voltages on the source line. Simulation results demonstrated that the voltages of the reflection and crosstalk which are on the victim line with mismatched loads are larger than that with matched loads, and the fluctuate time of the signal on the victim line with mismatched loads is over two times than it with matched loads. So the space transient interference can cause serious reflection and crosstalk. The simulation results are significant in devising systems to reduce crosstalk, reflection and enhance signal integrity.

ACKNOWLEDGMENTS

This work was supported by the National Nature Science Foundation of China under Grant 51209055, the Fundamental Research Funds for the Central Universities of China (HEUCF150818), the China Postdoctoral Science Foundation Funded Project (3236310246) and the Heilongjiang Science Funded (F2015028).

REFERENCES

[1] T. B. Jan, "Wavelet-based approach to evaluation of signal integrity," *IEEE Transaction on Industrial Electronics*, vol. 60, pp. 4590-4598, 2013.

[2] J. K. Du, "Analysis of coupling effects to PCB inside wave guide using the modified BLT equation and full-wave analysis," *IEEE Transaction on Microwave Theory and Techniques*, vol. 61, pp. 3514-3523, 2013.

[3] E. Song, "Modeling and design optimization of a wide-band passive equalizer on PCB based on near-end crosstalk and reflections for high-speed serial data transmission," *IEEE Transaction on Electromagnetic Compatibility*, vol. 52, pp. 410-420, 2010.

[4] A. Shahid, "Finite-difference time-domain analysis of electromagnetic modes inside printed coupled lines and quantification of crosstalk," *IEEE Transaction on Electromagnetic Compatibility*, vol. 51, pp. 1026-1033, 2009.

[5] K. Lee and H. K. Jung, "Serpentine microstrip lines with zero far-end crosstalk for parallel high-speed DRAM interfaces," *IEEE Transaction on Advanced Packaging*, vol. 33, pp. 552-558, 2010.

[6] M. Shin, "A wide-band passive equalizer design on PCB based on near-end crosstalk and reflections for 12.5 Gbps serial data transmission," *IEEE Microwave and Wireless Components Letters*, vol. 18, pp. 794-796, 2008.

[7] F. Buesink, "Overview of signal integrity and EMC design technologies on PCB: fundamentals and latest progress," *IEEE Transaction on Electromagnetic Compatibility*, vol. 55, pp. 624-638, 2013.

[8] Y. Peerawut, "Lightning-induced voltage over lossy ground by a hybrid electromagnetic circuit model method with cooray–rubinstein formula," *IEEE Transaction on Electromagnetic Compatibility*, vol. 51, pp. 975-985, 2009.

[9] Q. Peng, "Electromagnetic coupling terminal response for microstrip line based on BLT equation," *High Power Laser and Particle Beams*, vol. 25, pp. 1241-1246, 2013.

[10] D. Poljak, "Time-domain generalized telegrapher's equations for the electromagnetic field coupling to finite length wires above a lossy ground," *IEEE Transaction on Electromagnetic Compatibility*, vol. 54, pp. 218-223, 2012.

[11] F. Rachidi, "A review of field-to-transmission line coupling models with special emphasis to lightning-induced voltages on overhead lines," *IEEE Transaction on Electromagnetic Compatibility*, vol. 54, pp. 898-911, 2012.

[12] M. Brignone, "An effective approach for high-frequency electromagnetic field-to-line coupling analysis based on regularization techniques," *IEEE Transaction on Electromagnetic Compatibility*, vol. 54, pp. 1289-1297, 2012.

[13] M. Paolone, "Lightning electromagnetic field coupling to overhead lines: theory numerical simulations and experimental validation," *IEEE Transaction on Electromagnetic Compatibility*, vol. 51, pp. 532-547, 2009.

[14] C. R Pual, "A SPICE medal for multiconductor transmission lines excited by an incident electromagnetic field," *IEEE Transaction on Electromagnetic Compatibility*, vol. 32, pp. 342-

354, 1994.

[15] E. Gad, "Circuit-based analysis of electromagnetic field coupling with no uniform transmission lines," *IEEE Transaction on Electromagnetic Compatibility*, vol. 50, pp. 149-165, 2008.

[16] F. G. Canavero, "Analytic iterative solution of electromagnetic pulse coupling to multiconductor transmission lines," *IEEE Transaction on Electromagnetic Compatibility*, vol. 55, pp. 451-466, 2013.

[17] S. A. Pignari, "Plane-wave coupling to a twisted-wire pair above ground," *IEEE Transaction on Electromagnetic Compatibility*, vol. 53, pp. 508-523, 2011.

[18] A. Amedeo, "Electromagnetic coupling of lightning to power lines: transmission-line approximation versus full-wave solution," *IEEE Transaction on Electromagnetic Compatibility*, vol. 53, pp. 421-428, 2011.

[19] L. Qi, "Calculation of interference voltage on the nearby underground metal pipeline due to the grounding fault on overhead transmission lines," *IEEE Transaction on Electromagnetic Compatibility*, vol. 55, pp. 965-975, 2013.

Compact Band-Stop X-Band Filter Using Triple Meander-Line-Ring Defected Ground Structures

Hamid Keivani [1], Nahid Adlband [1], and Yasser Ojaroudi [2]

[1] Department of Electrical Engineering
Kazerun Branch, Islamic Azad University, Kazerun, Iran

[2] Young Researchers and Elite Club
Germi Branch, Islamic Azad University, Germi, Iran

Abstract ─ This paper work deals with design and development of compact microstrip band-stop filter (BSF) for radar applications. The microstrip filter configuration consists of a transmission line and a modified ground plane with three meander-line ring defected ground structures (DGS). The proposed microstrip filter fabricated on a *Rogers* RT/Duroid 5880 substrate with a relative dielectric constant of 2.2 and has a very small size of 10×15×0.635 mm^3. The proposed BSF has a flat impedance bandwidth of 8-12 GHz with an insertion loss which is larger than 35 dB and a return loss which is less than 0.5 dB at the center of the band-stop frequency range. The operating frequencies of the filter can be easily controlled by changing the dimensions of the meander-line rings without changing the area taken up by the structures. The introduced filter has an excellent out-of-band performance. A good agreement between measured and simulated results was obtained. The proposed filters are promising for use in wireless technologies for radar communications due to their simple structure, compact size, and excellent performance.

Index Terms ─ Band-stop filter, meander-line structure, radar system, X-band application.

I. INTRODUCTION

In modern communications, one of the important parameter is isolation between channels in a given bandwidth. Filters with different configurations are essential components in communication systems and these are generally used as signal rejection for unwanted signals and simultaneously allow the wanted signals in required bands [1]. In recent times, the design of filters has become an active research area as filtering is important when used in close proximity to other circuit components, like power amplifiers in the transmitter part and low noise amplifiers in receiver part, for various RF applications [2].

Conventionally the microwave band-stop filter (BSF) is implemented either by all shunt stubs or by series connected high-low stepped-impedance microstrip line sections. However, generally these are not easily available in microwave band due to the high impedance microstrip line and the spurious pass-bands. To remove these disadvantages, defected ground structures for microstrip lines have been presented in recent years. They have been presented in a number of different shapes for filter applications [3]-[4]. The DGS applied to a microstrip line causes a resonant character of the structure transmission with a resonant frequency controllable by changing the shape and size of the slot. This technique is suitable for periodic structures and for both band-stop and band-pass filters, e.g., [5-7].

In this paper, a novel design of microstrip band-stop filter for X-band application is proposed. The reason for the choice of meander-line-ring DGSs is that these structures provide an almost constant tight coupling with three transmission zeroes at the lower, middle and upper frequencies of X-band frequency range which are important to generate a good frequency response. The designed filter has small dimensions of 10×15×0.635 mm^3.

II. MICROSTRIP FILTER DESIGN

The proposed microstrip filter configuration is shown in Fig. 1. This band-stop filter was designed on a *Rogers* RT/Duroid 5880 substrate with 0.635 mm in thickness and with a relative dielectric constant of 2.2. For the input/output connections 50-Ohm microstrip lines are used. The microstrip band-stop filter was designed on both substrate sides by opening aperture in the ground metallization under the low-impedance transmission line. Final values of the presented band-

Submitted On: April 1, 2014
Accepted On: December 11, 2014

stop filter design parameters are specified in Table 1.

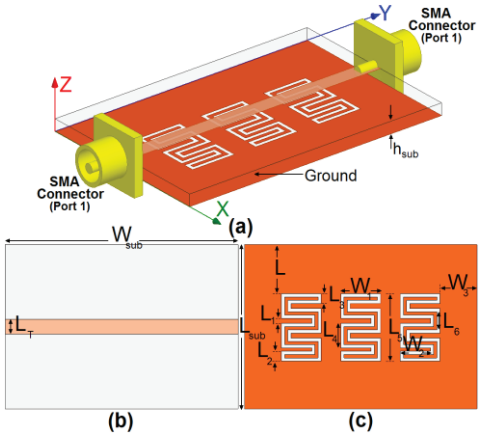

Fig. 1. Geometry of proposed microstrip band-stop filter: (a) side view, (b) top layer, and (c) bottom layer.

Table 1: The final dimensions of the filter

Parameter	Value (mm)
W_{sub}	15
L_{sub}	10
h_{sub}	0.635
W	1.25
L	3
W_1	2.5
L_1	3.55
W_2	1.9
L_2	0.6
W_3	2.5
L_3	0.6
L_4	1.5
L_5	4.1
L_6	1.1
L_T	0.9

III. RESULTS AND DISCUSSIONS

The proposed microstrip band-stop with various design parameters was constructed, and the experimental results of the S-parameter characteristics are presented and discussed. The simulated results are obtained using the Ansoft simulation software high-frequency structure simulator (HFSS) [7].

The configuration of the various structures used for simulation studies were shown in Fig. 2. S-parameter characteristics for the microstrip filter with an ordinary transmission line (Fig. 2 (a)), the filter with a single meander-line-ring slot (Fig. 2 (b)), and the proposed filter (Fig. 2 (c)) structures are compared in Fig. 3. As illustrated in Fig. 3, by these modified structures in the ground plane, three transmission zeroes at the lower, middle and upper frequencies can be achieved, which provide X-band frequency range. Good impedance matching for insertion/return loss (S_{11}/S_{21}) characteristics is generated [3-5].

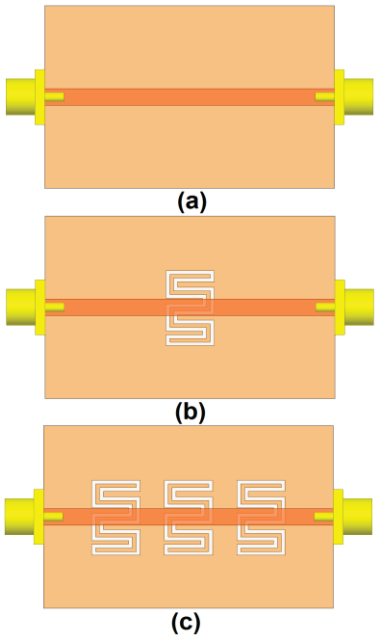

Fig. 2. (a) Basic structure (ordinary microstrip filter), (b) microstrip filter with a meander-line-ring DGS, and (c) the proposed microstrip filter structure.

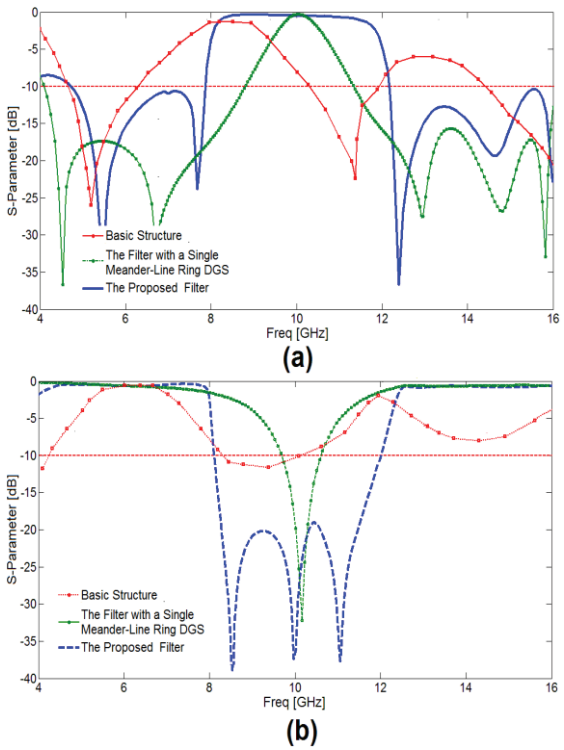

Fig. 3. Simulated S-parameters for various structures shown in Fig. 2.

Figure 4 shows the current distribution of the proposed filter at the transmission zeroes. It can be seen that using the modified meander-line ring slots as a defected ground structures have effect on the overall performance of the filter. As shown in Fig. 4 (a), at the second transmission zero resonance, the current flows are more dominant around the middle structure. The first and third zero transmission resonances at the insertion loss response of the filter (8.5 and 11 GHz) are affected from corners meander-line strutures. Figure 4 (b) and 4 (c) clearly show at the first and third zero transmission resonances, the meander-line rings at the corners side of ground plane act as half-wave resonant structures [8].

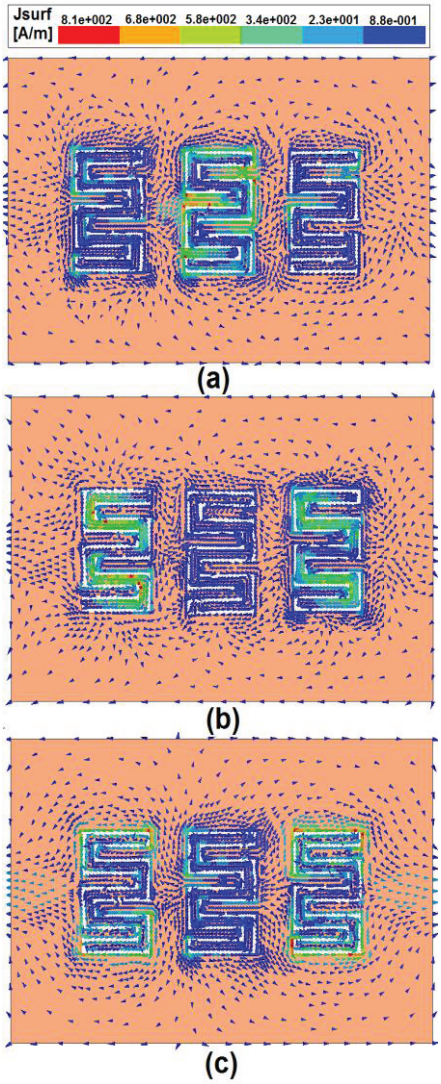

Fig. 4. Simulated surface current distributions for the proposed microstrip filter in the ground plane at: (a) 10 GHz, (b) 8.5 GHz, and (c) 11 GHz.

After checking all dimensions and final adjustments, the proposed filter with final design as shown in Fig. 5 was fabricated. After milling and drilling and plating processes, the filter is completed by adding the test port SMA connectors for measurements. The proposed filter performance is measured by using HP 8720ES network analyzer. The network analyzer is first calibrated for the operating frequency range. Measurement set-up of the proposed filter is shown in Fig. 6. The microstrip filter has good S-parameters (S_{11}/S_{21}) which are introduced to the filter response from 8 to 12 GHz.

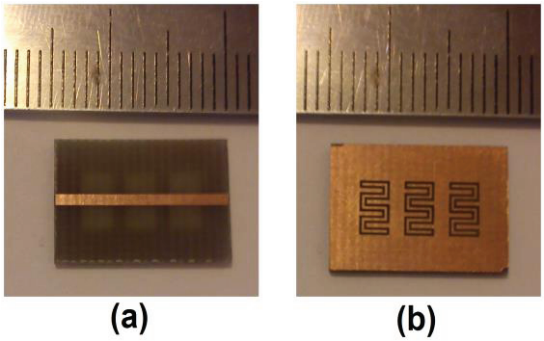

Fig. 5. Photograph of the realized printed band stop filter: (a) top view, and (b) bottom view.

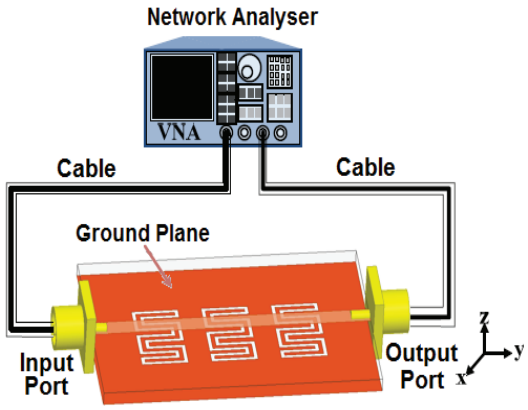

Fig. 6. The measurement setup of the proposed filter performance, using Network Analyzer.

Figure 7 shows the simulated and measured insertion and return losses of the filter. As shown in the figure, by using the proposed DGSs, we have a constant and flat impedance bandwidth at the X-band frequency range. The proposed band-stop filter has a constant and flat impedance bandwidth around of 8-12 GHz X-band with an insertion loss which is larger than 35 dB and a return loss which is less than 0.5 dB at the center of the band-stop frequency range [9].

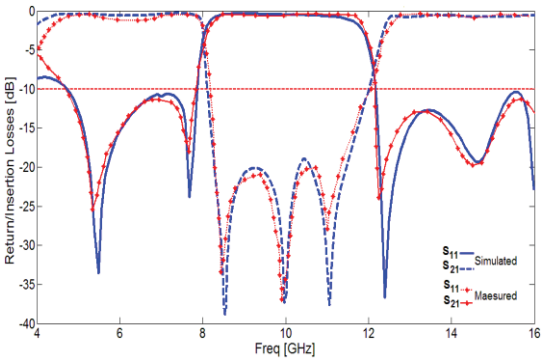

Fig. 7. Measured and simulated S-parameters for the proposed filter.

In order to investigate DGSs further, parametric analysis of W_1 and L is studied in Figs. 8 and 9, respectively. Figure 8 shows the effect of various dimension of W_1 on return loss (S_{11}). As observed in Fig. 8, with the increase of W_1, the three transmission zeroes shift to the lower frequency band. As illustrated, when the exterior widths of the meander-line DGSs (W_1) increase from 2 mm to 3 mm, the lower stop-band frequency is increases from 7.5 GHz to 11 GHz and also the upper stop-band frequency increases from 10.8 GHz to 13.7 GHz.

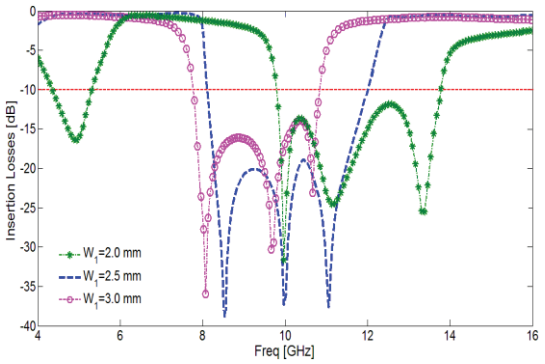

Fig. 8. Simulated insertion loss (S_{21}) characteristics of the filter for different values of W_1.

It is obvious that the variation of W_1 can change the physical length of DGSs significantly. Additionally, the zero separation approximately remains unchanged. From these results, we can conclude that the stop-band operation is controllable by changing the size of the employed meander-line DGSs.

The distance of embedded DGSs from corners of ground plane is set to L. By tuning its length, the characteristics impedance of proposed filter can be changed. Figure 9 shows the return loss characteristics of the filter with different values of L. The parametric study showing the relationship between the length of L and the corresponding characteristics impedance. As illustrated in Fig. 9, by properly tuning the dimensions and spacing of L, the proposed BSF has a flat impedance bandwidth of 8-12 GHz with a return loss which is less than 0.5 dB at the center of the band-stop frequency range. As seen, the proposed filter with L=3 mm, has a good out-of-band property in compared with different values of L.

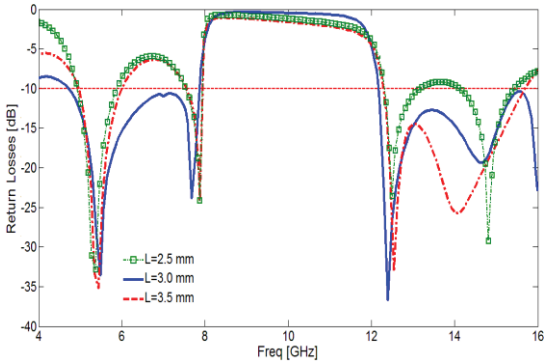

Fig. 9. Simulated return loss characteristics of the filter with different values of L.

IV. CONCLUSION

In this paper, a novel design of band-stop microstrip filter that covers frequency bandwidth of 8-12 GHz has been presented. Configuration of the presented filter consists of a transmission line and a ground plane with triple meander-line rings as a DGS. The measured results have shown that the fabricated filter has a band-stop characteristic that extends from 8 to 12 GHz. The proposed filter configuration is simple, low-profile and can be integrated into any radar system.

ACKNOWLEDGMENT

The authors are thankful to Microwave Technology (MWT) Company staff for their beneficial and professional help (www.microwave-technology.com).

REFERENCES

[1] G. L. Matthaei, L. Young, and E. M. T. Jones, *Microwave Filters, Impedance-Matching Network, and Coupling Structures*, Norwood, MA, Artech House, 1980.

[2] J. A. Kong, *Electromanetic Wave Theory*, EMW Publishing, Cambridge, 2000.

[3] K. L. Finch and N. G. Alexopoulos, "Shunt posts in microstrip transmission lines," *IEEE Trans. Microwave Theory Tech.*, vol. MMT.-38, pp. 1585-1594, 1990.

[4] D. S. La, Y. H. Lu, S. Y. Sun, N. Liu, and J. L. Zhang, "A novel compact band stop filter using defected microstrip structure," *Microw. Opt. Technol. Lett.*, vol. 53, pp. 433-435, Feb. 2011.

[5] N. Ojaroudi, "Novel design of low-profile microstrip band-stop filter (BSF) with koch fractal RSLRs," *22nd Telecommunications Forum, TELFOR 2014*, Belgrade, Serbia, Nov. 25-27, 2014.

[6] R. Habibi, Ch. Ghobadi, J. Nourinia, M. Ojaroudi, and N. Ojaroudi, "Very compact broad band-stop filter using periodic L-shaped stubs based on self-complementary structure for X-band application," *Electron. Lett.*, vol. 48, pp. 1483-1484, 2012.

[7] Ansoft High Frequency Structure Simulator (HFSS), ver. 13, Ansoft Corporation, Pittsburgh, PA, 2010.

[8] M Ojaroudi and N. Ojaroudi, "Microstrip low-pass filters by using novel defected ground structure slot with a pair of protruded T-shaped strips inside the slot," *Advanced Electromagnetics Symposium, AES 2012*, Paris, France, Apr. 16-19, 2012.

[9] N. Ojaroudi, M. Ojaroudi, and R. Habibi, "Design and implementation of very compact band-stop filter with petal-shaped stub for radar applications," *Microw. Opt. Technol. Lett*., vol. 55, pp. 1130-1132, 2013.

Tunable Bandstop Filter with Bandwidth Compensation

Qianyin Xiang, Quanyuan Feng, Xiaoguo Huang, and Dinghong Jia

School of Information Science and Technology
Southwest Jiaotong University, Chengdu, Sichuan, 610031, China
qyxiang@swjtu.edu.cn

Abstract ─ In this paper, a tunable bandstop filter with bandwidth compensation is proposed. The equivalent circuit model of the tunable capacitor network is presented to study the tunable mechanism. The electric coupling factor of the tunable capacitor network increases while the tunable capacitor increases. This mechanism can be used to compensate the bandwidth of the tunable filter. In our work, semiconductor varactor diode loaded microstrip LC resonator is adopted to design a tunable bandstop filter. Each resonator requires only one varactor diode for both central frequency and resonator coupling coefficient control. The *S*-parameters and group delays of the tunable bandstop filter are presented. The measurement shows that the -30 dB absolute bandwidth varies from 371 MHz to 305 MHz, while the central frequency of the stopband varyies from 3.195 GHz to 2.285 GHz.

Index Terms ─ Electric coupling, tunable bandstop filter.

I. INTRODUCTION

Microwave bandstop filter is one of the most important components to filter out the unwanted signals or nearby huge power signals, and avoid frequency aliasing in the intermediate frequency [1-3]. Recently, it is very popular to add tuning ability to conventional microwave components to realize electrically tunable/reconfigurable microwave components, which can well satisfy the requirements of modern multi-band and programmable wireless systems [3]-[16]. Tunable microwave bandstop filters will play a key role in the future radio frequency front-end.

Various tuning techniques have been utilized for tunable filter designs. Magnetic materials, i.e., ferrite were employed to tune the stopband. However, the magnetic bias circuit is complex and the filter size is bulky [7]. Semiconductor varactor diode [9]-[16], liquid metal [5], and micro-electro-mechanical (MEMS) [6], [8] tuned planar resonators are used in compact tunable bandstop filter designs. Recently, tunable filters with constant bandwidth or controllable bandwidth are becoming an attractive topic in this area [10]-[16]. However, few works on tunable bandstop filter with constant bandwidth or controllable bandwidth have been reported in the literature. In [15], a constant bandwidth tunable bandstop filter was designed based on a dual-band circuit with a wide passband and integrated narrow stopband. In [16], a mixed electric and magnetic coupling structure is introduced to obtain tunable bandstop filter with constant absolute bandwidth.

In this paper, a novel approach is proposed to design electrical tunable bandstop filter with bandwidth compensation. A tunable capacitor network with controllable electric coupling coefficient is proposed. Based on the simple electric coupled tunable capacitor network, the bandwidth of the bandstop filter can be compensated. The tunable bandstop filter is designed, fabricated and measured.

II. FILTER DESIGN THEORY

From the microwave filter coupling matrix theory [17], the coupling matrix between the resonators can be written as:

$$M_{i,j}=\frac{k_{i,j}f_0}{ABW}=\frac{k_{i,j}}{FBW}, \tag{1}$$

where, $k_{i,j}$ (i,j=1,2,...) is the coupling coefficient, FBW is the fractional bandwidth, ABW is the absolute bandwidth, f_0 is the center frequency.

Since the frequency response of the filter is determined by the coupling matrix, equation (1) shows that constant ABW tunable filter requires the product of coupling coefficient and center frequency is constant. It means that, the coupling coefficient should increase while the central frequency of the tunable filter decreases.

Figure 1 (a) shows a second order LC resonant network with electric coupling (C_m). The resonant frequency decreases when capacitor C increases. The coupling coefficient k can be expressed as:

$$k=k_e=\frac{C_m}{C}, \tag{2}$$

where, k_e is the electrical coupling coefficient, C is the resonant capacitance, C_m is the electrical coupling

Submitted On: April 9, 2014
Accepted On: May 25, 2015

capacitance. Since the coupling capacitor is too small to be efficiently tuned by semiconductor process in microwave band, it can be seen from equation (2) that the coupling coefficient decreases when the capacitor C increases, therefore the FBW decreases when the resonant frequency of the LC resonator decreases.

The traditional method to control the coupling coefficient is based on mixed coupling (L_m, C_m), as shown in Fig. 1 (b). Due to the cancellation of magnetic and electric coupling, the coupling coefficient can be written as [18]:

$$k \approx k_m - k_e = \frac{L_m}{L} - \frac{C_m}{C}, \tag{3}$$

where, k_m is the magnetic coupling coefficient, L is the resonant inductance, L_m is the mutual inductance. The resonant frequency decreases when capacitor C increases, and the coupling coefficient increases. Therefore the FBW increases when the resonant frequency decreases. The bandwidth can be compensated. However, this method cannot be used in the filter topologies with pure electric coupling.

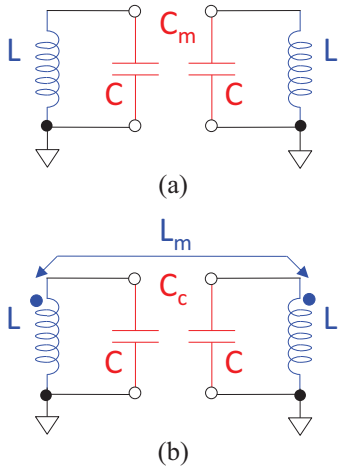

Fig. 1. Second order coupling network: (a) electrical coupling, (b) mixed coupling.

Figure 2 shows the proposed tunable capacitor network with controllable electrical coupling coefficient. The traditional capacitor network of C and C_m is replaced by the novel capacitor network of C_T, C_f and C_c. By using the symmetry of the circuit model in Fig. 2, the odd- and even-mode capacitor C_{odd} and C_{even} can be written as:

$$C_{odd} = \frac{C_T \ C_f + 2C_c}{C_T + C_f + 2C_c}, \tag{4}$$

$$C_{even} = \frac{C_T C_f}{C_T + C_f}. \tag{5}$$

Based on equation (4) and (5), the electric coupling factor k_e of the tunable capacitor network can be written as [18]:

$$k_e = \frac{C_{odd} - C_{even}}{C_{odd} + C_{even}} = \frac{C_c}{C_f + C_c + \frac{C_f^2 + 2C_f C_c}{C_T}}. \tag{6}$$

By studying (6), it shows that k_e increases when C_T increases, and the slope of k_e to C_T can be controlled by C_c and C_f. Let C_T to be the tunable capacitor, it can be seen from equations (4) and (5) that the tunable ratio of C_{odd} and C_{even} is limited mainly by C_f. While C_f increases, the tunable ratio increases. Benefiting from the resonant frequency splitting effect, the bandwidth can be controlled by the coupling coefficient. Thus, this mechanism can be applied to compensate the bandwidth of the tunable filter.

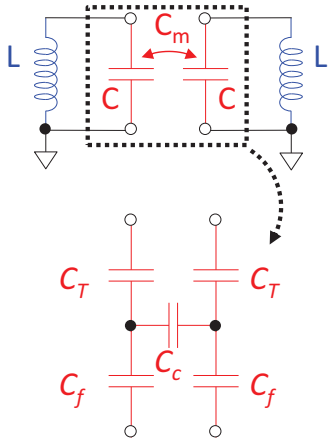

Fig. 2. Tunable capacitor network with controllable electrical coupling coefficient.

III. DESIGN AND MEASUREMENT

Figure 3 shows the layout of the proposed bandstop filter based on novel tunable capacitor network with controllable electric coupling coefficient. The filter is designed on 0.8 mm F4B-2 substrate (ε_r=2.65, $tan\theta$=0.001). Skyworks SMV1405 is chosen as the varactor diode, the anode and cathode terminals of the varactor diodes are connected between the capacitor and inductor of the LC resonators, respectively. Three 100 kΩ resistors are chosen as the biasing RF choke, as shown in Fig. 3. A lumped element equivalent circuit model for the tunable capacitor network of the LC resonators is depicted in Fig. 3. In this model, the microstrip patch of the LC resonators is modeled as the capacitor C_f. C_c indicates the electric coupling effect between the two resonators, and C_T is the varactor diodes.

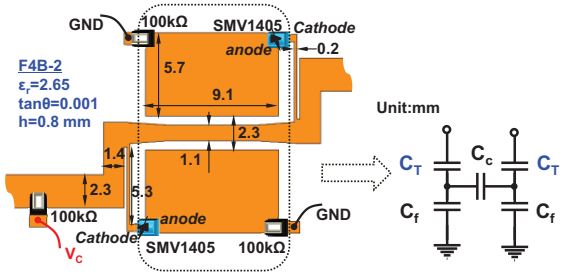

Fig. 3. Schematic diagram of the proposed tunable bandstop filter.

Figures 4 (a) and (b) show the simulated $|S_{21}|$, -30 dB *ABW* and *FBW* of the tunable filter. The passive structure of the filter is simulated by electromagnetic (EM) simulator *SONNET*. Then, the EM simulated touchstone file (S*n*P file) of the passive filter loaded with tunable elements, i.e., SMV1405, 100 kΩ resistor, and an additional ideal electric coupling capacitor ΔC as shown in the inset of Fig. 4 (a) and (b), is simulated in *Agilent Advanced Design System* (ADS).

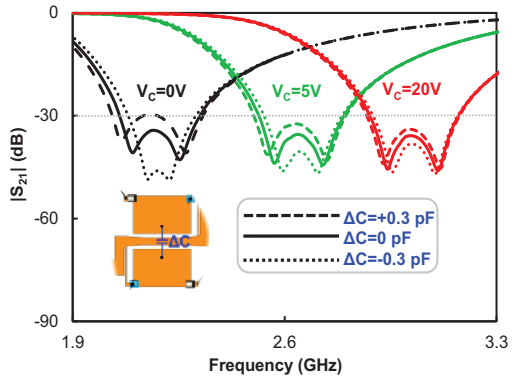

(a)

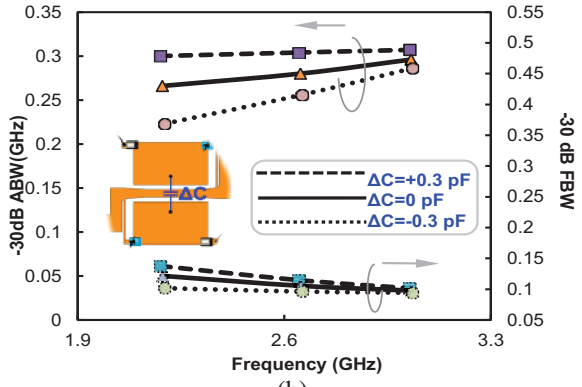

(b)

Fig. 4. Simulated results when the reverse voltage of the varactor diode varies from 0 V to 20 V, and an additional coupling capacitor ΔC between the resonators varies from -0.3 pF to 0.3 pF: (a) $|S_{21}|$, (b) -30 dB *ABW* and *FBW*.

It shows that, the *FBW* of the tunable filter increases while the working frequency decreases. The slope of *FBW* to the central frequency can be controlled by the electric coupling capacitor. Therefore, the bandwidth of the tunable filter can be compensated.

The tunable bandstop filter is fabricated and measured for the validation of the proposed method. The layout shown in Fig. 3 is fabricated on 0.8 mm F4B-2 substrate (ε_r=2.65, *tanθ*=0.001). The core area is 15 mm × 14 mm. Skyworks SMV1405 is chosen as the varactor diode, and the varactor diodes are biased through 100 kΩ resistor RF choke, as shown in Fig. 5. The measurement is done by *Agilent* E5071C vector network analyzer. The measured results are shown in Fig. 6.

Figure 6 (a) shows the *S*-parameters of the tunable bandstop filter; the stopband of the filter can be tuned very well. Since the filter is a lumped-element microstrip filter, it exhibits small physical size and broad spurious-free frequency bands. While the reverse bias voltage V_C of the varactor diodes is 0 V, 5 V, and 20 V, the $|S_{21}|$ and group delay are shown in Figs. 6 (b), (c), and (d), respectively. The measured group delays of the passbands are less than 1 ns and the rejection of the stopband is better than 30 dB. Figure 6 (e) summarizes the measured -30 dB *ABW* and *FBW* versus the central frequency of the stopband. The *FBW* varies from 11.14% to 13.35%, and the ABW varies from 371 MHz to 305 MHz, while the center frequency of the filter varies from 3.195 GHz to 2.285 GHz.

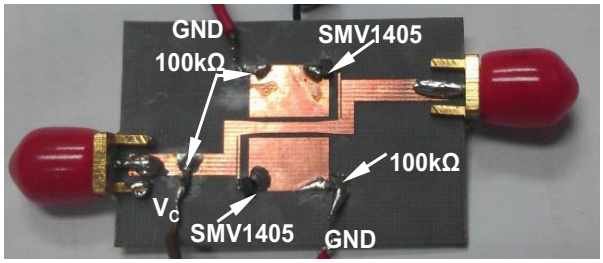

Fig. 5. The photograph of the fabricated tunable bandstop filter.

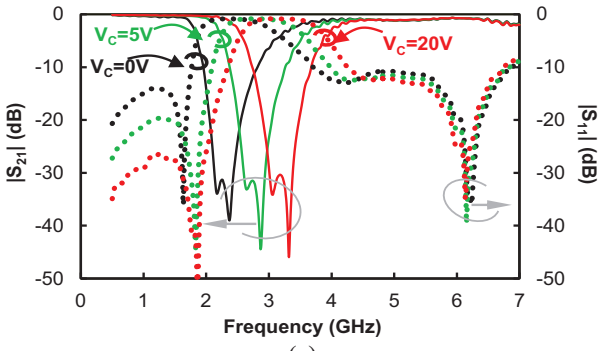

(a)

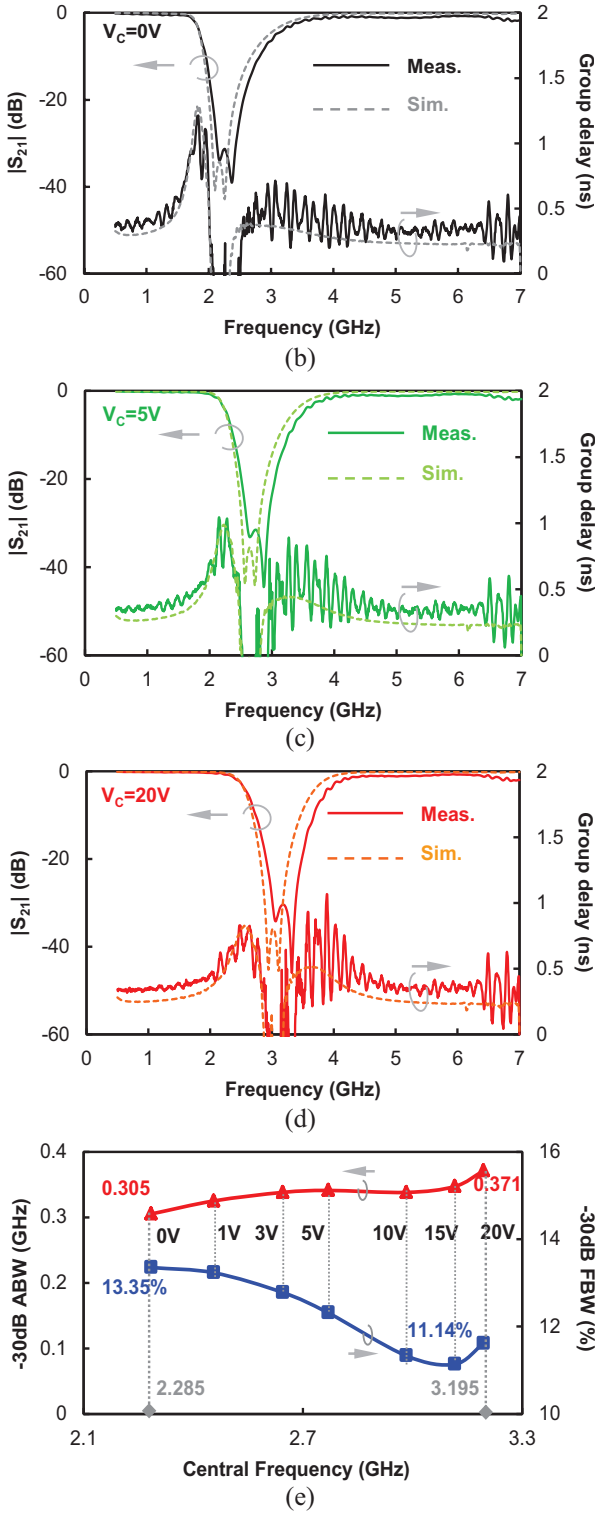

Fig. 6. The simulated and measured characteristics of the tunable filter: (a) the S-parameters of the tunable bandstop filter, (b) the $|S_{21}|$ and group delay when control voltage V_C=0 V, (c) the $|S_{21}|$ and group delay when V_C=5 V, (d) the $|S_{21}|$ and group delay when V_C=20 V, and (e) the measured -30 dB *ABW* and *FBW*.

Therefore, the proposed bandwidth compensation method has been validated. Comparing with [15] and [16], only electric coupling is used to compensate the bandwidth in this method, and the lumped tunable capacitor network is simple and easy to design.

IV. CONCLUSION

This paper has presented a tunable capacitor network to tune bandstop filter. The electric coupling factor of the tunable capacitor network increases when the tunable capacitor increases. This mechanism can be used to compensate the bandwidth of the tunable bandstop filter since the bandwidth can be controlled by the coupling factor through the resonant frequency splitting effect. Microstrip LC resonator loaded with Skyworks SMV1405 semiconductor varactor diode has been adopted to implement the tunable bandpass filters. It shows that the -30 dB fractional bandwidth varies from 11.14% to 13.35%, and the -30 dB absolute bandwidth varies from 371 MHz to 305 MHz, while the center frequency of the stopband varies from 3.195 GHz to 2.285 GHz. The tunable method presented in this paper is simple to implement and is a good candidate for the radio systems requiring flexible channel control.

ACKNOWLEDGMENT

This work was supported by the National Natural Science Foundation of China (NSFC) under Grant 61401375, 61271090, the Fundamental Research Funds for the Central Universities under Grant 2682014RC24, 2682015CX065, the Sichuan Province Science and Technology Support Program 2015GZ0103, and the Cultivation Project of Sichuan Province Science and Technology Innovation Seedling Project 2014-047.

REFERENCES

[1] M. Ojaroudi, N. Ojaroudi, and N. Ghadimi, "UWB slot antenna with band-stop operation by using H-shaped parasitic structures for UWB applications," *Applied Computational Electromagnetics Society (ACES) Journal*, vol. 28, no. 12, pp. 1259, 2013.

[2] Y. Ma, W. Che, W. Feng, and J. X. Cheng, "Square dual-mode quasi-elliptic bandpass filter with wide upper stopband," *Applied Computational Electromagnetics Society (ACES) Journal*, vol. 28, no. 11, pp. 1056, 2013.

[3] Q. Xiang, Q. Feng, and X. Huang, "Tunable bandstop filter based on split ring resonators loaded coplanar waveguide," *Applied Computational Electromagnetics Society (ACES) Journal*, vol. 28, no. 7, pp. 591-596, 2013.

[4] Z. H. Bao, Q. Y. Lu, C. Shao, J. X. Chen, and S. Zhang, "Novel bandwidth-agile bandpass filter using defected ground structure," *Applied*

Computational Electromagnetics Society (ACES) Journal, vol. 28, no. 11, pp. 1050, 2013.

[5] G. Mumcu, A. Dey, and T. Palomo, "Frequency-agile bandpass filters using liquid metal tunable broadside coupled split ring resonators," *IEEE Microw. Wireless Compon. Lett.*, vol. 23, no. 4, pp. 187-189, Apr. 2013.

[6] D. Bouyge, D. Mardivirin, J. Bonache, A. Crunteanu, A. Pothier, M. Durán-Sindreu, P. Blondy, and F. Martín, "Split ring resonators (SRRs) based on micro-electro-mechanical deflectable cantilever-type rings: application to tunable stopband filters," *IEEE Microw. Wireless Compon. Lett*., vol. 21, no. 5, pp. 243-245, May 2011.

[7] K. C. Hwang and H. J. Eom, "Tunable notch filter of ferrite-filled grooves in parallel plates," *IEEE Microw. Wireless Compon. Lett*., vol. 15, no. 5, pp. 363-365, May 2005.

[8] H. S. Lee, D.-H. Choi, and J.-B. Yoon, "MEMS-based tunable LC bandstop filter with an ultra-wide continuous tuning range," *IEEE Microw. Wireless Compon. Lett*., vol. 19, no. 11, pp. 710-712, Nov. 2009.

[9] Q. Y. Xiang, Q.Y. Feng, and X.G. Huang, "A novel microstrip bandstop filter and its application to reconfigurable filter," *Journal Electromag. Waves Applica.*, vol. 26, no. 8-9, pp. 1039-1047, June. 2012.

[10] Q. Y. Xiang, Q. Y. Feng, X. G. Huang, and D. H. Jia, "Electrical tunable microstrip LC bandpass filters with constant bandwidth," *IEEE Trans. Microw. Theory Tech.*, vol. 61, no. 3, pp. 1124-1130, Mar. 2013.

[11] X. Huang, Q. Feng, and Q. Xiang, "Bandpass filter with tunable bandwidth using quadruple-mode stub-loaded resonator," *IEEE Microw. Wireless Compon. Lett*., vol. 22, no. 4, pp. 176-178, Apr. 2012.

[12] X. Huang, L. Zhu, Q. Feng, Q. Xiang, and D. Jia, "Tunable bandpass filter with independently controllable dual passbands," *IEEE Trans. Microw. Theory and Tech*., vol. 61, no. 9, pp. 3200-3208, Sept. 2013.

[13] J. R. Mao, W. W. Choi, K. W. Tam, W. Q. Che, and Q. Xue, "Tunable bandpass filter design based on external quality factor tuning and multiple mode resonators for wideband applications," *IEEE Trans. Microw. Theory and Tech*., vol. 61, no. 7, pp. 2574-2584, 2013.

[14] X. Y. Zhang, Q. Xue, C. H. Chan, and B. J. Hu, "Low-loss frequency-agile bandpass filters with controllable bandwidth and suppressed second harmonic," *IEEE Trans. Microw. Theory Tech.*, vol. 58, no. 6, pp. 1557-1564, Jun. 2010.

[15] A. I. Abunjaileh and I. C. Hunter, "Tunable bandpass and bandstop filters based on dual-band combline structures," *IEEE Trans. Microw. Theory Tech*., vol. 58, no. 12, pp. 3710-3719, Dec. 2010.

[16] X. Y. Zhang, C. H. Chan, Q. Xue, and B. J. Hu, "RF tunable bandstop filters with constant bandwidth based on a doublet configuration," *IEEE Trans. Ind. Electron*., vol. 59, no. 2, pp. 1257-1265, Feb. 2012.

[17] R. J. Cameron, "Advanced coupling matrix synthesis techniques for microwave filters," *IEEE Trans. Microw. Theory Tech.*, vol. 51, no. 1, pp. 1-10, 2003.

[18] J.-S. Hong and M. J. Lancaster, *Microstrip Filters for RF/Microwave Applications*, New York: Wiley, 2001.

Qianyin Xiang received the B.Eng. degree in Communication Engineering and the Ph.D. degree in Communication and Information Systems from Southwest Jiaotong University (SWJTU), Chengdu, China, in 2005 and 2013, respectively. Xiang is a Member of Applied Computational Electromagnetics Society (ACES), Institute of Electrical and Electronics Engineers (IEEE) and IEEE Microwave Theory and Techniques Society (MTT-S).

His research interests include tunable/reconfigurable/ software defined RF devices, RFID systems.

Quanyuan Feng received the M.S. degree in Microelectronics and Solid Electronics from the University of Electronic Science and Technology of China (UESTC), and the Ph.D. degree in Electromagnetic Field and Microwave Technology from Southwest Jiaotong University (SWJTU), Chengdu, China, in 1991 and 2000, respectively.

Feng has been honored as the "Excellent Expert" and the "Leader of Science and Technology" of Sichuan province for his outstanding contribution. He is the Reviewer of more than 20 journals, such as IEEE Trans. Vehic. Tech., IEEE Trans. Magn., IEEE Magn. Lett., IEEE Microw. Wireless Compon. Lett., Chinese Physics, Acta Physica Sinica, etc. He is the recipient of the "First Class Award of Scientific and Technologic Progress of Sichuan Province," "Third Class Award of Scientific and Technologic Progress of Electronic

Industry Ministry," "National Mao Yisheng Scientific and Technologic Award of Chinese Scientific and Technologic Development Foundation".

His research interests include power electronics, antennas and propagation, integrated circuits design, electromagnetic compatibility and environmental electromagnetics, microwave materials and devices.

Xiaoguo Huang received the B.Eng. degree in Microelectronics from Southwest Jiaotong University (SWJTU), Chengdu, China, in 2008, where he is currently working towards his Ph.D. degree. His research interests include passive circuit design, tunable filters, and metamaterials.

Dinghong Jia received the B.Eng. degree in Microelectronics from Southwest Jiaotong University, Chengdu, China. He is currently working towards his Ph.D. degree in Communication and Information Systems at Institute of Microelectronics, Southwest Jiaotong University, Chengdu, China. His research interests include passive circuit design, tunable filters, and antennas.

Circuit Model Analysis of a Polarization and Wide Angle Independent Hexagonal Shaped Metamaterial Absorber

M. Bahdorzadeh Ghandehari [1], N. Feiz [1], and M. Alipoor [2]

[1] Department of Electrical Engineering
College of Engineering, Mashhad Branch, Islamic Azad University, Mashhad, Iran
m.bahadorzadeh@mshdiau.ac.ir, Nooshin.feyz@gmail.com

[2] Department of Electrical Engineering
International University of Imamreza, Mashhad, Iran
mehdialipour70@yahoo.com

Abstract ─ This paper presents an equivalent circuit model of metamaterial absorber (MA) based on triple hexagonal shaped resonators. This metamaterial unit cell absorber possesses a nearly wide angle perfect absorption of incidence wave and polarization independence. The absorption is occurred in three different frequencies. The absorptivity is as high as 98%, 93% and 94%, at 3.5 (GHz), 4.7 (GHz) and 6.6 (GHz), respectively. The equivalent circuit model of a single hexagonal ring has been extended to the triple band absorber structure. The simulation of the circuit model agrees well with the full-wave simulation, regarding to return loss and absorption. The important features of this method are simple fabrication of metamaterial absorber and maximum absorption in three frequencies. The proposed metamaterial absorber has wide applications such as thermal detector, stealth technology and imaging. Moreover, a very good agreement between simulation and measurement results has been observed.

Index Terms ─ Circuit model analysis, metamaterial absorber, triple band, wide angle independent.

I. INTRODUCTION

Electromagnetic metamaterials (MTMs) are defined as artificial and effectively homogeneous electromagnetic structures with unusual and unique properties that do not exist in the nature. Metamaterials were first introduced theoretically by Veselago [1]; his research was continued by Pendry, et. al. and Smith, et. al. [2-4].

These constructed engineered electromagnetic materials are composed of natural materials such as highly conductive and shaped metals and dielectric materials that will be selected according to the frequency range and the application. The advantage of the variability of the structural parameters has been implemented to create the resonant metamaterial absorbers. Basically, to design an absorber, we have to maximize the absorption coefficient. It is equivalent to minimize both the transmission (T) and reflection (R) coefficients in the equation:

$$A = 1\text{-}T\text{-}R, \quad (1)$$

where A is absorption coefficient [5].

In this paper, we propose a novel planar metamaterial absorber which absorb the electromagnetic wave at nearly 3.5 (GHz), 4.7 (GHz) and 6.6 (GHz) with absorption rate 98%, 93% and 94%, respectively. It is observed that the metamaterial absorber is polarization insensitive for both transverse electric (TE) and transverse magnetic (TM) waves. Also, measured and simulated results are compared. Accordingly, it can be concluded that these results are very close to each other. The proposed metamaterial absorbers in many articles have only one absorbtion frequency [10]-[12]; also, some of them do not have the feature of simple construction and the absorption is not close to the maximum value [13], but the proposed metamaterial absorber in this paper has the advantage of simple fabrication and the maximum absorption at three absorber frequencies.

II. DESIGN AND SIMULATION

As shown in Fig. 1, the proposed metamaterial unit cell is considered as a hexagonal shape. The metallic structures on the top and bottom layers of the substrate are chosen as copper, the electrical conductivity and thickness is $5.8\times10^{7}(s/m)$ and 0.036 (mm), respectively. The substrate of absorber is FR4 ($\varepsilon_r = 4.3, \tan\delta = 0.025$) with 1.6 (mm) thickness.

The simulation is done by Ansoft HFSS and CST software's with periodic boundary conditions. The boundary surfaces perpendicular to the incident electrical field (E) are defined as perfect electric conductor (PEC) surfaces, while the surfaces perpendicular to the incident magnetic field (H) are

Submitted On: September 10, 2014
Accepted On: June 14, 2015

defined as perfect magnetic conductor (PMC) surfaces. Finally, the surfaces perpendicular to propagation vector (k) are defined as open ports.

The absorption is calculated as:

$$A(\omega) = 1 - |S_{11}|^2 - |S_{12}|^2 , \quad (2)$$

where

$$R(\omega) = |S_{11}|^2 , \quad (3)$$

represents the reflection, and

$$T(\omega) = |S_{12}|^2 , \quad (4)$$

represents the transmission. Due to the presence of the metallic ground plane on the bottom side of the absorber the T(ω) is zero so, the absorption can be expressed as:

$$A(\omega) = 1 - |S_{11}|^2 . \quad (5)$$

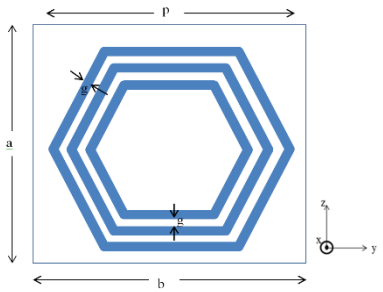

Fig. 1. Unit cell geometry and design parameters: a=b=20 mm, p=17.4 mm, and g=1.2 mm.

The absorption and reflection of the proposed structure is shown in Fig. 2. It is evident that near the frequencies of 3.5 (GHz), 4.7 (GHz) and 6.6 (GHz) the reflection reaches its minimum value and the absorption rate reaches to 98%, 93% and 94%, respectively.

The first absorption frequency is occurred due to the largest perimeter hexagonal and the medium and smallest hexagonal will result in the second and third absorption.

Figure 3 shows the surface current's distribution on the smallest hexagonal which causes the third absorption at the resonant frequency (6.6 GHz). It implies the absorption mechanism of such metamaterial absorber.

For electromagnetic wave normal incidence, the currents on the absorber are symmetrical and counter-circulated between the left and right parts, providing an electric response similar to an electric-LC resonator. There is a magnetic response associated with a circulating displacement current between the resonator and the ground plane (bottom side of substrate). The electric and magnetic response appeared simultaneously at the absorption frequency. In this resonance condition, the effective impedance is defined as [10]:

$$Z(\omega) = \sqrt{\frac{\mu(\omega)}{\varepsilon(\omega)}} . \quad (6)$$

In order to make the minimum reflection, the effective impedance has to be matched to free space impedance. This phenomenon is happening in the resonance frequency.

Moreover, due to the resonant loss in the metallic resonator and the dielectric loss of substrate, the transmission in the metamaterial absorber is effectively reduced.

So, the metamaterial absorber proposed in this paper can absorb both the incident electric and magnetic fields. This absorption mechanism is similar to the common published metamaterial absorbers as shown in [6-9].

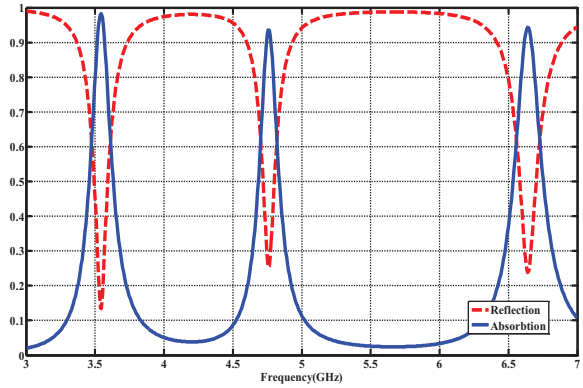

Fig. 2. Simulated reflection and absorption of the proposed metamaterial absorber.

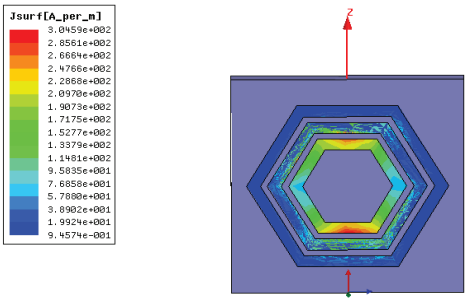

Fig. 3. Current distribution on the metamaterial unit cell at third resonance frequency (6.6 GHz).

In order to find the influence of polarization and incident angle on the performance of the proposed metmaterial absorber some simulations were performed. The structure was simulated by a 3D full wave electromagnetic simulator CST based on the FDTD method as shown in Fig. 4. The result of the absorption under different incident angles for TE and TM polarizations have been demonstrated in Figs. 5 and 6 respectively. As shown in these figures, the strength of the absorption is close to maximum for all incident angles from 0° to 45° regardless of the mode. This fact represents the independence of metamaterial absorber to the angle of incident for a wide range.

It is evident that the main peak of the absorption is above 90% for both TE and TM cases at different angles. Also, the resonant frequencies for both TE and TM polarization are the same implies the polarization independence of the absorber.

So, the proposed metamaterial unit cell is flexible and has multi directional structure. It is evident that a very small and negligible difference is observed between the TE and TM modes by changing the polarization angle. The simulated results show that the proposed metamaterial absorber can be operated for a wide range of incident angles with arbitrary polarizations.

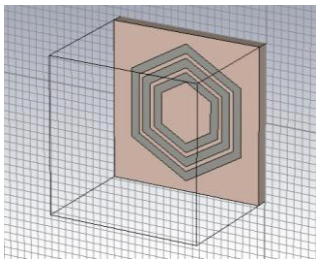

Fig. 4. The simulated structure by CST.

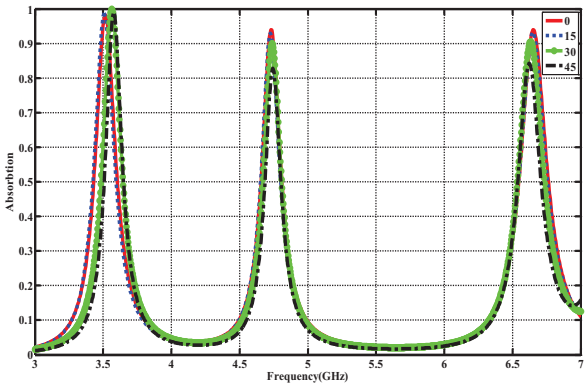

Fig. 5. Absorption at the different incident of polarization angles ranging from 0° to 45° for TE mode.

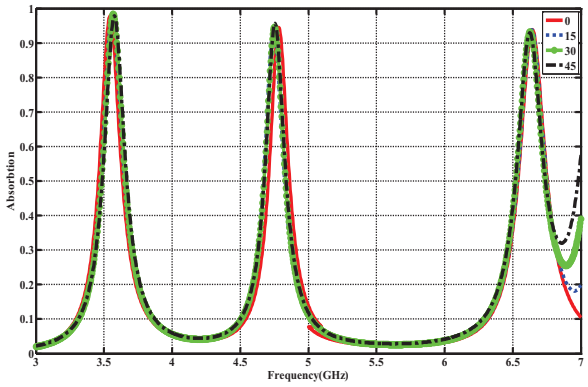

Fig. 6. Absorption at the different incident of polarization angles ranging from 0° to 45° for TM mode.

III. CIRCUIT MODEL ANALYSIS

A circuit model for an individual closed ring resonator (CRR) based structure backed by copper lamination is proposed in [14]. A closed ring could be modeled by the circuit model which is presented simply in Fig. 7 (a).

The resonance is modeled by the parallel inductance and capacitance. A single band absorber can be considered as a parallel LC circuit. The resistive part in series with the inductive part models the resonator losses. The magnetic and electric excitations give rise to the effective inductance and capacitance respectively in the circuit model. The result of s parameter simulation with AWR has been presented in Fig. 7 (b) shows a good agreement with the EM simulation.

When the electromagnetic plane wave impinges the proposed absorber all the three CRRs will be excited simultaneously. The complete circuit model of the absorber with all three coupling resonator circuits has been shown in Fig. 8. The extra capacitances were used to model the mutual coupling effects between resonators. The reflection coefficient of the complete circuit model is presented in Fig. 9, which represents a good agreement with EM simulation. Through this circuit model the resonance frequencies could be tuned easily.

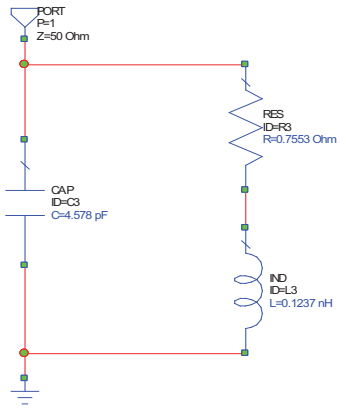

(a) Circuit model of small ring

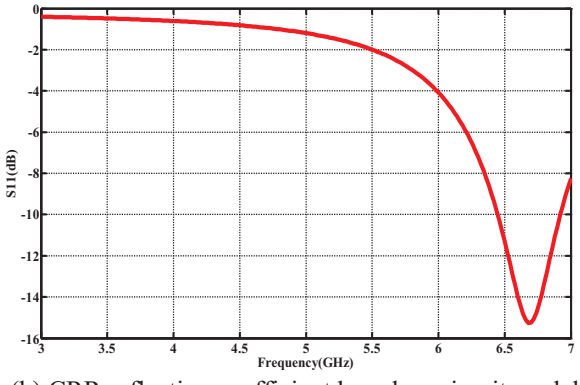

(b) CRR reflection coefficient based on circuit model

Fig. 7. CRR unit cell circuit model and simulated S-parameter.

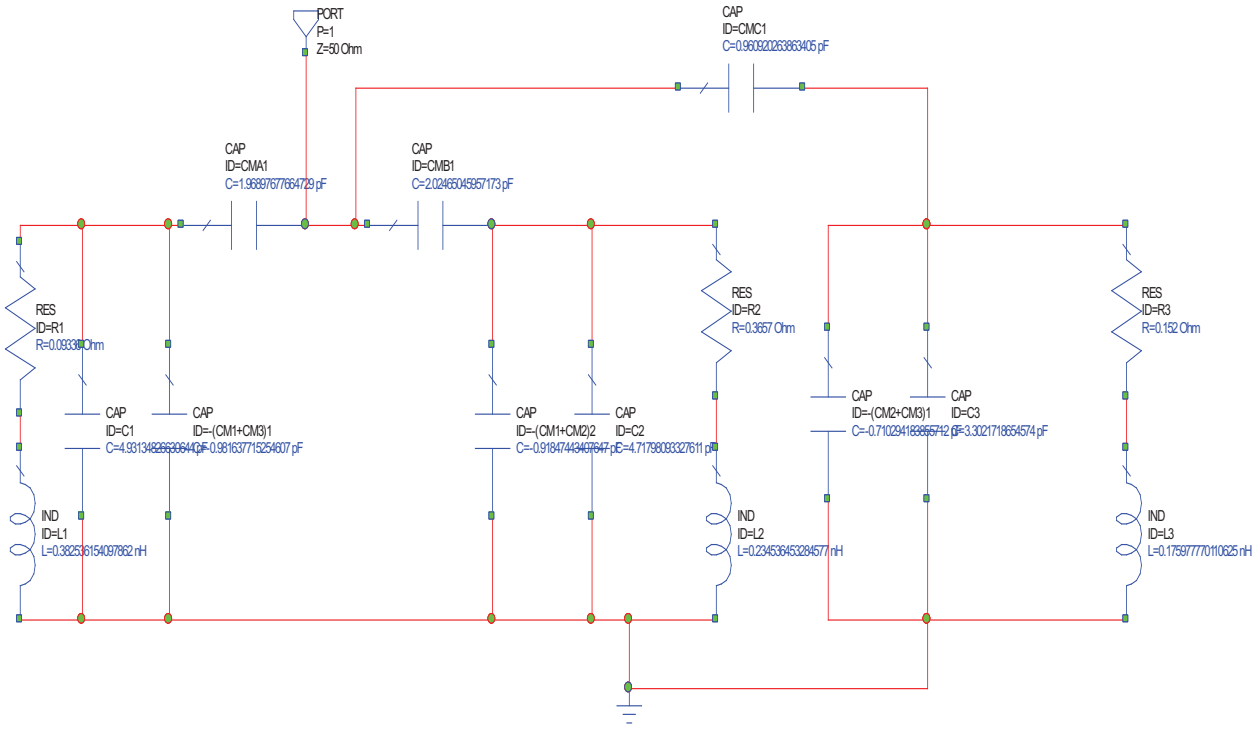

Fig. 8. Circuit model of triple band absorber.

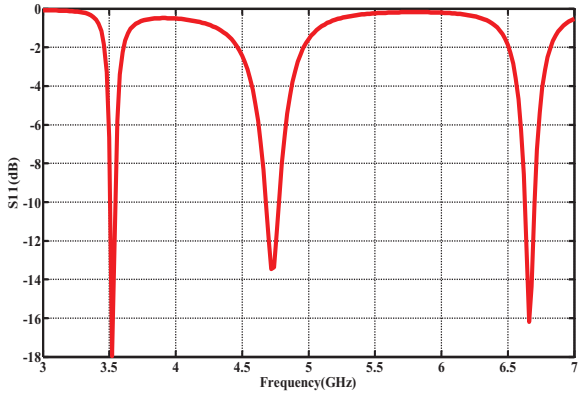

Fig. 9. S-parameter of simulated circuit model.

IV. FABRICATION AND EXPERIMENT RESULTS

To verify the full-wave simulations, a 15×15 unit cells sample (300 mm × 300 mm × 1.5 mm) was fabricated by printing a planar array of designed hexagonal shaped structure on the front side. A complete ground plate was placed on the back side of a FR-4 substrate. The thickness of the substrate is considered 1.5 mm and printed-circuit-board (PCB) technology was used for fabrication. The photograph of the experimental sample of proposed MA is shown in Fig. 10. A vector network analyzer Agilent E8363C and two linear polarized horn antennas were used to transmit TEM waves in the range from 3 GHz to 7 GHz to sample and receive the reflected signals. The location of the absorber was far enough from the horn antennas so that the incidence could be recognized normal to the sample. As demonstrated in [11], the experimental measurement is carried out in two steps. In the first step, the reflection measurements should be calibrated using a copper sample-sized sheet as a reflecting mirror. The measurement is done by a ground copper plane with the same dimension as the sample used for measurement and this is used as measurement reference.

In the second step, the fabricated sample of the metamaterial absorber is tested and the S-parameters are recorded. The differences between the measured results of the first and second steps represent the modified reflection coefficient from the proposed MA [11]. The reflection coefficient and the absorption of the experimental proposed metematerial absorber is shown in Fig. 11. The measured and simulated absorption of TE and TM modes as a function of the frequency are shown in Fig. 12 and Fig. 13, respectively. It is observed that the simulation and experimental results are in a good agreement.

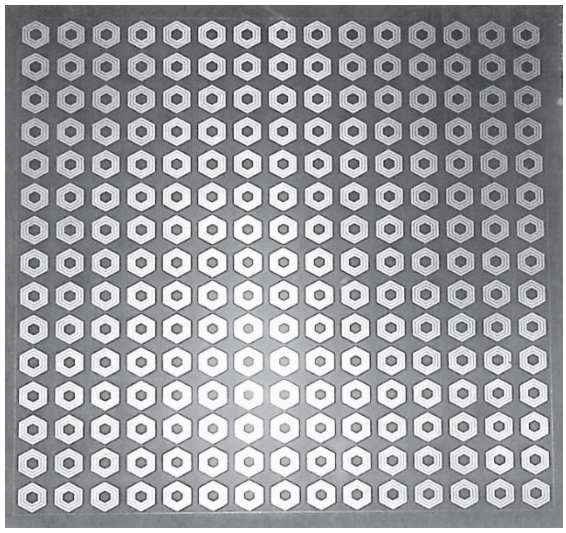

(a) Fabricated metamaterial absorber

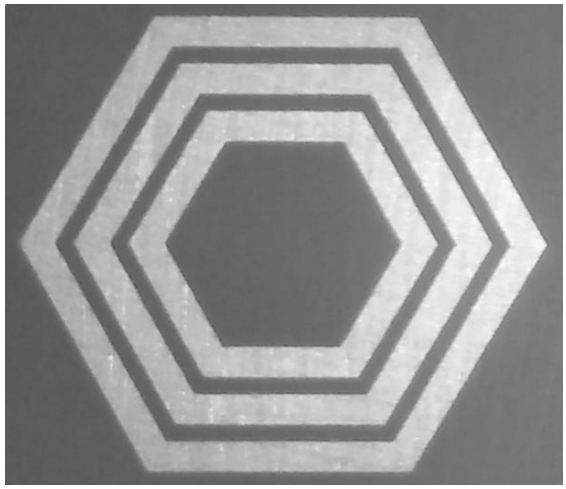

(b) An isolated unit cell

Fig. 10. Photograph of fabrication of proposed metamaterial absorber.

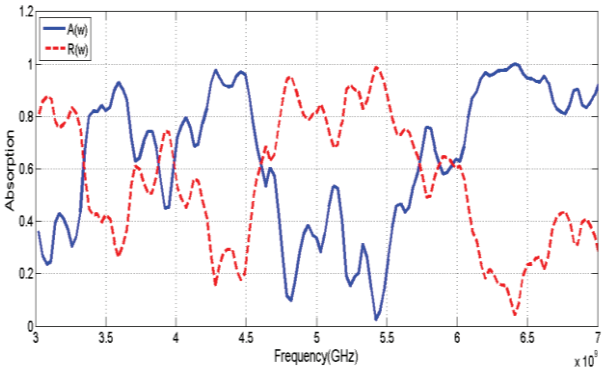

Fig. 11. The reflection coefficient and absorption of the experimental proposed metematerial absorber.

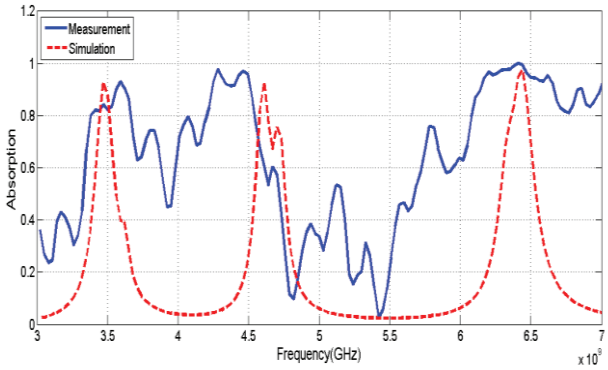

Fig. 12. The measured and simulated absorption of TE mode as a function of the frequency.

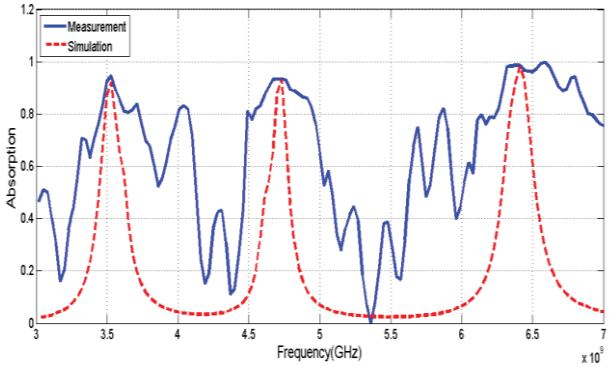

Fig. 13. The measured and simulated absorption of TM mode as a function of the frequency.

V. CONCLUSION

In this paper, a novel metamaterial unit cell absorber based on triple hexagonal shapes has been presented. Simulations demonstrated that due to the hexagonal with different perimeters, absorption occurs at three different frequencies. Metamaterial absorbers that were used in many articles have only one absorption frequency, but in this paper, maximum absorption is observed in three frequencies. Compared to other researches, absorption is very close to its maximum value. It could be found that the absorber is polarization independent and could be worked for a wide angle of incidence. An equivalent circuit model was represented for modeling the absorber. The results are in a good agreement with simulation and measurement results. The geometric parameters that influence the resonance of the absorber were further discussed, which shows that the absorbing frequency could be shifted by adjusting the space of hexagonal. Also, the fabrication results of the proposed metamaterial absorber are demonstrated that the simulation and experimental results are in a good agreement.

REFERENCES

[1] V. G. Veselgo, "The electro dynamics of substances with simultaneously negative value of ε and μ," *Sov. Phys. Usp*., vol. 10, no. 4, pp. 509-514, Feb. 1968.

[2] J. B. Pendry, A. J. Holden, D. J. Robbins, and W. J. Stewart, "Low frequency plasmons in thin-wire structure," *J. Phys. Condens. Matter*, vol. 10, pp. 4785-4809, 1998.

[3] J. B. Pendry, A. J. Holden, D. J. Robbins, and W. J. Stewart, "Magnetism from conductors and enhanced nonlinear phenomena," *IEEE Trans. Microwave Theory Tech*., vol. 47, pp. 2075-2084, 1999.

[4] D. R. Smith, W. J. Padilla, D. C. Vier, S. C. Nemat-Nasser, and S. Schultz, "Composite medium with simultaneously negative permeability and permittivity," *Phys. Rev. Lett*., vol. 84, no. 18, pp. 4184-4187, May 2000.

[5] S. Jamilan, M. N. Azarmanesh, and D. Zarifi, "Design and characterization of a dual band metamaterial absorber based on destructive interferences," *Progress In Electromagnetics Reseach C*, vol. 47, pp. 95-101, 2014.

[6] M. H. Li, H-L. Yang, X-W. Hou, Y. Tian, and D-Y. Hou, "Perfect metamaterial absorber with dual bands," *Prog. Electromagn. Res*., 108:37-49, 2010.

[7] X-J. He, Y. Wang, J-M. Wang, T-L. Gui, and Q. Wu, "Dual-band terahertz metamaterial absorber with polarization insensitivity and wide incident angle," *Prog. Electromagn. Res*., 115:381-397, 2011.

[8] L. Huang and H. Chen, "Multi-band and polarization insensitive metamaterial absorber," *Prog. Electromagn. Res*., 113:103-110, 2011.

[9] L. Li, Y. Yang, and C. Liang, "A wide-angle polarization-insensitive ultra-thin metamaterial absorber with three resonant modes," *J. Appl. Phys*., 110:063702, 2011.

[10] Y. J. Huang, G. J. Wen, J. Li, W. R. Zhu, P. Wang, and Y. H. Sun, "Wide angle and polarization independent metamaterial absorber based on snowflake shaped configuration," *Journal of Electromagnetic Waves and Applications*, vol. 27, no. 5, pp. 552-559, 2013.

[11] F. Dincer, M. Karaaslan, E. Unal, E. Akgol, E. Demirel, and C. Sabah, "Polarization and angle independent perfect metamaterial absorber based on discontinuous cross-wire-strips," *Journal of Electromagnetic Waves and Applications*, vol. 28, no. 6, pp. 741-751, 2014.

[12] S. Fallahzadeh, K. Forooraghi, and Z. Atlasbaf, "Design, simulation and measurement of a dual linear polarization insensitive planar resonant metamaterial absorber," *Prog. Electromagn. Letter*, vol. 35, pp. 135-144, 2012.

[13] P. K. Singah, S. Kabiri, L. Chao, M. N. Afsar, and S. Sonkusale, "Boardband millimeterwave metamaterial absorber based on embedding of dual resonators," *Prog. Electromagn. Res*., vol. 142, pp. 625-638, 2013.

[14] S. Bhattacharyya, S. Ghosh, and K. V. Srivastava, "Equivalent circuit model of an ultra-thin polarization-independent triple band metamaterial absorber," *AIP Advances 4*, 097127, 2014.

Mehdi Bahadorzadeh G. was born in Mashhad, Iran in September of 1981 and he received his B.Sc. from Ferdowsi University in 2003, his M.Sc. from Shahed University in 2005, and his Ph.D. from Islamic Azad University in 2009, all in Telecommunication Engineering. He also cooperates with the Iranian Telecommunication Research Center (ITRC) and Iranian Research Institute for Electrical Engineering as a Research Assistant since 2007. His main areas of interest are electromagnetic compatibility, numerical methods in electromagnetics, microstrip antenna, microwave engineering and RF circuit design.

Nooshin Feiz was born in Mashhad, Iran in 1987. She received the B.S. from Fredowsi University, Mashhad Iran, in 2009 and the M.S. degree from Shiraz University, Shiraz, Iran in 2011. Her research interest is in electromagnetic waves in complex media, metamaterial applications such as absorbers and antenna.

Mehdi Alipoor was born in Tehran, Iran, on February 16, 1992. He is now a Bachelor Student of Telecommunication Engineering at the International University of Imamreza, Mashhad, Iran. His research interest is in microwave engineering, RF circuit design, electromagnetic waves in complex media, metamaterial applications such as absorbers and antenna, etc.

Distributed Signal and Noise Modeling of Millimeter Wave Transistor Based on CMOS Technology

Z. Seifi, A. Abdipour, and R. Mirzavand

Electrical Engineering Department, Institute of Communications Technology and Applied Electromagnetics, Micro/mm-wave & Wireless Comm. Research Lab., Amirkabir University of Technology, Tehran, 15914, Iran
z.seifi@aut.ac.ir, abdipour@aut.ac.ir, rmirzavand@aut.ac.ir

Abstract ─ This paper presents a complete distributed transmission line signal and noise modeling of millimeter wave CMOS transistor. In this model, the MOSFET transistor is considered as a three-coupled active transmission line structure, exciting by the noise equivalent sources distributed on its conductors. According to the transmission line theory, closed form expressions of the signal and noise parameters for a high frequency CMOS transistor are derived as the function of device width. By using the proposed model, the scattering and noise parameters of a 130 nm MOSFET are computed over a frequency range up to 100 GHz. The results obtained by this approach is compared with the lumped elements model and verified by the simulation results of Cadence SpectreRF simulator.

Index Terms ─ Cadence, CMOS transistor, coupled active transmission line, distributed transmission line model, lumped MOSFET model, millimeter wave.

I. INTRODUCTION

With the advancement in CMOS technology, the MOS transistors are scaled down into deep submicron regime with higher transit frequency. The high frequency capabilities of MOSFETs are very attractive for millimeter (mm) wave circuit design due to their ability of chip integration, low cost and low power consumption [1]. As the operating frequency of MOSFETs increases to the mm-wave range, the width of the device becomes comparable to the wave length. In such cases, the distributed transmission line effect needs to be considered accurately, in device modeling.

In previous works [2], [3] and [4] the distributed transmission line effect along the gate width has been studied. In these distributed models, the gate width is divided into finite number of slices that are connected together by using of series of scaled gate resistor. In [2], the thermal noise due to the gate resistance was incorporated in the model. In [3], MOSFET distributed model of [2] is improved by including the distributed charging resistance and the induced gate noise along the gate width. Nevertheless, in these studies only distributed behavior of transistor along gate electrode width is modeled and other electrodes are ignored. Furthermore, the effects of the transmission line capacitances and inductances along the device width are not considered.

In this paper, a complete distributed transmission line signal and noise modeling of mm-wave MOSFET transistor that considered it as the excited three-coupled active transmission line structure, exciting by noise equivalent sources distributed on the conductors, is presented. The details of the proposed model are described in the next section. In Section III, the introduced approach is used in signal and noise modeling of 130 nm MOSFET and its results are discussed and compared with lumped and previous distributed models. Finally, the paper is concluded in the last section.

II. DISTRIBUTED MM-WAVE MOSFET MODELING

A. Distributed signal analysis

The proposed distributed model considers the MOSFET as three-coupled active transmission line, is shown in Fig. 1 (a). In this model, the device width is divided into an infinity number of segments, while each segment is separated into parallel intrinsic and extrinsic contributions. The parameters G_m, C_{gs}, C_{ds}, C_{gd}, R_g, R_d and R_{ds} taken together are referred to as the intrinsic elements and standard BSIM4 model [5] is employed to compute them. BSIM4 is the physical MOSFET model supplied with Berkeley SPICE and models the channel current by using a complete single equation for both linear and saturation regions as:

$$I_{ds} = \frac{V_{dseff} I_{ds0}(V_{dseff})}{V_{dseff} + R_{ds} I_{ds0}(V_{dseff})} \left(1 + \frac{V_{ds} - V_{dseff}}{V_A}\right) \left(1 + \frac{V_{ds} - V_{dseff}}{V_{ASCBE}}\right), \quad (1)$$

and transistor conductance G_m can be obtained as:

$$G_m = \left.\frac{\partial I_{DS}}{\partial V_{GS}}\right|_{V_{DS}=\text{Const.}}. \quad (2)$$

Submitted On: May 11, 2014
Accepted On: May 25, 2015

The detailed equations of I_{ds0}, V_{dseff}, V_{ASCBE} and V_A have been given in [5]. In this model, capacitances are derived from the charges to ensure charge conservation. The space charge of a MOS structure consists of three fundamental components: the charge on the gate electrode, Q_G, the charge in the bulk depletion layer, Q_B, and the mobile charge in the channel region, Q_{INV}. Generally, the following relationship holds in a MOSFET:

$$Q_G + Q_{INV} + Q_B = 0, \tag{3}$$

and

$$Q_{INV} = Q_D + Q_S, \tag{4}$$

where Q_D and Q_S are the channel associated with the drain node and the source node, respectively. Capacitance between any two of the four terminals (gate, source, drain, and bulk) is defined as:

$$C_{ij} = \frac{\partial Q_i}{\partial V_j}, \qquad i \; or \; j \in (g, d, s, b). \tag{5}$$

BSIM4 provides three options for selecting different capacitance models. By selecting different capMod options, different model equations can be used to describe the characteristics of the charge and the capacitances [5]. In this model, the source/drain series resistances are modeled by a bias-independent diffusion resistance and bias-dependent LDD resistances. Accurate modeling of the bias-dependent LDD resistances is important for deep submicron CMOS technologies. The LDD source/drain resistance $R_{ds}(V)$ is modeled internally through the I-V equation. The detailed relationships for modeling of intrinsic resistances have been given in [5]. Then the values of the per-unit-length intrinsic elements can be obtained by using scaling rules [6].

The extrinsic part models the transmission line and distributed behavior of transistor along the electrodes width. Therefore, the per-unit-length 3-by-3 square impedance and admittance matrices of transmission line MOSFET model, as a six-port structure, can be written as:

$$\begin{aligned}\left[\hat{Y}\right] &= \left[\hat{Y}_{extrinsic}\right] + \left[\hat{Y}_{intrinsic}\right] \\ &= [G] + j\omega[C] + \left[\hat{Y}_{tr}\right],\end{aligned} \tag{6}$$

$$\left[\hat{Z}\right] = [Z_s] + j\omega[L] = [R] + j\omega[L_i] + j\omega[L], \tag{7}$$

where [C], [G] and [L] are the per-unit-length matrices of capacitance, conductance and inductance, respectively. The entries in these matrices can be obtained by applying numerical methods of calculating the per-unit-length parameters for multi-conductor transmission lines [7], according to the electrical and physical characteristics of the transistor. Furthermore, $[Z_s]$ is the surface impedance matrix and demonstrates the distributed effects and frequency-dependent losses caused by the skin effect. The real part of $[Z_s]$ represents the electrode resistance and the imaginary part, the internal inductance [6]. $[Y_{tr}]$ is used to model the intrinsic parallel part of the distributed transistor model. By applying the transmission line theory to the transistor model of Fig. 1 (b), the second-order coupled equations in the frequency-domain can be written as:

$$\frac{d^2[\hat{V}]}{dz^2} = \frac{d^2}{dz^2}\left[\hat{V}_d \;\; \hat{V}_g \;\; \hat{V}_s\right]^T = -\left[\hat{Z}\right]\left[\hat{Y}\right]\left[\hat{V}\right], \tag{8}$$

$$\frac{d^2[\hat{I}]}{dz^2} = \frac{d^2}{dz^2}\left[\hat{I}_d \;\; \hat{I}_g \;\; \hat{I}_s\right]^T = -\left[\hat{Y}\right]\left[\hat{Z}\right]\left[\hat{I}\right], \tag{9}$$

where [V] and [I] are 1-by-3 voltage and current matrices of electrodes, respectively and functions of z and ω. For solving the above equations, the well-known similarity transformation solution is used [8]. By implementing this method, the general solutions for the voltages and current matrices can be obtained as:

$$\left[\hat{V}\right] = \left[\hat{T}_V\right]\left(\left[e^{-\hat{\gamma}z}\right][\hat{V}_m^+] + [e^{+\hat{\gamma}z}]\left[\hat{V}_m^-\right]\right), \tag{10}$$

$$\left[\hat{I}\right] = \left[\hat{Y}_c\right]\left[\hat{T}_V\right]\left(\left[e^{-\hat{\gamma}z}\right]\left[\hat{V}_m^+\right] - [e^{+\hat{\gamma}z}]\left[\hat{V}_m^-\right]\right), \tag{11}$$

where $[\hat{Y}_c] = [\hat{Z}]^{-1}[\hat{T}_V][\hat{\gamma}][\hat{T}_V]^{-1}$ is defined as characteristic admittance matrix. The elements of $[\hat{\gamma}]$ and $[\hat{T}_V]$ matrices are the eigenvalues and eigenvectors of $[\hat{Z}][\hat{Y}_c]$, respectively. By evaluating the general forms of the solutions in (10) and (11) at z = 0 and z = W and omitting the unknown coefficients $[\hat{V}^{\pm}_{m}]$, the 6-by-6 chain matrix of MOSFET model shown in Fig. 1 (b), which can be transformed to the scattering matrix form, will be obtained as follows:

$$\begin{aligned}\left[\hat{V},\hat{I}\right]^T_{(W,\omega)} &= -\hat{\Phi}\big|_{(W)}\left[\hat{V},\hat{I}\right]^T_{(0,\omega)} \\ &= \begin{bmatrix}\hat{\Phi}_{11\;3\times3} & \hat{\Phi}_{12\;3\times3} \\ \hat{\Phi}_{21\;3\times3} & \hat{\Phi}_{22\;3\times3}\end{bmatrix}_{(W)}\left[\hat{V},\hat{I}\right]^T_{(0,\omega)},\end{aligned} \tag{12}$$

$$\begin{aligned}\hat{\Phi}_{11}\big|_{(W)} &= \frac{1}{2}\hat{T}_V(e^{\hat{\gamma}W} + e^{-\hat{\gamma}W})\hat{T}_V^{-1}, \\ \hat{\Phi}_{12}\big|_{(W)} &= -\frac{1}{2}\hat{T}_V(e^{\hat{\gamma}W} - e^{-\hat{\gamma}W})\hat{\gamma}^{-1}\hat{T}_V^{-1}\hat{Z}, \\ \hat{\Phi}_{21}\big|_{(W)} &= -\frac{1}{2}\hat{Y}_c\left[\hat{T}_V\left(e^{\hat{\gamma}W} - e^{-\hat{\gamma}W}\right)\hat{T}_V^{-1}\right], \\ \hat{\Phi}_{22}\big|_{(W)} &= \frac{1}{2}\hat{Z}^{-1}\hat{T}_V\left(e^{\hat{\gamma}W} + e^{-\hat{\gamma}W}\right)\hat{T}_V^{-1}\hat{Z}.\end{aligned} \tag{13}$$

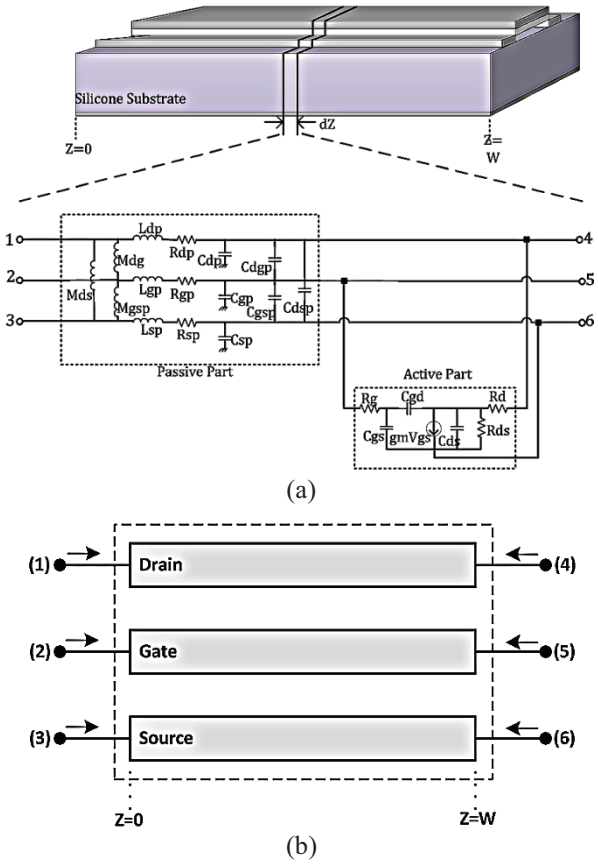

Fig. 1. (a) Differential part of distributed signal model of the mm-wave MOSFET, and (b) the six-port distributed transmission line model of MOSFET.

B. Distributed noise analysis of millimeter wave MOSFET

To consider the distributed electrodes width effect, the excited three-coupled transmission line structure, exciting by noise equivalent sources distributed on the conductors, is proposed for modeling of noise performance of millimeter wave MOSSFETs. A full description of the proposed model is clearly shown in Fig. 2. The noise originated within the active region is computed by using BSIM4 model [5]. It includes the flicker noise, channel thermal noise, induced gate noise and their correlation and thermal noise due to the resistances at the terminals. Two flicker noise models are included in BSIM4. In this paper, unified physical flicker noise model is used. In this model, the spectral drain current noise power density is formulated as:

$$S_{id}(f) = \frac{S_{id,inv}(f).S_{id,sub}(f)}{S_{id,inv}(f) + S_{id,sub}(f)}, \tag{14}$$

where $S_{id,inv}(f)$ and $S_{id,sub}(f)$ are the spectral drain current noise power density of the device in the inversion and the sub-threshold regions, respectively, which the detailed equations of them have been given in [5]. Such as flicker noise, two options for the channel thermal noise are provided in BSIM4. One is the charge-based model from BSIM3v3 and the other is the holistic model. In the holistic model, which is used in this paper, all the short-channel effects including the velocity saturation effect incorporated in the I–V model as well as the induced gate noise with partial correlation to the channel thermal noise are all captured in the new "noise partition" model. In this model, two current and voltage noise source is used for modeling. The noise voltage source partitioned to the source side is given by:

$$\overline{v_d^2} = 4k_B T \theta_{tnoi} \frac{V_{dseff}\,\Delta f}{I_{DS}}, \tag{15}$$

and the noise current source put in the channel region with gate and body amplication is given by:

$$\overline{i_d^2} = \frac{4k_B T V_{dseff}\Delta f}{I_{DS}}\left[G_{DS} + \beta_{tnoi}(G_m + G_{mbs})\right]^2 - \overline{v_d^2}\left(G_{DS} + G_m + G_{mbs}\right)^2. \tag{16}$$

Finally, the power spectral density of the thermal noise current from the electrodes resistance is given by [5]:

$$S_{it,R_{g,d,s}} = \frac{4K_B T}{R_{g,d,s}} \cdot \frac{1}{2}. \tag{17}$$

Aside from the intrinsic noise sources, the thermal noise generated within the passive part is considered. By considering the noise sources as excited sources, the transistor noise behavior can be analyzed by using excited multi conductor transmission lines solutions [9].

As shown in Fig. 2, all the noise sources of any differential subsections of the model can be transformed into correlated input-referred voltage and current noise sources of a noise free network, by using circuit analysis [10]. Then, by using Kirchhoff's voltage (KVL) and current (KCL) laws for the differential segment, the frequency domain coupled first-order ordinary differential equations of the noise transmission line model of the transistor will be obtained:

$$\frac{d}{dz}\begin{bmatrix}\hat{V}\\ \hat{I}\end{bmatrix}_{(z,\omega)} = \begin{bmatrix}0 & -\hat{Z}\\ -\hat{Y} & 0\end{bmatrix}\begin{bmatrix}\hat{V}\\ \hat{I}\end{bmatrix}_{(z,\omega)} + \begin{bmatrix}\hat{v}_n\\ \hat{i}_n\end{bmatrix}_{(z)}, \tag{18}$$

where $[\hat{v}_n]_{(z)}$ and $[\hat{i}_n]_{(z)}$ are 1-by-3 matrices of the linear density of voltage and current noise sources, respectively. Equation (18) is in the same form as state-variable equation, thus the solution of it can be written as [11]:

$$\begin{bmatrix}\hat{V}\\ \hat{I}\end{bmatrix}_{(z,\omega)} = \hat{\Phi}\Big|_{(z-z_0)}\begin{bmatrix}\hat{V}\\ \hat{I}\end{bmatrix}_{(z_0,\omega)} + \int_{z_0}^{z}\hat{\Phi}\Big|_{(z-\tau)}\begin{bmatrix}\hat{v}_n\\ \hat{i}_n\end{bmatrix}_{(z)} d\tau. \tag{19}$$

By substituting $z_0 = 0$ and $z = W$, the effect of the internal noise sources on the voltage and current of the transistor port can be determined as follows:

$$\begin{bmatrix}\hat{V}\\ \hat{I}\end{bmatrix}_{(W,\omega)}=\begin{bmatrix}\hat{\Phi}_{11} & \hat{\Phi}_{12}\\ \hat{\Phi}_{21} & \hat{\Phi}_{22}\end{bmatrix}_{(\mathrm{W})}\begin{bmatrix}\hat{V}\\ \hat{I}\end{bmatrix}_{(0,\omega)}+\begin{bmatrix}\hat{V}_{NT}\\ \hat{I}_{NT}\end{bmatrix}_{(W)}, \quad (20)$$

where:

$$\begin{bmatrix}\hat{V}_{NT}\\ \hat{I}_{NT}\end{bmatrix}_{(W)}=\underbrace{\int_0^W\begin{bmatrix}\hat{\Phi}_{11} & \hat{\Phi}_{12}\\ \hat{\Phi}_{21} & \hat{\Phi}_{22}\end{bmatrix}_{(\tau)}d\tau}_{[\hat{A}(W)]_{6\times6}}.\begin{bmatrix}\hat{v}_n\\ \hat{i}_n\end{bmatrix}. \quad (21)$$

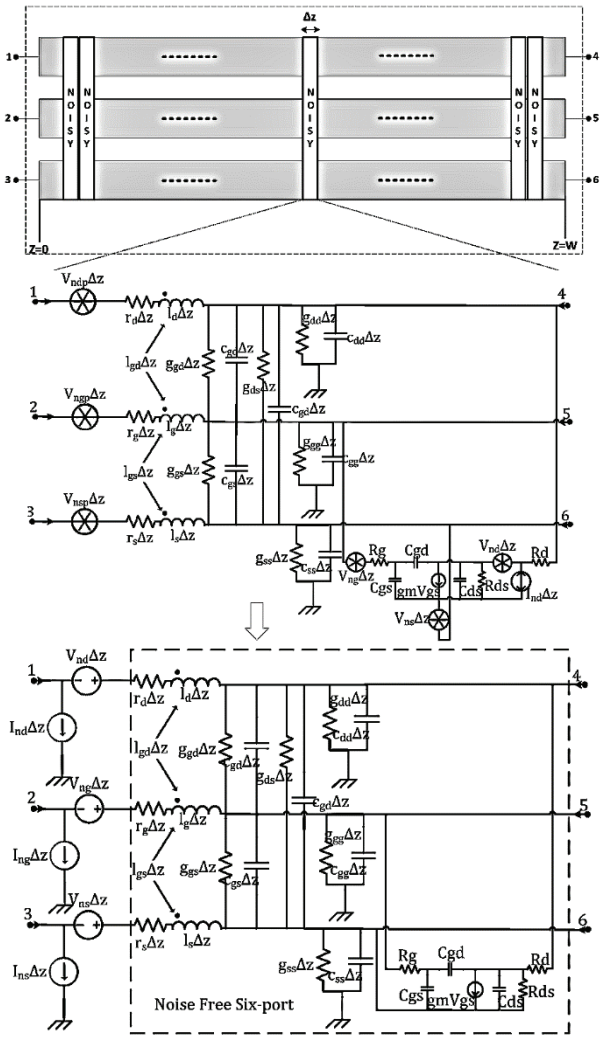

Fig. 2. Complete details of distributed noise model of the mm-wave MOSFET as excited three-coupled transmission line structure.

The distributed noise sources of differential part in (21) are assumed to be independent of the device width, since the BSIM4 model is chosen for them. The correlation matrix for admittance representation can be obtained by determination of the currents in short-circuited ports of transistor [12]. By enforcing boundary conditions to equation (20), the noise currents at the short-circuited ports, as a six-port active network, can be written in the following matrix form:

$$\begin{bmatrix}\hat{I}_{n0}\\ \hat{I}_{nW}\end{bmatrix}=\begin{bmatrix}-\hat{I}|_{(0,\omega)}\\ +\hat{I}|_{(W,\omega)}\end{bmatrix}=\underbrace{\begin{bmatrix}\hat{Z}^{-1} & \mathrm{K}\\ -\hat{Z}^{-1} & \mathrm{K}\end{bmatrix}}_{P}\times\begin{bmatrix}\hat{v}_n\\ \hat{i}_n\end{bmatrix}, \quad (22)$$

for $\mathrm{K}=-\hat{T}_I\hat{\gamma}^{-1}\sinh^{-1}(\hat{\gamma}W)(\cosh(\hat{\gamma}W)-1_{3\times3})\hat{T}_I^{-1}$. Finally, the correlation matrix for admittance representation of the six-port noise model of the MOSFET can be written as equation (23). CAU is the per-unit-length noise correlation matrix for chain representation of the transistor:

$$CY_{tr}=\begin{bmatrix}I_{n0}\\ I_{nW}\end{bmatrix}\begin{bmatrix}I_{n0}\\ I_{nW}\end{bmatrix}^{\dagger}=P\underbrace{\begin{bmatrix}\hat{v}_n\\ \hat{i}_n\end{bmatrix}\begin{bmatrix}\hat{v}_n\\ \hat{i}_n\end{bmatrix}^{\dagger}}_{CAU}P^{\dagger}. \quad (23)$$

III. RESULTS AND DISCUSSION

The proposed approach is used for modeling of a 130 nm bulk CMOS transistor. It is sufficient to consider introduced model for a single finger structure. Multiple fingers transistors can be accounted as parallel multiple single finger transistors. The transistor is biased at Vds = 1.2 V and Ids = 7 mA. As was mentioned in the previous section, the BSIM4 model [5], is used to compute elements and noise sources of active part and the per-unit-length parameters of passive part is evaluated by using numerical method of moments technique [7]. As shown in Fig. 1, the beginning of the gate and the end of drain electrodes are considered as the input and output nodes, respectively. Moreover, the source electrodes are grounded.

The scattering and noise parameters of proposed distributed model and Cadence SpectreRF post-layout simulation results are displayed in Figs. 3 and 4, for an NMOS transistor with gate width of 10 μm. The excellent broadband accuracy of the distributed model compared to the simulation results verifies that the introduced model is correct and complete. Furthermore, comparing these curves with lumped model, one can see that third models agreed well at low frequency but at high frequencies, the distributed effects of the transmission line capacitances and inductances along the device width become significant and can no longer be ignored. The scattering parameters of the transistor with gate width of 90 μm, over a frequency range of DC–100 GHz, calculated by using proposed distributed and lumped models are drawn in Fig. 5. The results clearly show that the distributed and lumped models are the same at the low frequency and by increasing the frequency, the difference between two models also increasing. The S11 and S21 of the transistor for three values of the gate width, 10, 60 and 90 μm, are plotted in Fig. 6.

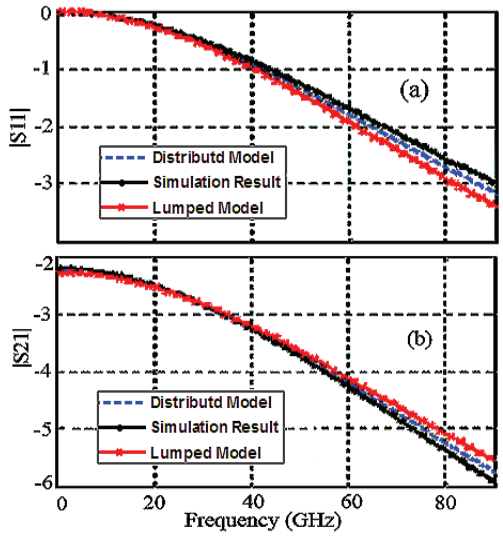

Fig. 3. Scattering parameters of 10 µm MOSFET.

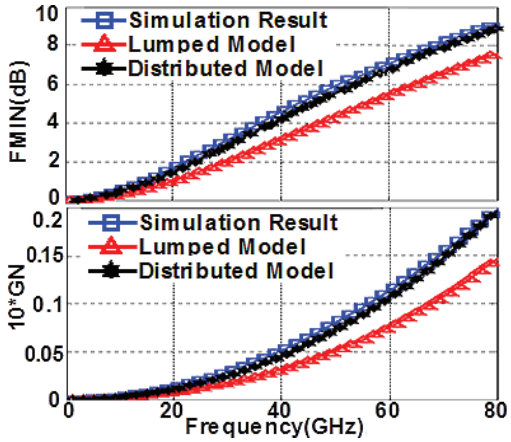

Fig. 4. Noise parameters of 10 µm MOSFET.

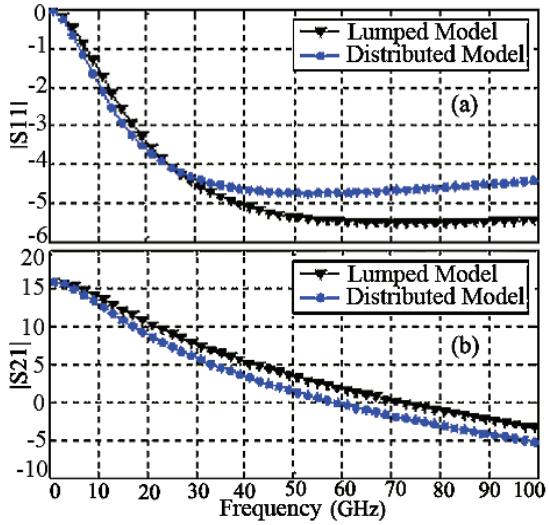

Fig. 5. Scattering parameters of 90 µm MOSFET.

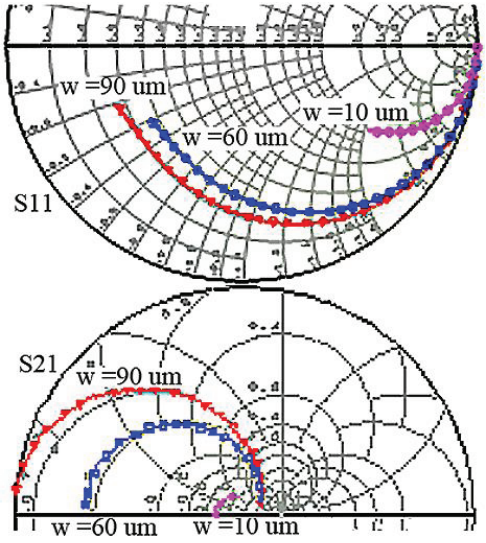

Fig. 6. Scattering parameters of 10, 60, and 90 µm MOSFETs computed by distributed model.

By using introduced model, four noise parameters, including minimum noise figure, normalized equivalent noise admittance, the amplitude and the phase of optimum reflection coefficient, are plotted in Fig. 7 and compared with lumped model. Moreover, Fig. 8 shows the behavior of minimum noise figure of the transistor for the different values of the gate width. Studying these figures illustrates the importance of distributed transmission line modeling of MOSFET by increasing the device width and the frequency.

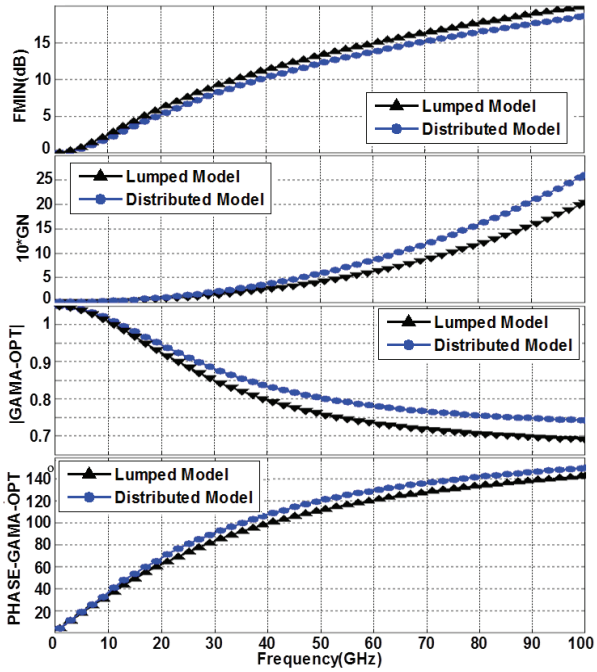

Fig. 7. Noise parameters of the MOSFET.

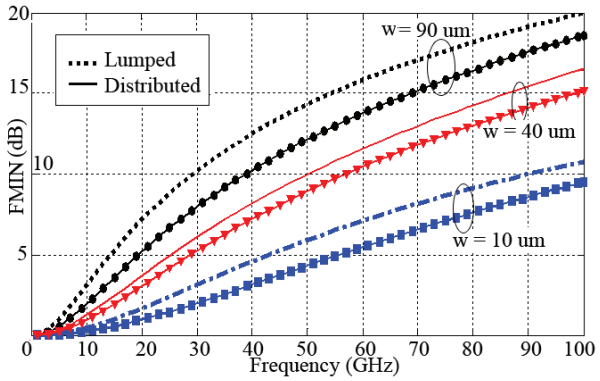

Fig. 8. Minimum noise figure of the MOSFET.

Figure 9 demonstrates the constant noise figure and available power gain circles of the MOSFET at 20 and 60 GHz. Thus, based on the information obtained from the proposed approach, accurate design of mm-wave circuits, containing the MOSFET, for a specified noise figure and available power gain is possible.

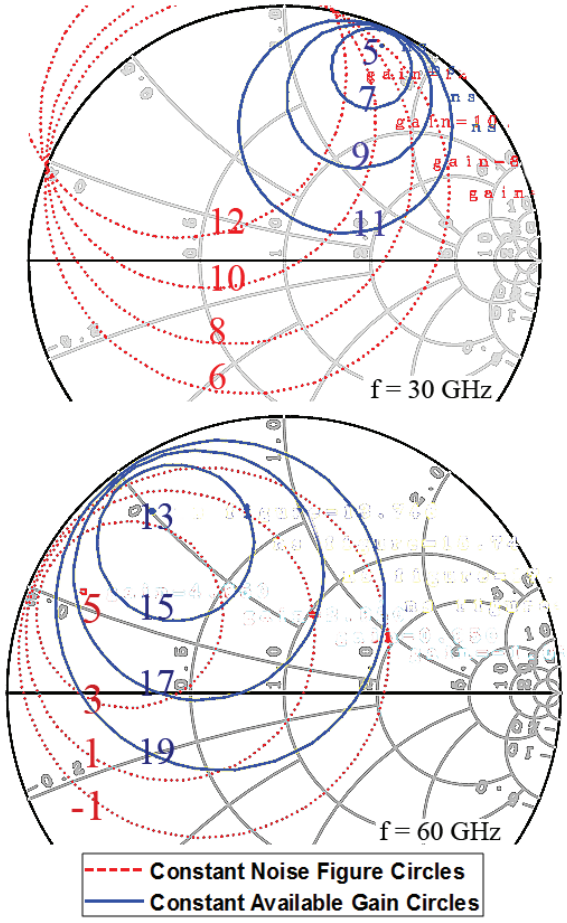

Fig. 9. Constant noise figure and available gain circles calculated by distributed model for f = 30 and 60 GHz.

IV. CONCLUSION

As the operating frequency of MOSFETs increases to the mm-wave range, the width of the device become comparable to the wave length. In such cases, the distributed transmission line effect needs to be considered accurately, in device modeling. According to that in the previous lumped models this effect wasn't considered, this paper introduces a new distributed transmission line signal and noise modeling and analysis of mm-wave MOSFET transistor. In this model, the MOSFET transistor is considered as the excited three-coupled active transmission line structure, exciting by noise equivalent sources distributed on its conductors. Comparing the signal and noise parameters of MOSFET calculated with the proposed distributed model and lumped model was shown that two models have the same results at low frequencies. But, by increasing frequency to the mm-wave range, where the electrodes widths are comparable with the wavelength, a difference appears between the results of two models. It is demonstrated that the distributed effects of the transmission line along the device width become significant and can no longer be ignored. Therefore, the accuracy of high-frequency noise simulation in the Nano-scale RF CMOS transistors can be facilitated by using the proposed model. Moreover, based on the proposed modeling approach, the influence of important factors such as the effect of electrode loading and the location and number of excitation/ extraction contact points, can be investigated and optimized for improving the performance of the mm-wave MOSFETs.

REFERENCES

[1] A. M. Niknejad and H. Hashemi, *mm-Wave Silicon Technology 60 GHz and Beyond*, Springer Science+Business Media, LLC, 2008.

[2] B. Razavi, R.-H. Yan, and K. F. Lee, "Impact of distributed gate resistance on the performance of MOS devices," *IEEE Trans. Circuits Syst. I*, vol. 41, pp. 750-754, Nov. 1994.

[3] E. Abou-Allam and T. Manku, "An improved transmission-line model for MOS transistors, *IEEE Transactions on Circuits and Systems - II: Analog and Digital Signal Processing*, vol. 46, no. 11, Nov. 1999.

[4] Y. Lin, M. Obrecht, and T. Manku, "RF noise characterization of MOS devices for LNA design using a physical-based quasi-3-D approach," *IEEE Transactions on Circuits and Systems - II: Analog and Digital Signal Processing*, vol. 48, no. 10, Oct. 2001.

[5] The BSIM 4.4 Manual, http://www-device.eecs.berkeley.edu/bsim4.

[6] A. Abdipour and A. Pacauds, "Complete sliced model of microwave FETs & comparison with

lumped model & experimental results," *IEEE Trans. on MTT*, vol. MTT-44, pp. 4-9, Jan. 1996.
[7] C. R. Paul, *Analysis of Multiconductor Transmission Lines*, 2nd edition, John Wiley & Sons, Inc., Hoboken, New Jersey, 2008.
[8] F. E. Hohn, *Elementary Matrix Algebra*, 2nd edition, Macmillan, New York, 1964.
[9] F. M. Tesche, T. K. Liu, S. K. Chang, and D. V. Giri, "Field excitation of multiconductor transmission lines," *Technical Report AFWL-TR-78-185*, Air Force Weapons Lab, Albuquerque, NM, 1979.
[10] B. Razavi, *RF Microelectronics. Upper Saddle River*, NJ: Prentice-Hall, 1998.
[11] "Useful matrix chain parameter identities for the analysis of multiconductor transmission lines," *IEEE Transactions on Microwave Theory and Techniques*, 23(9), 756-760, 1975.
[12] H. A. Haus and R. B. Adler, *Circuit Theory of Linear Noisy Networks*, M.I.T. Press, 1959.

Zahra Seifi was born in Iran in 1988. She obtained his B.Sc. in Electrical Engineering in 2011 and the M.Sc. in Communication in 2013 from Amirkabir University, Tehran, Iran. Her research areas include High frequency signal and noise EM modeling of active devices and circuits and RF, microwave and mm-wave MMIC circuit design .She is currently a Ph.D. student at Amirkabir University of Technology.

Abdolali Abdipour was born in Alashtar, Iran, in 1966. He received his B.Sc. degree in Electrical Engineering from Tehran University, Tehran, Iran, in 1989, his M.Sc. degree in Electronics from Limoges University, Limoges, France, in 1992, and his Ph.D. degree in Electronic Engineering from Paris XI University, Paris, France, in 1996. He is currently a Professor with the Electrical Engineering Department, Amirkabir University of Technology (Tehran Polytechnic), Tehran, Iran. He has authored four books in Persian and authored or co-authored over 300 papers in refereed journals and local and international conferences. His research areas include wireless communication systems, RF/microwave/millimeter-wave circuit and system design, electromagnetic modeling of active devices and circuits, high-frequency electronics (signal and noise), and nonlinear modeling. Currently, he is Director of the Institute of Communications Tech. and Applied Electromagnetics, Amirkabir University of Technology, Tehran, Iran.

Rashid Mirzavand received the B.Sc. degree from Isfahan University of Technology, Isfahan, Iran, in 2004, M.Sc. and Ph.D. degrees from Amirkabir University of Technology, Tehran, Iran, in 2007 and 2011, all in Electrical Engineering. In 2009, he joined the Centre for Analysis, Scientific Computing and Applications, Eindhoven University of Technology, Eindhoven, The Netherlands, as a visiting Ph.D. student. Since 2011, he is a Research Assistant Professor with the Institute of Communications Tech. and Applied Electromagnetics, Amirkabir University of Technology, Tehran, Iran. He is the recipient of the Alberta Innovates Technology Futures (AITF) Post-doctoral Fellowship and is currently a Research Associate with the Intelligent Wireless Technology Laboratory, University of Alberta, Edmonton, Canada. His research interests are in the areas of intelligent integrated sensors and antennas, Microwave & mm-wave circuits and wireless systems, and computational electromagnetic.

Dynamic Modeling of Linear Actuator Using Fuzzy System to Approximate Magnetic Characteristics

Meisam Hassani and Abbas Shoulaie

Department of Electrical Engineering
Iran University of Science and Technology (IUST), Tehran, Iran
meisam_hassani@elec.iust.ac.ir, shoulaie@iust.ac.ir

Abstract ─ This paper proposes a dynamic model of a linear actuator using a fuzzy system to approximate its magnetic subsystem. Magnetic characteristics of the linear actuators indicate a nonlinear behavior, making the whole system complex. Deriving an accurate and proper model, results in the implementation of different control methods in the simulation procedure. This research developed dynamic equations of linear actuator with closed type magnetic circuit. Due to high capabilities of fuzzy approximators in the modeling of nonlinear systems, they are employed to approximate the magnetic subsystem of the linear actuator. According to the results, the model described in this paper, shows significant improvements in comparison with the previous models. Moreover, the proposed model apart from the nominal area, could accurately predict the behavior of linear actuator for out of the nominal operation area. This matter is important in transient situations and short-term overloads. High accuracy and performance is obviously demonstrated by comparing experimental and simulation results both in static and dynamic features.

Index Terms ─ Dynamic modeling, flux linkage, fuzzy system, linear actuator, magnetic characteristics.

I. INTRODUCTION

Linear actuators are widely used in industrial applications due to their simple construction, high ruggedness, and low prime cost. Electromagnetic valves [1], fluid flow control in hydraulic systems [2] and magnetic suspension are some typical applications. Many contactors and relays working in switching (on-off) state have the same operation of linear actuators [3]. There are two types of linear actuators, known as on-off and proportional [4]. The former is simpler owing to its specific design and applicable structure.

On-off actuators are being used in electrical contactors and electromagnetic valves. Since position control in force operators with high accuracy is so common, the entire plunger trajectory in proportional actuator is controlled. Transfer function in proportional actuators is more linear than on-off actuators but the design in proportional actuators is much more complex. Also, proportional actuators require position sensor; thus, they are more expensive [4]. Converting an on-off actuator to a proportional one using power electronic converters and external sensors with operating range of below 10 mm has been investigated in [5]. Having extracted a precise model for linear actuator, various control methods could be applied and also improvement on proportional operation of on-off actuators would be obtained. Figure 1 shows the structure of linear actuators. Linear actuators are separated into two actuators: actuator with open type magnetic circuit, and actuator with closed type magnetic circuit [6]. Linear actuators with open magnetic circuit are described by their linear behavior; whereas, actuators with closed magnetic circuit show nonlinear behavior due to core saturation. Owing to more rugged mechanical and electrical structure and also larger force density, closed magnetic circuit actuators are more popular. Moreover, to increase the output force, those actuators are designed in a way that saturation occurs in rated current [7]. Therefore, nonlinear magnetic behavior of the linear actuators should be taken into account in their modeling.

One of the most important parts in the modeling of linear actuator with closed magnetic circuit is magnetic characteristics of motor. They are directly in correlation with electrical and mechanical subsystems. Moreover, nonlinear behavior of magnetic characteristics makes the whole system nonlinear and more complex.

To date, different models have been proposed to describe dynamic characteristics of linear actuators. Those models considered different aspects and effective parameters of the linear actuator behavior. In some researches, for linear actuator modeling, several numerical methods have been proposed such as FEM[1]. In order to achieve a mathematical model, inductance estimation, force levels, and eddy currents effect is investigated [8]-[13]. In [14], a nonlinear model including

[1] Finite Element Method

Submitted On: July 31, 2013
Accepted On: December 11, 2014

experimental detection of the system parameters is proposed to attain transient magnetic characteristics. Moreover, hysteresis and saturation features have been taken into account and have been focused on "system designing" in the modeling. In [15], core saturation curve is separated into linear and nonlinear parts and a model has been presented employing a first-order and second-order approximation. The experimental data are gained by employing a sinusoidal voltage to actuator winding.

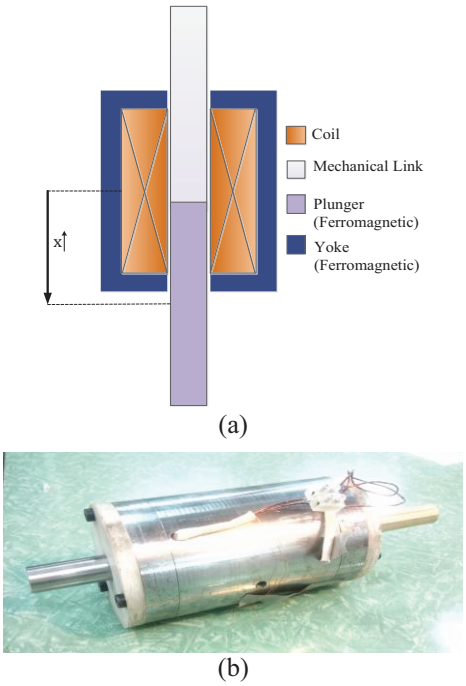

(a)

(b)

Fig. 1. (a) Schematic of a linear actuator, and (b) a laboratory sample of actuator.

It should be noted that, in the modeling of linear actuator, in addition to the nominal operation area of the motor, a proper model must be sufficiently accurate for the currents out of nominal current. This matter is important in transient situations and short-term overloads that may be occurred in the motor. There is no remarkable study about this in previous researches. The proposed model in this paper, in addition to the nominal operating area, could accurately predict the behavior of actuator, out of nominal operation area. This has been achieved by using capabilities of the fuzzy systems.

Fuzzy theory has so many applications in various systems especially nonlinear ones. Describing or controlling of the systems where there is connoisseur person experience or input-output data, leads to appropriate results. In order to completely model the linear actuator, information of both fields is used in this paper. Having used fuzzy theory in this paper, a full description of linear actuator characteristic is presented which covers both nominal and over-current areas with adequate accuracy. A proper dynamic model is subsequently proposed according to system's dynamic equations. Eventually, comparison between simulation and experimental results, both in dynamic and static states, validates the proposed model. The results indicate desired accuracy both in dynamic and static states and also contain both nominal and over-current areas.

II. SYSTEM'S DYNAMIC EQUATIONS

According to the most researches, the equations of an electrical motor are divided into three parts: electrical, mechanical, and magnetic. In order to achieve an appropriate and accurate model, a block diagram consisting of electrical, magnetic, and mechanical blocks, is proposed in Fig. 2. Supply voltage and load force are inputs of the system, and plunger position is the output.

Electrical and magnetic subsystems connect with each other through λ and i; whereas, magnetic block is in relation with mechanical one through F_{mag} and x.

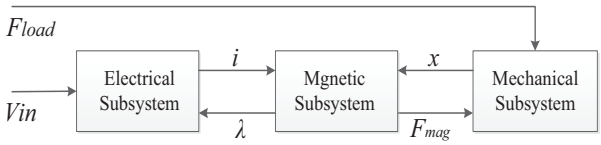

Fig. 2. Block diagram of linear actuator's model.

A. Mechanical analysis

Sub d, assuming that the actuator is in vertical position, dynamic equation of the mechanical subsystem is defined as:

$$-W_p - F_f + F_{mag} - F_{load} = m_p \ddot{x}. \quad (1)$$

In equation (1), W_p is the plunger weight, F_f is the friction force, F_{mag} is the magnetic force, and F_{load} is the load force. m_p is the mass of the plunger and x is the position of the plunger. The friction force value of the actuator is in proportion with the plunger velocity [16].

B. Electrical analysis

As shown in Fig. 1 (a), the linear actuator contains a winding fed by a voltage source. The total equation in electrical subsystem is:

$$V = Ri + N\frac{d\phi}{dt}. \quad (2)$$

In (2), V is the actuator's voltage, R is the winding resistance, N is the number of winding turns, and ϕ is the flux inside the winding. Considering $\lambda = N\varphi$, equation (2) would be rewritten as the following:

$$V = Ri + \frac{d\lambda}{dt}, \tag{3}$$

λ is the flux linkage that plays a fundamental role in the modeling. Its value is defined by magnetic analysis at any plunger position and anytime. V is the instantaneous voltage of winding, therefore when the actuator is modeled by power electronic components with PWM[2], it is modeled with $V=0$ at off periods, due to the presence of Freewheeling diode.

C. Magnetic analysis

According to the system's structure, the flux linkage value in linear magnetic systems is determined regarding the ampere-turn of the winding and equivalent magnetic reluctance (R_{eq}):

$$\frac{Ni}{R_{eq}} = \phi = \frac{\lambda}{N}, \tag{4}$$

$$\lambda = \frac{N^2 i}{R_{eq}}. \tag{5}$$

In (5), R_{eq} is the equivalent magnetic reluctance from the viewpoint of the winding. When the magnetic behavior of the system is linear, R_{eq} and therefore λ, are easily calculated via analyzing the linear magnetic circuits. However, it should be noted that the design must be conducted considering the saturation region in order to increase the output force and the effective density of force [7]. Thus, using equation (5) in the actuators with closed type magnetic circuit is not effective.

In the actuators with closed type magnetic circuit, the flux linkage value and therefore the inductance, apart from the plunger position, is dependent on the electrical operating point. This relation is nonlinear and is affected by the saturation. Accordingly, inductance could not be used only as a function of position. Thus, the flux linkage of the actuator should generally be considered as a function of x and i.

Figure 3 shows sets of λ-i curves related to the actuator for different positions of the plunger. In order to attain these characteristics, some experiments on the actuator are applied and sets of input-output data are obtained. Applying an adjustable alternating voltage (autotransformer) results in the measurement of the coil's current and voltage, and therefore λ values is obtained for different currents and positions. According to Fig. 3, the magnetic characteristics get nonlinear when $x<70$ mm. It means that for $x<70$ mm, the actuator behavior is nonlinear.

In the dynamic modeling of the actuator, magnetic characteristics (λ-x-i curves) are highly significant considering dynamic equations of current and voltage and magnetic force definition.

[2] Pulse Width Modulation

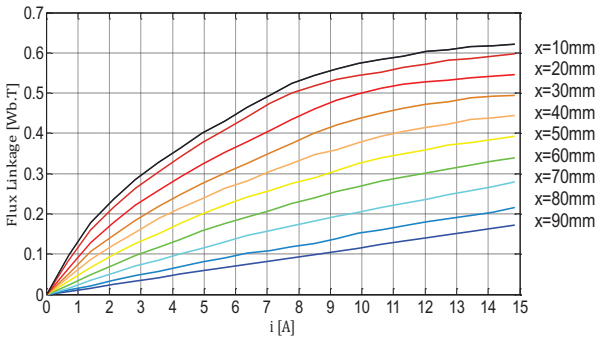

Fig. 3. Flux linkage characteristics of the actuator versus current for different positions of the plunger.

D. Calculation of magnetic force

Overall, there are different methods to calculate the magnetic force [17]-[21]. One of the most common methods is using the stored energy in the system. According to the theory of this method, magnitude and direction of the force in the conservative vector fields equals to the negative of the gradient of stored potential energy in those fields. Hence, if a magnetic body has a moving part, a force in the direction exerts on the moving part to decrease the magnetic potential energy stored in the body [6]. Thus, the force exerted on the moving part is expressed as:

$$F_{mag} = -\frac{\partial W_f'(i,x)}{\partial x}\Big|_{i=cons}, \tag{6}$$

where W_f' is co-energy and is defined by:

$$W_f'(i,x) = \int_0^i \lambda(i,x)\,di. \tag{7}$$

In linear magnetic systems, like actuators with open type magnetic circuit or systems that saturation effect is ignorable, the co-energy and the energy terms are equal. Moreover, λ has a linear relation with i and the output force is described as equation (8) after the inductance is defined:

$$F_{mag} = \frac{1}{2} i^2 \frac{dL(x)}{dx}. \tag{8}$$

When the magnetic characteristics is nonlinear and core saturation is not ignorable, force values should be calculated according to the (6) and (7), thus (8) is not usable.

III. FLUX LINKAGE DETERMINATION

As explained previously, the magnetic characteristic data of the linear actuators is obtained from experimental measurements. In order to complete the actuator modeling, data should be employed properly. The simplest method to use the data is lookup table. Applying the LUT decreases the simulation accuracy. In order to define the input intermediate values which is among the LUT inputs' values, linear

interpolation method should be utilized. Since the derivatives of λ with respect to current and position are required in the simulation, the parameters are calculated discretely, thus it is different from the system nature. Based on the mentioned reasons, LUT has not been used in this research for modeling.

Another method to use the data of λ is to approximate λ-x-i characteristics employing polynomial functions [22]-[24]. The main advantage of this method is significant decrease in the calculations complexity. Nevertheless, the relatively much increase of the error in the extrapolation is the fundamental disadvantage. The current increase results in decrease in the flux linkage increase rate, whereas in the polynomial approximation, the estimated value of the flux linkage out of the relevant range might get large values. Since for the large values of ac current, there is restriction in the characteristic measurement, this issue is regarded as a significant disadvantage. By contrast, the actuator can easily operate in high DC currents. On the other hand, in the short-term over currents and transient situations, the amount of winding current could be increased in comparison with the nominal current. However, a proper model must predict the behavior of the system with the minimum error in different situations.

Fuzzy systems, regarded as general approximators, would be employed to estimate unknown nonlinear functions with any required accuracy. However, one of the fuzzy system features is that saturation occurs for the values out of the available data scope. This feature shows the primary advantage of fuzzy systems.

A. Flux linkage fuzzy approximator

Various engineering subjects are applied in fuzzy theory. A significant application is that a fuzzy system with a desired design is usually a general approximator [25]. It means, any system approximation with any accuracy could be performed via a proper design. Therefore, a desired fuzzy system was designed in order to model the magnetic characteristic of the system. Moreover, this fuzzy system estimates the flux linkage for different values of the plunger's position and the winding current. In order to design and model a fuzzy system, its features are required. These features may involve a connoisseur person experience, experimental results or a combination of both.

In order to use a fuzzy system, if-then rule is defined and equation (9) is described by [25]:
If x_1 is A_1 and x_2 is A_2 then y is B,

$$f(x_1,x_2)=\frac{\sum_{l=1}^{M} y^l.\mu_{A1}^l(x_1).\mu_{A2}^l(x_2)}{\sum_{l=1}^{M}\mu_{A1}^l(x_1).\mu_{A2}^l(x_2)}, \tag{9}$$

where the parameters μ_{A1}^l and μ_{A2}^l are membership functions of the input variables and would be triangular, pseudo-triangle, trapezium, and Gaussian. When triangular or trapezius functions are applied, the system is approximated to a piecewise linear curve. Equation (9) deals with a fuzzy system with Mamdani inference engine, individual fuzzifier, center average defuzzifier, and if-then fuzzy rule base. In this paper, Gaussian functions are used as input membership functions. Hence, the fuzzy system considering equation (9) is described as [25]:

$$f(x_1,x_2)=\frac{\sum_{l=1}^{M} y^l\left[a_1^{\,l}\exp(-(\frac{x_1-\bar{x}_1}{\sigma_1^{\,l}})^2).a_2^{\,l}\exp(-(\frac{x_2-\bar{x}_2}{\sigma_2^{\,l}})^2)\right]}{\sum_{l=1}^{M}\left[a_1^{\,l}\exp(-(\frac{x_1-\bar{x}_1}{\sigma_1^{\,l}})^2).a_2^{\,l}\exp(-(\frac{x_2-\bar{x}_2}{\sigma_2^{\,l}})^2)\right]}. \tag{10}$$

According to available data and the change range of each variable, a membership function is defined with respect to different states and different values of each variable. The output membership functions are defined in a same procedure. Finally, a fuzzy system is designed by defining a Mamdani inference engine and fuzzy rule base such as if-then rule.

B. Fuzzy system design

In order to extract the magnetic characteristics of the linear actuator, experimental measurements were conducted and λ values were calculated for different plunger positions with 10 mm steps and different effective currents with 0.5 Amp. steps. Thus, there are 11 and 22 states for the position and the current respectively, and the conclusion is 11×22=242 states for input-output pairs. Applying these pairs in equation (10) and considering some assumptions, a fuzzy system in order to model the actuator is obtained. According to the measured data, the following vectors and matrix are defined as:

$$\begin{cases}\bar{i}=[\bar{i}_k]\\ \bar{x}=[\bar{x}_j] \qquad k=1,2,...,22\ ,\ j=1,2,...,11\ ,\\ \bar{\lambda}=[\bar{\lambda}_{kj}]\end{cases} \tag{11}$$

where vectors $\bar{i}$ and $\bar{x}$ are the points of input data and matrix $\bar{\lambda}$ is the output data.

It should be noted that current value of the actuator may outnumber the maximum tested value of the system. As mentioned before, this phenomenon would be occurred in short-term overloads or transient situations. Thus, one membership function for the values higher than the maximum current is defined. The value of this membership function is permanently "1" for the current values higher than the maximum actuator current. Defined membership function together with other membership functions of the actuator current

is employed to complete the design and to avoid the flux linkage decrease with current increase.

Equation (10) is rewritten as:

$$\lambda(i,x)=\frac{\sum_{k=1}^{23}\sum_{j=1}^{11}\bar{\lambda}_{kj}.\exp(-(\frac{i-\bar{i}_k}{\sigma_i})^2).\exp(-(\frac{x-\bar{x}_j}{\sigma_x})^2)}{\sum_{k=1}^{23}\sum_{j=1}^{11}\exp(-(\frac{i-\bar{i}_k}{\sigma_i})^2).\exp(-(\frac{x-\bar{x}_j}{\sigma_x})^2)}. \quad (12)$$

According to equation (12), different values of λ could be calculated for different currents and positions. σ_i and σ_x are smoothing parameters. The smaller the values of σ_i and σ_x get, the less difference the function values in sample points obtains, compared to real values. However, the function error increases for intermediate or out of range values, thus the function is not regarded as general. The function is smooth when the values of σ_i and σ_x are large enough.

In practice, through trial and error attempt and comparing the function characteristics with measured ones, proper values for σ_i and σ_x could be acquired. It should be remarked that proper values of σ_i and σ_x are different from each other due to the different change range of current and position. Figure 4 shows the membership function of input parameters.

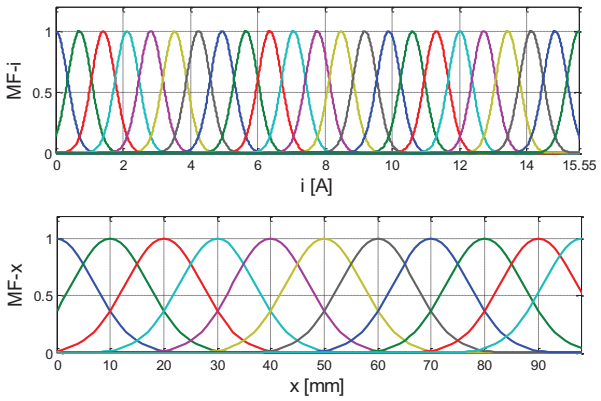

Fig. 4. Membership functions of the designed system as input parameters.

IV. RESULTS

The results of proposed model were thoroughly investigated in this section and were compared with the experimental data. Therefore, an experimental setup was designed and built to conduct different experiments and measure the system characteristics. Features of the system would be highlighted as a static features and dynamic behavior. Static features contain flux linkage values and actuator output force for different currents and different positions of the plunger. Moreover, due to the changes of the system's state variable along the time, actuator dynamic behavior could be analyzed with injecting step input. The designed setup in this research has the possibility of measuring magnetic force of the actuator for different positions and via adjustable current values. In addition, it's possible to inject a step voltage with different amplitudes and to measure plunger's current and position values.

Experimental setup includes a linear actuator, a power electronic convertor, a position sensor and other control and measurement circuits. Power electronic convertor is a bulk convertor which can inject regulated and controllable voltage into the actuator. Position sensor is an IR distance sensor and a *DSPIC30F4011* microcontroller is the main controller of system. Moreover, a sampling device (*USB47n-A, Advantech Automation*) is used to sample the required data. Figure 5 illustrates the experimental setup. The results of the actuator's static features and dynamic behavior are investigated in the following.

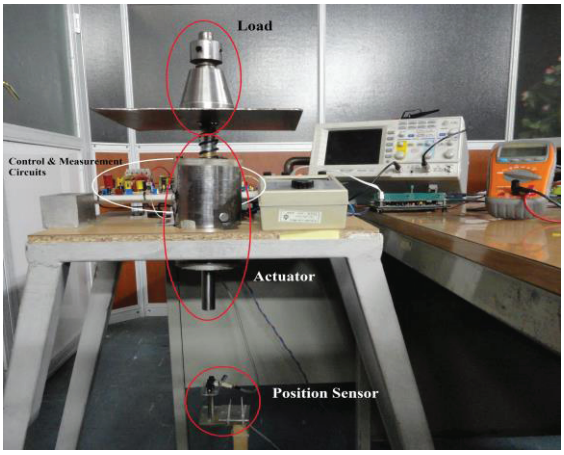

Fig. 5. Experimental setup to study the actuator.

A. Static features

In order to validate the designed system, first the flux linkage values and their change procedure, stemmed from the designed system, are compared with their real values. As shown in Fig. 6, the flux linkage values are calculated for large currents to ensure that the flux linkage value change is not inappropriate for the current increase. As mentioned before, for $x<70$ *mm*, the actuator behavior is nonlinear. The results indicate a closely match and less error of the approximator. Figure 7 shows the error value of the flux linkage estimation for different values of x. Figure 7 demonstrates that the error value is less than 2.5 percent and the total average of the approximation error is 1.22%.

The next step is to compare the magnetic force values concluded from designed system and equation (6), with experimental values. Figure 8 shows the comparison for some different positions. Within the measured data range of the flux linkage, the

approximation is highly accurate and the estimation for out of the range, however, is satisfactory. According to (3), if the behavior of the magnetic characteristics is linear, the force value, when x is constant, will be in relation with the square of the current. However, as it's clear in Fig. 8, this issue would not occur due to saturation. The average values of force estimation error for different positions are illustrated in Table 1. According to Table 1, x=40 has the most error and x=60 has the least error. Mean value of the estimation error related to the output force is 2.17%.

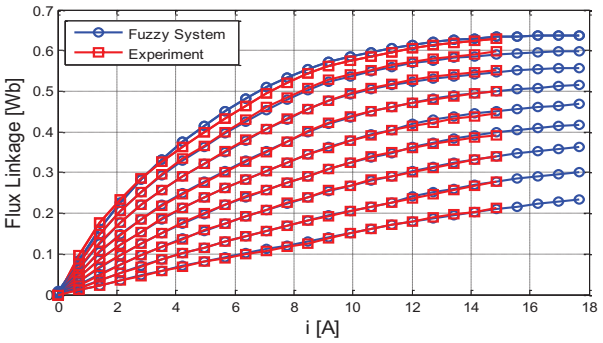

Fig. 6. Comparison of the flux linkage values for different currents and positions.

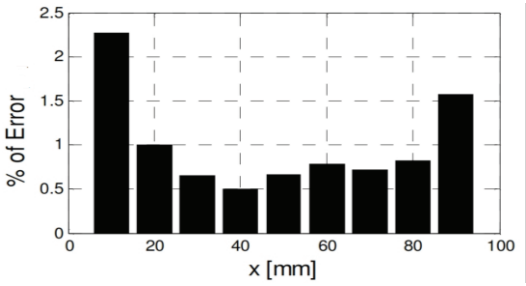

Fig. 7. Flux linkage error for different positions.

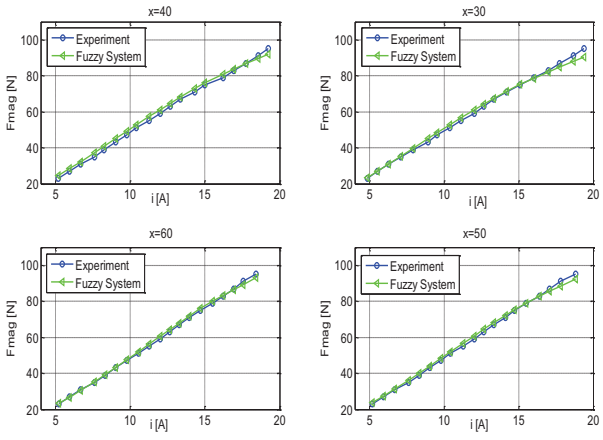

Fig. 8. Experimental and fuzzy approximator comparison for the output force.

Table 1: Estimation error of output force

Position [mm]	30	40	50	60
Error [%]	1.99	3.4	1.98	1.3

B. Dynamic behavior

In order to describe the dynamic behavior of the linear actuator in accordance with the equations of Section 3 and the designed fuzzy system, the simulation of the actuator is implemented. To determine magnetic force and also change rate values of the flux linkage versus position and current, the designed fuzzy system was applied. Dynamic behavior of the actuator for different loads was compared with experimental results. Injecting a step waveform as the input voltage to the actuator coil, time waveforms of the winding current and the plunger position for different loads were measured and recorded. Afterwards, dynamic behavior of the actuator was investigated and compared with the simulation results under equal conditions. Figure 9 shows two waveforms in relation to these comparisons for 35[N] and 55[N] loads. The current and position changes of the winding is determined in Fig. 9. Ripples related to position change for 55[N] load diagram originates from the noise in the position sensor. This noise has been increased when the current produced and increased. The comparison between the waveforms indicates desired accuracy of the modeling.

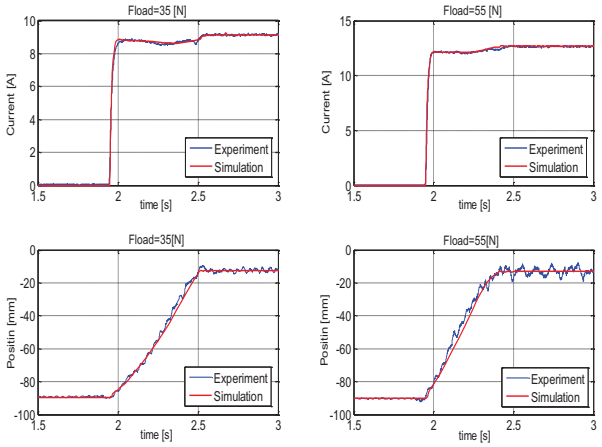

Fig. 9. Dynamic behavior of the linear actuator for two different loads.

V. CONCLUSION

Dynamic modeling of the linear actuator has been investigated in this paper. Having analyzed dynamic equations for mechanical, electrical and magnetic subsystems, the flux linkage was highlighted as a fundamental parameter making the system behavior nonlinear. Moreover, the flux linkage had a relatively high impact on mechanical, electrical and magnetic subsystems. Due to high capabilities of fuzzy systems

to approximate nonlinear systems, a desired fuzzy system was designed to estimate the flux linkage of the linear actuator. Since behavior of the system is known and also according to the data concluded from the measurement of the actuator's magnetic characteristic, this fuzzy approximator was designed such as a system with Gaussian membership functions, individual fuzzifier, Mamdani inference engine and center average defuzzifier. In order to validate the designed fuzzy system, static data of the actuator was employed. These features include the values of the flux linkage and the magnetic force of the actuator. The comparison between the designed fuzzy system's estimation and experimental measurements indicates that the error of the flux linkage estimation is 1.22% and the error of the magnetic force estimation is 2.17%. This proves that the accuracy of the proposed system is desirable both in nominal area and out of it. In addition, dynamic behavior of the actuator and its simulation were compared to validate the proposed model. This comparison was drawn for 35[N] and 55[N] loads with different currents. Having injected a step voltage to the winding, the changes of the plunger's position and the winding current over a period of time were recorded and then compared. The comparison in experimental and simulation fields demonstrates a proper accuracy for the proposed dynamic modeling.

REFERENCES

[1] P. Eyabi and G. Washington, "Modeling and sensorless control of an electromagnetic valve actuator," *Mechatronics*, 16, pp. 159-175, 2006.

[2] D. T. Kovácsházy, "Modelling of a linear proportional electromagnetic actuator and possibilities of sensorless plunger position estimation," *12th International Carpathian Control Conference (ICCC)*, pp. 89-93, May 2011.

[3] J. Katic, N. Maridor, Y. Perriard, and D. Ladas, "Sensorless position detection of a linear actuator using the resonance frequency," *Electrical Machines and Systems, ICEMS International Conference*, Nov. 2009.

[4] S. T. Wu and W. N. Chen, "Self-sensing of a solenoid valve via phase detection," *International Conference on Advanced Intelligent Mechatronics*, Suntec Convention and Exhibition Center, Singapore, Jul. 2009.

[5] M. F. Rhaman, N. C. Cheung, and K. W. Lim, "Converting switching solenoid to a proportional actuator," *JIEE Proc. Int. Power Electron. Conf., IPEC'95*, vol. 3, pp. 1628-1633, Japan, Apr. 1995.

[6] A. Mosallanejad, "Design and optimization of multilevel reluctance accelerator," *Ph.D. Thesis* (in Persian), IUST, 2011.

[7] S. A. Nasar and I. Boldea, *Linear Lectrical Motors: Theory, Design, and Practical Application*, Prentice-Hall, 1987.

[8] A. Shiri and D. Esmaeil Moghadam, "Analytical and FEM based calculation of electromagnetic forces exerted on cylindrical coils due to their own current," *ACES Journal*, vol. 27, no. 11, pp. 866-872, Nov. 2012.

[9] B. Tomczuk and M. Sobol, "Field analysis of the magnetic systems for tubular linear reluctance motors," *IEEE Tran. on Magnetics*, vol. 41, no. 4, Apr. 2005.

[10] A. Mosallanejad and A. Shoulaie, "Calculation of coil inductance in tubular linear reluctance motor using three dimensional FEM," *Electrical Review*, Nov. 2011.

[11] A. Espírito Santo, M. R A. Calado, and C. M. P. Cabrita, "Dynamic simulation of electromagnetic actuators based on the co-energy map," *ACES Journal*, vol. 25, no. 12, pp. 1118-1128, Dec. 2010.

[12] G. W. Slade, "Fast finite-element solver for a reluctance mass accelerator," *IEEE Tran. on Magnetics*, vol. 42, no. 9, Sep. 2006.

[13] B. Tomczuk and M. Sobol, "A field-network model of a linear oscillating motor and its dynamics characteristics," *IEEE Trans. on Magnetics*, vol. 41, no. 8, Aug. 2005.

[14] N. D. Vaughan and J. B. Gamble, "The modeling and simulation of a proportional solenoid valve," *Transactions of the ASME*, vol. 118, pp 120-125, Mar. 1996.

[15] N. C Cheung, K. W. Lim, and M. F. Rahman, "Modeling a linear and limited travel solenoid," *IEEE 19th International Conference of on Industrial Electronics*, 1993.

[16] P. B. Eyabi, "Modeling and sensorless control of solenoidal actuators," *Ph.D. Thesis*, Ohio State University, 2003.

[17] A. Shiri and A. Shoulaie, "Calculation of the magnetic forces between planar spiral coils using concentric rings," *ACES Journal*, vol. 25, no. 5, pp. 468-475, May 2010.

[18] A. Shiri and A. Shoulaie, "Investigation of frequency effects on the performance of single-sided linear induction motor," *ACES Journal*, vol. 27, no. 6, pp. 497-504, Jun. 2012.

[19] A. Musolino, R. Rizzo, and E. Tripodi, "Tubular linear induction machine as a fast actuator: analysis and design criteria," *Progress in Electromagnetics Research*, vol. 132, pp. 603-619, 2012.

[20] S. Babic and C. Akyel, "Magnetic force between inclined circular filaments placed in any desired position," *IEEE Trans. on Magnetics*, vol. 47, pp.

69-80, 2012.
[21] J. H. Alwash and L. J. Qaseer, "Three-dimension finite element analysis of a helical motion induction motor," *ACES Journal*, vol. 25, no. 8, pp. 703-712, Aug. 2010.
[22] G. Yuan, "Speed control of switched reluctance motors," *M.S. Thesis*, Hong Kong University of Science and Technology, Aug. 2000.
[23] C. L. Xia, M. Xue, and T. N. Shi, "A new rapid nonlinear simulation method for switched reluctance motors," *IEEE Tran. on Energy Conversion*, vol. 24, no. 3, 2009.
[24] A. A. Abdallh, G. Crevecoeur, and L. Dupre, "A robust inverse approach for magnetic material characterization in electromagnetic devices with minimum influence of the air-gap uncertainty," *IEEE Tran. on Magnetics*, vol. 47, no. 10, 2011.
[25] L. X. Wang, A Course in Fuzzy Systems and Control, Prentice-Hall, 1997.

Meisam Hassani was born in Zanjan, Iran in 1987. He received the B.Sc. degree from Zanjan University and M.Sc. degree from Iran University of Science and Technology (IUST), both in Electrical Engineering in 2010 and 2013, respectively. His areas of research interests include linear electric machines, electromagnetic systems and actuators, power electronic simulation and design.

Abbas Shoulaie was born in Isfahan, Iran, in 1949. He received the B.Sc. degree from Iran University of Science and Technology (IUST), Tehran, Iran, in 1973, and the M.Sc. and Ph.D. degrees in Electrical Engineering from U.S.T.L, Montpellier, France, in 1981 and 1984, respectively. He is a Professor at the department of Electrical Engineering, IUST. He is the author of more than 100 journal and conference papers in the field of power electronics, electromagnetic systems, electrical machine, linear machine and HVDC.

A New Closed-Form Expression for Dispersion Characteristics of Fundamental Mode of SIW by Least Squares Method

Mohammad GH. Alijani and Mohammad H. Neshati

Department of Electrical Engineering
Ferdowsi University of Mashhad, Mashhad, Iran
rrdirin@yahoo.com, neshat@um.ac.ir

Abstract ─ A new and accurate closed-form expression is introduced using least squares method (LSM) to calculate propagation constant of substrate integrated waveguide (SIW) at its fundamental mode of operation. The derived equation is a function of geometrical parameters of the structure and accurately estimates cutoff frequency of the dominant mode. The LSM is used to determine the effective width of the SIW structure. A review and comparisons with recently published simulation and measurement results are also provided, which verify the accuracy of the proposed method.

Index Terms ─ Dispersion, least squares method (LSM), substrate integrated waveguide (SIW).

I. INTRODUCTION

In recent years the SIW technology has been widely used in implementation of microwave devices and antennas [1-5] due to their attractive features such as simple and planar structure. A variety of numerical methods including method of moments (MOMs), finite difference time domain (FD-TD), boundary integral resonant mode expansions (BI-RME), method of lines (MOL), and mode matching have been reported in literature to study the dispersion characteristics of these structures. In spite of the accuracy of those methods, they consume lots of time and need large amount of memory.

In this paper, an accurate closed-form expression is derived using least squares method to calculate the effective width of the SIW structures. The effects of geometrical parameters of the SIW structure on propagation constant and cutoff frequency are investigated for four specific SIW structures. It is shown that the proposed method accurately estimates dispersion characteristic of the SIW and an excellent agreement is obtained between the results of the proposed method with those obtained by measurement.

II. THEORY OF THE PROPOSED METHOD

A linear system of m equations in n unknowns $x_1,..., x_n$ is a set of equations of the form:

$$\begin{cases} a_{11}x_1 + ... + a_{1n}x_n = b_1 \\ a_{21}x_1 + ... + a_{2n}x_n = b_2 \\ \cdots\cdots\cdots\cdots\cdots \\ a_{m1}x_1 + ... + a_{mn}x_n = b_m \end{cases}. \quad (1)$$

The system is called linear because each variable x_j appears in the first power only, just as in the equation of a straight line. $a_{11},\ldots, a_{mn}$ are given numbers, called the coefficients of the system. $b_1,\ldots, b_m$ on the right are also given numbers. A solution of (1) is a set of numbers $x_1,\ldots,x_n$ that satisfies all m equations. From the definition of matrix multiplication we see that m equations of (1) may be written as a single vector equation $\mathbf{Ax}=\mathbf{b}$, where the coefficient matrix $\mathbf{A} = [a_{jk}]$ is $m\times n$ matrix, $\mathbf{x}$ and $\mathbf{b}$ are column vectors.

It is assumed that the coefficients a_{jk} are not all zero, so that $\mathbf{A}$ is not a zero matrix. Note that x has n components, whereas b has m components. If $m=n$ and $\mathbf{A}$ is nonsingular, the answer is simply $\mathbf{x}=\mathbf{A}^{-1}\mathbf{b}$. But if $m>n$ so that we have more equations than unknowns, the problem is called over determined, and generally no $\mathbf{X}$ vector satisfies $\mathbf{Ax}=\mathbf{b}$ exactly. Given an m-*by*-n matrix $\mathbf{A}$ and an m-by-1 vector $\mathbf{b}$, the least squares problem is to find an n-by-1 vector $\mathbf{X}$ which minimize $\mathbf{Ax}=\mathbf{b}$ [6]. The norm of the vector $\mathbf{Ax}-\mathbf{b}$ is defined as $\| \mathbf{Ax}-\mathbf{b} \| = \sqrt{(\mathbf{Ax}-\mathbf{b})^T (\mathbf{Ax}-\mathbf{b})}$, in which $(\mathbf{Ax}\text{-}\mathbf{b})^{\mathrm{T}}$ is transpose of the $\mathbf{Ax}\text{-}\mathbf{b}$ matrix. The least squares solution is $\hat{\mathbf{x}}$ vector which minimize error expression $E = \| \mathbf{Ax}-\mathbf{b} \|^2$. This is the sum of squares of the errors in m equations ($m>n$). The best $\hat{\mathbf{x}}$ comes from the normal equations $\mathbf{A}^T\mathbf{A}\hat{\mathbf{x}} = \mathbf{A}^T\mathbf{b}$. If marix $\mathbf{A}$ is left-invertible, then $\hat{\mathbf{x}} = (\mathbf{A}^T\mathbf{A})^{-1}\mathbf{A}^T\mathbf{b}$ is the unique solution of the least squares problem [6].

III. SIW STRUCTURE

The geometry of the SIW structure with its physical parameters is shown in Fig. 1. It consists of two rows of conducting cylinders implanted in a

Submitted On: May 23, 2014
Accepted On: April 8, 2015

dielectric substrate which connects two conductor parallel plates at the top and bottom of the substrate. Therefore, a synthetic rectangular waveguide filled with dielectric material is made in planar form. The diameter of cylindrical posts is d and they are separated in transverses and axial plane by S and W respectively.

Experimental and numerical methods reveal that the propagation characteristics of dominant mode of the SIW structures are equivalent to those of an equivalent metallic rectangular waveguide with the effective width of W_{eff}. So, it is assumed that the effective width is generally related to the geometrical parameters. Thus, two expressions using unknown coefficients are defined for evaluating the effective width of SIW structures [7-10].

$$W_{eff} = \gamma_1 W + \gamma_2 \frac{d}{S} W + \gamma_3 \frac{d^2}{S} + \gamma_4 \frac{d^2}{W}, \quad (2)$$

$$W_{eff} = \sigma_1 W + \sigma_2 S + \sigma_3 d + \sigma_4 \frac{d^2}{S} + \sigma_5 \frac{d^2}{W}. \quad (3)$$

Unknown coefficients can be calculated using LSM procedure. Table 1 shows the calculated unknown coefficients.

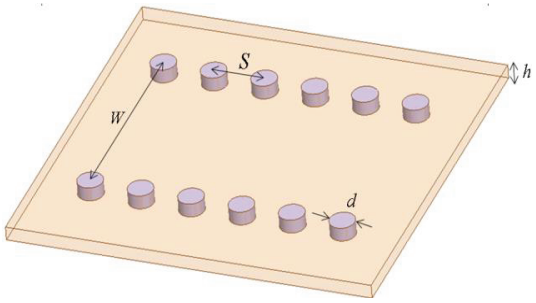

Fig. 1. Geometry of the SIW structure.

Table 1: Calculated unknown coefficients using LSM

i	γ_i	σ_i
1	1.3	1.103
2	-1.026	0.552
3	7.957	-3.222
4	-22.015	4.553
5	0	-10.974
E(error)	2.9×10^{-4}	2.3×10^{-4}

IV. RESULTS VERIFICATION

To verify the accuracy of the proposed method, four examples are presented.

A. Example I

In the first one, a specific SIW structure with geometrical parameters of W=3.97 mm, d=0.635 mm, S=1.016 mm and relative permittivity of 9.9 is considered. Numerical results for cutoff frequency of TE_{10} mode of this structure is shown in Fig. 2. It can be seen that a very good agreement is obtained between the measured results and those obtained by the proposed W_{eff} using Equation 3. A small deviation between results can be seen, but still proposed W_{eff} method using Equation 2 in this paper accurately predicts propagation constant of the structure.

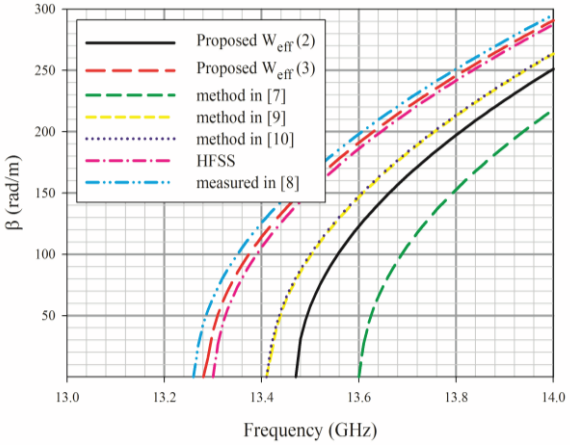

Fig. 2. Propagation constant of TE_{10} mode versus frequency for SIW structure I.

B. Example II

In the second example, another specific SIW structure with geometrical parameters of W=7.2 mm, S=2 mm and relative permittivity of 2.33 is considered. Cutoff frequency of TE_{10} mode of this SIW structure versus via diameter d, is shown in Fig. 3. These results indicate that both proposed W_{eff} using Equations 2 and 3 predicts same dispersion characteristics and agree well with other published methods.

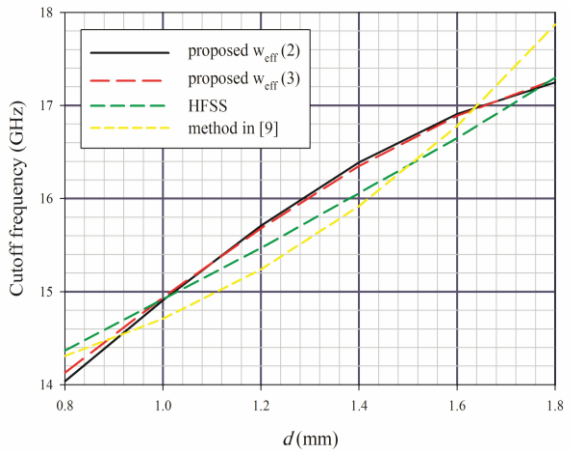

Fig. 3. Cutoff frequency of TE_{10} mode versus via diameter d for the 2^{d} SIW structure.

C. Example III

A SIW structure with parameters W=5.25 mm, d=0.8 mm, S=1.5 mm and ε_r=2.2 is considered in the third example. Numerical results of the propagation constant of the mentioned structure at TE_{10} mode versus frequency of the presented method in this paper are shown in Fig. 4. It shows that our results and measured results in [10] agree very well.

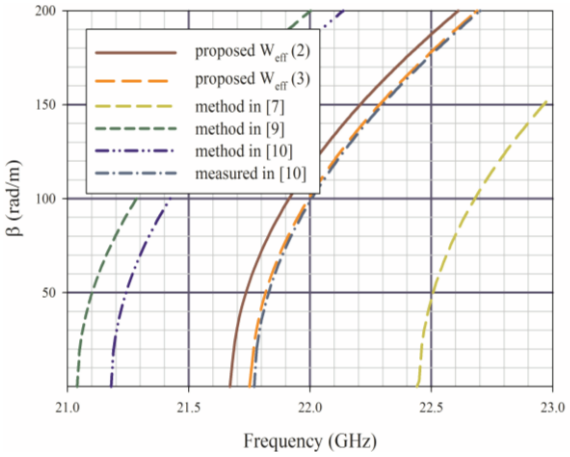

Fig. 4. Propagation constant of TE_{10} mode versus the 3[d] SIW structure.

D. Example IV

In the fourth example, a specific SIW structure with geometrical parameters of S=1.5 mm and relative permittivity of 2.2 is considered. Numerical results of cutoff frequency for this structure at TE_{10} mode are shown in Fig. 5 versus W, width of the structure for different values of via diameter d. It can be concluded that the results of the proposed method in this paper agree very well with those presented in [9].

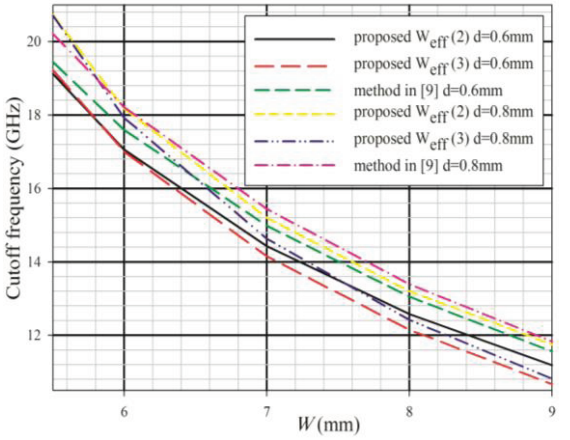

Fig. 5. Cutoff frequency of TE_{10} mode versus W for different values of d for 4[th] SIW structure.

V. CONCLUSION

In this paper, an accurate closed-form expression is introduced using least squares method (LSM) to calculate the effective width of the substrate integrated waveguide (SIW). The effects of geometrical parameters of the structure on propagation constant and cutoff frequency are investigated for four specific SIW structures. The results for propagation constant and cutoff frequency of the dominant mode of the SIW structures are in a very good agreement with other reported simulation and measured results. The proposed method using LSM accurately predicts the dispersion characteristics of the SIW for a wide range of structure parameters. Therefore, it could be used for designing wide variety of SIW structure.

REFERENCES

[1] F. Giuppi, A. Georgiadis, M. Bozzi, S. Via, A. Collado, and L. Perregrini, "Hybrid electromagnetic and non-linear modeling and design of SIW cavity-backed active antennas," *Journal of Applied Computational Electromagnetic Society, ACES*, vol. 25, no. 8, 2010.

[2] S. E. Hosseini-Nejad, N. Komjani, H. Oraizi, and M. T. Noghani, "Optimum design of SIW longitudinal slot array antennas with specified radiation patterns," *Journal of Applied Computational Electromagnetic Society, ACES*, vol. 27, no. 4, 2012.

[3] D. Jiang, Y. Xu, R. Xu, and W. Lin, "A novel band pass filters using complementary split ring resonator loaded half mode substrate integrated waveguide," *Journal of Applied Computational Electromagnetic Society, ACES*, vol. 28, no. 2, 2013.

[4] W. Shao and J. L. Li, "Design of a half-mode SIW high-pass filter," *Journal of Applied Computational Electromagnetic Society, ACES*, vol. 26, no. 5, 2011.

[5] R. Li., X. Tang, and F. Xiao, "A novel substrate integrated waveguide square cavity dual mode filter," *Journal of Electromagnetic Waves and Applications*, vol. 23, no. 2, pp. 17-18, 2009.

[6] C. Wylie, *Advanced Engineering Mathematics*, McGraw-Hill, New York, 1960.

[7] W. Che, K. Deng, D. Wang, and Y. L. Chow, "Analytical equivalence between substrate-integrated waveguide and rectangular waveguide," *IET Microwave Antennas Propagation*, vol. 2, no. 1, pp. 35-41, 2008.

[8] D. Deslandes and K. Wu, "Accurate modeling, wave mechanism, and design considerations of substrate integrated waveguide," *IEEE Trans. Microwave Theory & Techniques*, vol. 54, no. 6 pp. 2516-2526, 2006.

[9] F. Xu and K. Wu, "Guided-wave and leakage characteristics of substrate integrated waveguide," *IEEE Trans. Microwave Theory & Techniques*, vol. 53, no. 1, pp. 66-73, 2005.

[10] Y. Cassivi, L. Perregrini, P. Arcioni, M. Bressan, K. Wu, and G. Conciauro, "Dispersion characteristics of substrate integrated rectangular waveguide," *IEEE Microwave and Wireless Components Letters*, vol. 12, no. 9, pp. 333-335, 2002.

Mohammad Gh. Alijani was born in Mazandaran, Iran, 1988. He received the B.Ss. degree in Electrical Engineering from the University of Mazandaran, Babol, Iran, in 2011 and the M.Sc. degree in Electrical Engineering from Ferdowsi University of Mashhad, Mashhad, Iran, in 2013. He is interested in electromagnetic, microwave and millimeter-wave active and passive devices, antennas, and electromagnetic wave scattering.

Mohammad H. Neshati (M'07) was born in Yazd, Iran. He received the B.Sc. degree in Electrical Engineering from Isfahan University of Technology, Isfahan, Iran, the M.Sc. degree from Amir-Kabir University of Technology, Tehran, Iran, and the Ph.D. degree from the University of Manchester (UMIST), Manchester, U.K.

His current research works include electromagnetic, antenna theory and design, and microwave active and passive circuit design. Neshati is a Member of the *IEEE* Antennas and Propagation Society (AS-P) and the Microwave Theory and Techniques Society (MTT-S).

Effect of Various Slot Parameters in Single Layer Substrate Integrated Waveguide (SIW) Slot Array Antenna for Ku-Band Applications

S. Moitra [1] and P. S. Bhowmik [2]

[1] Department of Electronics & Communication Engineering
Dr. B. C. Roy Engineering College, Durgapur, West Bengal-713206, India
souravmoitra25@yahoo.in

[2] Department of Electrical Engineering
National Institute of Technology, Durgapur, West Bengal-713209, India
psbhowmik@gmail.com

Abstract ─ Extended study on SIW slot array antenna based on substrate integrated waveguide (SIW) has been proposed in this paper. Unlike recent publications, the effect of offset gap, gap between the slots and the gap between the last slot with the edge of the SIW antenna are extensively studied and effective formulation for proper positioning of the slots has been done. The structure consists of an array of slot antenna designed to operate in Microwave Ku Frequency bands. The basic structure is designed over a dielectric substrate with dielectric constant of 3.2 and with a thickness of 0.782 mm. The design consists of a SIW antenna fed with a microstrip to SIW transition. Multiple slot array effects are also being studied and analyzed using CST full wave EM Simulator. The designs are fabricated and supported with variation of return loss and radiation pattern characteristics due to appropriate slot offset. The analysis is being carried out to support integration to system-on-substrate (SoS) which promises more compact layouts.

Index Terms ─ Substrate Integrated Waveguide (SIW), slot array, slot offset, System-on-Substrate (SoS), Ku-band, Di-electric Filled Waveguide (DFW).

I. INTRODUCTION

Substrate integrated waveguide (SIW) has emerged as a new concept for millimeter-wave (mm-wave) integrated circuits and systems for the next decade due to their manifold advantages. SIW yields high performance from very compact planar circuits.

Recent past witnessed several substrate integrated waveguide (SIW) slot array antennas have been analyzed for their wide application in millimeter-wave communication systems due to advantages like high gain, efficiency and low-profile [1]. They are found to have manifold applications collision avoidance automotive radar, monopulse radar and synthesis aperture radar (SAR). Slotted SIW antennas also have special characteristics like accurate beam forming as well as low side lobe levels [2]. These antennas also find application in high-speed wireless communication and direct broadcast satellite systems which require specific linear or circular polarization.

The concept of waveguide slot antenna has been implemented on SIW slot antenna arrays in this study and several aspects are elaborately studied and presented with required details.

II. SIW ANTENNNA DESIGN

SIW are integrated waveguide-like structures fabricated by using two rows of conducting cylinders and slots embedded in a dielectric substrate that connect two parallel metal plates.

This concept was proposed by Bozzi, Xu, Deslandes and Wu in several papers. The non-planar rectangular waveguide can thus be made in planar form compatible with existing planar processing techniques [1]-[2], as in Fig. 1.

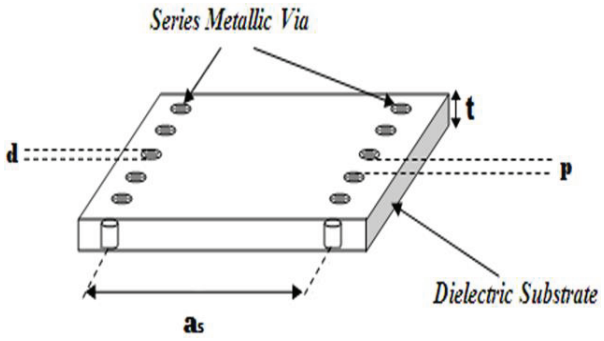

Fig. 1. Basic SIW structure realized on a dielectric substrate.

Submitted On: December 12, 2014
Accepted On: June 4, 2015

SIWs exhibit propagation characteristics similar to the ones of classical rectangular waveguides. The modes of the SIW practically coincide with a subset of the modes of the rectangular waveguide, namely with the TE_{n0} modes, with n=1, 2, … In particular, the fundamental mode is similar to the TE_{10} mode of a rectangular waveguide, with vertical electric current density on the side walls. TM modes cannot exist in the SIW, due to the gaps between metal vias; in fact, transverse magnetic fields determine longitudinal surface current. Due to the presence of the gaps, longitudinal surface current is subject to a strong radiation, preventing the propagation of TM modes. Moreover, SIW structures preserve most of the advantages of conventional metallic waveguides, namely, high quality-factor and high power handling capability [3].

Stern, et. al., has presented the theory of longitudinal slots over waveguide section in [2], where method of moments type solution yield the design parameter of the longitudinal slots as well as the offset. Henry, et. al., applied the concept for development of millimeter wave slot antennas over multi-layer substrates at 70 GHz bands in [4].

This concept was further developed with study on 79 GHz antennas by Cheng, et. al., in [5]. However, Ku-band slot array antennas have been presented by Navarro, et. al., in [7] with ten element linear resonant longitudinal SIW slot arrays. In all these articles, the designers obtained good results with the efficient use of inter slot spacings and slot offsets as needed for their designs.

This has been the major area of concern in this paper and it is found that the slot spacing and slot offset has direct effect on the performance of the design. This aspect, which was to some extent undescribed till date, and our study presents full details of these effects with accurate formulations which will prove to be the basic building blocks starting with SIW slot antenna array designs. Zeng, et. al., successfully studied the SIW slot array effects producing dual band structures in [8]. Several other related designs and studies are obtained in [9]-[11].

The proposed structure is fed using conventional microstrip line. The section of the microstrip line connecting the radiating surface has been tapered for proper impedance matching. The dimension of the taper is properly optimized with CST Microwave Studio to ensure maximum power transfer to the proposed SIW slot array antenna. The structure used is commonly known to us as 'Microstrip-to-SIW Transition,' as in Fig. 2. Several other transition techniques can be consulted in [2].

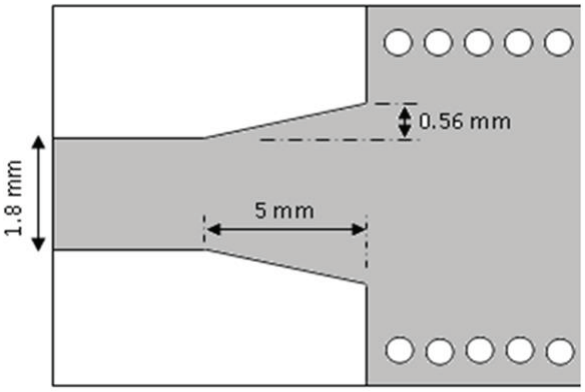

Fig. 2. Microstrip-to-SIW Transition.

The design equations for SIW, which may be given as:

$$a_s = a_d - \frac{d^2}{0.95p}, \tag{1}$$

where, a_s is the separation between via rows (centre to centre), a_d is the width of di-electric filled waveguide (DFW), d is the diameter, p is the pitch as shown in Fig. 1.

The cut-off frequency of the SIW can be obtained using the above design equations:

$$f_c = \frac{C}{2W_{eff} \times \sqrt{\varepsilon_r}}. \tag{2}$$

In this paper, the antenna has been designed to resonate at frequency of 17.4 GHz. The dimensions of the slots are important for the antenna to behave as a slot antenna. The dimensions of the slots can be obtained in [6] with the help of the following relations:

$$b = \frac{\lambda_0}{\sqrt{2(\in_r + 1)}}. \tag{3}$$

Dimension of c as in Fig. 3, doesn't matter much but should be less than half of b. The gap between centre to centre of slots g' is considered as $\lambda_g/2$ in several articles [3]-[5], whereas the gap between the last slot and the closing face (edge) g has been extensively analysed for obtaining a maximum return loss at the impedance bandwidth. The offset slot gap is denoted by d. To implement accurate analysis of these gaps (g and g') for exact positioning of the slots, all necessary plots are provided in this paper as obtained using CST Microwave Studio.

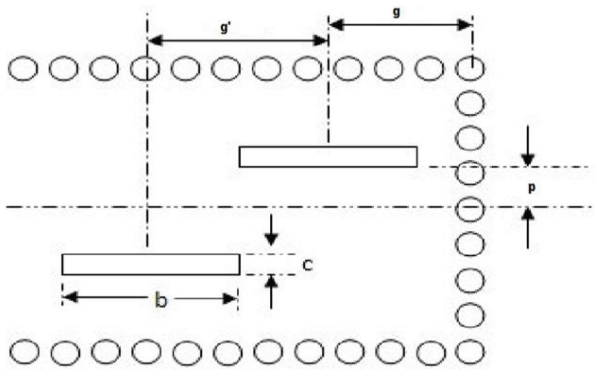

Fig. 3. Slot dimensions and gap between slots.

The proposed structure as obtained after a microstrip to SIW transition with 2 slots is depicted in Fig. 4. The top and bottom view of the fabricated prototypes are shown in Fig. 5. Comparison of the return loss of the 2 slot structure as obtained using EM CAD tool and after measurement is provided in Fig. 6. The antenna has been found to resonate at 17.5 GHz with a return loss of 23 dB for a slot offset of 0.25 mm.

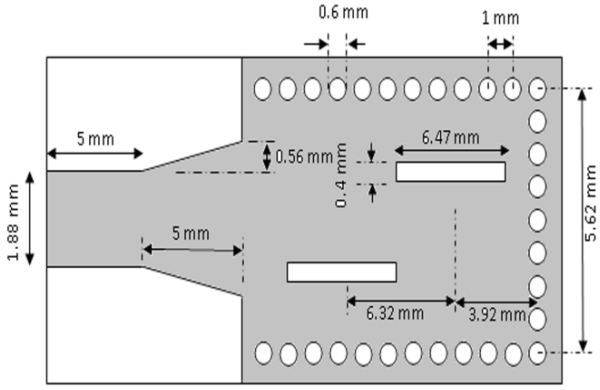

Fig. 4. Dimension for 2 slot SIW array antenna.

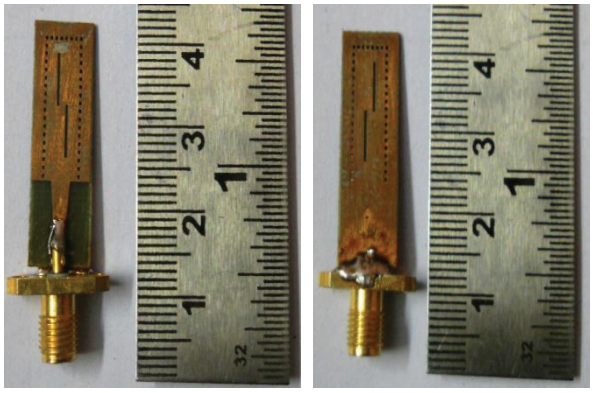

Fig. 5. Fabricated prototype of SIW slot antenna with 0.25 mm offset; top (left) and bottom (right).

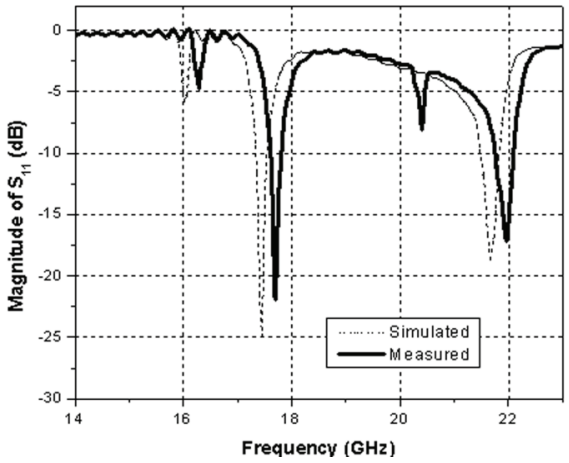

Fig. 6. Simulated and measured return loss for 2 slot SIW array antenna.

The antenna as noticed from the S-parameter tends to resonate at another frequency at about 21.5 GHz (image frequency/secondary resonance), which happens to be a function of the distance between the edges of the antenna to the last radiating slot. In this paper, primary focus is to study the effect of offset gap variation over the return loss and the gain of the SIW antenna. After obtaining proper offset gap, the effects of *g* & *g′* are studied further.

III. PARAMETRIC ANALYSIS

The variation of several antenna parameters are analyzed with variation of offset gap. Figure 7 depicts the variation of return loss as well as frequency obtained by varying the slot offset gap. The analysis clearly shows that for smaller offset gap, the return loss increases while antenna resonating frequency shifts to the lower side of the band.

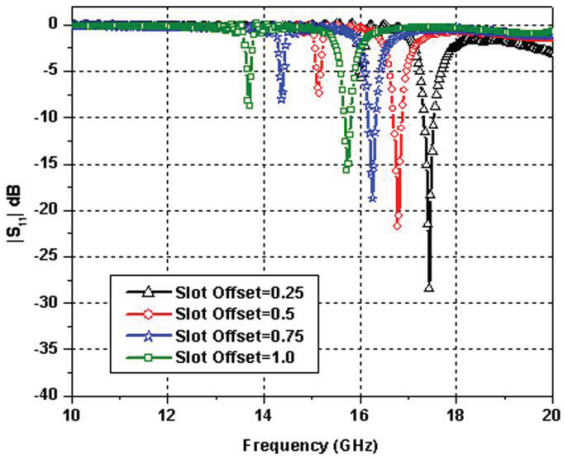

Fig. 7. Parametric analysis of several slot offset gap (p).

The fabricated SIW slot antennas with different slot offsets are shown in Fig. 8. Positioning of the slots, i.e., the slot offset has its effects over the resonating frequency, return loss and the gain of the radiating systems. The resonating frequency of the antenna is found to vary inversely with the increase of the offset. This can be related to the increased obstructions caused by the slots to the surface current of conventional rectangular waveguides, and hence, the slight shift in the return loss and gain of the system has been observed.

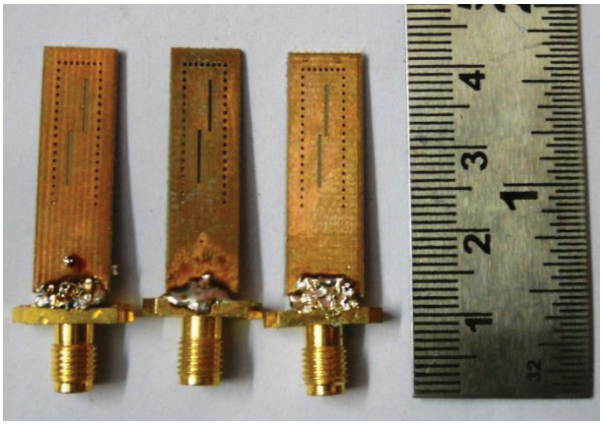

Fig. 8. Fabricated SIW slot antenna prototypes with different slot offsets.

The experimental set-up for measurement of the fabricated prototypes is shown in Fig. 9.

Fig. 9. Experimental set-up for radiation pattern measurement.

Also for lower offset, an improved return loss characteristics have been observed which is found to degrade with increase of offset values. The system shows better gain with lower offset values. The results of extensive studies as mentioned above have been shown in Fig. 10, Fig. 11 and Fig. 12.

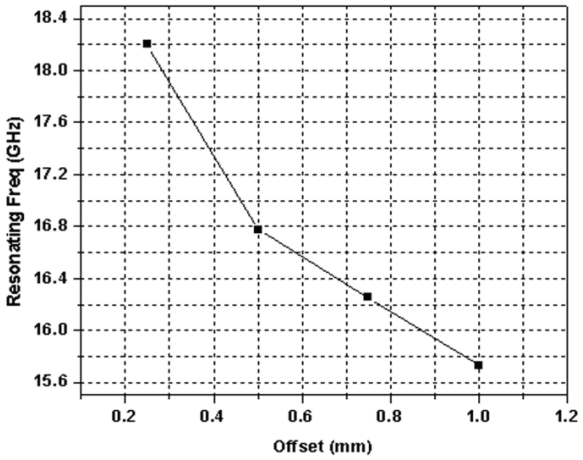

Fig. 10. Variation of resonating frequency (GHz) for variation of slot offset gap (p) (measured).

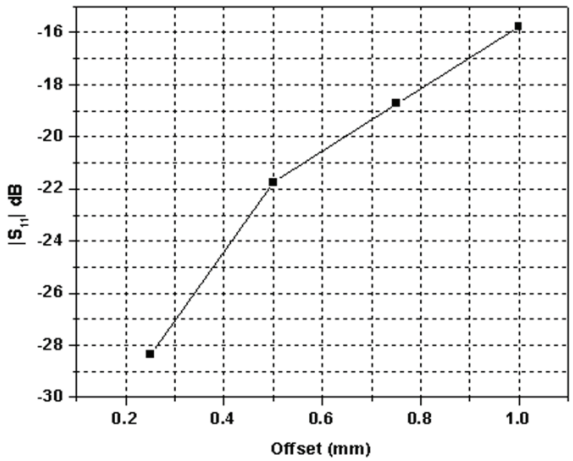

Fig. 11. Variation of return loss for different slot offset gap (p) (measured).

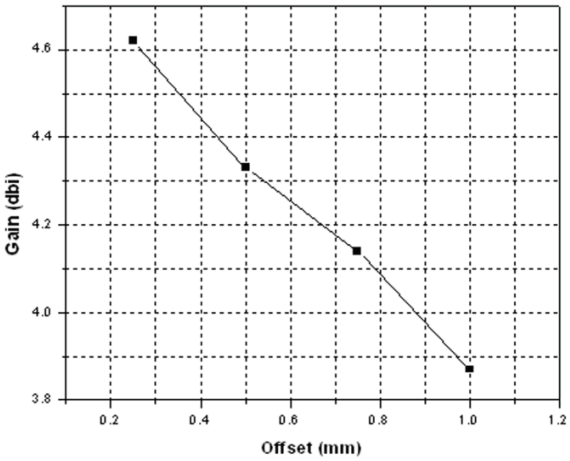

Fig. 12. Variation of antenna gain for different slot offset gap (p) (measured).

Detailed analysis on the effect of the gap between slots *g'* is also studied and presented with appropriate outcome. The results re-established that for a gap of $\lambda g/2$, maximum return loss will be achieved. The study further provides possible effects arise for gap length other than $\lambda_g/2$. The effect of the secondary resonance of the antenna has been found to vary with various slot gap *g'* and position of the slot from the end wall *g*. The return loss of the secondary resonance varies with spacing between the slots. For a gap of about 6 mm between the slots, both the return loss of the resonating frequency and the return loss of the secondary resonance have been found with acceptable results. The effects of s and *g'* over the various SIW slot antenna paramters are shown in Figs. 13-16. The results provide direct solution for several slot effects and enhance the possibility to design more compact layouts.

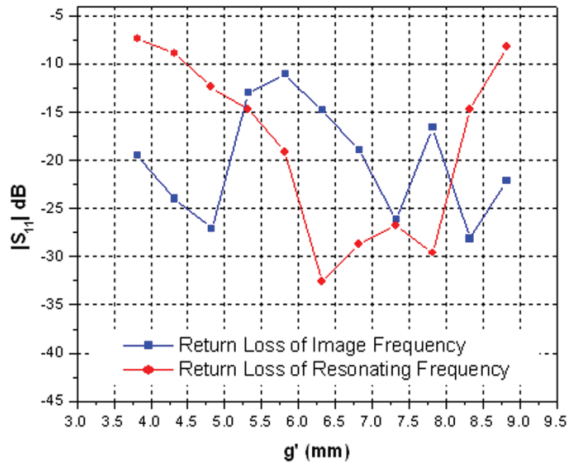

Fig. 13. Effect of various slot gap *g'* for on return loss of resonating frequency and image frequency (measured).

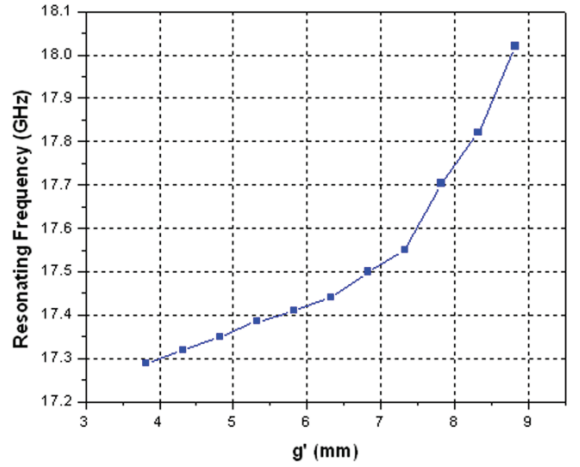

Fig. 14. Effect of various slot gap *g'* for on resonating frequency (measured).

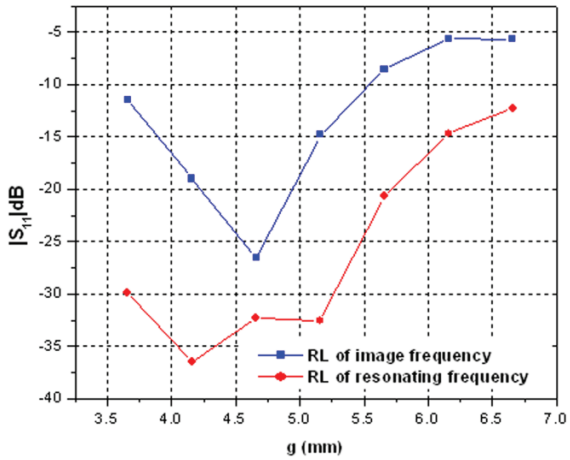

Fig. 15. Effect of slot position from end wall *g* on return loss of resonating frequency and image frequency (measured).

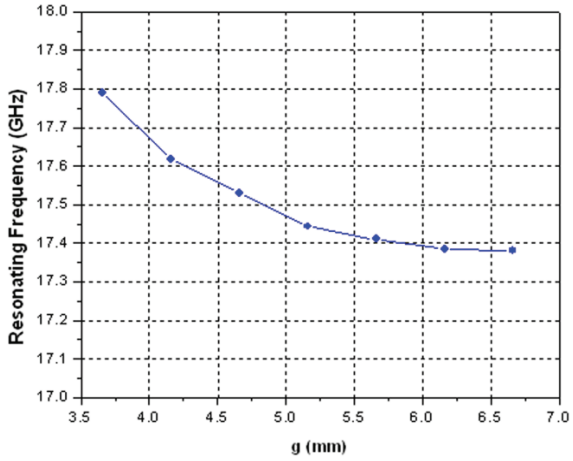

Fig. 16. Effect of slot position from end wall *g* on resonating frequency (measured).

IV. CONCLUSION

The effect of various slot offset, gap between slots and position of last slot from the end wall has been presented in details in this paper. The design comes with a microstrip to SIW transition feeding technique. Positioning of the slots has been found to have an impact over the gain as well as the return loss of the structure. The designs are fabricated and validated with the measured results. The results prove to be a direct solution to the SIW antenna design engineers for effective and accurate designs as required for different applications with consultation of the results presented in this paper, and thus, reducing time as well as human effort.

REFERENCES

[1] M. Bozzi, A. Georgiadis, and K. Wu, "Review of

substrate-integrated waveguide circuits and antennas," *Special Issue on RF/Microwave Communication Subsystems for Emerging Wireless Technologies*, doi: 10.1049/iet-map.2010.0463.

[2] G. J. Stern and R. S. Elliot, "Resonant lengths of longitudinal slots and validity of circuit representation: theory and experiment," *IEEE Transactions on Antennas and Propagation*, vol. AP-33, no. 11, Nov. 1985.

[3] M. Bozzi, F. Xu, D. Deslandes, and K. Wu, "Modeling and design considerations for substrate integrated waveguide circuits and components," *Telsiks 2007*, Serbia, Nis, Sept. 26-28, 2007.

[4] M. Henry, C. E. Free, B. S. Izqueirdo, J. Batchelor, and P. Young, "Millimeter wave substrate integrated waveguide antennas: fesign and fabrication analysis," *IEEE Trans. on Advanced Packaging*, vol. 32, no. 1, Feb. 2009.

[5] S. Cheng, H. Yousef, and H. Kratz, "79 GHz slot antennas based on substrate integrated waveguides (SIW) in a flexible printed circuit board," *IEEE Trans. on Antennas and Propagation*, vol. 57, pp. 71, 2009.

[6] A. J. Farrall and P. R. Young, "Integrated waveguide slot antennas," *IEEE Electronics Letters*, vol. 40, pp. 975, 2004.

[7] D. V. Navarro, L. F. Carrera, and M. Baquero, "A SIW slot array antenna in Ku-band," *Proceedings of the Fourth European Conference on Antennas and Propagation*, Apr. 2010.

[8] Z. Zeng, W. Hong, Z. Kuai, H. Tang, and J. Chen, "The design and experiment of a dual-band omnidirectional SIW slot array antenna," *Proceedings of Asia-Pacific Microwave Conference*, 2007.

[9] J. Liu, D. R. Jackson, and Y. Long, "Substrate integrated waveguide (SIW) leaky-wave antenna with transverse slots," *IEEE Trans. on Antennas and Prop*., vol. 60, no. 1, Jan. 2012.

[10] F. Xu, K. Wu, and X. Zhang, "Periodic leaky-wave antenna for millimeter wave applications based on substrate integrated waveguide," *IEEE Trans. Antennas Propag.*, vol. 58, no. 2, pp. 340-347, Feb. 2010.

[11] J. Wei, Z. N. Chen, X. Quing, J. Shi, and J. Xu, "Compact substrate integrated waveguide slot antenna array with low back lobe," *Antenna and Wireless Propagation Letters*, vol. 12, pp. 999-1002, Aug. 2013.

Sourav Moitra received his B.Tech (Electronics & Communication Engineering) in 2005 from the West Bengal University of Technology. He was associated with several electronics industries between 2005 to 2007. He received his M.Tech (Microwave Engineering) in 2009 from The University of Burdwan. He has been associated with the Dept. of Atomic Energy, Govt. of India on a project related to the development of high power RF tubes. At present he is associated with Dr. B. C. Roy Engineering College, Durgapur, India as Assistant Professor in the Dept. of Electronics & Communication Engineering. He has several publications in international journals and conferences. His current research interest includes design and development of microwave & millimeter wave passive circuits based on microstrip line and substrate integrated waveguides applicable in wireless networks.

Partha Sarathee Bhowmik obtained his B.Tech degree in Electrical Engineering from National Institute of Technology, Agartala, India in 2000 and M.Tech degree from The University College of Technology, University of Calcutta, India in 2002. He received his Ph.D. (Engineering) from Jadavpur University in 2015. Currently he is employed as Assistant Professor in the Dept. of Electrical Engineering, National Institute of Technology, Durgapur. His current research includes in energy system engineering, numerical computation of electrostatic fields, RF and microwave engineering and advanced signal processing applications in electrical machines and power system.